Author:
Hall, Charlie

Title:
Novel Approaches to the formation of metastable polymorphs of organic molecules

Novel Approaches to the Formation of Metastable Polymorphs of Organic Molecules

Eutectics, Chalcones and Crystal Engineering

By

CHARLIE L. HALL

School of Chemistry
UNIVERSITY OF BRISTOL

A dissertation submitted to the University of Bristol in accordance with the requirements of the degree of DOCTOR OF PHILOSOPHY in the School of Chemistry.

JUNE 24, 2021

ABSTRACT

Control of the internal structure of organic crystals is paramount in producing materials functionalised in a predictable, practical and reproducible manner. This thesis explores and builds upon the current knowledge of organic crystal growth, intending to expand the tools available to crystallographers, along with testing our ability to predict the properties that crystalline materials exhibit. The first section of this work looks at developing a new tool for the crystallisation of organic materials. The first chapter highlights how the use of volatile deep eutectic solvents affords an element of crystallographic control in a variety of pharmaceuticals, including the production of the elusive form II paracetamol at room temperature and pressure, without the use of additives. Following this, the second chapter looks at the structural and thermodynamic properties of the volatile deep eutectic solvents during thermal cycling. These data were collected using the concurrent techniques of synchrotron powder X-ray diffraction and differential scanning calorimetry, which was carried out using the I12 beamline at Diamond Light Source. This analysis is the first of its type to be carried out on deep eutectic systems, allowing an insight into the fundamental structure that these mixtures exhibit at different temperatures. In particular, the formation of metastable crystalline phases during the thermal cycles is revealed, strongly supporting the hypothesis that intermediary phases can direct the crystallographic pathway of organic molecules during their formation from the volatile deep eutectic solvent medium.

The final chapter of this thesis looks at the crystallographic case study of two functionalised chalcones, which exhibit polymorphism of crystals ranging in colour across the optical spectrum. A variety of crystallographic techniques are used to acquire structural control, to analyse the crystals in terms of structural, optical and thermodynamic properties. Theoretical modelling is applied to these structures, demonstrating our current ability to predict crystalline properties using quantum chemical calculations. In particular, a new method for determining optical properties is established, which gives information about the relative shifts in absorption spectra between crystals, while also indicating the most optically-relevant bonding motifs within each structure.

DEDICATION AND ACKNOWLEDGEMENTS

The time that I have spent at the University of Bristol has been nothing less than fantastic, in no small part due to the amazing people that I have been lucky enough to have around me. I don't believe that any paragraph can give enough thanks to those that have helped me along the way during my PhD. Starting with those who have taught me the most : Simon and Jason, your enthusiasm for discovery has certainly pushed me throughout my PhD, there has been no idea too exuberant to try, and this has only ever led to a judicious admixture of enjoyment and learning. Moreover, I could not have wished for a better team to work with: Vicky, Joe, Spayne, Wil, Emily, Torsten, Julie, Julia, Nicole, Omar; thank you so much for all your support over the years. Additionally, thank you to the whole of the Magna family, who have helped tremendously with my growth throughout the PhD. Thank you, Hazel and Natalie, for your consistent help with everything concerning crystal structures and X-rays. I would also like to thank Dr Asma Buanz for teaching me about all things DSC. Outside of the academic setting, I have also had a huge amount of support and many people I have to thank for putting up with me. Dr Thomas Gauntlett Sunderson and Kat, thank you for living with me throughout my studies (I know it can't have been easy). To Mum, Dad, Alex, Tory, (an extended list full of fantastic family members), Sophie, Rocky, Honey, the whole of the generic boy band, you have managed to make this very strange year one still full of special moments and limitless support, I could not have done this without all of you.

AUTHOR'S DECLARATION

I declare that the work in this dissertation was carried out in accordance with the requirements of the University's Regulations and Code of Practice for Research Degree Programmes and that it has not been submitted for any other academic award. Except where indicated by specific reference in the text, the work is the candidate's own work. Work done in collaboration with, or with the assistance of, others, is indicated as such. Any views expressed in the dissertation are those of the author.

SIGNED: .....CHARLIE L. HALL..... **DATE:** .....09/03/2021.....

TABLE OF CONTENTS

Page

1 Introduction **1**

1.1 The Crystalline State . . . 1

1.1.1 Types of Crystalline Structures . . . 2

1.1.2 Describing Crystal Structures . . . 3

1.1.3 Emergent Properties of Materials: Pharmaceutical Relevance . . . 6

1.2 The Thermodynamics of Crystal Formation . . . 6

1.2.1 The Stability of The Crystalline State . . . 6

1.2.2 Polymorphism . . . 10

1.3 The Kinetics of Crystal Formation . . . 11

1.3.1 Nucleation . . . 11

1.3.2 Crystallisation of Metastable Polymorphs . . . 14

1.4 Crystal Morphology . . . 14

1.5 Novel Approaches to the Controlled Formation of Crystal Polymorphs . . . 16

2 Experimental and Computational Techniques **19**

2.1 Crystallisation . . . 19

2.1.1 Materials . . . 19

2.1.2 Glassware Cleaning . . . 19

2.1.3 Crystallisation Methods . . . 19

2.2 Structural Analysis of Crystals . . . 20

2.2.1 Diffraction of Crystals . . . 20

2.2.2 Calculating Powder Patterns . . . 20

2.2.3 Rietveld Refinement . . . 23

2.2.4 Single-Crystal X-ray Diffraction . . . 23

2.2.5 Solving Crystal Structures Via Electron Diffraction . . . 23

2.3 Optical Spectroscopy . . . 24

2.4 Differential Scanning Calorimetry . . . 25

2.4.1 Modulated Differential Scanning Calorimetry . . . 25

2.4.2 Concomitant Synchrotron X-ray Diffraction and Differential Scanning Calorimtery . . . 25
2.5 Nuclear Magnetic Resonance Spectroscopy . . . 27
2.6 Computational Analysis . . . 27
2.6.1 Visualisation Tools . . . 27
2.6.2 Molecular Optimisations Using ORIENT . . . 27

3 Volatile Deep Eutectic Solvents 29
3.1 Interactions in Solution as a Crystal Engineering Tool . . . 29
3.2 Ionic Liquids and Deep Eutectic Solvents . . . 30
3.3 Deep Eutectic Solvents Containing a Volatile Component . . . 32
3.4 The Control of Polymorphism in Paracetamol . . . 34
3.5 Form III Benzamide from Volatile Deep Eutectic Solvents . . . 42
3.6 Phenol as a Solvate Molecule . . . 44
3.7 Other Molecules Forming Volatile Deep Eutectic Solvents . . . 48
3.7.1 Formation of Glasses in Verapamil Hydrochloride Volatile Deep Eutectic Solvents 48
3.7.2 2-Methoxybenzamide Volatile Deep Eutectic Solvents . . . 50
3.7.3 Estradiol - A Hydrate Forming Volatile Deep Eutectic Solvent . . . 51
3.7.4 Metaxalone, Metacetamol and Orthocetamol Volatile Deep Eutectic Solvents 52
3.8 Summary . . . 53

4 Metastable Crystalline Phase Formation in Deep Eutectic Systems 55
4.1 Differential Scanning Calorimetry . . . 55
4.2 The Phase Behaviour of Deep Eutectic Solvents . . . 57
4.3 Thermograms of Volatile Deep Eutectic Solvents . . . 59
4.3.1 Preliminary Screening Using Phenol:Paracetamol Volatile Deep Eutectic Solvents 59
4.3.2 Screening of Volatile Deep Eutectic Solvent Thermograms . . . 61
4.3.3 Paracetamol . . . 62
4.3.4 Benzamide . . . 63
4.3.5 2-Ethoxybenzamide . . . 64
4.3.6 2-Methoxybenzamide . . . 64
4.3.7 Metacetamol . . . 65
4.4 Metastable Phases in Volatile Deep Eutectic Solvents . . . 66
4.4.1 Concomitant Synchrotron X-Ray Diffraction and Differential Scanning Calorimtery . . . 67
4.4.2 CXRD-DSC of Phenol:Metacetamol VODES . . . 69
4.4.3 CXRD-DSC of Phenol:2-Ethoxybenzamide VODES . . . 72
4.4.4 CXRD-DSC of Phenol:Benzamide VODES . . . 75
4.4.5 Evaluation of CXRD-DSC Results . . . 78

4.5 Summary 84

5 Colour in Dimethylamino, Nitro Substituted Chalcones 85
5.1 Colour and Polymorphism 85
5.2 Crystallisation of Chalcones 91
5.3 Polymorphism in Gm8m and Gm8p 94
5.3.1 Synthesis 94
5.3.2 Polymorph Screening 95
5.3.3 3D Electron Diffraction and Crystal Structure Prediction on the Third Polymorph of Gm8p 103
5.3.4 UV-Vis Spectroscopy 105
5.3.5 Fluorescence Spectroscopy 110
5.3.6 Thermal Analysis 113
5.3.7 Computational Prediction of Colour 124
5.4 Conclusion 128

6 Conclusions 131
6.1 Summary and Outlook 131

A An experimental and computational study into the crystallisation propensity of second-generation sulflower 135

B Design of a Copper Crystallisation Cooling Rig 139

C Scripts for ORIENT Optimisations 141

D The Crystal Structure of Orthocetamol Solved by 3D Electron Diffraction 147

E Phase Diagrams of Volatile Deep Eutectic Solvents 149

F List of Publications 161

References 163

CHAPTER 1

INTRODUCTION

1.1 The Crystalline State

The structure of a material is inexorably linked to the fundamental properties that it exhibits. As humans, we are used to realising the macroscopic properties of the materials that we come into contact with: metals tend to be shiny, whereas woods are dull; we see sapphires as blue, whereas emeralds are green; water spreads out on a surface, whereas ice will hold the shape it is frozen in indefinitely. The extent to which we can functionalise the matter around us, to exhibit properties necessary for human survival and evolution, is directly linked to our understanding and control of the particular properties exhibited by materials.

Crystals are a group of materials with a well defined internal structure. Their uniqueness lays in the structural symmetries that they possess, which leads to a plethora of distinctive properties and possibilities. As such, in the last 400 years, we have come from the point of observing a correlation between certain uniquely faceted materials, to being able to determine the exact atomic structure of a crystal, and now to the point where it is common practice to try and predict the formation of unknown crystalline materials.

Crystalline materials are defined by the translational symmetry of a repeating motif, with the assertion that each repeating unit must be indistinguishable from all others. Consequently, the concept of a crystal is an idealism, where it is assumed that the translational symmetry extends infinitely with no defects or boundaries. Nevertheless, the length-scale of the building blocks of crystalline materials means that this approximation tends to sit very close to reality, with fundamentally powerful implications due to the simplicity of the construct far outweighing deviations within real systems.

1.1.1 Types of Crystalline Structures

Within the class of crystalline materials, there are a vast range of different properties that can be exhibited, which depend both on the building block that makes up the structure, and how it is held together in space. In general, the building blocks contain atoms, ions or molecules, held in place via covalent, ionic or weaker intermolecular forces. In the case of molecules, we define intermolecular forces (forces between different molecules) and intramolecular forces (the forces holding the atoms of the molecule together). The contrasting strength and character of these interactions are the main factors leading to crystalline materials with dramatically different properties. Moreover, there are several different ways that these interactions can be combined, each of which forming its own crystal structure sub-class.

The most frequently observed crystal structure classes are highlighted in Figure 1.1, represented in 2-dimensions for simplification. Each of the grey dashed boxes represents a repeating motif that extends infinitely in space, though only four of the repeating units are shown. A purely ionic crystal is highlighted in Figure 1.1a. Within this crystal class, electrons are transferred between atoms, leading to the formation of oppositely charged ions. Due to the discrete nature of the charges formed, the forces between ions tend to be very strong, leading to the well-known salts, such as table salt (NaCl). Similarly, Figure 1.1b depicts a covalently bonded crystal structure, where each of the connecting black lines represents a covalent bond. Covalent bonds involve the sharing of electrons between atoms and tend to be very strong, leading to the high melting point and hardness of materials like diamond.

Intermolecular forces describe interactions far weaker than pure ionic and covalent forces, occurring in part due to partial charges caused by intramolecular charge transfer and the displacement of weakly bound electrons. The interplay between intramolecular and intermolecular bonding opens up the possibility for sequential classes of crystal structures, bonding via different forces in different directions. As discussed in Desiraju's Crystal Engineering: A Textbook,[1] the idea of molecularity is a helpful tool in defining how intermolecular bonding is responsible for the translation of a crystal structure in any number of crystallographic dimensions. The degree of molecularity describes directions in which there are breaks in the covalently bonded chain of the crystal. For example, graphite is well known to exist as a crystal containing 2-dimensional sheets connected via intermolecular forces, described as having molecularity only in the direction perpendicular to the sheets.[2] Figure 1.1c shows a modification of the covalent crystal in Figure 1.1b to a crystal with molecularity in one dimension. Following this process, there becomes a point at which molecularity translates in all crystallographic dimensions. At this point, the crystal consists of molecules of finite size, each comprised of intramolecular bonds and attracted to each other by intermolecular forces. Such a crystal is known as a molecular crystal, as highlighted in Figure 1.1d. These molecular crystals can be further classified, depending on whether they contain more than one different species (co-crystals - Figure 1.1e) or contain discretely charged elements (molecular salts - Figure 1.1f). The anisotropic interactions exhibited by molecules mean that these crystals can possess various complex symmetries, leading to

vast differences caused by only marginal molecular modifications. As such, the field of molecular crystallography is accustomed to the observation of unforeseen phenomena, including disappearing structures,[3] unobtainable structures[4] (appendix A), and unsolved structures.[5]

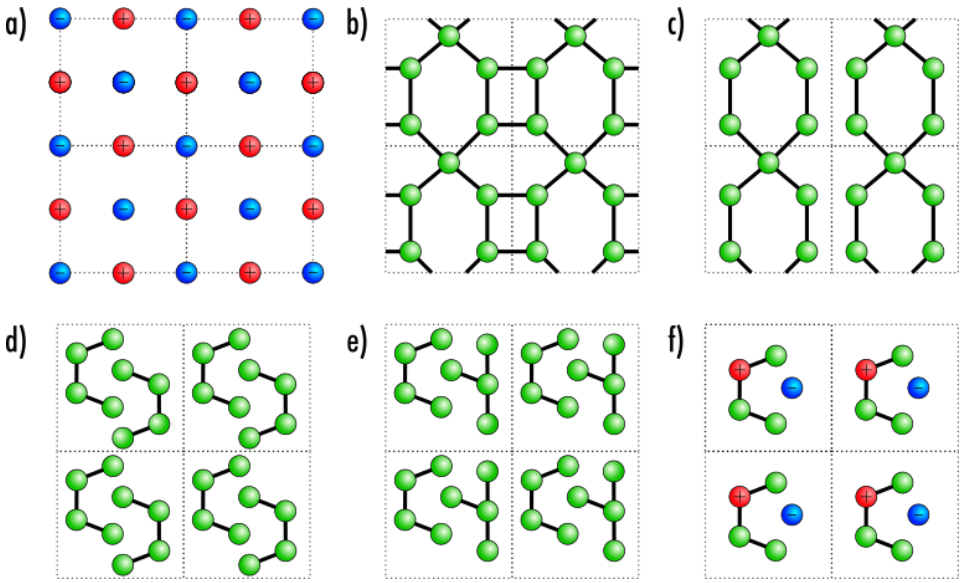

Figure 1.1: Representation of the different types of crystals in two dimensions: a) ionic crystal, b) covalent crystal, c) molecular crystal, d) covalent crystal with 1-dimensional molecularity, e) molecular co-crystal, and f) molecular salt.

1.1.2 Describing Crystal Structures

The smallest repeating motif in a crystal is known as the unit cell. The unit cell definition requires that translational symmetry leads to an unambiguous description of the crystal in space; that is, there should be no coordinate in which the crystal is not defined. The shape and size of the unit cell are defined by the parameters a, b and c, which represent the length of each side of the unit cell, and the angles α, β and γ, which represent the direction in space of the unit cell axes. These parameters are highlighted in Figure 1.2, where the unit cell axes are shown in their common colours: blue (a), green (b) and red (c). At each corner of the unit cell sits a lattice point, representing an element of the crystal that is translated in space. Arbitrarily, an origin is chosen at one of the lattice points, where the coordinates of the crystal system are chosen to be (0,0,0) in 3-dimensional space.

Within the unit cell, there may be additional symmetry elements, which include: reflections, inversions, rotations, rotary inversions, glide planes, screw axes, and additional translations. The smallest motif within the unit cell that can not be reduced via symmetry relationships is the asymmetric unit. A combination of the asymmetric unit with the symmetry, angles and lengths of the unit cell gives a full representation of a crystal structure. Additional translational symmetry within the unit cell is known as cell centring. Given that the asymmetric unit is placed at the origin, additional lattice points can occur in the centre of the unit cell or at the centre of the faces of the unit cell. The

possible cell centring follows the notation: P - primitive, I - body centred, F - all face centred, A or C - face centred, as shown in Figure 1.3.

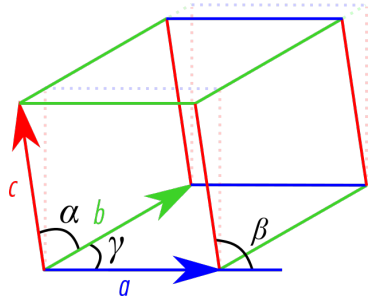

Figure 1.2: Unit cell parameters in 3-dimensional space, highlighting the unit cell lengths a, b and c, and angles α, β and γ.

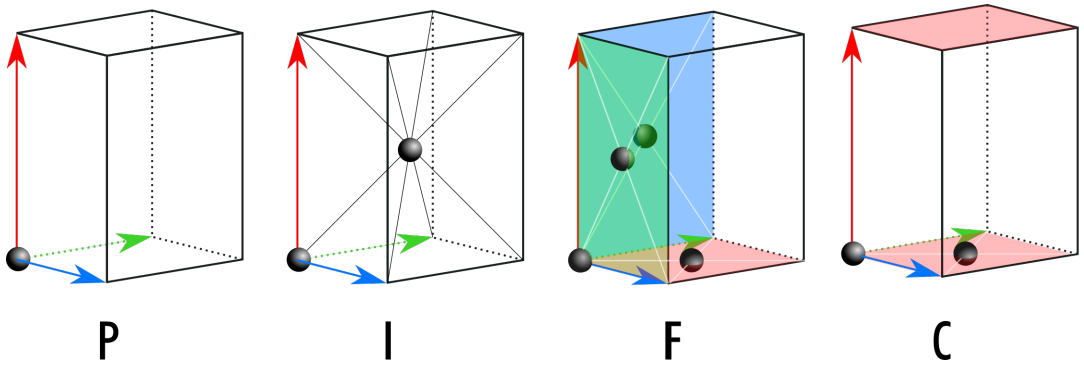

Figure 1.3: The possible crystallographic centring that can occur: P - primitive, I - body centred, F - all face centred, A or C - face centred.

Restriction of the unit cell parameters reduces the number of possible crystallographic symmetries that can occur. For example, if none of the unit cell angles are equal to 90°, then the only available symmetry within the unit cell is an inversion. Such a crystal is said to be in the triclinic crystal system. The full mathematical description of the possible symmetries that can occur within a unit cell has an interesting history, with several iterations of the possible groups suggested[6] before the, now well-established, 230 space groups were determined.[7] These space groups are distributed across seven crystal systems, each representing a restriction of the unit cell parameters. A summary of the possible crystal systems is given in Table 1.1. Within crystallography, a well-established notation for the 230 space groups exists, highlighting the centring of the unit cell and any symmetries that occur with respect to each of the crystallographic axes. An example of space group notation is shown in Figure 1.4.

Table 1.1: Crystal systems grouped by valid point group operations, including the possible cell centring for each.

Crystal System	Cell Lengths	Cell Angles	Primitive (P)	Body Centred (I)	Face Centred (F)	Base Centred (C)
Triclinic	a, b, c	$\alpha \neq 90°$ $\beta \neq 90°$ $\gamma \neq 90°$	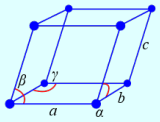	Triclinic (P)	Triclinic (P)	Triclinic (P)
Monoclinic	a, b, c $a \neq c$	$\alpha = 90°$ $\beta \neq 90°$ $\gamma = 90°$	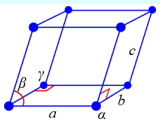	Monoclinic (C)	Monoclinic (C)	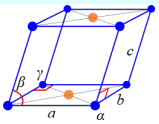
Orthorhombic	a, b, c $a \neq b \neq c$	$\alpha = 90°$ $\beta = 90°$ $\gamma = 90°$	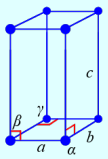	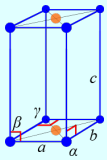	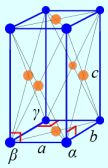	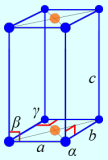
Tetragonal	a, b, c $a = b \neq c$	$\alpha = 90°$ $\beta = 90°$ $\gamma = 90°$	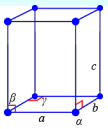	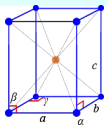	Tetragonal (I)	Tetragonal (P)
Trigonal	a, b, c $a = b = c$	$\alpha = 90°$ $\beta = 90°$ $\gamma \neq 90°$	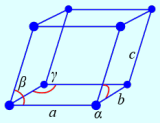	Trigonal (P)	Trigonal (P)	Trigonal (P)
Hexagonal	a, c	$\gamma = 120°$	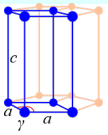	Monoclinic (C)	Orthorhombic (P)	Monoclinic (C)
Cubic	a, b, c $a = b = c$	$\alpha = 90°$ $\beta = 90°$ $\gamma = 90°$	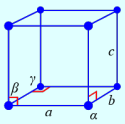	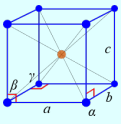	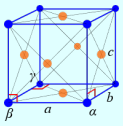	Tetragonal (P)

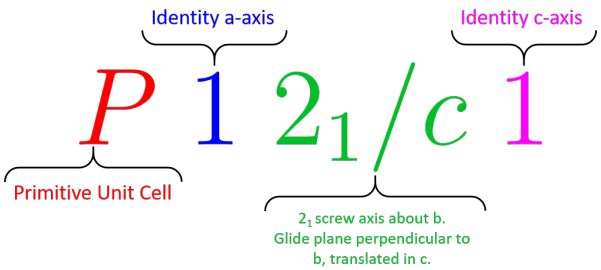

Figure 1.4: A description of the notation of the space group $P2_1/c$, given in the long-hand notation $P\,1\,2_1/c\,1$

1.1.3 Emergent Properties of Materials: Pharmaceutical Relevance

Within this thesis, I will be focused on the discussion of the crystallisation of molecular compounds. In this subset of crystals, the covalent forces acting between a finite group of atoms allows them to be considered as an independent chemical species.[8] This entity in itself may be constructed to exhibit certain bespoke properties, such as pharmaceutical[9] or agrochemical[10] potency. However, our utilisation of such molecules is dependent on how well we can control their properties in the solid-state. In particular, I will focus on molecules that are effective as active pharmaceutical ingredients (APIs), which interact with the human body to gain a positive medicinal outcome. The molecularity of these crystals extends in all three spatial dimensions, meaning that their melting or solubilisation leads to a mobile form of the API that the human body can absorb.

The formulation of a new small-molecule pharmaceutical will inevitably go through the process of finding an optimum solid-state structure. This optimisation should consider the solubility of the final form, the purity of the crystal after formation, the processability of the drug, and the stability of both the molecule in the crystal and the crystal structure itself.[11] Large numbers of potentially life-saving drugs never progress through solid-state formulation due to their low water solubility (bioavailability), which is proportional to the strength of the interactions present between molecules in the crystal structure. Additionally, the optical properties of pharmaceutical crystals are critical for both consumer compliance in taking the drugs,[12] and utilisation for unique purposes such as in biologically active tracers.[13] Hence, our ability to control the properties of APIs in the solid-state has far-reaching implications for our capacity to expand the tools available within healthcare.

1.2 The Thermodynamics of Crystal Formation

The most basic understanding of the crystalline state emerges from the laws of thermodynamics. As a system tends towards absolute zero, the most stable state of a pure substance that can exist is a perfect crystalline structure. This crystalline stability is a consequence of the minimisation of the entropy of the system, that is, the number of possible micro-states that can exist.[14] Therefore, to understand the properties of crystals at a finite temperature, it is necessary to determine how the system increases in internal energy as it is heated.

1.2.1 The Stability of The Crystalline State

The equilibrium state of a system can be understood in terms of the state functions known as thermodynamic potentials. When considering systems at constant pressure, it is common to use the Gibbs Free Energy, given by the equation,

$$G = H - TS, \tag{1.1}$$

where H is the enthalpy, T is the temperature, and S is the entropy of the system. At any given temperature, the system will minimise the Gibbs Free Energy,

$$\left.\frac{\partial G}{\partial t}\right|_{T,p} \leq 0, \tag{1.2}$$

where t is time, and p is pressure, which allows a theoretical basis to the understanding of phase transitions.[15]

When a material is heated at constant pressure, it absorbs heat equal to the enthalpy change needed to raise the temperature by a certain amount. The rate of the enthalpy change of a material with respect to temperature is known as the specific heat capacity C_p (the p subscript is used when assuming a system at constant pressure). The additional energy in the system will also cause an increase in entropy due to the accessibility of extra micro-states. The enthalpy and entropy of a particular phase at temperature T can be written as,

$$H(T) = \int_0^T C_p(T')dT', \tag{1.3}$$

$$S(T) = \int_0^T \frac{C_p(T')}{T'}dT'. \tag{1.4}$$

The difference in Gibbs Free Energy between the crystalline and liquid states can be determined by calculating the differences in enthalpy and entropy between them,

$$\Delta G^{c,l}(T) = \Delta H^{c,l}(T) - T\Delta S^{c,l}(T), \tag{1.5}$$

where the superscript c,l represents the difference between the crystalline and liquid states. As the crystalline phase has the lowest entropy at absolute zero, this is the state that we observe at low temperatures. Figure 1.5 shows the characteristic trend in Gibbs Free Energy and entropy as a material is heated past its melting (T_m) and vaporisation (T_v) temperatures. At each of the phase transitions, there is a discontinuity in the entropy of the system. As the Gibbs Free Energy at the temperature of the phase transition must be equal to zero, this change is given by,

$$\frac{\Delta S^{c,l}(T_m)}{T_m} = \Delta H^{c,l}(T_m). \tag{1.6}$$

At the transition temperature, the entropy of the system can increase by $\Delta H^{c,l}(T_m)$, which is known as the enthalpy of fusion.

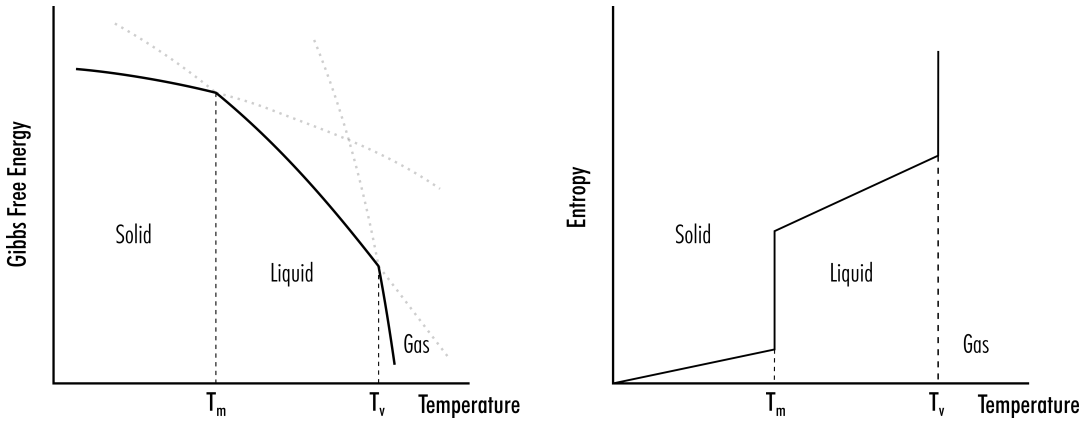

Figure 1.5: Graphical representations of the Gibbs Free Energy and the entropy of a material as it is heating through the solid, liquid and gas phases.

A mathematical description for the difference in Gibbs Free Energy between the solid and liquid states can be determined by constructing a Hess diagram of the process, involving the heating, melting and cooling of the crystalline solid, as shown in Figure 1.6. Following this cycle leads to the expressions,[16]

$$\Delta H^{c,l}(T) = \underbrace{\int_T^{T_m} C_p^c(T')dT'}_{\mathbf{1}} + \underbrace{\Delta H_m}_{\mathbf{2}} + \underbrace{\int_{T_m}^{T} C_p^l(T')dT'}_{\mathbf{3}} = \int_T^{T_m} \Delta C_p^{c,l}(T')dT' + \Delta H_m, \tag{1.7}$$

$$\Delta S^{c,l}(T) = \underbrace{\int_T^{T_m} \frac{C_p^c(T')}{T'}dT'}_{\mathbf{1}} + \underbrace{\frac{\Delta H_m}{T}}_{\mathbf{2}} + \underbrace{\int_{T_m}^{T} \frac{C_p^l(T')}{T'}dT'}_{\mathbf{3}} = \int_T^{T_m} \frac{\Delta C_p^{c,l}(T')}{T'}dT' + \frac{\Delta H_m}{T}, \tag{1.8}$$

which are commonly used in the pharmaceutical industry to determine solid-state stability as a function of temperature. These expressions simply rely on the determination of the specific heat capacity of a material and its liquid form, and the enthalpy of fusion.[17] An archetypal graph of $\Delta G^{c,l}$ as a function of temperature is shown in Figure 1.7. The point at which $\Delta G^{c,l}$ goes below zero represents the melting point of the crystal T_m, at which point the enthalpy of fusion can be calculated as $\Delta H^{c,l}$.

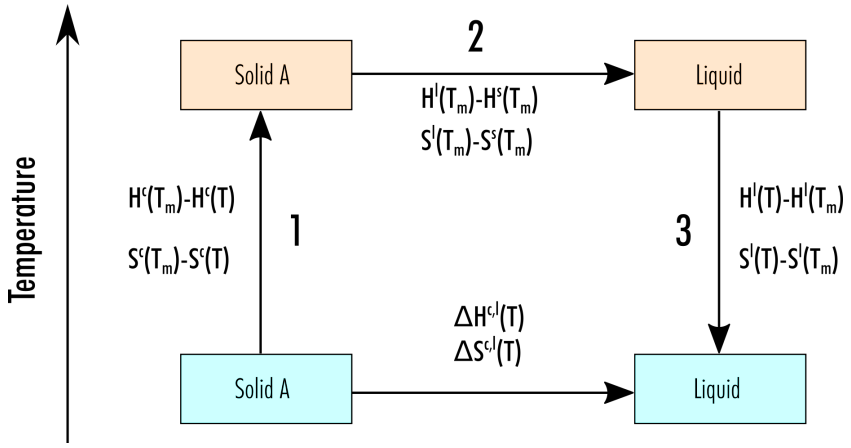

Figure 1.6: Hess cycle for calculating the Gibbs Free Energy difference between the crystalline and liquid states of a material. The numbers represent which terms in equations 1.7 and 1.8 each step of the cycle represents.

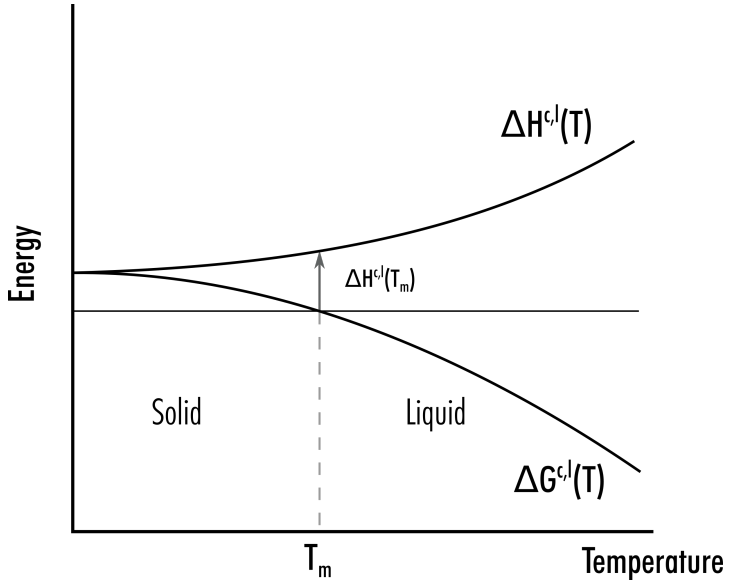

Figure 1.7: The difference in Gibbs Free energy and enthalpy of the solid and liquid states of a material as a function of temperature. The horizontal line represents the point at which $\Delta G^{c,l}$ crosses zero, meaning a phase transition between the solid and liquid states can occur.

1.2.2 Polymorphism

Polymorphism in molecular crystals is the ability of a single molecular unit to pack in a number of different ways.[18] This phenomenon has many implications for the solid-state formulation of crystals, as even small changes in intermolecular interactions can change a variety of properties, including the colour,[19] solubility[20] and processability[21] of a material. A simple two-dimensional representation of polymorphism is shown in Figure 1.8, highlighting two different valid crystallographic structures of the same repeating motif. Strictly speaking, this type of polymorphism is termed 'packing polymorphism'[22] to differentiate it from structural differences where molecular flexibility allows the molecules to change conformation, known as 'conformational polymorphism'.[23]

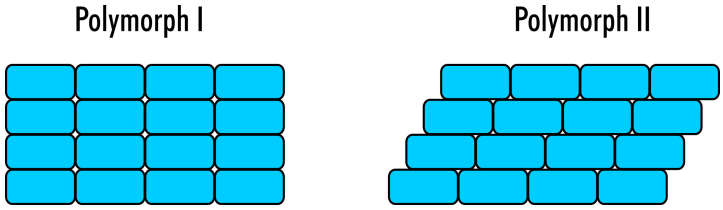

Figure 1.8: An example of packing polymorphism using a simple repeating motif in two dimensions.

The relative stability of the polymorphic forms of a molecule is temperature-dependent, much like the relative stability of the crystalline and liquid states discussed in the previous section. A crystal structure that is not the most stable at a particular temperature is defined as metastable. The lifetime of a metastable polymorph can vary dramatically depending on how easily the molecules can rearrange to form the necessary bonding motifs for a solid-state transformation. Polymorphs whose relative stability cross over with temperature are known as enantiotropic, and those with no such cross-over are termed monotropic. Examples of Gibbs Free Energy curves for monotropic and enantiotropic systems are shown in Figure 1.9. The idealised plots were created using specific heat capacities calculated from the Debye model,[24] along with equations 1.1, 1.7 and 1.8. Given enough mobility, an enantiotropic system will reversibly convert between polymorphic forms at a transition temperature (T_t), at which point a change in enthalpy ΔH_t will be observed. In a monotropic system, an irreversible transformation to a lower energy polymorph will only be seen if the thermal energy of the system can overcome any energy barrier caused by the restricted movement of molecules in the crystal structure.

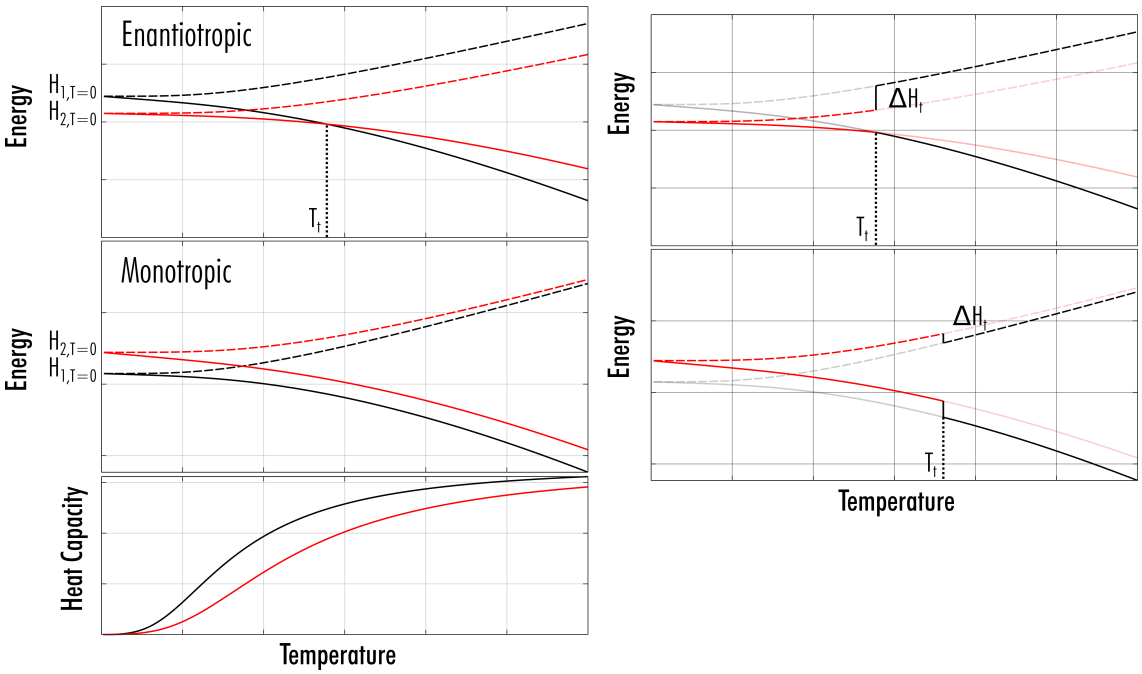

Figure 1.9: Graphs of the Gibbs Free Energy (solid lines) and enthalpy (dashed lines) against temperature for two crystal polymorphs (red and black lines). The top graphs show an enantiotropic behaviour with the Gibbs Free Energy crossing over. The bold lines on the right-hand graph highlight a possible transition between the two structures on heating from 0 K. Below this, a similar plot is shown for a monotropic system. The right-hand graph of the monotropic system assumes that the original crystal is metastable (red). The bottom graph shows the heat capacities used to produce the graphs, calculated using the Debye model.

1.3 The Kinetics of Crystal Formation

The rules of thermodynamics highlight the conditions under which the crystalline state is most stable at equilibrium. However, the molecular order necessary in such systems and the ideas of polymorphism highlight that observable systems are not always present in their equilibrium state. Crystallisation, the formation of a crystalline material, occurs via the process of nucleation from a system where molecules have enough mobility to rearrange into a more stable structure. The driving force leading to the formation of a crystalline material is known as supersaturation. When crystallisation occurs using a solvent medium, the two main ways of producing a supersaturation are cooling or evaporation of a saturated solution. These processes are highlighted in Figure 1.10.

1.3.1 Nucleation

The process of nucleation involves an energy barrier in going from a disordered to an ordered state. In general, this energy barrier can be thought of as the energetically unfavourable formation of a surface,

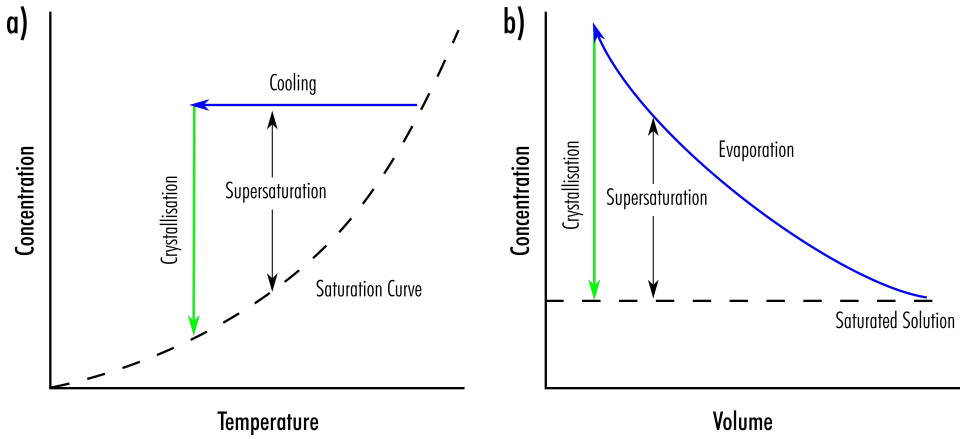

Figure 1.10: Graphs highlighting the formation of a supersaturated solution from a saturated solution via a) cooling and b) evaporation.

which causes surface tension. A basic understanding of nucleation is given by classical nucleation theory (CNT), which assumes a stabilisation force proportional to the volume of a sphere and a destabilisation force proportional to the surface area,

$$\Delta G^{CNT} = \frac{4}{3}\pi r^3 \Delta G^V + 4\pi r^2 \Delta G^S \tag{1.9}$$

where ΔG^{CNT} is the difference in Gibbs Free Energy between the nucleus and the disordered system, r is the radius of the sphere, ΔG_V is the loss of free energy due to the formation of the nucleus per unit volume, and ΔG_S is the gain of free energy due to the formation of a surface per unit area. A plot of the free energy of a nucleus as a function of its diameter is shown in Figure 1.11, where the surface and bulk free energy functions are included as dashed and dotted lines respectively. The radius at which ΔG^{CNT} is at a maximum is known as the critical radius,

$$r^c = \left| \frac{2\Delta G^S}{\Delta G^V} \right|, \tag{1.10}$$

as a nucleus reaching this size via thermal fluctuations can grow indefinitely without increasing the Gibbs Free Energy of the system. The simplistic view of CNT is not without flaws, rarely describing the nucleation rates of real systems with any degree of accuracy, and often relying on additional corrections in the energy terms.[25] Even with corrections for the differing shapes and bonding strengths present in molecular crystalline systems, it has become clear that it is necessary to consider nucleation processes that rely on several steps.[26] Such nucleation theories are known as non-classical nucleation theories (NCNTs), which have seen a recent increase in interest due to an improvement in our ability to observe processes on the length-scale of a single crystal nucleus.

The most recent understanding of NCNTs is a combination of the ideas of two-step nucleation theory (TSNT)[27,28] and pre-nucleation clusters (PNCs).[29] TSNT describes the formation of a stable, dense cluster within the crystallisation medium prior to crystallisation. This cluster may have some of the interactions present in the final crystal structure; however, ordering of the molecules is needed

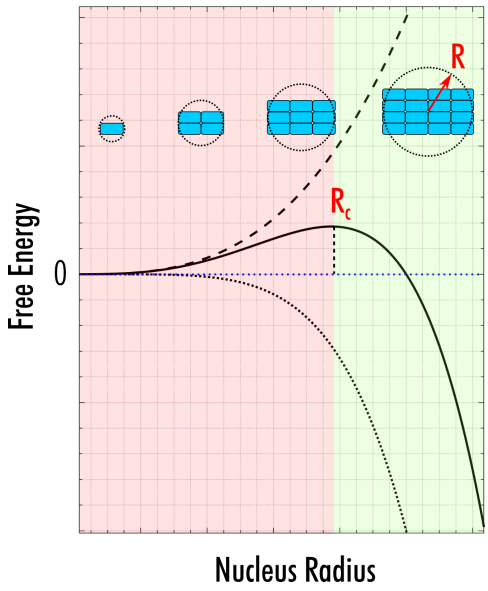

Figure 1.11: A graph of the Gibbs Free Energy of a nuclei with respect to a disordered state, as a function of nucleus radius. The critical radius of the nucleus is labelled R_c

after the dense cluster is formed. TSNT is well established for the crystallisation of a number of proteins.[30] For smaller molecules forming from a solvated state, such as the APIs of interest in this work, it has become apparent that solute rich clusters often form before crystallisation.[31] These clusters can be stable for long periods of time and have recently been observed directly during the crystallisation of flufenamic acid.[32] Figure 1.12 highlights the difference in crystallographic pathways between CNT and NCNT, showing how intermediate clusters can be stable in solution over long periods of time.

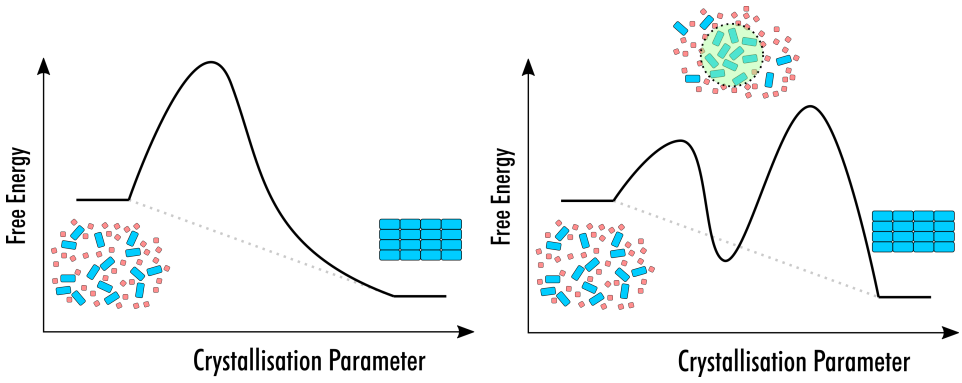

Figure 1.12: The Gibbs Free Energy of a nucleus during classical nucleation theory (left) and two-step nucleation theory (right). A dense cluster forms during two-step nucleation theory which sits in a local energy minimum, allowing the cluster to persist for long periods of time.

1.3.2 Crystallisation of Metastable Polymorphs

The complex nature of nucleation helps to give further insight as to why we observe the formation of metastable crystal structures. If we consider the ordering phase of a process following NCNT, the pre-nucleation dynamics of the molecules will determine the first crystalline structure that will form. Indeed, it has been shown that changes in pre-nucleation clusters can directly affect the dynamics of crystallisation.[33] If the first crystal structure to grow is metastable, it may transform or persist depending on the similarity of the other possible polymorphs, and how big the transformation energy barrier is between them. This is described by the empirical Ostwald's rule of stages, which highlights that the first appearing crystalline state is often metastable.[34]

Experimentally it is not possible to know if a particular polymorph of a molecule is the most stable structure; all that is known about a particular polymorph is whether it is the most stable known polymorph at a specified temperature. This fact can have far-reaching consequences. A common example of the implications of metastable polymorphs is that or Ritonavir,[35] an antiretroviral medication used in the treatment of HIV/AIDS, which was initially distributed in the solid-state in the only known crystal structure, form I. The form I structure turned out to be metastable with respect to another form, form II, which was less soluble. The appearance of this new polymorph led to lower bioavailability of the drug, forcing production to be halted. Occurrences such as this now mean that it is now commonplace to rigorously investigate the polymorphic landscape of drugs before they are moved forwards in production.[36]

Knowledge of the polymorphic landscape of a drug can be a powerful tool during solid-state formulation. Not only can it help prevent the formation of unknown structures, but it can also be used to search for potential long-lived metastable structures that may have improved material properties, such as bioavailability[37] and processability.[38] Computationally it is becoming common practice to search for the possible polymorphs of an API using crystal structure prediction (CSP),[39] allowing both a level of confidence that the lowest energy polymorph has been found, and the ability to suggest possible metastable polymorphs to try and crystallise experimentally. The outcome of these calculations is complex; many more polymorphs are predicted computationally by CSP than are seen via crystallisation experiments. The reasoning behind this is clearly laid out by Price,[40] who states that the necessary solution is in both improving our experimental capability to search for new polymorphs and our ability to rank the energies of the crystal structures at finite temperatures computationally.

1.4 Crystal Morphology

When considering the thermodynamic properties of crystalline materials, it is often useful to use the idealised picture of a material that extends infinitely in space and ignore the implications of not accounting for the boundaries that must occur in reality. However, discussion of crystal nucleation dynamics highlights that the finite size of such a material must be considered for a full kinetic

understating. Moreover, the anisotropy present in crystalline materials means that they rarely grow at equal rates in all directions, and their properties can differ depending on the particular crystal faces exposed.

One of the first observations of crystalline materials, before their internal structure was even understood, is that their edges are faceted, forming at specific angles. These facets are caused due to crystals cleaving down lattice planes and were the first indication of the internal structure of the crystalline state.[41] The morphology of a crystal is dependent on the growth rate in each of the crystallographic directions. The faster a crystal grows perpendicular to a particular plane, the less of that plane will be present in the final morphology. A general set of morphological rules were set out by Bravais and Friedel, which stated that: the most prominent faces present in the final morphology of a crystalline material are those with the highest density of lattice points. Equally, the growth rate perpendicular to a particular plane is inversely proportional to the distance between planes.[42] This rule is valid in many systems, simply because it is less easy to attach a crystallographic unit to a plane with smaller 'gaps' for the unit to sit in. An extension to this rule was formulated by Donnay and Harker, who took into account the change in density in certain crystallographic dimensions when glide planes and screw axes are symmetrically allowed.[43] Based on these rules, one can predict the morphology of crystals from a purely geometrical perspective given the unit cell of a particular polymorph. Such calculations are common in crystallographic programs, with the prediction known as the BFDH morphology (after Bravais, Friedel, Donnay and Harker). An example of a change in crystalline morphology due to differing directional growth rates is shown in Figure 1.13a,b.

However, in many cases, the crystal morphology may differ from that proposed by the BFDH morphology due to strong intermolecular interactions between crystalline surfaces and solvent or additive molecules during crystal growth (Figure 1.13c,d). Therefore, it may be more accurate to calculate the attachment energy of a 'slice' of each of the possible planes, which gives a growth rate based on how energetically favourable it is to form a new layer of molecules. Many codes have be written to run this type of calculation and can even include solvent molecules attached at the surface, which need to be displaced to form the new layer.[44] Finally, it may be necessary to calculate the thermodynamic morphology of a crystal, which minimises the surface energy of a particular structure. This is particularly useful if crystals are left in solution and allowed to 'ripen' into their equilibrium state.

The morphology of crystals can be a significant factor for properties that are dependent on the orientation of the unit cell, such as conductivity and refractive index. Most importantly in the pharmaceutical industry, crystalline morphology can affect the processability of the final API form due to changes in flowability[45] and surface adhesion.[46] In general, the formation of needle-like crystals is undesired due to the large surface areas they exhibit. As such, many studies have looked into changing the morphology of grown crystals by modifying crystallisation conditions, such as the tuning of solvent crystallisation media,[47–49] additives[50–53] and temperature profiles.[54]

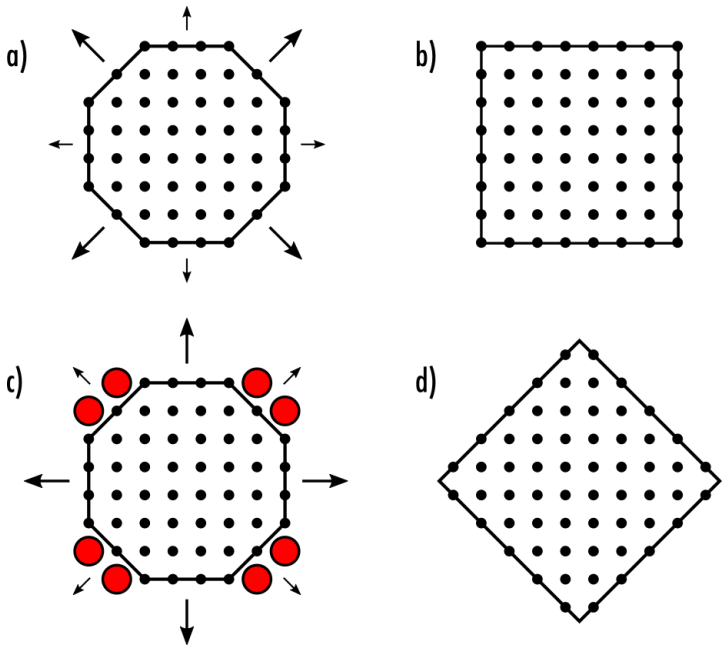

Figure 1.13: A 2-dimensional representation of the effect of differing crystal growth rates on the final crystalline morphology. a) Example growth rates expected from the BFDH morphology rules. The less-dense faces grow more rapidly, leading to the crystal morphology shown in b). c) A representation of the effect of slowing the growth rate at certain faces due to solvent or additive attraction. This modification to the growth rates leads to the morphology shown in d).

1.5 Novel Approaches to the Controlled Formation of Crystal Polymorphs

Given the detrimental implications of a late-forming metastable polymorph, along with the possibilities of control of material properties if long-lived metastable structures can be discovered, it is not surprising that the study of polymorphic control in organic crystal systems is an area of a tremendous amount of modern cutting-edge research. The ability for minimal changes in crystallisation conditions to change the polymorph of a molecular crystal means that pharmaceutical companies must perform thorough crystallographic screening studies before an API can be sold commercially.[55] These screens involve crystallisation of the target API in an array of solvents,[56,57] including binary and higher-order mixtures,[58] which are used as crystallisation media. The crystallisation process within these systems is highly dependent on how supersaturation is achieved,[59,60] and any polymorphic changes after initial crystallisation must be carefully tracked[61,62] to ensure stability.

Beyond the well-established methods for polymorph screening that are used industrially, there are a plethora of alternative methods that have been studied in the search for structural control of organic crystals. Recent advances in applying pressure to organic systems have allowed pressure-temperature phase diagrams to be produced, highlighting a number of high-pressure polymorphs[63–65] and polymorphic phase transitions.[66] The application of external fields has also shown promise as

a method for polymorphic control, utilising strong electric fields[67,68] or lasers with carefully chosen polarisation.[69,70] Similarly, the application of external magnetic fields was shown to cause a polymorphic change in the polyaromatic hydrocarbon coronene.[71]

Recent studies have looked into the production of new polymorphs using premeditated templates, such as modified growth surfaces.[72–77] This polymorphic control relies on seeding the growth of polymorphs by forcing the initial heterogeneously-grown layers of molecules to form a particular packing motif, which seeds subsequent growth. Work by Price built on this work, using CSP on molecules in the fenamate family to determine possible structural similarities. Using these similarities, previously experimentally-unrecognised polymorphs were successfully seeded.[78]

The use of templates to control polymorphism utilises the favouring of certain bonding motifs in the region of the template. In a sense, this is likely very similar to what happens when solvent interactions control polymorphism; it is just that one needs to find the correct system to achieve the desired intermolecular interactions. The difference is that the interactions with the solvent will be happening across the whole system, whereas templated growth can only occur at the template surface. An intermediary between these systems is the formation of viscous, tightly-bound solutions, where interactions between the target molecule and solvent are strong, but not so strong that co-crystals form or molecular mobility is completely halted. An example of this is the polymorphic control that has been seen by utilising supra-molecular gels,[79,80] and via the heating of molecules in their glassy state.[81]

The first two experimental chapters of this thesis will look at a novel route towards crystallographic control, which utilises low-melting mixtures of materials known as deep eutectic solvents. The first chapter will highlight how crystallisation is achieved in these systems, leading to crystallographic control of a number of APIs. The second chapter will look more deeply into the formation of the deep eutectic systems, highlighting how it is likely that metastable solvates are mediating crystal growth of the final API product.

The final chapter of the thesis looks at another set of molecules known as chalcones, which sit as the backbone to several pharmaceutically active molecules. This chapter looks at the occurrence of colour in a set of polymorphic chalcones, which is compared to a new computational method of predicting the colour of organic crystals.

CHAPTER 2

EXPERIMENTAL AND COMPUTATIONAL TECHNIQUES

2.1 Crystallisation

2.1.1 Materials

All materials were all purchased from chemical suppliers, and care was taken during crystallisation experiments to minimise contamination of samples. Paracetamol (Sigma: A7085, >99%), benzamide (Sigma: 135828, >99%), estradiol (Sigma: E8875, >98%), 2-ethoxybenzamide (Alfa Aesar: B25455, >97%), 2-methoxybenzamide (Alfa Aesar: A12520, >98%), verapamil hydrochloride (Sigma: V4629, >99%) and phenol (Sigma: P1037, >99%) were all purchased and stored in a fridge below 10 °C. Crystallisation experiments were carried out in dry, pure solvents (>99%) purchased from Sigma to avoid the unwanted formation of hydrate crystal structures. Laboratory grade solvents were used during cleaning procedures.

2.1.2 Glassware Cleaning

All glassware to be used for crystallisation experiments was cleaned thoroughly before use. New glassware was cleaned with de-ionised water, acetone, and ethanol, respectively before use, and kept in a 65 ° C oven to dry. Any reused glassware was first thoroughly cleaned with soap and water.

2.1.3 Crystallisation Methods

All crystallisation was carried out in a temperature and humidity controlled room. Temperature and humidity were constantly recorded so that any anomalous crystallisation results could be attributed to atmospheric changes if necessary. Prior to experiments, solutions of desired concentration were prepared in sealed vials at the required temperature for the start of the crystallisation experiment.

Solvent volumes were measured using an M1000E Gilson Microman. Solid samples were weighed using a Fisherbrand analytical 4-point scale.

Cooling crystallisation experiments were carried out using a copper sample holder designed to house six test tubes. The blocks were cooled by a Julabu water bath via internal pipes. De-ionised water mixed with 20% glycerol (by mass) was used to reduce the freezing point of the coolant water. Using this system, samples could be cooled and heated between -10 °C and 80 °C using the Julabu EasyTEMP Professional (Version: 3.10.1) software. The design of the cooling apparatus is highlighted in Appendix B.

2.2 Structural Analysis of Crystals

2.2.1 Diffraction of Crystals

Powder X-ray diffraction (pXRD) data were collected using a Bruker D8 Advance diffractometer with an X-ray wavelength of 1.5418 Å (Cu-Kα), using a PDS LynxEye detector attachment. Before measurements, samples were powdered using a pestle and mortar to reduce the preferential orientation of crystallites. A low-background silicon wafer holder was used to reduce any background signal. Unless stated, scans were taken over the 2θ range 5-50° at a rate of 0.75°·min^{-1} and compared to simulated patterns using the Mercury software package.[82] Low-temperature diffraction experiments were carried out using a Phenix sample stage, allowing data to be collected between 12 K and 300 K.

Single crystal X-ray diffraction data were acquired using a Bruker Apex II CCD diffractometer with an X-ray wavelength of 0.71073 Å (Mo-Kα). Unless stated, the temperature of the crystal was held at 100 K to reduce the thermal motion of the atoms. Intensities were integrated in SAINT,[83] and absorption corrections based on equivalent reflections were carried out using SADABS.[84] Structural solution was performed in Olex2[85] using Superflip[86,87] and refined in SHELXL.[88]

2.2.2 Calculating Powder Patterns

A basic understanding of X-ray crystallography can be acquired on the basis of Bragg reflection. Incoming X-rays are reflected by the planes of a crystal, producing a diffraction pattern following Bragg's Law,

$$n\lambda = 2d\sin\theta, \tag{2.1}$$

where n is an integer, λ is the X-ray wavelength, d is the distance between lattice planes, and θ is the angle between the incident ray and the lattice plane (Figure 2.1). Powder samples are prepared by grinding crystals small enough that their planes are distributed isotropically. X-rays irradiate the sample, scanning an angle 2θ. This process means that there will always be an angle that will satisfy Bragg's law for each plane.

Points within the lattice can be written in terms of direct lattice vectors,

$$\boldsymbol{R} = h\boldsymbol{a_1} + k\boldsymbol{a_2} + l\boldsymbol{a_3}, \tag{2.2}$$

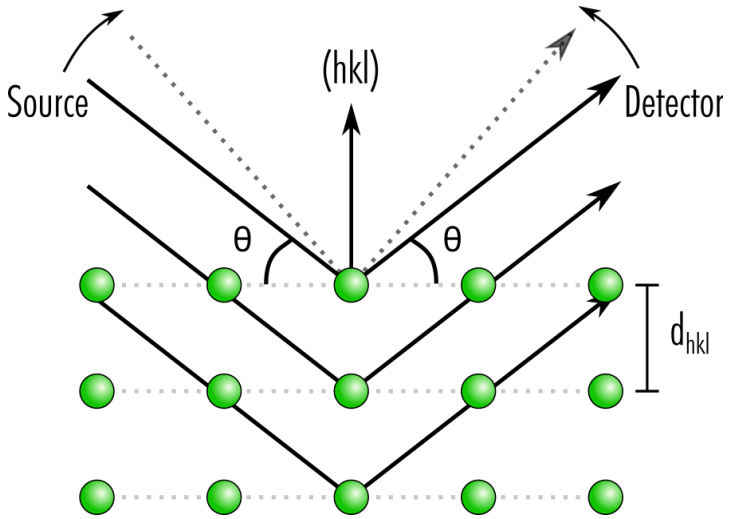

Figure 2.1: A representation of Bragg reflections leading to constructive interference in powder diffraction.

where $[h,k,l]$ are integers, and $\boldsymbol{a_x}$ are the direct lattice vectors. It then holds that $\boldsymbol{R}$ can represent every point in the lattice. As diffraction is concerned with the planes of the crystal, it is useful to transform into a system with vectors that describe such planes. This transformation leads to the well known reciprocal lattice vectors,

$$\boldsymbol{G} = h\boldsymbol{b_1} + k\boldsymbol{b_2} + l\boldsymbol{b_3}, \tag{2.3}$$

where $\boldsymbol{b_x}$ are reciprocal lattice vectors so that $\boldsymbol{G}$ contains information for all the possible planes of the crystal. The reciprocal lattice vectors are defined so that their magnitudes are inversely proportional to the distance between the planes,

$$\boldsymbol{b_1} = \frac{2\pi \boldsymbol{a_2} \times \boldsymbol{a_3}}{V} = \frac{2\pi \hat{\boldsymbol{b_1}}}{d_{100}}, \quad \boldsymbol{b_2} = \frac{2\pi \boldsymbol{a_3} \times \boldsymbol{a_1}}{V} = \frac{2\pi \hat{\boldsymbol{b_2}}}{d_{010}}, \quad \boldsymbol{b_3} = \frac{2\pi \boldsymbol{a_1} \times \boldsymbol{a_2}}{V} = \frac{2\pi \hat{\boldsymbol{b_3}}}{d_{001}}, \tag{2.4}$$

where V is the volume of the unit cell, and d_{hkl} is the distance between the (hkl) planes. Directions in real space are given by Miller indices, denoted using square brackets - $[hkl]$ and directions in reciprocal space given in curved brackets - (hkl). Figure 2.2 highlights the definition of reciprocal and real space lattice vectors along with examples of Miller indices.

Given reciprocal lattice vectors, incident X-ray angles that give rise to constructive interference can be calculated,

$$\sin\theta = \frac{n\lambda}{2d} = \frac{|\boldsymbol{G_{hkl}}|n\lambda}{4\pi}, \tag{2.5}$$

where hkl are miller indices denoting a particular plane.

To calculate the intensities of the constructive interference, the position of atoms in the crystal must be considered. Each atom will contribute to the interference of the X-rays, causing a phase change. This phase change is accounted for by the structure factor,

$$\boldsymbol{F_{hkl}} = \sum_j f_j e^{2\pi i(hx_j + ky_j + lz_j)} \tag{2.6}$$

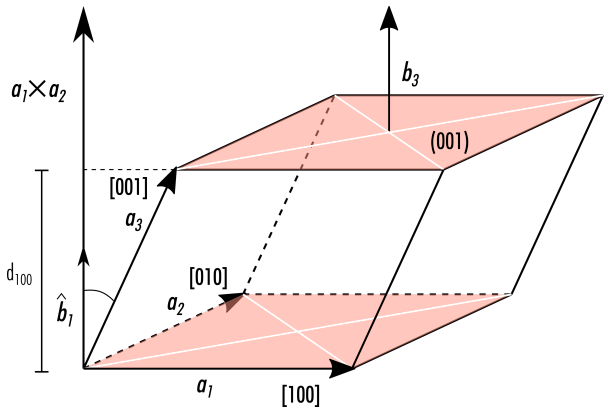

Figure 2.2: Example unit cell highlighting the definition of real space and reciprocal space vectors. The cross product $\boldsymbol{a_1} \times \boldsymbol{a_2}$ is highlighted, which is in the same direction as $\boldsymbol{b_1}$, along with the distance between the (001) planes. Examples of Miller indices for the real space directions $\boldsymbol{a_1}$, $\boldsymbol{a_2}$ and $\boldsymbol{a_3}$, and in the reciprocal space direction of $\boldsymbol{b_2}$ are given.

where f_j is the atomic form factor (a number dependent on the type of atom and the incoming wavevector) and (x_j, y_j, z_j) represents the position of the j^{th} atom in the unit cell. The intensity of each peak is then proportional to the square of the structure factor. Several other factors have to be considered in real systems, including anomalous scattering (a change in phase due to X-ray absorbance), the Lorentz correction, a polarization correction and multiplicity (the fact that several planes will cause the same reflection).

By considering the possible symmetries of the crystalline state, further insight into the structure of the crystal can be achieved. Certain symmetries in a crystal will guarantee that the form factor will become zero for particular planes. These missing points of intensity are known as systematic absences and are essential for determining the space group of a crystal. An example of crystal absences is shown in Table 2.1 for the different types of lattice centring.

Table 2.1: Examples of systematic absences for different types of cell centring.

Centring Type	**Systematic Absence Condition**	**Example Plane Absences**
P	-	-
I	$h+k+1=2n+1$	(100),(300),(120)
F	$h+l \neq 2n$, $k+l \neq 2n$, $h+k \neq 2n$	(100),(110),(011)
C	$h+k=2n+1$	(100),(120),(124)

2.2.3 Rietveld Refinement

Comparative analysis of pXRD patterns with known crystal structures was carried out using Profex (version: 3.14.3),[89] a graphical interface for the BGMN Reitveld refinement backend. This refinement method allows pXRD data fitting by modelling peak positions and intensities to generate experimental crystal structures from previously solved systems. Fitting involves a combination of parameters based on both the sample and the experimental setup. Parameters for the Bruker D8 Advance diffractometer have been carefully calibrated to give accurate peak shapes and relative shifts. Care was taken to grind samples to reduce preferential orientation, which increases the intensity of certain peaks due to crystallites in the sample not being of uniform size and distribution. Modelling of preferential ordering can be carried out in Profex; however, reducing the effect leads to more accurate analysis.

Reitveld analysis outputs both a predicted unit cell for an experimental powder pattern (based on a previously solved structure) and a confidence level for the fit. Gaining an acceptable confidence level is imperative before drawing any conclusions from the data. Therefore, Rietveld analysis allows for the determination of unit cells at finite temperature, and allows a confidence level to be applied to whether a powder pattern matches a particular structure. Additionally, the analysis can be carried out with multiple phases, allowing a percentage of each phase to be calculated.

2.2.4 Single-Crystal X-ray Diffraction

An extension to pXRD comes from using a crystal with a single domain. Equation 2.5 shows that when using powder diffraction a single angle θ is used, resulting in all vectorial information about $\boldsymbol{G_{hkl}}$ to be lost. When using a single crystal, diffraction will appear as points in 3D space and information about $\boldsymbol{G_{hkl}}$ is retained. The intensity of the spots will still be proportional to the square of the form factor in equation 2.6, meaning the phase information will still be lost. However, there are methods to overcome this,[90] and full structure solution via single-crystal X-ray diffraction (sc-XRD) is routinely carried out.

2.2.5 Solving Crystal Structures Via Electron Diffraction

Although sc-XRD is the most common method used for crystal structure determination, the technique can be difficult or impossible to use in certain situations. The main constraint on structures that can be solved via X-ray diffraction is the need for a single crystal domain of appropriate size (ideally 0.2 mm in all dimensions). The crystal is needed to fill the incident X-ray beam to generate diffraction spots with appreciable intensities. Another factor to take into account is that crystals that look to be singular may be twinned. Twinning occurs when multiple crystal domains are packed together due to energetically competitive unit cell boundaries, which are common with space groups such as $P2_1/c$ with β close to 90°.[91]

Multiple methods can be used when sc-XRD cannot be applied; however, each comes with a substantial amount of work. A common method is the use of crystal structure prediction along with

pXRD data to search for a particular structure.[92] This technique requires the powder data to be of a single phase, and for large unit cells can use a huge amount of computational power. A recent novel approach to overcome the downfalls of powder diffraction is the use of magnetic fields to align the polycrystalline domains.[93] However, these ideas lack the routine use available with sc-XRD.

An emergent technique in the field of crystal structure solution is 3-dimensional electron diffraction (3DED).[94] The use of a scanning transition electron microscope (STEM) allows for the detection of nano-sized crystals, the diffraction of which can be observed with extremely sensitive single-electron detectors.[95] Although the use of 3DED is becoming more common, several factors are hindering routine use. One of these issues is secondary electron scattering due to the high cross-section of electron-electron interactions compared to photon-electron scattering. This secondary scattering leads to predicted systematic absences having finite intensities, resulting in difficulties when determining the space group.[96] In many cases, small crystals (of a few 10s of nanometers) are actually preferred in 3DED to minimise the amount of secondary scattering. The first pharmaceutical to be solved ab-initio by 3DED, without the use of sc-XRD to confirm the structural model, was that of orthocetamol.[5]

2.3 Optical Spectroscopy

Ultraviolet-visible spectroscopy (UV-Vis) of solutions was carried out using a PerkinElmer Lambda 650 spectroscope. Solution measurements were taken using two 10 mm path length quartz cuvettes, one containing a reference solvent and the other the sample solution, as shown in Figure 2.3. Absorption of the sample is calculated by comparing the intensity of each beam, using the equation,

$$A = \log(I/I_0), \tag{2.7}$$

where I is the intensity of the sample beam, and I_0 that of the reference beam.

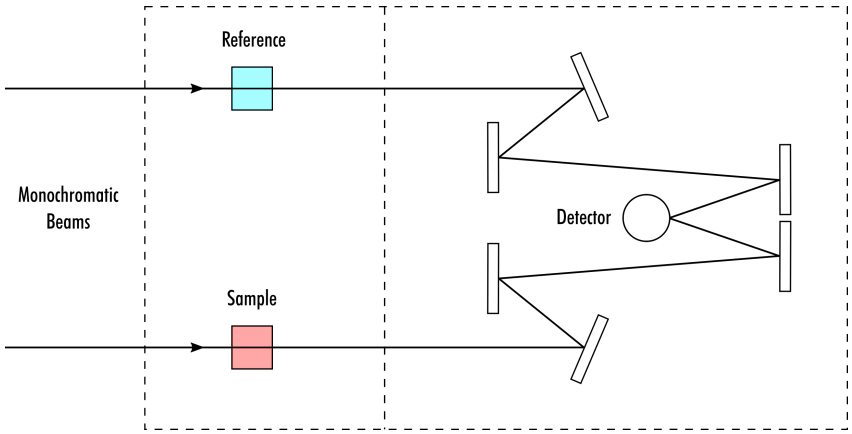

Figure 2.3: Experimental setup for solution UV-Vis spectroscopy utilising a sample and reference beam. Reproduced from [97].

UV-Vis spectra of solid-state samples were collected using a 60 mm integrating sphere attachment to the spectrometer. Samples were crushed with a pestle and mortar before being added to a sample holder, and reference spectra were taken using a spectralon®sample.

2.4 Differential Scanning Calorimetry

Differential scanning calorimetry (DSC) of samples was carried out using a TA Instruments Discovery DSC25. N_2 gas was used as a purge gas, which was flowed into the sample chamber at a rate of 50 mL.min^{-1}. The TRIOS software package (version: 4.5.0.42498) was used to analyse the thermograms of each sample. Temperature and cell constant calibrations were performed using a certified indium standard (temperature = 156.6 ± 0.5 °C, enthalpy = 28.72 J.g^{-1} ± 4%).

2.4.1 Modulated Differential Scanning Calorimetry

Modulated differential scanning calorimetry (MDSC) of samples was carried out using a TA Instruments Discovery DSC25. The temperature was modulated with an amplitude of 1 °C and a period of 60 s. Samples were heated with an underlying rate of 1 °C.min^{-1}. A sapphire reference sample was used for specific heat calibrations. As a technique, MDSC is useful for accurate measurements of specific heat and the deconvolution of overlapping thermodynamic transitions. The technique has been shown to produce accurate heat capacities for a number of systems using the TA Instruments Discovery DSC25. During the heating ramp, the total and non-reversing heat flow to the samples are measured. This can be understood by examining the fundamental heat flow equation,

$$\frac{dQ}{dt} = C_p \frac{dT}{dt} + f(t,T), \tag{2.8}$$

where $\frac{dQ}{dt}$ is the total heat flow of the sample relative to the reference, C_p is the heat capacity of the sample at constant pressure, $\frac{dT}{dt}$ is the heating rate of the DSC and $f(t,T)$ is a function that describes the heat flow of kinetic processes (such as crystallisation and evaporation) at time t and temperature T. During MDSC, the total heat flow is given by the rolling average of the modulated heat flow. The heat capacity of a sample can be calculated using a discrete Fourier transform of the modulated heat flow,[98] from which the reversing ($C_p \frac{dT}{dt}$) and non-reversing ($f(t,T)$) heat flows can be calculated. Figure 2.4 shows idealised MDSC curves, including the total and modulated heat flows.

2.4.2 Concomitant Synchrotron X-Ray Diffraction and Differential Scanning Calorimtery

Concomitant synchrotron X-ray diffraction and differential scanning calorimetry (CXRD-DSC) was carried out using a modified TA Instruments Q20 DSC, with holes drilled (entry: 3 mm, exit: 5 mm) to allow an X-ray beam to pass through. Experiments were carried out at the I12 beamline (JEEP) at Diamond Light Source. A 0.5 mm diameter X-ray beam was used, and diffraction was collected using

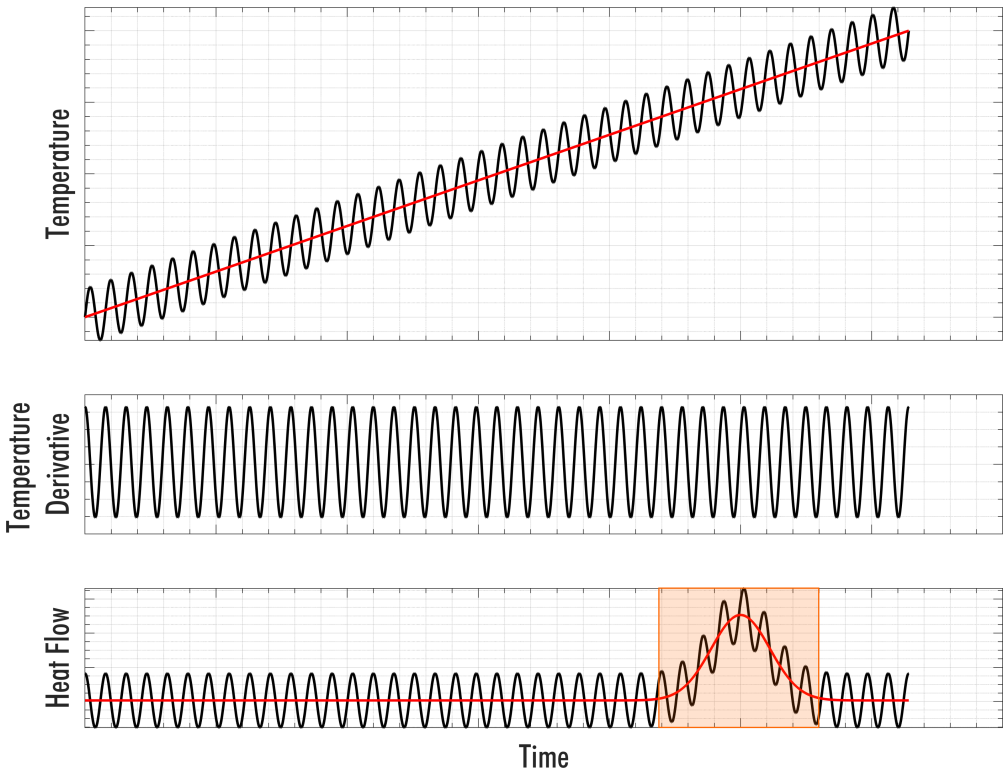

Figure 2.4: Example parameters during a modulated differential scanning calorimetry experiment. The temperature is increased linearly with an underlying sinusoidal periodicity (top). The derivative of the temperature as a function of time follows a sinusoidal function. The resultant heat flow is shown in the bottom pane, with an example transition highlighted in the orange area.

a Pilatus 2M CdTe detector placed 1.887 m behind the sample. The detector was calibrated using a cerium dioxide sample. Each diffraction pattern was collected for 4 s, with a 2 s pause between each pattern.

A TA Instruments RSC 90 cooler controlled the temperature of the DSC. Samples were sealed hermetically in TZero aluminium pans, which could be placed so that encased sample was in the path of the X-ray beam. The aluminium pan did cause diffraction, but the peaks occurring due to this could be easily disregarded. In general, DSC measurements were performed at a heating rate of 10 °C.min^{-1}, so that powder patterns were produced at 1 °C intervals.

Diffraction data were analysed using the DAWN[99] software package, where the 2-dimensional diffraction data were integrated to produce 1-dimensional traces.[100] Unrepresentative spots of high intensity, caused by large crystal grain sizes, were removed in post-processing. DSC and synchrotron diffraction data were aligned via interpolation of absolute time using MATLAB 2019a (version: 9.6.0.1072779). The interpolated data were calibrated using a snapshot of the DSC data taken when a trigger was received from the DAWN software. This trigger allows alignment of the Q20 and Pilatus data. DSC data were analysed using TA Instruments Universal Analysis software (version:

5.5.24). Data was combined an overlaid using MATLAB, along with all subsequent analysis.

2.5 Nuclear Magnetic Resonance Spectroscopy

Nuclear Magnetic Resonance (NMR) characterisation experiments were carried out on a JEOL ECS-400. Solutions for NMR were prepared by dissolving each sample in 0.5 ml of deuterated solvent. Analysis of all samples was carried out using MestreNova (12.0.4).

2.6 Computational Analysis

2.6.1 Visualisation Tools

Solved crystal structures were analysed and viewed using the Mercury[82] software package. Gaussian09[101] was used for the quantum chemical calculations of molecular properties using density functional theory, which were analysed using GaussView 5.[102] Within GaussView 5, molecular orbitals and molecular electrostatic potential (ESP) maps were produced. ESP maps were plotted onto a total electron density isosurface to give information of both the steric and electronic properties of molecules. The 64-bit intel cluster Grendel was used to carry out computationally expensive calculations. Basis sets and functionals were chosen based on each particular calculation and given in the text alongside any calculations discussed.

2.6.2 Molecular Optimisations Using ORIENT

The software package ORIENT[44] was used to carry out large numbers of optimisations on rigid molecules. ORIENT uses distributed multipoles to model molecular interactions, which can be calculated using a combination of the Gaussian09 and GDMA[103] programs. Multipole analysis of all atoms was carried out up to rank 4 (hexadecapole). Multiple optimisations using the same sets of molecules were run using scripts written in Perl, and executed on the Grendel cluster. Example input files are given in Appendix C.

CHAPTER 3

VOLATILE DEEP EUTECTIC SOLVENTS

The results of this chapter were published in part in the paper: Crystallisation from Volatile Deep Eutectic Solvents,[104] which was first-authored by Dr Jason Potticary. I would like to thank everyone who took part in this work. Unless stated, the research presented in this chapter was carried out by myself.

3.1 Interactions in Solution as a Crystal Engineering Tool

The use of crystallisation as a tool to form reproducible materials of known composition is highly dependent on the control that one has during the process of crystal formation. Although there is now substantial expertise in analysing the crystalline form once it is produced, the process of crystallisation is still not well understood, with nucleation dynamics being particularly difficult to probe. Nonetheless, protocols for the experimental exploration of the crystallographic landscape of a molecule are well established. One of the major routes to crystallisation is via the liquid form, often using solvents as effective media. The use of solvents allows for the mobility of the target crystallisation molecule while still allowing species in the solution to interact via intermolecular interactions. In studies concerning the tuning of the final crystalline product, these intermolecular interactions are particularly important. In many cases, it has been shown that the strategic selection of solvent molecules and crystallisation conditions can lead to changes in both crystal morphology[105,106] and polymorphism.[107,108]

Many solvents are appropriate for use as crystallisation media, which tend to be small organic molecules with melting points below room temperature. For crystallisation, the pairing of solvent and solvate is carefully chosen so that the solute can be dissolved at concentrations high enough to produce reasonable material yields. In these solutions, the supersaturation of the solvate (via cooling or evaporation) is increased until the solvate crystallises out into the remaining solvent-solute

solution. In this sense, the solute crystallisation has little effect on the phase of the solvent, meaning the solvent and solute are well-defined entities (Figure 3.1).

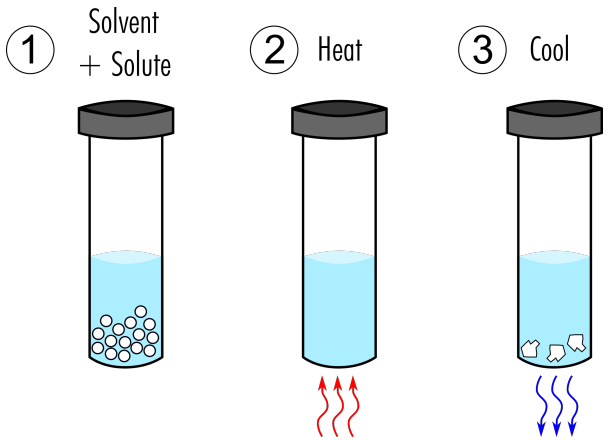

Figure 3.1: The process for the formation of crystalline material via the cooling of a common solute-solvent system.

Although there are a large number of molecules that are used ubiquitously as solvents, their diversity is limited by the need for solvents to be in the liquid phase. In this chapter, I discuss a diversion from this limitation by exploring the use of a class of ionic liquids (ILs), known as deep eutectic solvents (DESs), as a medium for crystal growth.

3.2 Ionic Liquids and Deep Eutectic Solvents

Over the last century, the study of ILs has grown exponentially into a field that has found uses in a huge range of disciplines. Their discovery is rooted in an early search for neoteric solvents that could exhibit a range of properties that were not well established in common solvents.[109] The particular solvents explored were molten salts, which were known to be highly stable, non-volatile, cheap and have a large electrochemical window. However, the issue with molten salts was that they tended to need very high temperatures to form, and were therefore particularly difficult to handle, introduced material incompatibilities and also cost a lot to maintain in the liquid phase. Given this restraint, the acquisition of a low-temperature molten salt was highly sought after. Over 150 years since the observation of such a material, a low-temperature molten salt is now termed an IL.

Although not understood at the time, the first known observation of an IL was the appearance of a "red oil" from Friedel-Crafts reactions in the mid-19th century. The advent and expanded use of NMR spectroscopy more recently determined that this liquid resulted from the formation of an aluminium chloride salt (Figure 3.2), which was suppressing the melting point of the mixture. P. Walden made another early observation of an IL in 1914, where he recorded the formation of a low melting alkylammonium nitrate,[110] subsequently leading to a class of ILs analysed for their use as

liquid propellants.[111] These materials are also still of modern theoretical interest when trying to determine the hydrogen bonds present in ILs.[112]

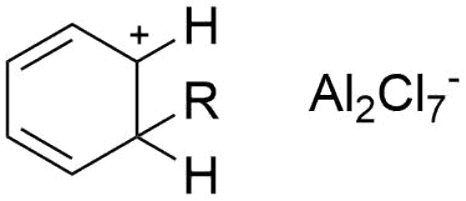

Figure 3.2: Chemical components of the "red oil" observed in early Friedel-Crafts experiments. Structures are taken from a review of ionic liquids by Wilkes.[109]

The active search for IL systems began with the need for efficient and stable electrolyte systems, the work on which was funded by the U.S. Air Force Academy. This saw the rise in CuCl alkylammonium chlorides,[113–115] before the field really started to grow after the invention of water-stable 1-ethyl-3-methylimidazolium based ILs in 1992.[116] The ideas gained from these studies resulted in the discovery of a large number of possible anion and cation combinations, and in 1998 Freeman termed the phrase "designer solvent" to describe this new group of neoteric solvents.[117] It appears that this idea sold itself easily to the chemical community and lead to the utilisation of ILs in a variety of fields, including chemical reaction solvents,[118–120] biomass processing,[121] lubrication,[122] solvent separation[123] and pharmaceutical applications.[124]

In 2003 Abbott discovered a new IL-type system containing choline chloride (m.p. 302 °C) and urea (m.p. 133 °C), which, when mixed at a ratio of 1:2 choline chloride:urea, had a melting point of 12 °C.[125] This type of mixture was not considered an IL, as it did not consist entirely of discrete ions, and was given the name deep eutectic solvent (DES) to distinguish them from classic ILs.[126] In DESs, the depression in melting point is attributed to the formation of large ions containing combinations of urea and Cl^- or choline chloride and urea via hydrogen bonding.[127] Following the first observations of DESs, many similar systems were found and hailed as a green alternative to common organic solvents due to their low volatility and high stability.[128] The hydrogen bonding capability of DESs has since led to their use as solvents in metal extraction,[129] catalysis[130] and pharmaceutical formulation.[131] The group of DESs has also further expanded to include mixtures that do not necessarily include an ionic element; the natural deep eutectic solvents (NADES)[132] and therapeutic deep eutectic solvents (THEDES)[133] can contain mixtures of neutral molecules, such as the 3:1 menthol:benzoic acid mixture. These systems exemplify how the competition between different hydrogen-bonding motifs can be strong enough to significantly reduce the melting point of a mixture without ionic species.

The road to the discovery of room temperature molten salts was therefore transformed into a continuous search for new solvent systems. With the current understanding of ILs and DESs, it is estimated that there could be in the region of 10^6 possible such systems. The understanding of the formation of ILs is still not well-defined, as the length scales needed to observe to fully understand

them are in a particularly difficult region for current technology. The use of neutron scattering[134] and theory[135] show us that extensive hydrogen bonding is present in the molecular mixtures, and the melting points of mixtures tend to reduce with increased hydrogen bond strength and reduced molecular symmetry. Therefore, any processes requiring liquid media with strong hydrogen bonding are at the forefront of prospective interest in the field.

3.3 Deep Eutectic Solvents Containing a Volatile Component

Fundamentally, the properties of DESs do not seem to make them particularly compelling candidates to consider as crystallisation media for pharmaceutical compounds. Although they have shown their efficacy as reaction media, the known solutions tend to be inherently non-volatile, and the fact that their phase behaviour is concentration-dependent makes cooling-crystallisation parameters difficult to predict. However, disregarding these apparent difficulties, the strong hydrogen bonding present in the DESs could present a possible pathway to engineering interactions that could not be produced from standard solvent-mediated crystallisation.

In this vein, it was considered that a molecule with inherent volatility and strong hydrogen bonding potential could be used to produce deep eutectic systems amenable to evaporative crystallisation. The molecule chosen to test this hypothesis was phenol. Phenol is the smallest molecule containing both an aromatic ring and a hydroxy group, which are both ubiquitous groups of pharmaceutical compounds. Moreover, phenol has a melting point of 40 °C, meaning that even small melting point depressions can cause the formation of a liquid at room temperature, and the vapour pressure of phenol allows for milligrams of sample to be evaporated over a time period of hours.

Phenol was found to produce stable liquid solutions when mixed with several common active pharmaceutical ingredients containing functional groups amenable to hydrogen bonding, such as amino and hydroxy groups. In these binary systems, phenol is termed the volatile component (VC) and the second constituent the non-volatile component (NVC). To distinguish eutectic systems containing a VC from common DESs of low volatility, the name volatile deep eutectic solvent (VODES) is used. The stoichometries of interest when crystallising from these mixtures often contain a high proportion of the VC, and therefore it is useful to describe VODES in terms of a molar ratio (VC:NVC).

Figure 3.3 highlights the simple process for producing crystals of the NVC from VODESs. In step one, the VC and NVC are mixed at a specific ratio and gently heated and shaken to increase the rate at which the liquid phase is formed. Once formed, a droplet of the VODES can be exposed to the atmosphere to evaporate off the VC, leaving the NVC to crystallise. Figure 3.4 shows the full process of VODES formation and NVC crystallisation.

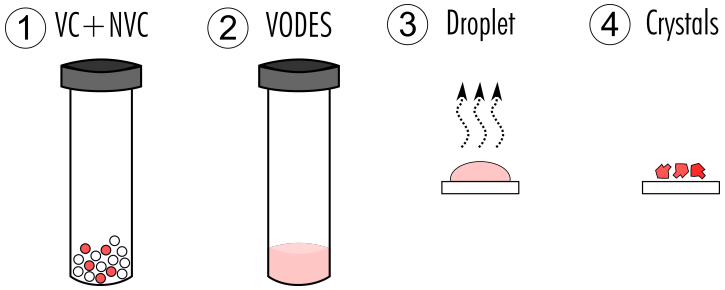

Figure 3.3: The process for the formation of volatile deep eutectic solvents and the subsequent crystallisation of the non-volatile component via evaporation of the volatile component.

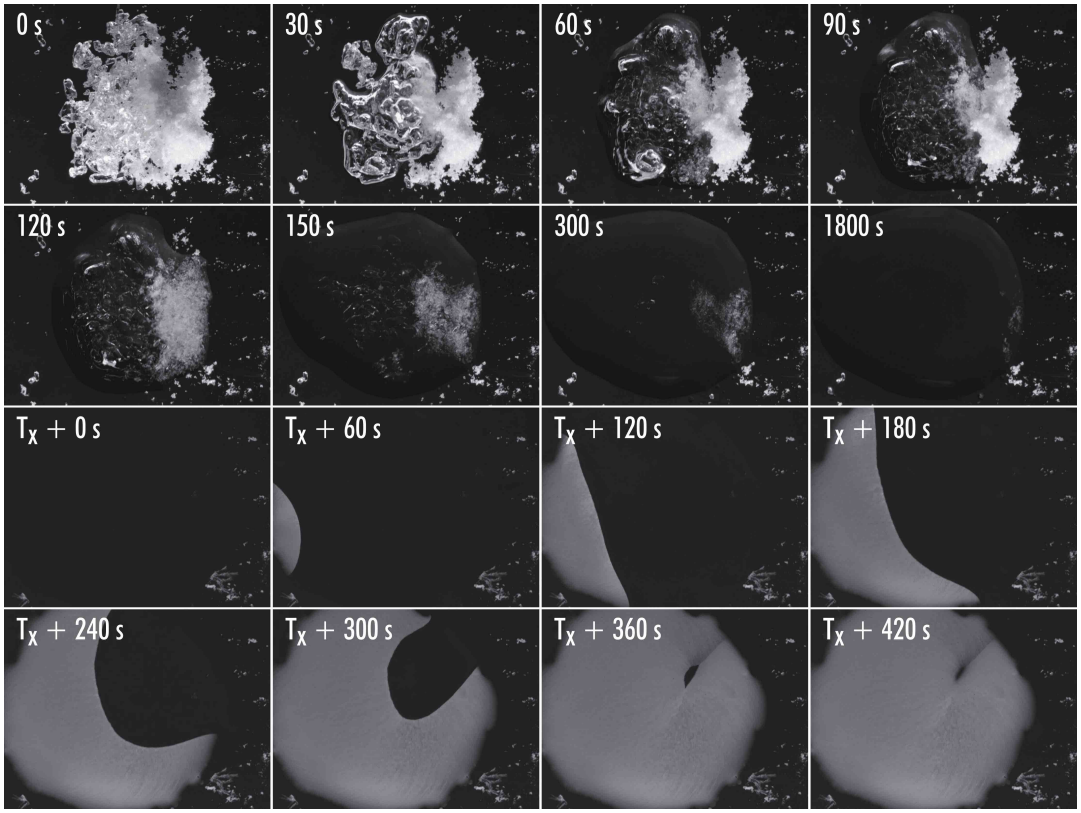

Figure 3.4: A time-lapse of the formation of a VODES. The two samples were put in contact and left to mix without any external interference. T_x represents the time at which the first crystal nuclei was seen. By the end of the time-lapse only crystals of 2-methoxybenzamide remain.

3.4 The Control of Polymorphism in Paracetamol

Paracetamol (4-acetaminophen) is one of the most well known and rigorously studied pharmaceuticals in the world. It is a small organic molecule (Figure 3.5), first synthesised in 1877, which is generally distributed in tablets containing a crystallised form of the molecule. The polymorphic landscape of the molecule has been thoroughly analysed both experimentally and computationally.[21] It is known to be polymorphic, crystallising as the thermodynamically stable, monoclinic form I from standard solvent crystallisation routes, and as the metastable, orthorhombic form II from the melt.

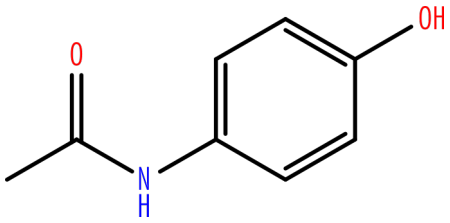

Figure 3.5: Chemical scheme of paracetamol (4-acetaminophen).

Many non-routine crystallisation procedures for the crystallisation of paracetamol have been experimentally conducted to find more crystallographic forms with high bioavailability. At this point in time, many of these investigations are likely purely academic, as it is well established that paracetamol is distributed as form I with no major bioavailability issues. Nevertheless, nine polymorphs of paracetamol have been discovered to date, having utilised crystallisation conditions involving high pressures,[136] precise temperature profiles from the melt[137,138] and targeted additives.[139]

Other than form I, the crystallographic form considered most widely to have commercial viability is form II. The differences in properties between form I and form II paracetamol are the most common introductory example of the possibilities that can arise from manipulating polymorphic forms. Due to the planar-like structure of form II paracetamol, its compressibility is greater than that of form I, and the fact that it is metastable compared to form I means that it is more soluble. Many studies have used these facts as suggestions for the medicinal use of form II paracetamol, but the ease of production of form I and the establishment of processes to produce the drug in this form have made the use of form II thus far unviable.

Paracetamol forms a VODES at room temperature when mixed with phenol at molar ratios of 4:1 - 9:1 phenol:paracetamol. These mixtures begin a spontaneous transition to a liquid form when in contact with each other. However, heating to 60 °C greatly increases the transition speed. When kept under sealed conditions at room temperature, the mixtures remained stable, clear liquids for at least a year. However, if left at elevated temperatures, the solutions started to go red. This reddening is likely caused by the oxidation of phenol, as the quinones produced from phenol degradation are known to be red in solution.[140] ^{1}H NMR spectroscopy of red solutions showed no evidence of any oxidised phenol in any measurable proportion. The red samples remained liquid over the same time period as the colourless liquids.

Crystals of paracetamol were produced from VODESs via evaporation of the VC from a drop of liquid. The drop of liquid was placed on a glass slide and exposed to the air in a dust-free environment. The temperature and humidity of the room were measured at all times to ensure that there were no dramatic changes in environmental conditions. Figure 3.6 shows images of the resultant paracetamol crystals from VODESs of ratio 4:1 - 9:1 VC:NVC. A clear change was seen between plate-like crystals and needle-like crystals as the ratio of phenol was increased. A transition appears around the ratio 6:1, above which the needle-like morphology is dominant. The 6:1 sample appears to contain both morphologies. In all cases, crystallisation from the VODES solution was fully completed within 24 hours, with no residual solution present.

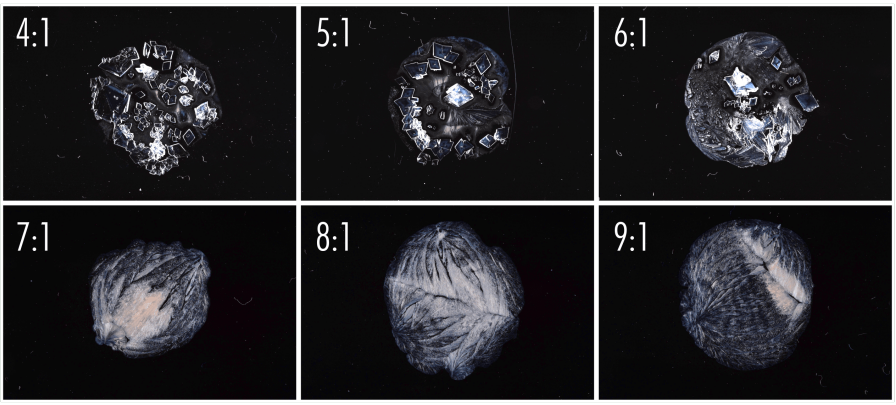

Figure 3.6: Images of paracetamol crystals obtained from volatile deep eutectic solvents of ratios varying from 4:1 - 9:1 phenol:paracetamol. Images were taken directly of the crystallised sample on the slide that it was grown on.

To determine the crystal structure of the paracetamol crystallised from the VODESs of various ratios, powder X-ray diffraction (pXRD) was acquired after each experiment. Figure 3.7 shows the diffraction patterns for the 4:1 and 9:1 samples shown in Figure 3.6. Each pattern was compared to the known polymorphs of paracetamol, and Rietveld analysis used to determine the dominant polymorph. The analysis of each pattern clearly showed that the crystals produced from VODESs with ratios 4:1 - 6:1 exhibited predominantly the form I crystal structure, wheres samples grown from ratios of 7:1 - 9:1 displayed the structure of form II. This is a clear case of polymorphic control, arising from a simple preparation based only on sample concentration at room temperature and pressure.

To assess the consistency of these results, a 5 g sample of each VODES ratio was prepared and kept in a sealed vial at room temperature. Each day a drop of the sample was taken from this solution and exposed to the atmosphere. These experiments allowed both the assessment of the reproducibility of the crystallisation procedure and the effect of ageing of the solution. The results of these experiments taken over 10 days are shown in Figure 3.8. The crystallographic form of each sample was determined primarily via the crystalline morphology; however, 10 samples were analysed via pXRD at random to ensure that this assumption was accurate. From the resultant tabulated data, it is clear that the crystal

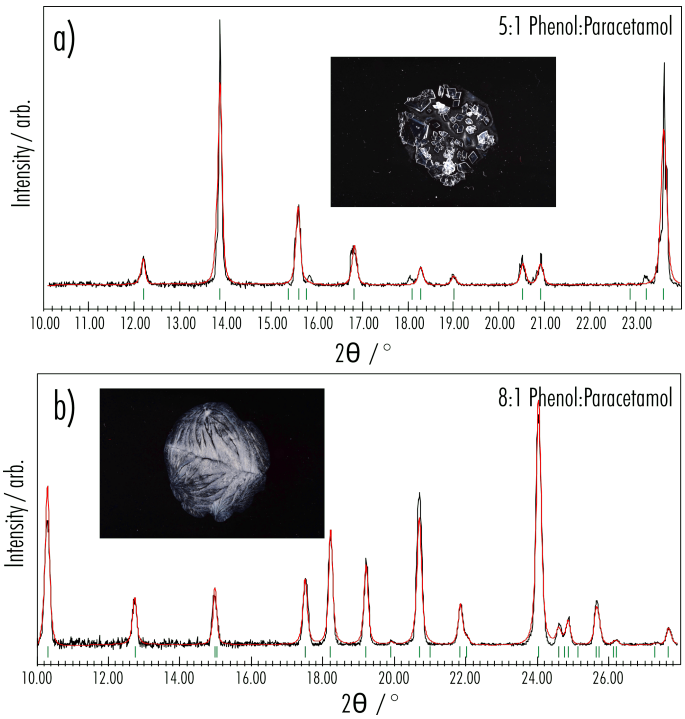

Figure 3.7: Experimental powder X-ray diffraction patterns of crystals produced from a 5:1 and 8:1 phenol:Paracetamol VODES. The experimental patterns are shown in black, and a fit to known crystallographic parameters using Reitveld refinement shown in red. a) Fit to paracetamol form I. b) Fit to paracetamol form II. Samples were crushed before powder X-ray diffraction was carried out.

structure of paracetamol produced depends on the ratio of the VODES used. Below the ratio of 7:1 VC:NVC 87% of samples produced form I paracetamol, whereas of the 7:1 - 9:1 mixtures 77% produced form II. This trend generally follows closely to that discussed with the first set of data. There does not appear to be any correlation between the age of the sample and the resultant crystallographic form. However, deviations from the expected crystal structure are seen, which are likely caused by small differences in experimental conditions such as humidity, temperature or the presence of unwanted nucleation sites. For example, all of the samples crystallised as form II paracetamol in the second set of experiments, and almost all in the seventh. Although these results appear to be anomalous, any commercial use of this process would require specific experimental parameters to ensure that the desired crystallographic structure is always produced.

Other than ensuring the production of the correct crystallographic phase, another issue when considering VODES as a potential commercial crystallisation medium is the quantity of phenol left in the sample. ^{1}H NMR of crystallised samples was assessed to determine the amount of phenol left in the sample after crystallisation. Figure 3.9 shows the NMR for a sample of paracetamol crystallised from a 9:1 VODES. It is clear that there was no detectable level of phenol to the sensitivity of the NMR (<0.25% w/v). This is below the FDA allowed limit for ingestion, topical application, and injection.[141]

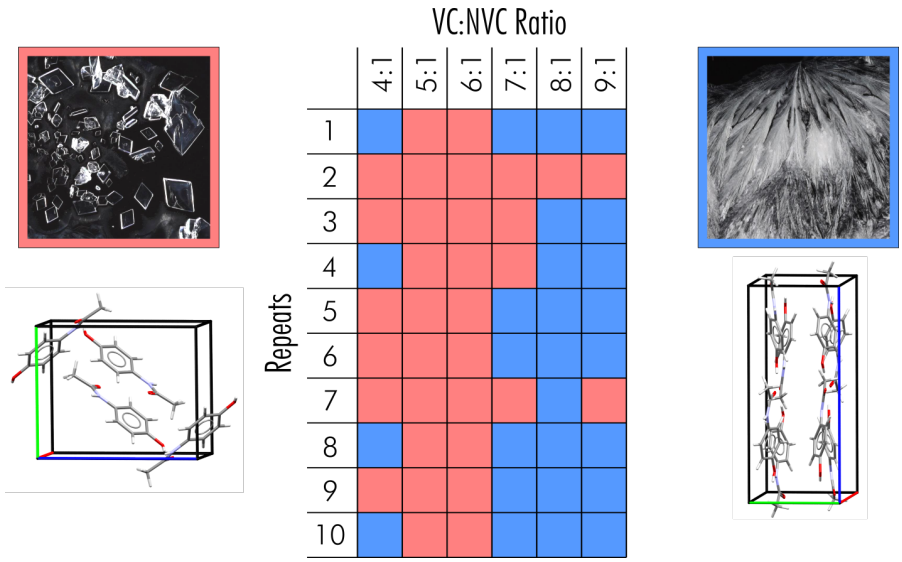

Figure 3.8: Results from 10 repeat crystallisations of paracetamol from VODESs of ratio 4:1 - 9:1 phenol:paracetamol. Crystallisation experiments resulting in form I paracetamol are shown in red (left), and form II shown in blue (right). Each repeat experiment was taken after 24 hours of the previous experiment. The Crystallographic form was determined primarily through observation of morphology, but some samples were selected to be analysed by powder X-ray diffraction to ensure correct determination. Adapted from reference [104].

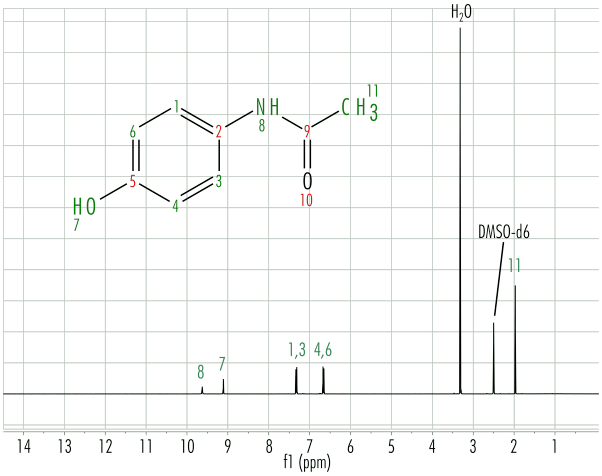

Figure 3.9: Nuclear magnetic resonance spectra for paracetamol following crystallisation from an 9:1 phenol:paracetamol VODES. Each peak is numbered depending on the hydrogen that it relates to. Water and solvent peaks are also highlighted.

The fact that the initial ratio of a VODES should affect the final crystallographic form of a sample after the VC has evaporated is not immediately intuitive. Any sample that is grown via the evaporation of a component goes through a progressive change in concentration. In general, the evaporation of solvent at a constant rate will lead to a supersaturation proportional to time, albeit not a linear proportionality. Considering VODESs as a crystallisation media, however, the driving force for crystallisation will actually decrease until the eutectic concentration is reached. In essence, this should not make any difference, as each sample will still go through the same set of concentrations and eventually reach that same supersaturation at which crystallisation occurs.

The formation of a VODES mixture is inherently connected to the competition between possible hydrogen bonding motifs that can form between the NVC and the VC. The difference between the VODES system and that of an ordinary solvent system is that the phase of the VC is directly related to the amount of NVC in the mixture. Hence, it is likely that the molecular dynamics of the solutions are highly concentration-dependent. Figure 3.10 and Figure 3.11 show time-lapse images of the formation of paracetamol crystals from 5:1 and 8:1 VC:NVC VODESs, respectively. In both cases, it took over 10 hours for all of the liquid in the system to have gone; however, there is a dramatic change in the time of the first onset of crystal nucleation. Even though there is only 10% more phenol in the 8:1 VC:NVC system, it takes an additional 9 hours before the first observable nucleation event. This strongly suggests that the internal structure of the liquid is different. In the following chapter, I discuss how differential scanning calorimetry is used to analyse this structure. However, advances in Brownian motion microscopy[31] and liquid cell electron diffraction[32] will also aid in confirming this in the future.

The morphologies of the crystals produced via crystallisation from the different VODES ratios may also provide some evidence of the cause of the polymorphic control. There is an obvious distinction between the crystals of form I and form II paracetamol that grew from the VODES media. Form I crystals are generally large with obvious single-crystalline properties, whereas form II crystals are polycrystalline and thin as if grown rapidly. The morphology of the grown paracetamol samples was assessed by carrying out pXRD without crushing the sample. Form I showed a clear preference of growth direction perpendicular to the (001) plane, which may be expected due to the plate-like appearance of the crystals. Although form II paracetamol grew as needles, there was a clear preference for growth perpendicular to the (002) face. The pXRD patterns highlighting the morphologies are shown in Figure 3.12, with BFDH predicted morphologies shown. For form II paracetamol, it appears that layers of molecules form perpendicular to the (002) face, which may be mediated by the movement of phenol through the system during the equilibrium process from phenol evaporation. This may indicate an intermediary phase where phenol and paracetamol molecules are tightly bound enough to modify the pre-nucleation dynamics of the system.

To assess the strongest intermolecular interactions between paracetamol and phenol, molecular optimisations of variable numbers of molecules were carried out using ORIENT.[44] Multipole analysis was carried out using the 6-31G(d)/B3LYP basis-set/functional combination, which is common for

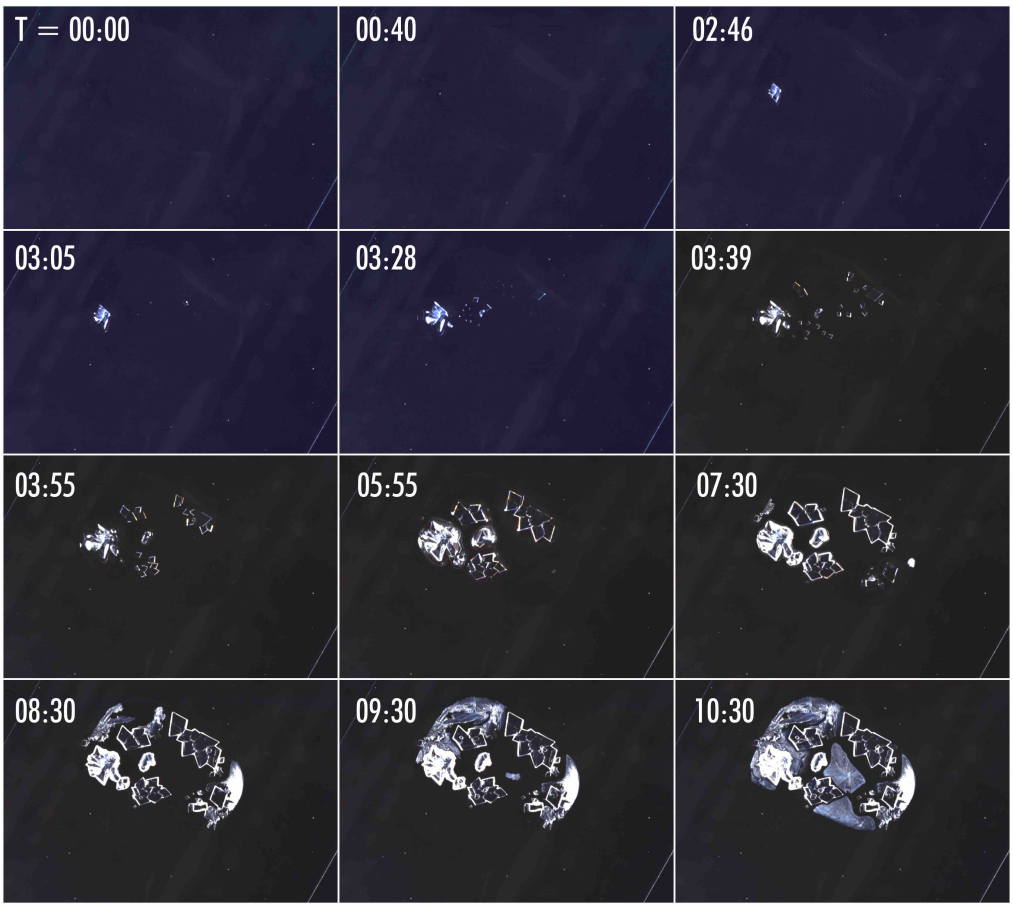

Figure 3.10: Time-lapse of the crystallisation of paracetamol form I from a 5:1 phenol:paracetamol VODES. The time is given in hours and minutes.

optimisations of small organic molecules.[142] To allow for a large number of calculations, molecules were kept rigid from the starting point of the calculation. Assessment of the crystal structures of form I and form II paracetamol shows that form I contains a herringbone-like structural motif, whereas form II contains planes of molecules. The basis of each motif can be represented by four molecules, as shown in Figure 3.13. For each structure, molecular optimisations were carried out, with the paracetamol motif of four molecules kept stationary and a phenol molecule allowed to move to a local energy minimum. Optimisations were carried out for 10,000 initial phenol positions, selected randomly from an isosurface of constant distance from the central structure.

The large number of optimisations highlighted only a small number of stable positions for each structure that the phenol molecule would sit in. In each case, the hydroxy group of the phenol sat in a region of local minima or maxima of electrostatic potential. The calculations highlighted that form II paracetamol had 14 possible phenol positions, whereas form I only had 11. Although having positions of lowest energy (most stable), the form I motif allowed for less possible phenol positions, and so would be a less favourable motif as more phenol molecules are introduced to the mixture.

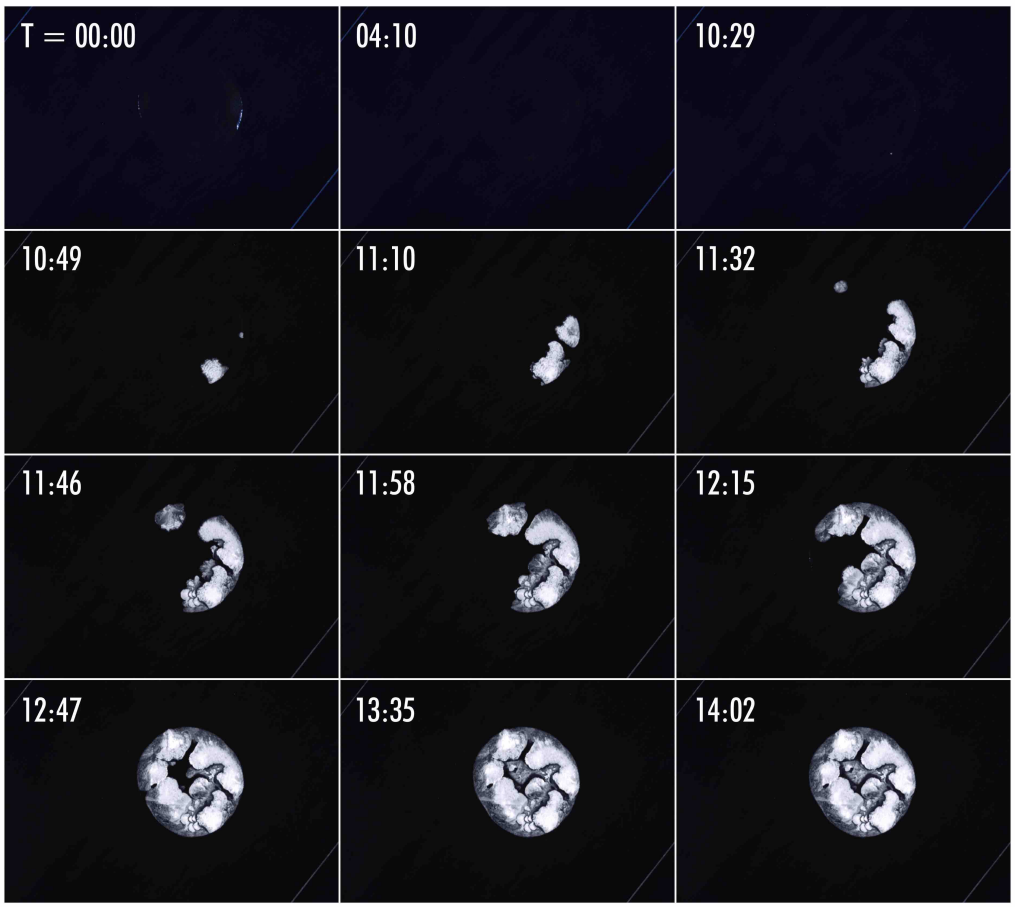

Figure 3.11: Time-lapse of the crystallisation of paracetamol form II from an 8:1 phenol:paracetamol VODES. The time is given in hours and minutes.

There are obvious drawbacks to this kind of calculation, as only a single phenol molecule was optimised at a time, which neglected effects from phenol-phenol interactions. However, as a basic theoretical approach, this does suggest a difference in the stability of the eutectic as the ratio of the solution is changed, which could lead to the observed polymorphic selectivity. The position of the oxygen of the phenol from each optimisation is shown in Figure 3.13. The colour is proportional to the energy of the conformation, with red being the most stable and white the least.

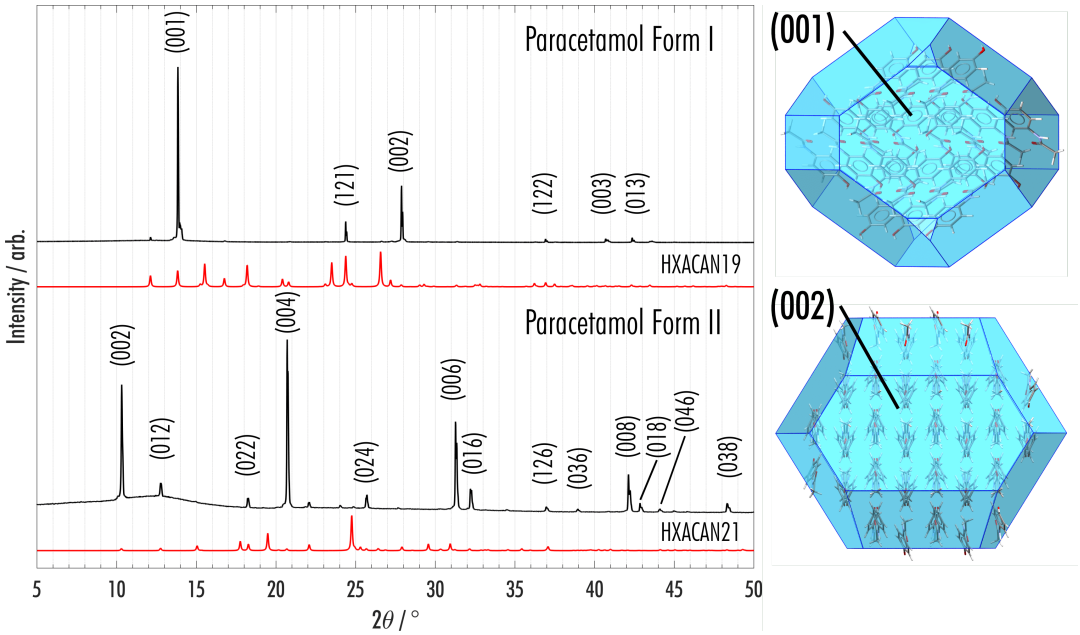

Figure 3.12: Powder X-ray diffraction patterns taken from crystals grown from 4:1 (top) and 9:1 (bottom) phenol:paracetamol VODES. To highlight the growth morphology, samples were not crushed during preparation. References to form I (HXACAN19) and form II (HXACAN21) are highlighted, and Miller indices for each experimental peak are given. The BFDH morphology for form I and form II paracetamol is shown to give a theoretical prediction for the morphology of each polymorph.

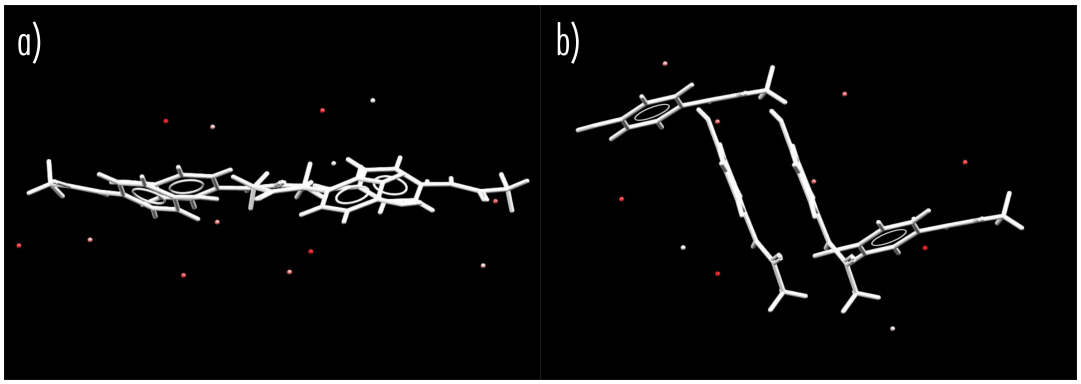

Figure 3.13: The final configurations of 10,000 optimisations of phenol with a) paracetamol form II and b) paracetamol form I using the ORIENT software package. Dots indicate the position that the oxygen of the phenol will adopt, with the colour representing the relative energy. Red indicates the most stable configurations and white the least stable. The 10,000 optimisations indicate 14 potential positions in form II and 11 in form I.

3.5 Form III Benzamide from Volatile Deep Eutectic Solvents

Benzamide is a small organic molecule (Figure 3.14) that sits as the backbone structure for a large set of antipsychotic medications. It is a simple amide derivative of benzoic acid, known for being the first observed case of organic crystal polymorphism. It is well documented historically that Wöhler and Liebig observed the solid-state transformation of a needle-shaped crystalline form to a rhombohedral form.[143] This is now known to be the transformation of the metastable form II benzamide to the thermodynamically stable form I benzamide.[144] Following this work, another metastable form (form III) of benzamide was observed, described as having been "hiding" behind the thermodynamic stable form I.[145] Both form I and form III appear concomitantly and have very similar pXRD due to similar crystallographic dimensions and symmetry (crystallographic space group $P2_1/c$). The structure of form III benzamide was solved using pXRD data, which was made difficult due to overlapping peaks with form I. Optimisation of crystallisation conditions eventually allowed single crystals of form III benzamide to be grown,[146] although form I was still present. Most recently, the use of nicotinamide as a nucleation seed allowed the isolation of form III,[147] with a small amount of nicotinamide present in the structure.

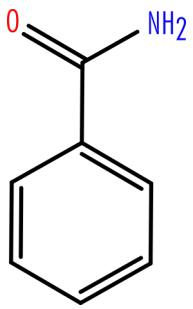

Figure 3.14: Chemical scheme of benzamide.

Benzamide forms a stable VODES when mixed with phenol at ratios of 3:1 - 10:1 phenol:benzamide at room temperature. Similarly to paracetamol mixtures, these samples are stable when kept in sealed conditions for at least a year. Storage above room temperature causes the sample to gradually turn a reddish colour, but does not cause any sample solidification. Keeping the samples at higher temperatures increases the rate of reddening.

A set of 10 repeat crystallisations was carried out for each stable VODES ratio at room temperature. As for paracetamol, each repeat was started 24 hours after the previous, under controlled conditions. The results are highlighted in Figure 3.15. Throughout the experiments, two different outcomes were observed. In the first case, plate-like crystals were observed, with a small amount of polycrystalline sample present on the edges of the crystals. In the second observed case, all the resultant crystals appeared polycrystalline due to an opaque, white appearance. In general, the polycrystalline sample seemed to follow a needle-like morphology; however, there were opaque, plate-like crystals in some cases.

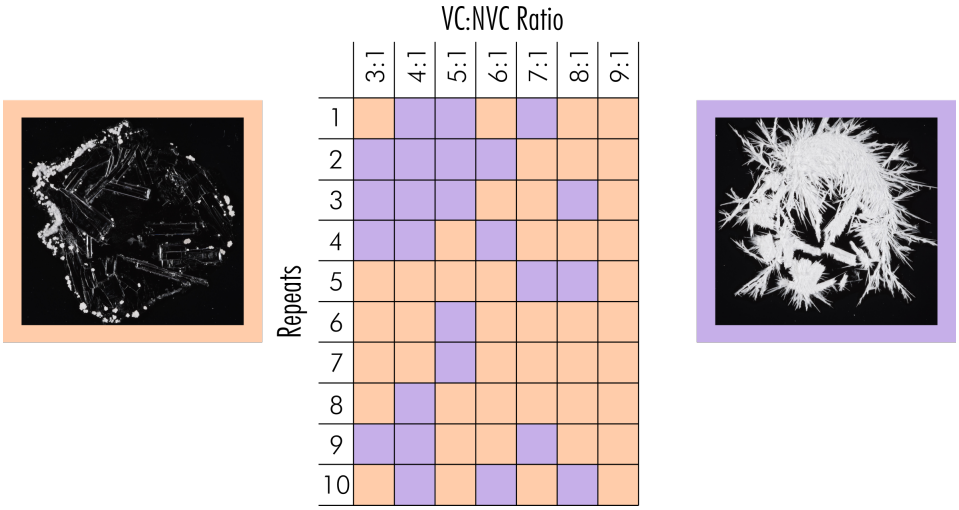

Figure 3.15: Results from 10 repeat crystallisations of benzamide from VODESs of ratio 3:1 - 9:1 phenol:benzamide. Crystallisation experiments resulting in form III benzamide are shown in orange (left), and a mixture of form I and form III shown in purple (right). Each repeat experiment was taken after 24 hours of the previous experiment. The crystallographic form was determined primarily through observation of morphology, but some samples were selected to be analysed by powder X-ray diffraction to ensure correct determination.

Powder X-ray diffraction of the samples, shown in Figure 3.16, determined that there was a structural difference between the two different crystallographic cases. In the first case, crystals of benzamide form III were produced and, in the second case, crystals of both form I and form III were present. The polycrystalline nature of the crystals produced in the second case appeared to be the result of the transformation from a metastable state. Thus, it is likely that the resultant form I benzamide forms as phenol is evaporated from a solvate crystal structure. Hence, the observation of these two cases can be explained as the stochastic appearance of a solvate crystal structure during crystallisation.

The stochastic nature of this polymorphic behaviour explains why there is no trend in the occurrence of the different crystallisation cases as a function of the VODES molar ratio. Although this highlights that the production of form III benzamide in this way is not polymorphic control, it is still a way of producing form III benzamide without the concomitant growth of crystals of form I. Therefore, this is the first case of the growth of pure form III benzamide without the use of additives, albeit that the phenol may be playing the same role as nicotinamide does in previous work. The advantage of this method is that the volatility of the phenol allows it to evaporate after the production of the form III crystal structure, meaning a pure sample of form III benzamide can be produced.

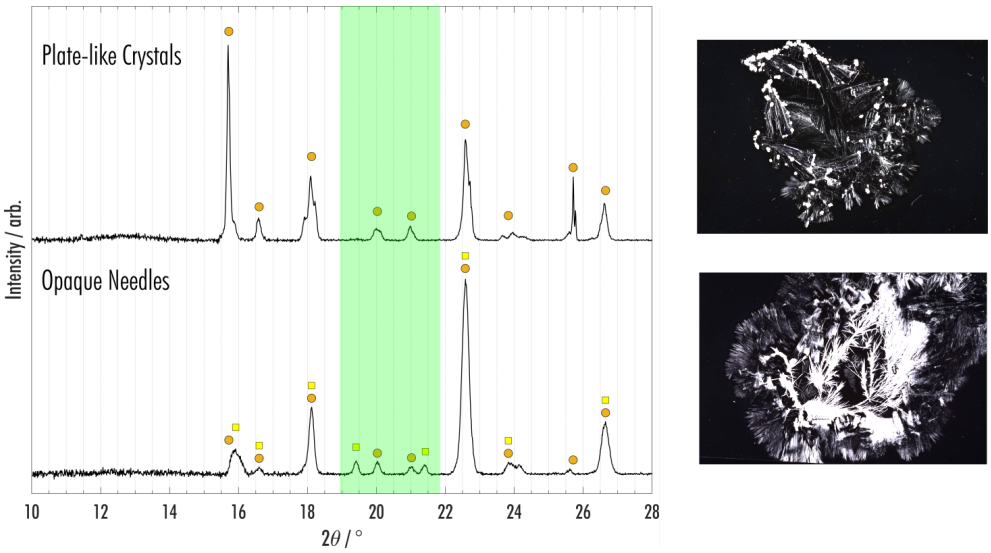

Figure 3.16: Example powder X-ray patterns for the two cases of crystallisation from VODESs containing phenol and benzamide, plate-like crystals (top) and opaque needles (bottom). Both patterns are referenced for form I and form III benzamide. Orange dots represent peaks from form III benzamide, and yellow squares represent form I benzamide. The region highlighted in green contains the peaks that most obviously distinguish the crystal structures of benzamide form I and form III.

3.6 Phenol as a Solvate Molecule

2-Ethoxybenzamide (Figure 3.17), otherwise known as ethanzamide, is a common anti-inflammatory drug used for minor pain relief. It is a small organic molecule with the benzamide structural motif as the backbone. It has only one known polymorph; however, is it predicted that kinetically hindered, lower stability structures may exist.[148] The known polymorph grows as fine needles and sits in the BCS class II (high permeability, low solubility), meaning inherent efficacy and processing improvements can be made. Due to this, co-crystals of 2-ethoxybenzamide with a variety of co-formers have been grown, which show stark improvements in both morphology and solubility.[149,150]

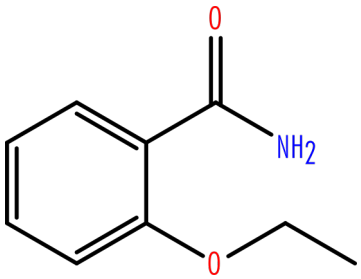

Figure 3.17: Chemical scheme of 2-ethoyxbenzamide.

2-Ethoxybenzamide produced VODESs with phenol at room temperature for ratios 5:1 - 9:1 phenol:2-ethoxybenzamide. These samples fully converted from solid to liquid after several minutes

of mixing. Gentle heating increased the rate of the conversion but was not necessary. Storage above room temperature led to a slight reddening of the sample, but at a much slower rate than for paracetamol and benzamide solutions. The liquid mixtures formed were stable for time periods greater than a year. Repeat experiments for crystals grown from VODESs containing 2-ethoxybenzamide and phenol are shown in Figure 3.18. In general, crystallisation from these VODESs resulted in thin, silky needles, which nucleated from a single point. However, in some cases, a large opaque mass was seen, which appeared to be the result of the transformation from a metastable crystal. It was clear that the original crystal was plate-like with well-defined edges, and a depletion of the needle-like crystals could be seen around the growth area. There did not appear to be any correlation between the ratio of the VODES and whether the plate-like crystals formed.

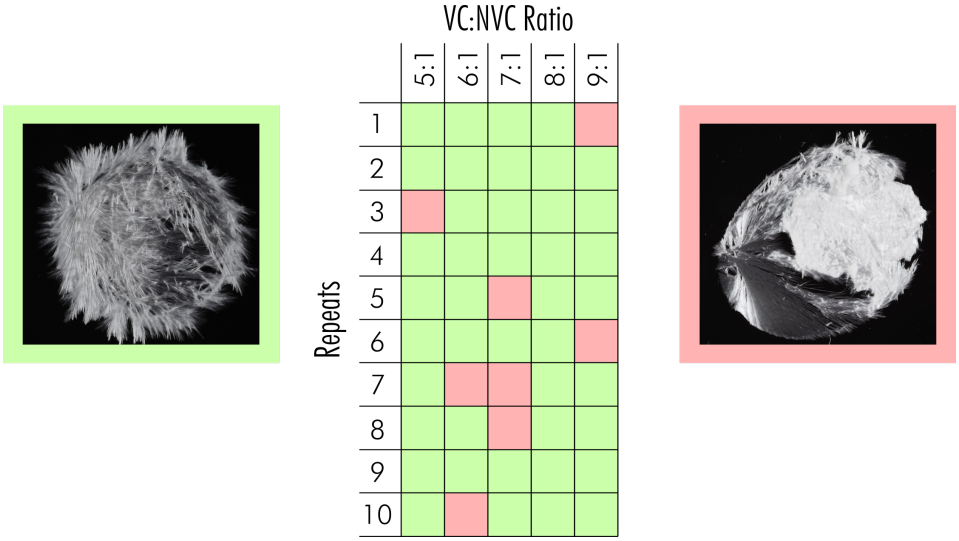

Figure 3.18: Results from 10 repeat crystallisations of 2-ethoxybenzamide from VODESs of ratio 5:1 - 9:1 phenol:2-ethoxybenzamide. Crystallisation experiments resulting in needles of 2-ethoxybenzamide are shown in green (left), and samples including an opaque plate-like crystal in pink (right). Each repeat experiment was taken after 24 hours of the previous experiment. The crystallographic form was determined primarily through observation of morphology, but some samples were selected to be analysed by powder X-ray diffraction to ensure correct determination.

Analysis via pXRD highlighted that the final crystal structure in all cases was the ubiquitous polymorph of 2-ethoxybenzamide. Figure 3.19 shows pXRD patterns for each case, fit to the known structure of 2-ethoxybenzamide. Scanning electron microscopy of an area of the opaque crystal is shown in Figure 3.20, confirming that the opacity of the crystal was caused by fracturing on the micron scale.

To assess the formation of the plate-like crystals, the crystallisation of several experiments were assessed in real-time. Due to the stochastic nature of the formation of the crystal, 20 experiments were run before the formation of the crystal could be followed. Figure 3.21 shows images of the metastable plate-like crystals before and after transformation to the ubiquitous 2-ethoxybenzamide

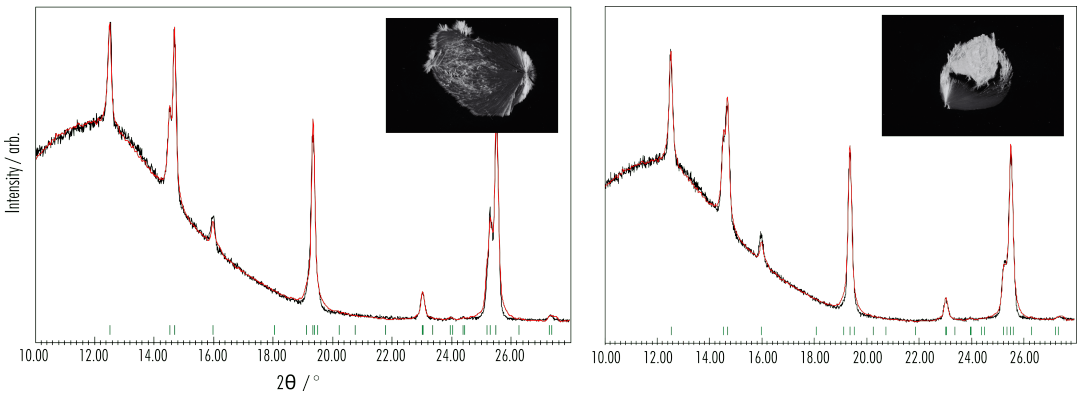

Figure 3.19: Powder X-ray Diffraction of 2-ethoxybenzamide samples grown from VODESs. The case of pure needle growth (left) and the concomitant needle and plate-like crystal growth are highlighted. Experimental patterns (black) are fit to the known crystal structure for 2-ethoxybenzamide (red) using Reitveld refinement.

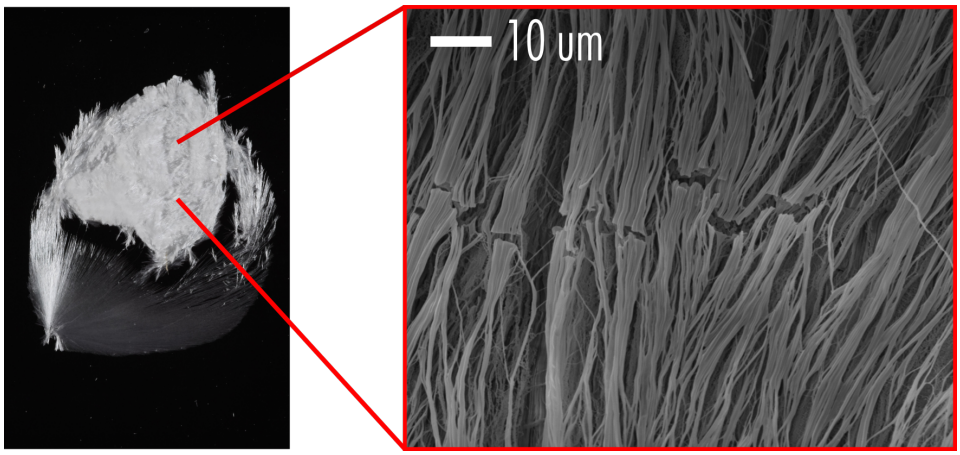

Figure 3.20: Scanning electron microscopy image of an opaque plate grown from a phenol:2-ethoxybenzamide VODES. The region shows the needle-like crystal morphology on the nano-scale, caused by the transformation of an intermediate metastable phase. Images were taken by Dr. Jason Potticary.

crystal structure. These experiments highlighted that the transformation happened rapidly after the liquid around the crystal had been depleted. However, the crystals were of the required quality and size to be solved by single-crystal X-ray diffraction. Therefore, subsequent experiments were run, and the crystals were moved to a fridge after they appeared so that further evaporation of the phenol could not occur.

Single crystal X-ray diffraction of the plate-like crystals revealed a monoclinic ($P2_1/c$) unit cell containing eight 2-ethoxybenzamide molecules and four phenol molecules (CCDC Ref code: VUKSEC). Therefore, the opaque crystals initially observed are formed via the desolvation of the phenol molecules from this crystal structure. Figure 3.22 shows the asymmetric unit (with thermal ellipsoids) and the unit cell for this new 2-ethoxybenzamide phenolate. Analysis of the crystal structure shows

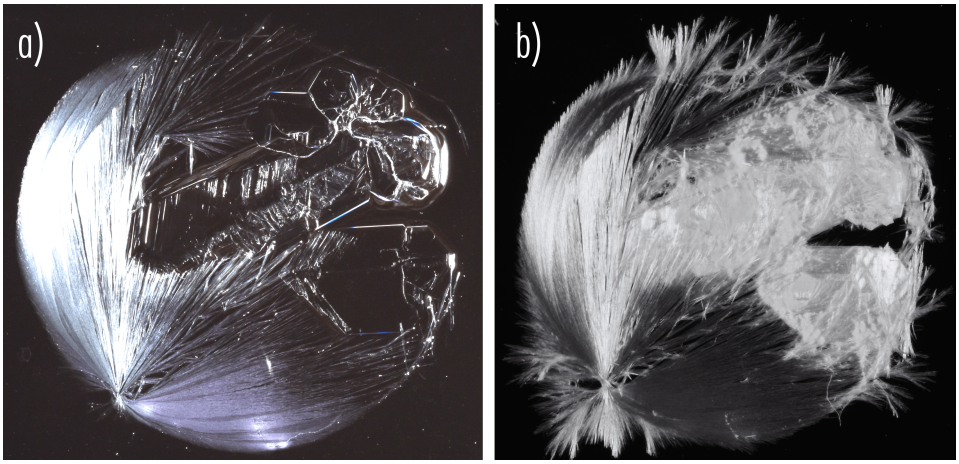

Figure 3.21: Optical images taken during the crystallisation of 2-ethoxybenzamide from a VODES. a) Clear plate-like single crystals can be seen during the evaporation of the phenol. b) After all the phenol has evaporated, the metastable crystals transform, causing them to become opaque.

that the phenol molecule sits between two 2-ethoxybenzamide molecules, allowing the favourable intramolecular N-H...O bond to form (Figure 3.23a). This interaction is not possible in the pure 2-ethoxybenzamide crystal structure due to the steric hindrance of the ethoxy group (Figure 3.23b).

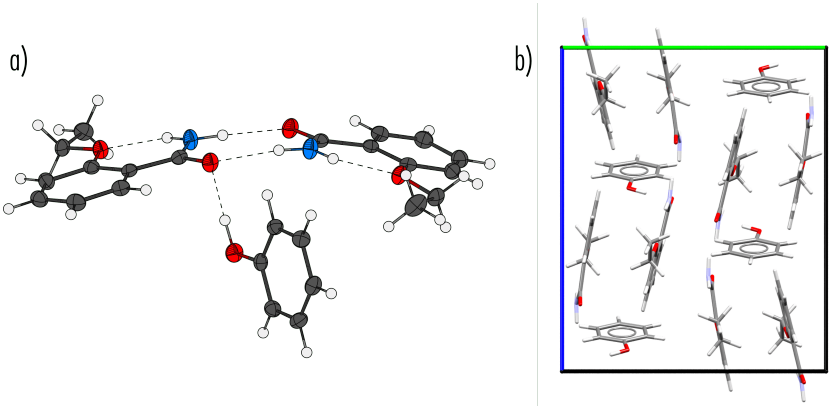

Figure 3.22: a) Thermal ellipsoid plot of the asymmetric unit of the solved 2-ethoxybenzamide phenolate crystal. b) Unit cell of the 2-ethoxybenzamide phenolate crystal viewed down the *a*-axis. Thermal ellipsoid plots are shown to the 50% probability level.

The observation of the phenol solvate of 2-ethoxybenzamide highlights the clear interplay between the formation of VODESs and co-crystals. Although it seemed to be the case that intermediary phases influenced the crystals of benzamide and paracetamol formed from VODESs, the structural solution of a phenol solvate is more definitive proof that phenol is affecting the crystallisation process. In the case of the 2-ethoxybenzamide, the phenol solvate did not cause any interesting subsequent crystal structures, but it does present a clear example of the complexities that can arise during

crystallisation when strong competing intermolecular interactions are present.

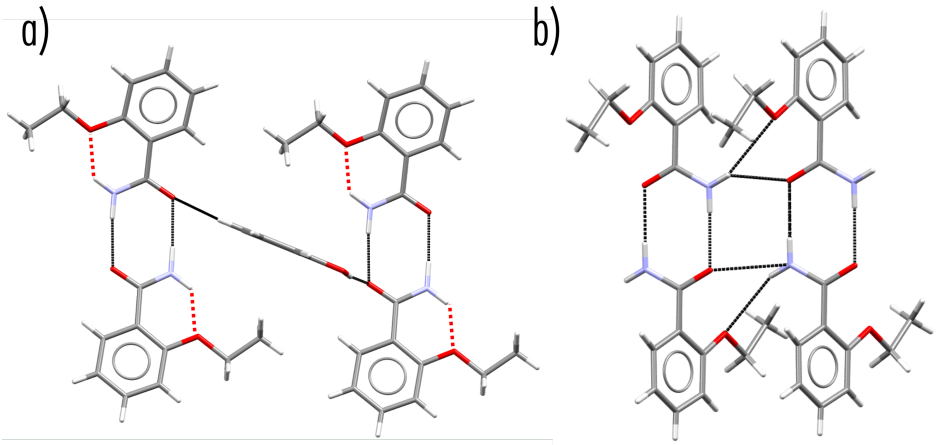

Figure 3.23: Dimer motifs present in the crystal structure of a) the 2-ethoxybenzamide phenolate and b) the stable form of 2-ethoxybenzamide. Intermolecular short contacts are shown in black and intramolecular contacts are highlighted in red.

3.7 Other Molecules Forming Volatile Deep Eutectic Solvents

In the process of exploring pharmaceutical molecules that would form VODESs with phenol, a large number of prospective NVCs were tested, containing an array of functional groups. In each case, mixtures of VC:NVC were produced of ratios between 1:1 - 10:1. Samples which did not spontaneously turn liquid were placed in an oven at 65 °C overnight. They were subsequently removed and placed on an insulated surface to cool. If there was no apparent crystallisation after 24 then crystallisation experiments were carried out.

The following section highlights a number of samples that were not exemplary crystallographically, but are essential in exploring the mechanism for VODES formation and subsequent use as a crystallographic medium.

3.7.1 Formation of Glasses in Verapamil Hydrochloride Volatile Deep Eutectic Solvents

Verapamil is a cardiovascular medication that sits on the list of essential medications distributed by the World Health Organisation.[151] It is often administered in the form of a salt (verapamil hydrochloride), which has one known polymorph.[152] Investigation of the formation of a VODES with a salt NVC is interesting to explore, as charged species are historically at the centre of the formation of eutectic mixtures. Verapamil hydrochloride formed stable VODESs with phenol at ratios of 3:1 - 10:1 VC:NVC. At these ratios, the mixture became liquid on contact, with only small amounts of mixing necessary.

For all VODESs ratios, evaporation of the VC leads to the formation of a glassy phase which persisted for at least a year. To understand this transition, differential scanning calorimetry (DSC) was

carried out on samples sealed in hermetic pans. Samples were cycled thermally between -70 °C and 70 °C. An initial ramp, up to the melting point of verapamil hydrochloride, was carried out to ensure that there was no remaining solid sample in the sample. Figure 3.24 shows DSC traces for the cooling and subsequent heating of verapamil hydrochloride VODESs of ratio 2:1 - 10:1 VC:NVC. Although no crystallisation or melting transitions occur, a clear, singular glass transition can be seen for the ratios 2:1 - 7:1. The temperature of this transition shows a clear trend to higher temperatures as the proportion of phenol is decreased. For a 10:1 VODES the midpoint of the glass transition on heating is at -55 °C, which linearly increases to -30 °C as the ratio is increased to 5:1. From here, the transition temperature increases more rapidly as ratios approach 2:1, where it is above room temperature.

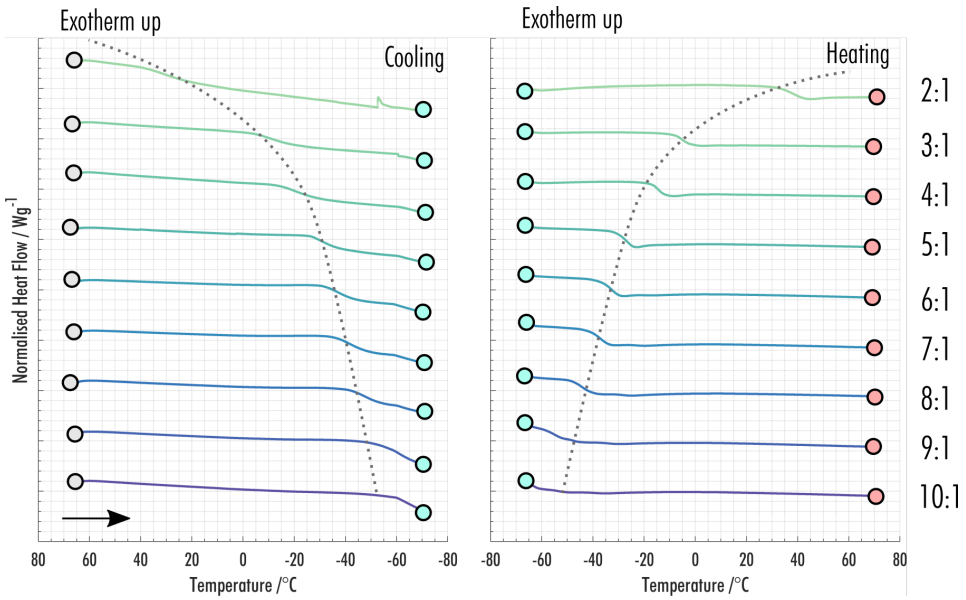

Figure 3.24: Thermograms for VODESs of verapamil hydrochloride and phenol across the range of ratios 10:1 (dark blue) - 2:1 (light green). The left panel shows the initial cooling from 70 °C to -70 °C, and the right panel the subsequent heating from -70 °C to 70 °C. A grey circle represents the start of each run, blue the point at which the heating begins and red the end of the cycle. A dashed line shows an approximate trend in the increase of the glass transition temperature.

This DSC analysis of the glass transition suggests that the VC evaporates off until the glass transition is reached, at which point stronger interactions will slow down the evaporation. An interesting observation for samples of ratio 8:1 - 10:1 is that multiple glass transitions appear to occur. To highlight this, an enlarged heating trace of the 9:1 VODES is shown in Figure 3.25, with red arrows highlighting the possible glass transitions. The transitions are difficult to resolve because of the small change in heat capacity and the appearance of a relaxation enthalpy on heating. Their appearance, however, helps to strengthen the suggestion that there is a complex structure within the liquid VODES mixtures, in this case, even a separation of glassy phases of different stoichiometry.

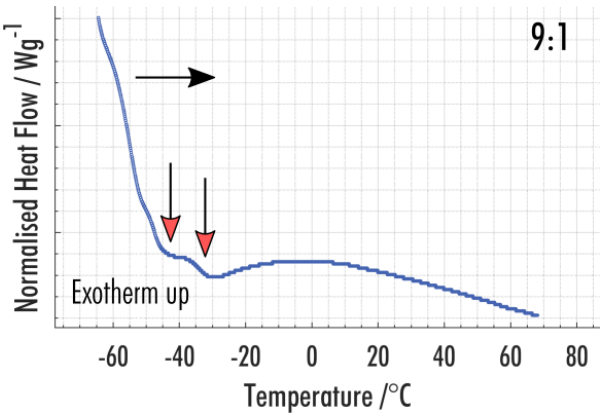

Figure 3.25: Enlarged view of the thermal trace for the heating of a 9:1 phenol:verapamil hydrochloride VODES. The black arrow shows the direction of heating. Red arrows are included to indicate the position of possible glass transitions.

3.7.2 2-Methoxybenzamide Volatile Deep Eutectic Solvents

The molecule 2-methoxybenzamide was evaluated due to the molecular similarity it has with benzamide and 2-ethoxybenzamide. In both of the previously discussed molecules, the formation of dimers plays an important role in the formation of the final crystal structure. There was evidence of the formation of a phenol solvate during the crystallisation of form I benzamide from VODESs, and a phenol solvate of 2-ethoxybenzamide was observed and solved for the first time. Both benzamide and 2-ethoxybenzamide form a large number of co-crystals with small organic molecules that can form similar hydrogen-bonding motifs.[149,153] Particularly in 2-ethoxybenzamide, the inclusion of an extra molecule allows for a more relaxed conformation of the molecule, allowing an intramolecular N-H…O bond to form. In contrast to these molecules, the stable and ubiquitous form of 2-methoxybenzamide forms a catemeric hydrogen-bonding motif,[154] while still allowing the intermolecular N-H…O bond to form. Furthermore, there are far fewer co-crystals of 2-methoxybenzamide on the CCDC; however, this may be due to less interest in the structure for pharmaceutical applications.

2-methoxybenzamide formed stable VODESs at room temperature with phenol for mixtures of ratio 2:1 - 9:1 VC:NVC. Solutions were stable under sealed conditions for at least a year. Transformation to the liquid phase occurred rapidly, as highlighted in the time-lapse shown in Figure 3.4. Similarly to 2-ethoxybenzamide, the liquids turned slightly pink over time when left at elevated temperatures (65 °C). Crystallisation from all ratios of the VODESs mixtures resulted in the formation of the ubiquitous crystalline form of 2-methoxybenzamide. There was no evidence of phenolate formation from any of the solutions.

Analysis of the sequence of the related molecules benzamide, 2-methoxybenzamide and 2-ethoxybenzamide allowed an insight into the propensity of VODES formation via sequential molecular alteration, in this case, the modification of an ortho- positioned side chain. The clearest ini-

tial difference is the formation of VODESs as the amount of VC is varied. 2-methoxybenzamide forms a VODES at the lowest ratio (2:1 VC:NVC), followed by benzamide (3:1 VC:NVC) and finally 2-ethoxybenzamide (5:1 VC:NVC). This trend intuitively aligns with the propensity of co-crystal formation with phenol, as the formation of such a state suggests that there are interactions within the VODES that favour the crystalline state over the liquid state. Correlation with the melting points of each of the pure NVC components suggests that the trend is not due to an increased propensity for the molecules to form as a pure crystal, as each of the pure crystalline phases have very similar melting points (benzamide - 127 °C; 2-methoxybenzamide - 127 °C; 2-ethoxybenzamide - 133° C).

3.7.3 Estradiol - A Hydrate Forming Volatile Deep Eutectic Solvent

Estradiol (17β-estradiol) is the major female sex hormone, playing a natural regulatory role in the human body. It is used in a pharmaceutical role as a medication for a number of hormone therapies. Crystallographically, estradiol forms very strong hydrogen bonds with water and therefore is almost always present as a hemihydrate.[155] The anhydrous form is only crystallised via sublimation or by dehydration of the hydrate at 170 °C. The difficulty in crystallisation is due to the hydrate being thermodynamically and kinetically favoured over the pure phase.

Crystallisation from VODESs containing estradiol and phenol were evaluated to see if the strong hydrogen bonding within the solution could disrupt the interactions forming the hydrate. VODESs of ratio 6:1 - 9:1 VC:NVC we stable at room temperature, although the samples needed to be left in an oven at 65 °C over 24 hours for the mixture to form within a reasonable time-frame. Repeat crystallisations of estradiol from each VODES ratio was carried out every day for 10 days. The resultant crystals were polycrystalline (Figure 3.26) and pXRD matched the known hemihydrate structure. Therefore, it is reasonable to assume that that water present in the initial sample and the atmosphere was enough to make the formation of the hemihydrate kinetically favourable. The crystalline nature of the sample may suggest a transformation from a transient phase, but if this was the case, the transformation was too rapid to observe during these experiments.

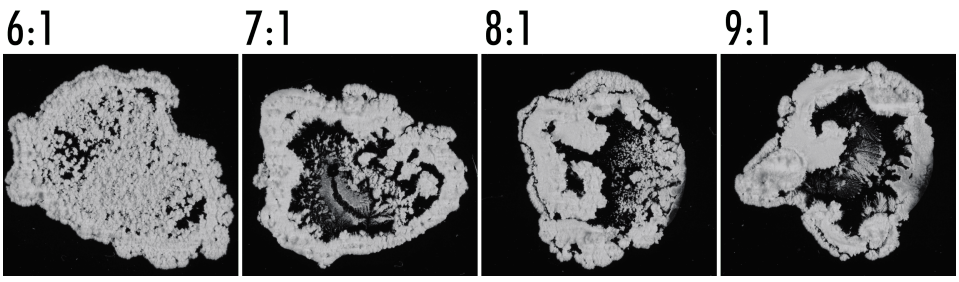

Figure 3.26: Resultant crystals from the crystallisation of estradiol from VODESs of ratio 6:1 - 9:1 phenol:estradiol.

3.7.4 Metaxalone, Metacetamol and Orthocetamol Volatile Deep Eutectic Solvents

The experimental results covered in this subsection were carried out by V. Hamilton (Metaxalone) and J. Potticary (Metacetamol).

Metacetamol (3-acetaminophen) forms stable VODESs with phenol at ratios of 5:1 - 10:1 VC:NVC. In a crystallisation experiment identical to that carried out for paracetamol, metacetamol showed a difference in crystal morphology for samples grown from 5:1 - 7:1 VODESs and 8:1 - 10:1.[104] Figure 3.27 shows the crystallisation experiments carried out for metacetamol. From these experiments, the metacetamol polymorph produced was always the stable form I, highlighting that the crystallographic change is purely morphological.

Similar work was carried out on metaxalone systems, with stable VODESs forming with phenol at ratios of 4:1 - 10:1 VC:NVC. In metaxalone, several metastable phases were directly observed crystallising from VODESs via pXRD. One of these metastable phases, which formed from 3:1 phenol:metaxalone VODESs, was shown to transform into a new conglomerate form A-R/S.[156]

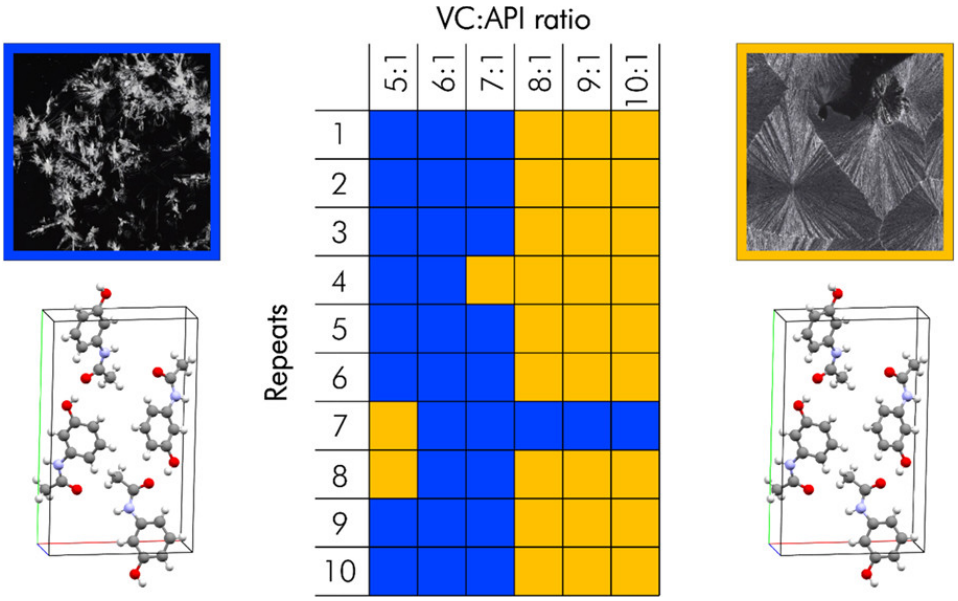

Figure 3.27: Results from 10 repeat crystallisations of metacetamol from VODESs of ratio 5:1 - 10:1 phenol:metacetamol. Crystallisation experiments resulting in rods of metacetamol are shown in blue (left), and needles in yellow (right). Each repeat experiment was taken after 24 hours of the previous experiment. Image created by J.Potticary[104]

The use of paracetamol, metacetamol and orthocetamol allows the evaluation of VODES formation propensity with changes in the position of the hydroxy functional group. Evaluation of the formation of VODESs shows that the minimum VC ratio at which a stable VODES forms for paracetamol is 4:1 VC:NVC, 5:1 VC:NVC for metacetamol, and no formation of VODES was seen at any ratio for orthocetamol. A comparison of the properties of each isomer highlighted that orthocetamol had a higher melting point than both paracetamol and metacetamol (paracetamol - 169 ° C; metacetamol

- 148 ° C; orthocetamol - 208 °C). Moreover, the crystal structure of orthocetamol had never been solved due to its tendency to form crystallites too small for single-crystal X-ray diffraction. In an attempt to decipher the differences in VODES formation propensity between the related molecules, the crystal structure of orthocetamol was solved via 3D electron diffraction (appendix D).[5]

Analysis of the orthocetamol crystal structure shows a particularly close interaction between the hydroxy and carbonyl groups of neighbouring molecules, leading to ribbons of molecules throughout the crystal. This strong interaction is not present in any paracetamol or metacetamol structures, where a combination of longer intermolecular interactions make up the 3D structures. Therefore, the VODES formation propensity in orthocetamol is either reduced by its more stable interactions with itself or an inability to form a large enough array of hydrogen bonds with phenol. This case study highlights that predicting mixtures of molecules that will form a VODES involves the same complexities as crystal structure prediction, as knowledge of all the possible phases a mixture can form needs to be evaluated. These phases will include all of the pure structures that the constituents of the mixture can form, any potential co-crystals, and any non-crystalline phases such as glasses.

3.8 Summary

The search for a crystallisation medium utilising DESs led to the discovery of VODESs, which rely on the same bonding interactions as DES but contain a volatile component. In a sense, this appears to be a modification of one of the defining features of DESs; however, the fundamental suppression of the mixture's melting point is still seen. It appears to be common that throughout the history of ILs and DESs, the properties of a few ILs are presented as general properties for all mixtures.[157] This initially helped to spark interest in ILs across multiple disciples but has left their definition very loose. In the cases discussed in this chapter, the main interest has been the depression of the melting point of a particular mixture. Such a depression allows crystallisation from the liquid state using molecules that would not normally be liquid at room temperature. Moreover, the fact that these molecules are liquid at these temperatures means that there are strong, competing hydrogen bonding interactions throughout the mixture.

The examples highlighted in this chapter show clear cases of crystallographic control and modifications. The cases of paracetamol, metacetamol and metaxalone all showed changes in crystalline properties, which depended on the ratio of the VODES mixture they were crystallised from. Furthermore, in benzamide, isolation of the form III polymorph was achieved within a solvent medium for the first time without the need for additive molecules.

The crystallographic modifications presented indirectly implied to formation the metastable phases, acting as intermediaries to the crystal structures and morphologies experimentally observed. This hypothesis is strengthened by the direct observation of metastable phases in metaxalone and 2-ethoxybenzamide. In 2-ethoxybenzamide, single-crystal X-ray diffraction showed that the metastable phase was a phenol co-crystal. Although solvates are not unusual from common solvent systems, it seems that the interplay of molecules forming a VODES makes it more likely for these metastable

phases to form, leading to a system that is susceptible to the presence of novel crystallisation dynamics.

The additional cases of verapamil hydrochloride, 2-methoxybenzamide and estradiol highlighted that there are many cases that the use of VODESs show little difference to conventional solvent crystallisation. However, these counter cases are useful when trying to establish an understanding of molecules that will form VODESs and be of interest crystallographically. The following chapter presents a method of evaluating VODESs in terms of their thermodynamic stability and internal crystallographic structure during thermal cycling. This is the first time these two properties have been assessed concomitantly in DESs, allowing an ability to highlight the complex interplay between the crystalline and eutectic liquid states.

CHAPTER 4

METASTABLE CRYSTALLINE PHASE FORMATION IN DEEP EUTECTIC SYSTEMS

The results of this chapter were published in part in the paper: Metastable crystalline phase formation in deep eutectic systems revealed by simultaneous synchrotron XRD and DSC.[158] I would like to thank Dr Asma Buanz for running all synchrotron experiments presented. Rietveld analysis was carried out by Dr Jason Potticary. Unless stated, the results presented in this chapter were analysed by myself.

4.1 Differential Scanning Calorimetry

Differential scanning calorimetry (DSC) is a well established technique for evaluating thermodynamic and kinetic properties of a variety of systems. The basic setup of a differential scanning calorimeter is shown in Figure 4.1. It consists of a cell that can house two pans (7 mm diameter), which sit on separate area thermocouples. The cell is purged with an inert gas (often N_2), and the temperature is carefully controlled. One of the pans contains the sample of interest and the other is an empty reference pan. The area thermocouples below the pans allow the difference in heat flow between them to be calculated, while the temperature of the cell is measured using a separate thermocouple. Any difference in heat flow between the sample and reference pans is directly related to exothermic and endothermic changes in the sample of interest, following the relationship given in Equation 2.8,

$$\frac{dQ}{dt} = C_p \frac{dT}{dt} + f(t,T). \tag{4.1}$$

DSC experiments are generally run at constant pressure, meaning that integration of the total heat flow as a function of time yields the change in enthalpy of the sample. The mass of the reference and sample pans are weighed to allow a normalised enthalpy to be calculated.

With modern advances in DSC technology, the furnace can be heated at ramp rates < 1 °C per minute and > 100 °C per minute. As an experiment is being run, a thermogram is produced like

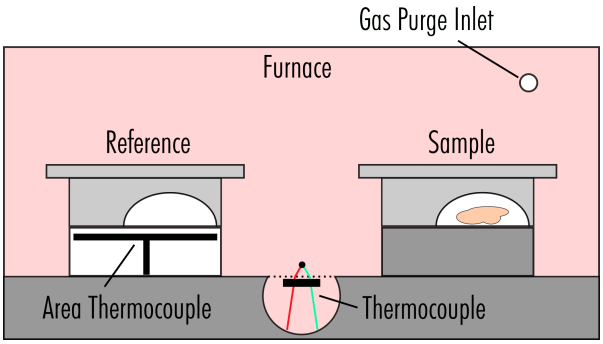

Figure 4.1: Schematic of the experimental setup of a differential scanning calorimeter. A reference and sample pan sit on separate area thermocouples which allows a measurement of the heat flow difference between them. The sample pan contains the sample of interest, whereas the reference pan is empty. Both pans sit inside a furnace, where a separate thermocouple measures the temperature. The cell is filled via the gas purge inlet with an inert gas.

those seen in Figure 4.2. An offset between the total heat flow on heating and cooling is caused by the heat capacity of the sample, making the output appear cyclic. The use of DSC to assess the thermal stability of molecular compounds has become an invaluable tool when studying organic molecules,[159] particularly in the pharmaceutical industry.[160]

Figure 4.2a shows the thermogram of a solid being heated above its melting point and then cooled past the point of re-crystallisation. Upon heating (red line), a trough is seen in the thermogram, representing an endothermal event due to the melting of the solid. Integration of this trough with respect to time gives the enthalpy of fusion of the solid. The onset of the endothermic transition gives the melting point of a pure solid; however, impurities often cause the beginning of the transition to be smeared out over a few degrees. In these cases, an extrapolated onset is calculated using the baseline and a tangent to the inflexion point of the trough (Figure 4.2b). Glass transitions can also be seen via DSC, which appear as a change in the baseline due to a difference in heat capacity between the liquid and glassy states (Figure 4.2c). On heating, glass transitions may occur with an enthalpy relaxation caused by a local redistribution of molecules below the glass transition. These enthalpy relaxations cause a trough in the thermogram, similar to a melting transition. Polymorphic or structural transitions can also be observed during DSC cycles, which can appear in several different ways. Figure 4.2d shows three possible cases of polymorphic transitions: (i) an endothermic solid-solid transition, (ii) a rapid melt-mediated transition and (iii) and slow melt-mediated transition.

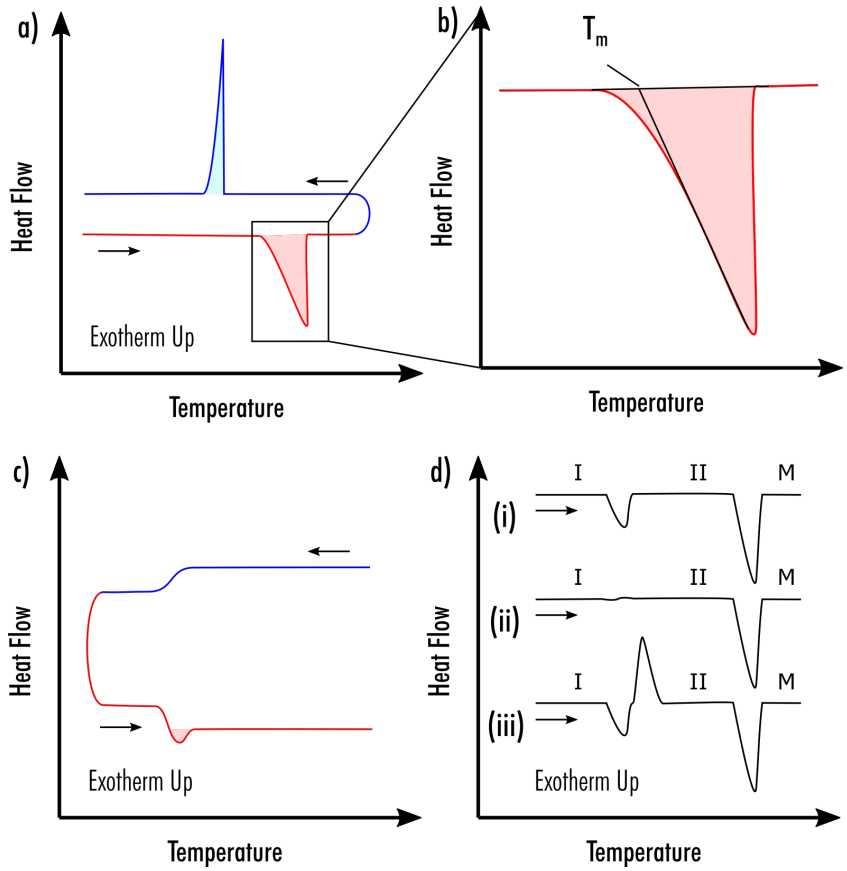

Figure 4.2: Example thermograms from differential scanning calorimetry experiments. a) A Crystalline material that melts on heating (red line) and crystallises on cooling (blue line). b) Inset of a) showing how extrapolated onset temperatures are determined. c) A liquid system passing through a glass transition on cooling (blue) and a glass transition with an enthalpy relaxation on heating (red). d) Solid crystalline samples going through a solid-solid transformation on heating and subsequently melting. (i) Endothermic solid-solid transition. (ii) Overlapping melt-mediated phase transformation endothermic and exothermic transitions. (iii) Melt-mediated phase transition.

4.2 The Phase Behaviour of Deep Eutectic Solvents

As phase changes can be easily analysed by utilising DSC, it is a particularly useful tool when evaluating the phase behaviour of DESs. In general, the phase behaviour of eutectic systems is presented on a phase diagram, highlighting the particular state of a system based on the temperature and molar fraction of each species. Figure 4.3 shows a simplified phase diagram for two molecules, A and B, with melting temperatures $T_{m,a}$ and $T_{m,b}$, respectively. In this scenario, it is assumed that both components are either liquid or solid, although approximations can also be made to include partial crystallisation of components.[161] The molar fraction at which the mixture has the lowest melting point is known as the eutectic point (X_e).

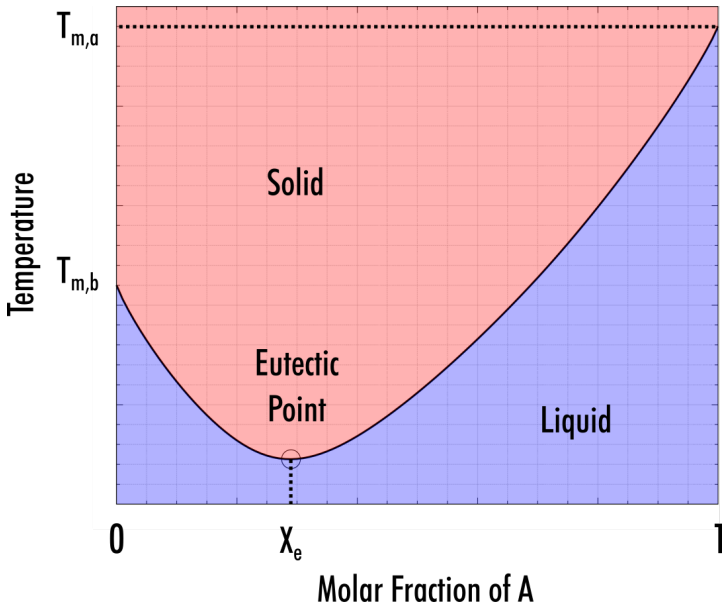

Figure 4.3: A theoretical phase diagram for a binary eutectic system containing species A and B. Regions at which the liquid and solid phases are more stable are highlighted, calculated based on the Gibbs free energy of the system.

To fully understand the phase diagrams of DESs, it is important to delve into how such a plot would be evaluated experimentally. In each DSC experiment, only a single molar fraction can be used, cycled in temperature to record crystallisation and melting points. As crystallisation is a stochastic event, the melting point of the solid after crystallisation tends to be used as the boundary between the liquid and solid regions of the phase diagram. The melting temperature used is the extrapolated onset temperature, as this is independent of sample mass and heating rate and ignores the peak broadening effect of impurities. This means that the experimental boundary between the liquid and solid regions of the phase diagram is dependent on which crystalline form is produced on cooling and requires a single melting event to occur.

Interestingly, work on the choline chloride:urea deep eutectic system highlighted that the formation of co-crystals might complicate the phase behaviour..[162] In this work, a choline chloride:urea co-crystal was observed via powder X-ray diffraction, forming at the eutectic point, whereas only pure choline chloride and urea were seen at other molar ratios. This difference in crystalline formation will clearly influence the shape of the eutectic curve. Moreover, given the crystalline phase behaviour of the VODESs seen in the previous chapter, it may be expected that interesting phase behaviour can occur in various systems and manners. To evaluate this, thermograms of the VODESs discussed in the previous chapter were produced.

4.3 Thermograms of Volatile Deep Eutectic Solvents

4.3.1 Preliminary Screening Using Phenol:Paracetamol Volatile Deep Eutectic Solvents

The first step in carrying out thermodynamic analyses of deep eutectic systems using DSC was to determine the ideal conditions for carrying out each experiment. As the DSC experiments aimed to compare the thermodynamics of each system, it was decided that the same experimental parameters should be used for each experiment unless a particular exception was identified.

The main parameters to consider were the temperature ramp rate, sample mass, type of pan and temperature bounds. In DSC, the ramp rate of a sample (usually measured in °C.min^{-1}) is important for both the resolution and signal magnitude. A higher ramp rate will cause a decrease in resolution due to the sampling rate of the DSC; however, the heat flow at any one time will increase with increasing ramp rate. Thus, the choice of ramp rate is a compromise between these two effects. Samples exhibiting very weak signals may need to be run at faster heating rates to increase the heat flow to a detectable level. Furthermore, the faster the ramp rate, the less time the sample has to reach thermodynamic equilibrium, leading to a number of kinetic effects. This kinetic effect can have implications for the formation of different crystalline phases and has been heavily studied for the characterisation of polymorphs,[163–166] formation of new crystalline forms[167] and accessing of amorphous phases.[168] The sample mass is a similar compromise to the ramp rate. Using more sample increases the heat flow during the DSC experiment. However, transitions will be less distinct, as the sample will not be completely homogeneous across the pan (grain size, thermal contact, etc.).

The phenol:paracetamol mixture was chosen as a model system to determine the correct parameters for the thermal cycling of VODESs. As the samples contained a volatile component, the sample pans were chosen to be sealed hermetically to reduce evaporative loss. Only samples that were liquid at room temperature were evaluated, which were pipetted into aluminium pans and weighed to a precision of 0.1 mg. Between 10 mg and 20 mg of sample was used to ensure a practicable signal-to-noise ratio without rupturing the pan due to evaporation of the volatile component at high temperatures. Upper a lower temperature bounds were chosen to be 70 °C and -70 °C. The upper limit was to ensure that all sample was liquid and the lower was based on the limit of the calorimeter.

Heating rates between 1 °C.min^{-1} and 20 °C.min^{-1} were evaluated to determine an ideal value. Thermograms of three of the phenol:paracetamol VODES are shown in Figure 4.4. Each sample showed both an endothermic and exothermic event, along with a glass transition at low temperatures. The glass transition is most easily observed in the 4.5:1 phenol:paracetamol system. As a glass transition is seen for all ratios, it is likely that a partial crystallisation of the system is occurring (exothermic event), followed by a glassy transition of the remaining mixture (glass transition) and the subsequent melting of the crystalline mixture on re-heating (endotherm).

Two trends can be seen in the thermograms shown in Figure 4.4. Firstly, as the heating rate of the sample is increased, the point at which the exothermic event occurs appears later in time. As crystallisation is a stochastic event, this trend is expected. In some cases, the crystallisation is suppressed

long enough that it does not happen until the sample is heated back up again, which is known as cold-crystallisation. In these cases, the whole system goes through (and back out of) the glassy phase before the exothermic event. Cold-crystallisation can become an issue if the endothermic and exothermic events overlap, making the determination of transition onsets difficult due to distortion of peaks. The second trend that can be seen is that the onset set of the endothermic event moves to lower temperatures as the molar ratio of phenol is reduced. Together, the two trends mean that the heating rate is most important when considering samples with lower phenol molar fractions. It is clear that in the 4.5:1 phenol:paracetamol system, the exothermic and endothermic events are overlapping.

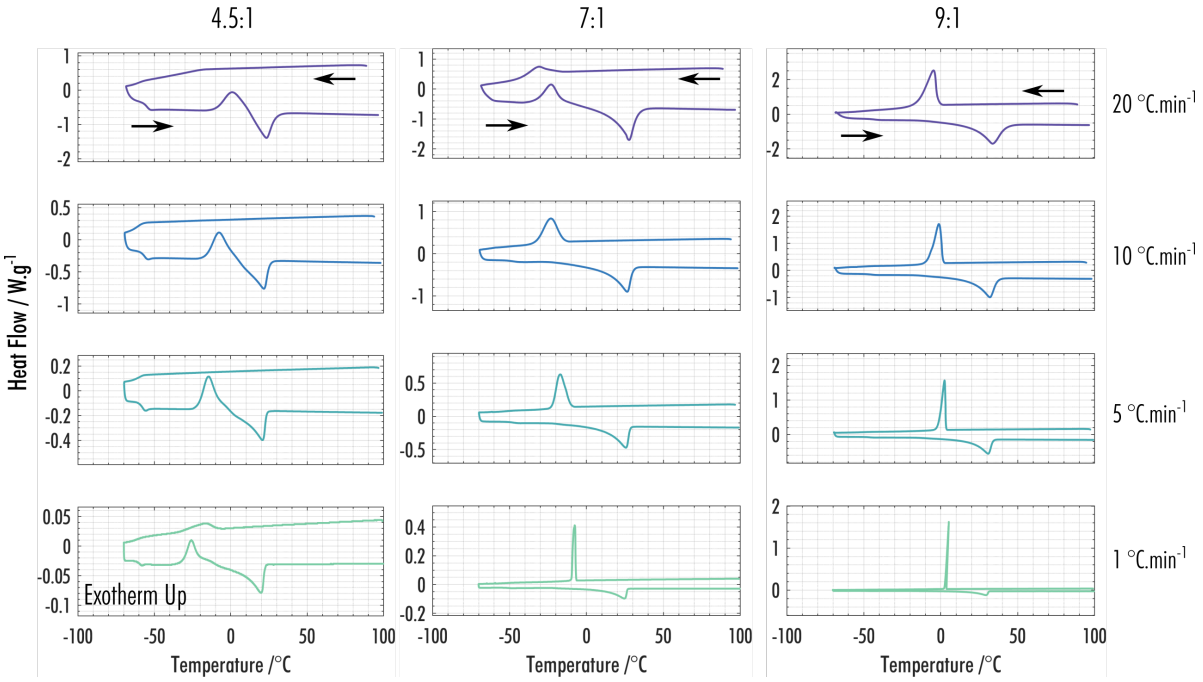

Figure 4.4: Thermograms of the phenol:paracetamol VODESs cycled between -70 °C and 70 °C. In the thermograms shown, the samples were initially cooled and subsequently heated at a constant ramp rate. Ramp rates between 1 °C.min^{-1} and 20 °C.min^{-1} are shown.

To evaluate the effect of the differing ramp rates on the phenol:paracetamol mixtures, the enthalpy of fusion and onset temperature of the endothermic events were determined for each sample. This event was far less dependent on the heating rate than the exothermic event, as would be expected for a melting transition. It should be noted that the endothermic transition is very broad, which is an observation often attributed to eutectic impurities.[169,170] Figure 4.5 shows a summary of the enthalpies and melting point onsets as a function of the molar fraction of paracetamol. For molar fractions below 0.16, the calculated enthalpy of fusions have a similar difference between their maximum and minimum values (5 J.g^{-1}). In all cases, the value of the enthalpy increases as the ramp rate is reduced. This is likely due to the heat capacity contribution, which will overlap more with the

transition at higher ramp rates. Above molar fractions of 0.16 there is a larger difference between the enthalpy values, which is caused by the overlap of crystallisation and melting transitions. The onset temperatures for ramp rates between 1 °C.min^{-1} and 10 °C.min^{-1} are all much closer together than at 20 °C.min^{-1}. This is likely due to the change in the shape of the melting transition peak, which is critical when calculating onset temperatures via linear extrapolation.

Due to the features seen in thermograms of the phenol:paracetamol systems, a compromise was made between the quality of the data and the time and resources necessary to carry out the experiments. As the main focus of the experiments was to acquire accurate melting point onsets, a ramp rate of 10 °C.min^{-1} was used to screen thermograms of VODES.

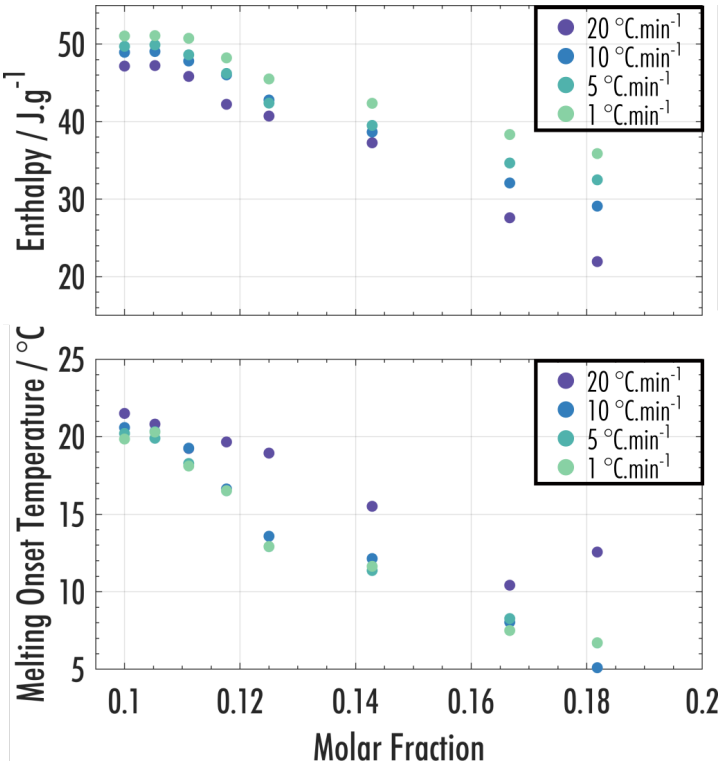

Figure 4.5: Graphs of the enthalpy of fusion and melting onset temperature of phenol:paracetamol VODESs. The enthalpy was calculated using a linear baseline and the melting onset using a linear extrapolation.

4.3.2 Screening of Volatile Deep Eutectic Solvent Thermograms

Due to the difficulties of accurately measuring out VODESs in the small quantities needed for DSC, an alternate method to standard weighing and mixing was used to produce samples of specific ratios. Initially, phenol and the chosen non-volatile component were dissolved in ethanol at a known concentration. The solutions were then mixed at the correct ratio, and the ethanol evaporated off in a 60 °C oven. As it has already been seen that phenol evaporated very slowly in a vial under such conditions, it was assumed that the ethanol would evaporate off far more quickly, leaving samples

of the correct ratio. In hindsight, this method caused more issues because it introduced a third component into the system (either ethanol or water). The consequences and resolution of this observation will be presented later in the chapter. The following sections highlight the thermograms for the VODESs systems discussed in chapter 3.

4.3.3 Paracetamol

Thermograms for the cooling and subsequent heating of phenol:paracetamol VODESs of molar ratio 4:1 to 10:1 are shown in Figure 4.6. For samples of molar ratio 6:1 - 10:1, only two transitions can be seen. These transitions appear to be a cold-crystallisation (exothermic event) followed by the subsequent melt of this crystalline material (endothermic event). In the 5:1 sample, the crystallisation appears to be suppressed by such a large amount that only a small exothermic event is seen, likely due to the overlap of a small crystallisation and subsequent melt. No enthalpic transition is seen in the 4:1 system, highlighting a complete suppression of any crystallisation event. In the 4:1 and 5:1 systems, a glass transition is seen, with a small entropy relaxation on heating.

These thermograms show stark differences to those seen in the preliminary screening. The melting onsets are at a lower temperature, and the crystallisation exotherms appear at a later time. This may be because of a small amount of water or ethanol in the system due to the difference in sample preparation, which has previously been shown to cause large differences in the choline chloride:urea DES phase behaviour.[171]

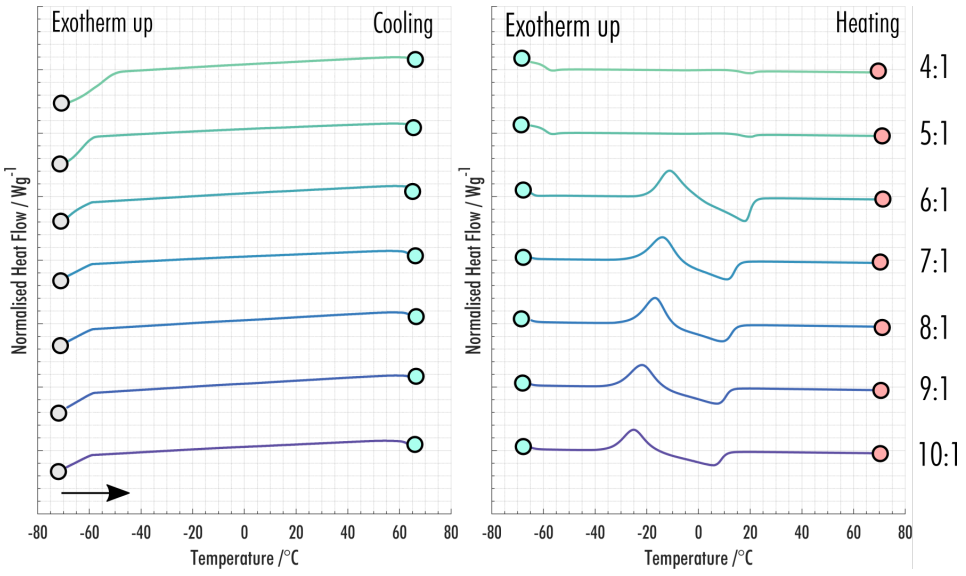

Figure 4.6: Thermograms for the cooling and subsequent heating of phenol:paracetamol VODES from 70 °C to -70 °C. Samples of molar ratios 4:1 (green) to 10:1 (blue) are shown, from top to bottom. The start of the DSC cycle is highlighted with a grey circle, the point between cooling and heating by a blue circle and the end of the cycle by a red circle. The black arrow shows the direction of the temperature ramp.

4.3.4 Benzamide

Thermograms for the cooling and subsequent heating of phenol:benzamide VODESs of molar ratio 3:1 to 10:1 are shown in Figure 4.7. The thermogram of the 10:1 mixture clearly shows three exothermic transitions on cooling and three endothermic transitions on heating. These transitions suggest that either three different crystalline structures form or multiple solid-state transformations occur between different phases. As the number of exotherms matches the number of endotherms seen on heating, this is likely showing three different crystalline phases. The 9:1 and 8:1 samples appear to have similar thermograms, with the highest melting peak shifting to lower temperatures as the amount of phenol is reduced. This peak also appears to reduce in size (melting enthalpy), suggesting that less of this phase is crystallising. For the 7:1, 6:1 and 5:1 samples, suppression of the final crystallisation exotherm results in a cold-crystallisation, distorting the melting endotherms. The final melting endotherm seems to have shifted to occur at the same temperature as the second exotherm, meaning it is difficult to distinguish the number of transitions. Only one exothermic and one endothermic transition is seen in the thermogram of the 4:1 sample, and no transitions are seen for the 3:1 sample.

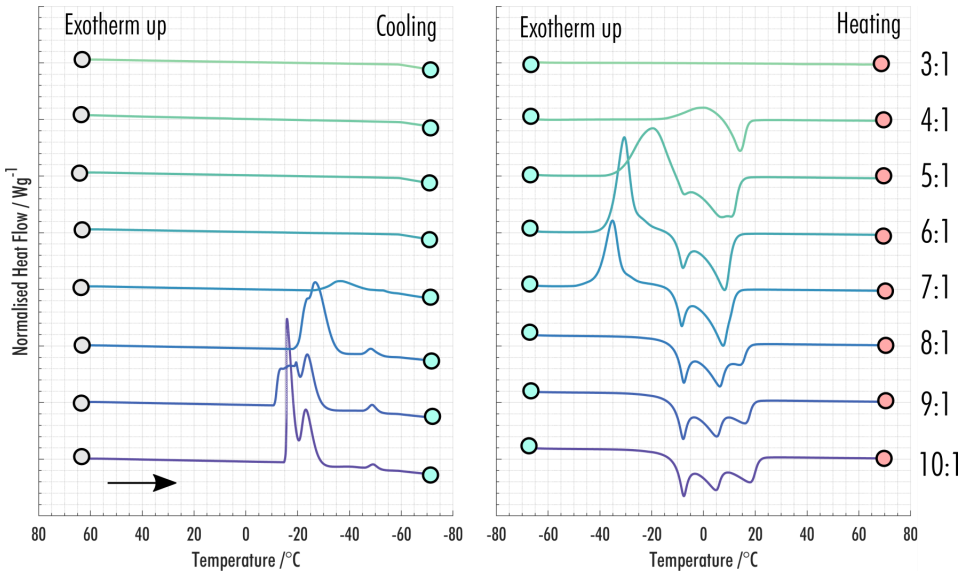

Figure 4.7: Thermograms for the cooling and subsequent heating of phenol:benzamide VODES from 70 °C to -70 °C. Samples of molar ratios 3:1 (green) to 10:1 (blue) are shown, from top to bottom. The start of the DSC cycle is highlighted via a grey circle, the point between cooling and heating by a blue circle and the end of the cycle by a red circle. The black arrow shows the direction of the temperature ramp.

4.3.5 2-Ethoxybenzamide

Thermograms for the cooling and subsequent heating of phenol:2-ethoxybenzamide VODESs of molar ratio 3:1 to 10:1 are shown in Figure 4.8. Thermograms of 10:1 and 9:1 mixtures show no transitions on cooling and a likely cold-crystallisation (exothermic transition) and melting (endothermic transition) on heating. The 8:1, 7:1 and 6:1 samples all show two melting endotherms on heating, suggesting that two crystallographic structures are forming. The crystallisation of these structures is suppressed as the amount of phenol is reduced, and in the 5:1 system, a single cold-crystallisation and melting endotherm seem to overlap. No transitions are seen in the thermogram of the 4:1 sample. The 3:1 sample exhibits two cold-crystallisation events on heating, followed by two melting endotherms.

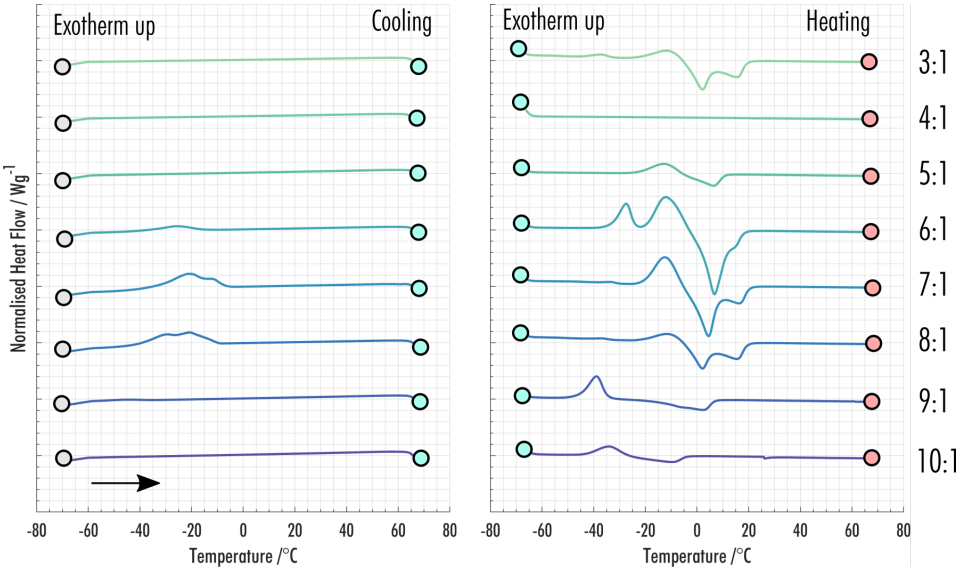

Figure 4.8: Thermograms for the cooling and subsequent heating of phenol:2-ethoxybenzamide VODES from 70 °C to -70 °C. Samples of molar ratios 3:1 (green) to 10:1 (blue) are shown, from top to bottom. The start of the DSC cycle is highlighted via a grey circle, the point between cooling and heating by a blue circle and the end of the cycle by a red circle. The black arrow shows the direction of the temperature ramp.

4.3.6 2-Methoxybenzamide

Thermograms for the cooling and subsequent heating of phenol:2-methoxybenzamide VODESs of molar ratio 3:1 to 10:1 are shown in Figure 4.9. The thermograms of samples of molar ratios 5:1 to 10:1 show a single melting endotherm on heating. It appears that the crystallisation is suppressed least in the 8:1 and 7:1 samples, which also have the highest melting onset temperatures. This is unusual, as the viscosity of the system is normally seen to decrease as more phenol is added. The 6:1 sample has an exothermic event on cooling and heating, but it is likely that the exothermic event on heating is

the completion of the initial crystallisation. The exothermic and endothermic events overlap in the 5:1 sample. The 4:1 and 3:1 samples show no visible transitions.

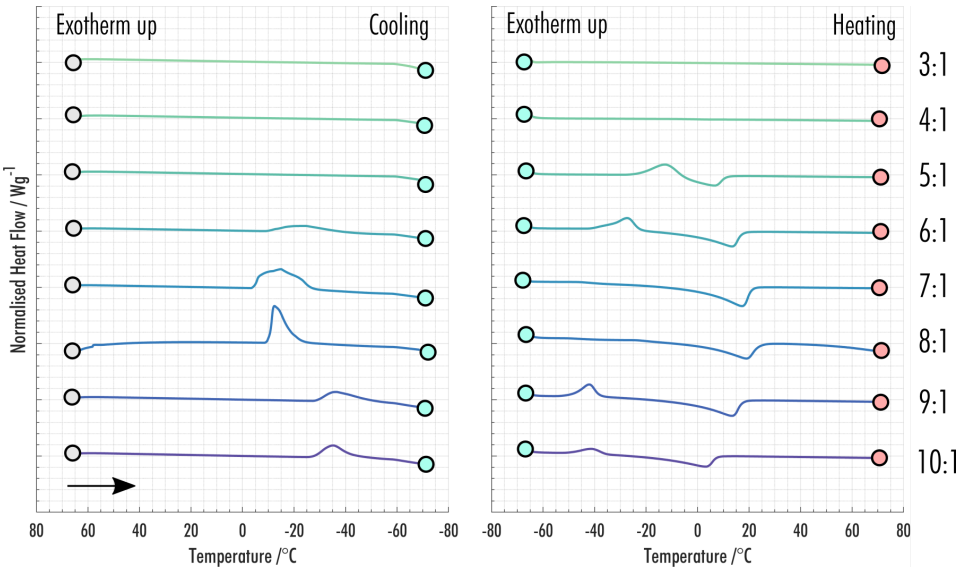

Figure 4.9: Thermograms for the cooling and subsequent heating of phenol:2-methoxybenzamide VODES from 70 °C to -70 °C. Samples of molar ratios 3:1 (green) to 10:1 (blue) are shown, from top to bottom. The start of the DSC cycle is highlighted via a grey circle, the point between cooling and heating by a blue circle and the end of the cycle by a red circle. The black arrow shows the direction of the temperature ramp.

4.3.7 Metacetamol

Thermograms for the cooling and subsequent heating of phenol:metacetamol VODESs of molar ratio 3:1 to 10:1 are shown in Figure 4.10. The thermogram for the 10:1 sample shows a single exothermic event on cooling and an endothermic even on heating, likely relating to the crystallisation and melt of a single crystalline phase. A similar exothermic event is seen in the thermogram of the 9:1 sample. However, two obvious endothermic events are seen on heating of the 9:1 sample, with a small third endothermic event. In the 8:1 system, similar endothermic transitions are seen, along with two exothermic crystallisation events on cooling and a cold-crystallisation event on heating. This highlights the possibility of three crystalline phases in the 9:1 and 8:1 systems. In the thermograms of the 7:1, 6:1 and 5:1 samples, a single cold-crystallisation event is seen, followed by a single melting endotherm. As the amount of phenol is reduced in these samples, the crystallisation becomes more suppressed, with the endothermic and exothermic events overlapping in the 5:1 sample. Thermograms of 4:1 and 3:1 samples show no observable transitions, other than a glass transition at -50 °C, which exhibit an enthalpy relaxation on heating.

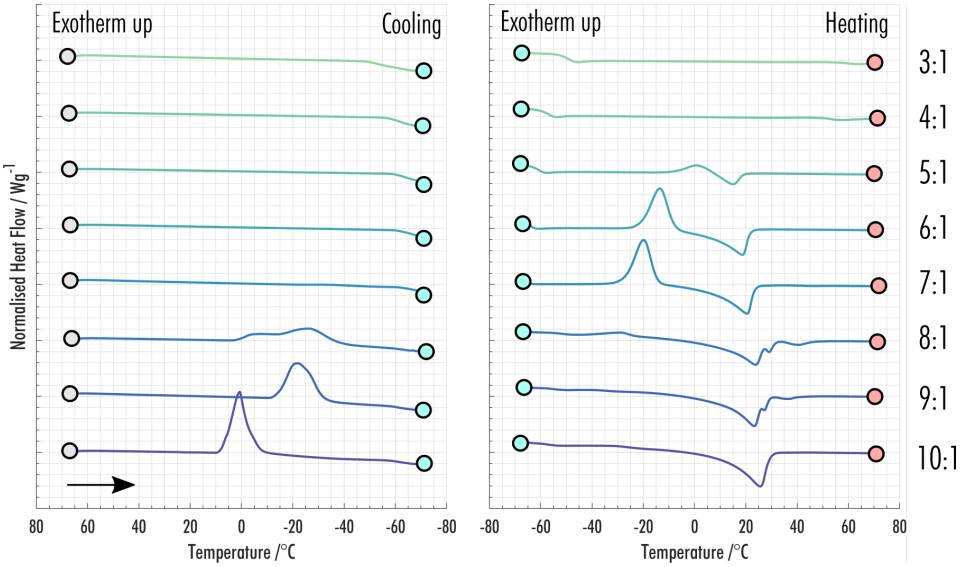

Figure 4.10: Thermograms for the cooling and subsequent heating of phenol:metacetamol VODES from 70 °C to -70 °C. Samples of molar ratios 3:1 (green) to 10:1 (blue) are shown, from top to bottom. The start of the DSC cycle is highlighted via a grey circle, the point between cooling and heating by a blue circle and the end of the cycle by a red circle. The black arrow shows the direction of the temperature ramp.

4.4 Metastable Phases in Volatile Deep Eutectic Solvents

It is clear from the thermograms presented in the previous section that there is a range of transitions that can occur during the thermal cycling of deep eutectic systems. The theoretical eutectic curve shown in Figure 4.3 depends on comparing the Gibbs free energy of the solid and liquid forms of the constituents of the system. In reality, however, DSC thermograms show that it is not the case that the pure components always crystallise out separately. As previously stated, the choline chloride:urea system was shown to form a co-crystal at the eutectic point. Moreover, many of the thermograms seen in the previous section showed multiple endotherms, exotherms and glass transitions. It is important to understand the crystalline landscape of deep eutectic systems, as such understanding may lead to more accurate predictions of possible molecular combinations and explanations of the structural phenomena seen via crystallisation from VODESs.

Due to the complex thermograms observed, it was hypothesised that a hierarchy of crystal structures can form as VODESs are cooled. A schematic of such a process is shown in Figure 4.11, highlighting how the formation of different co-crystals could lead to the observation of multiple crystalline forms.

Although DSC is very sensitive to phase transitions, accurate determination of the nature of specific transitions can require supplementary experiments. Much work has gone into the analysis of peak shapes for different DSC transitions,[173] however it can be easy to misinterpret structural changes that exhibit similar signals. For example, glass transitions with enthalpy relaxations often

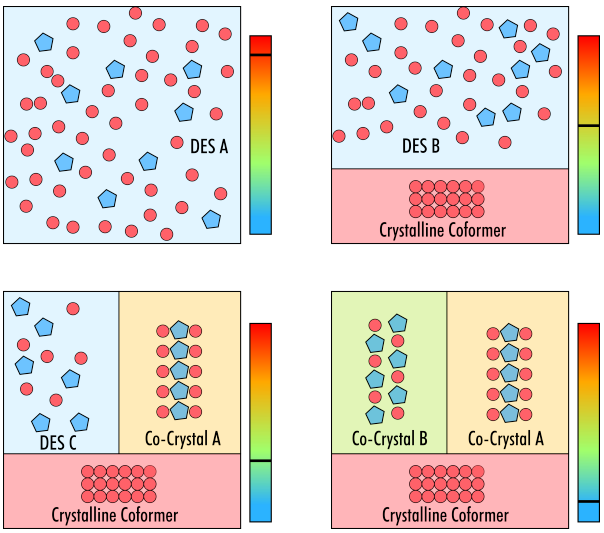

Figure 4.11: Schematic showing how a deep eutectic system could separate into phases as it is cooled from (a–d). In this example, (a) depicts a homogeneous liquid DES A, (b) one coformer crystallises out, leaving a liquid eutectic B with an altered stoichiometry, (c) co-crystal A forms, leaving a liquid C with a third stoichiometry. Finally, (d) a third crystalline phase forms as co-crystal B, with a different stochiometry to co-crystal A, leaving the whole system as a three-phase solid. Figure and caption from [172].

exhibit peak shapes very similar to melting endotherms. As the main interest of this project is the crystallographic structure of the eutectic systems, the most useful supplementary data to the DSC thermograms would be X-ray diffraction data of the sample in the DSC pan.

4.4.1 Concomitant Synchrotron X-Ray Diffraction and Differential Scanning Calorimtery

Concomitant synchrotron X-ray diffraction and differential scanning calorimetry (CXRD-DSC) is a technique, first used in 2016, that allows synchronous collection of X-ray diffraction and DSC data.[174] It has been successfully utilised to analyse a range of polymorphic transitions, including the stabilisation of form III paracetamol,[137] phase transitions in carbamazeipine and 10,11-dihydrocarbamazeipine,[175] analysis of β-estradiol hydrates,[155] the discovery of form IV olanzapine,[176] analysis of the phase transitions of mefenamic acid[177] and evaluation of the process of formation of a number of organic co-crystals.[178] The high-intensity monochromatic radiation available from the synchrotron source allows for high-quality powder X-ray diffraction data, meaning that accurate identification of known phases, and potentially structural solution of unknown phases, can be carried out using the data.

The setup for a CXRD-DSC experiment is shown in Figure 4.12. It consists of a standard heat-flux DSC setup (Figure 4.1), with pin-holes drilled to allow X-ray radiation to pass through the sample pan. A detector is placed in the path of the beam that has propagated through the sample, which

records a diffraction ring pattern. Aluminium pans are used to hold the sample. These pans exhibit diffraction at a known angle, which can be easily distinguished and disregarded, as there is often little overlap with the organic and inorganic peaks.

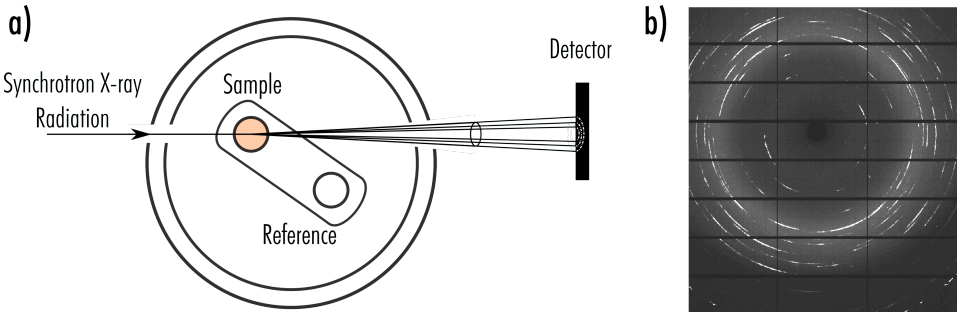

Figure 4.12: Experimental setup for a CXRD-DSC experiment. X-ray radiation, generated from a synchrotron, is passed through the sample pan and diffection patterns (b) collected on a detector.

As available experiment time was limited, only a small number of samples could be initially analysed. The samples chosen were phenol:metacetamol 8:1 molar ratio, phenol:2-ethoxybenzamide 8:1 and phenol:benzamide 9:1. These samples were chosen as they each exhibited more than one obvious phase transition from the preliminary DSC screen.

The representation of diffraction data as a function of DSC temperature is highlighted in Figure 4.13. Each diffraction pattern was matched with a temperature from the DSC thermocouple (Figure 4.13a), which was then mapped onto a surface plot using interpolated shading (Figure 4.13b). The use of the colour map allowed the data to be represented in 2D (Figure 4.13c). For ease of comparison of X-ray diffraction patterns to literature values, the 2θ axis was scaled to match data collected using a CuKα X-ray source. The experiments were carried out using a temperature ramp of 10 °C.min^{-1} on heating, with diffraction data collected in 1 °C intervals. Due to time constraints, the cooling of the samples was run with a ramp of 30 °C.min^{-1}.

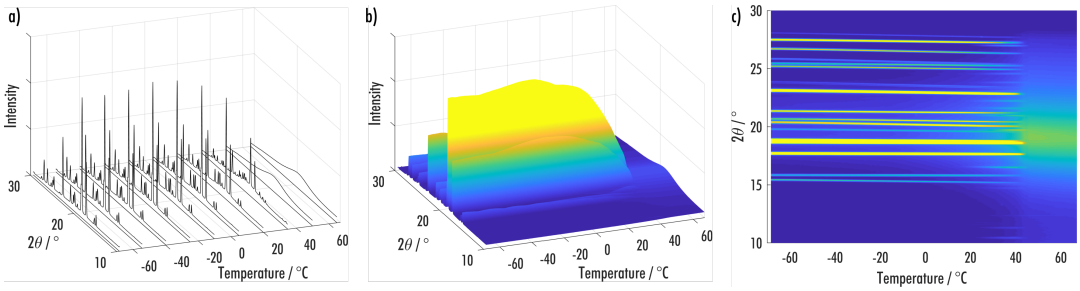

Figure 4.13: Representation of diffraction data from CXRD-DSC experiments. a) Each diffraction pattern is mapped to a temperature from the DSC. b) A colour map based on the diffraction intensity is applied, using shaded interpolation between patterns. c) The colour allows the mapping of diffraction patterns with temperature to be viewed in 2D.

4.4.2 CXRD-DSC of Phenol:Metacetamol VODES

Simultaneous X-ray diffraction and DSC data for the cooling and subsequent heating of the phenol:metacetamol 8:1 molar ratio sample is shown in Figure 4.14. The sample was initially heated from room temperature to 70 °C, followed by cooling to -70 °C and reheating to 70 °C. These parameters were chosen to keep the data in line with the preliminary DSC screen. At the start of the experiment the sample was in the liquid phase, meaning that only an amorphous peak can be seen, with a maximum intensity at 19 ° 2θ. As the sample is cooled, a clear exothermic crystallisation transition occurs at T_c = -12 °C, highlighted by both a peak in the DSC thermogram and the appearance of diffraction peaks. This transition occurs with a large reduction of the amorphous peak, highlighting the change from the amorphous liquid phase to a crystalline phase. This crystalline structure exists down to -70 ° with no additional change in the DSC or diffraction data, other than a continuous shift in diffraction peaks due to cell expansion and contraction. A small exotherm is seen on heating at T_t = 18 °C, which overlaps with an endothermic transition. Analysis of the diffraction data shows that the first event coincides with the appearance of a new set of diffraction peaks, before both sets of peaks disappear during the endothermic event, with all peaks depleted by T_m = 45 °C. The point where the new set of peaks occurs is denoted T_t, as it appears at the same time as the first phase is melting, highlighting that a phase transformation may be taking place. It should be noted here that T_m is stated as the point where the diffraction peaks have completely disappeared and not as the melting onset.

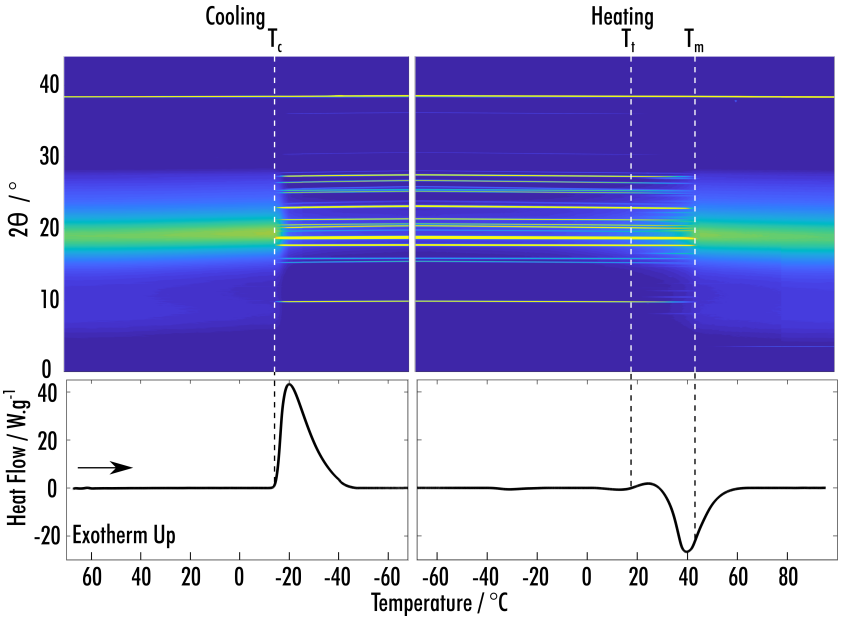

Figure 4.14: Simultaneous X-ray diffraction and DSC data for the cooling and subsequent heating of the phenol:metacetamol 8:1 molar ratio sample. The DSC and diffraction data are shown on the sample temperature x-axis, with the black arrow highlighting the direction of the temperature ramp. Figure adapted from [172].

A closer examination of the phase transition at T_t is shown in Figure 4.15. By looking at the range of 2θ between 7 ° and 17 °, it is clear that as the new phase appears, a reduction of the first phase occurs. It should also be noted that this transition is much more clear via analysis of the X-ray diffraction that it would have been by looking at the DSC data alone, where the small exotherm could have been easily missed or ignored.

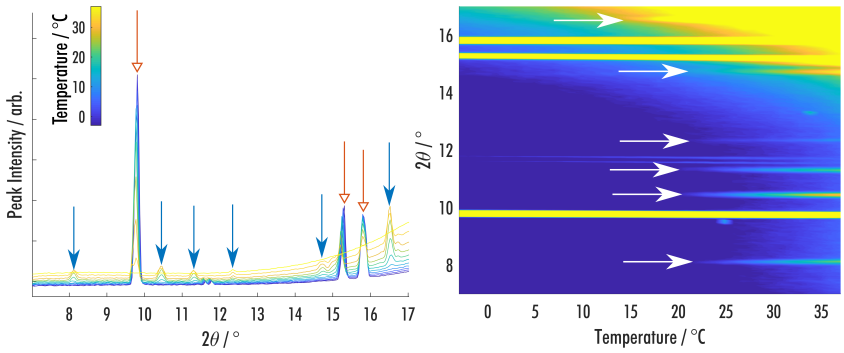

Figure 4.15: A detailed view of the pXRD data for metacetamol over the 2θ range 7 ° - 17 ° and temperature range 0 °C to 36 °C to show the crystallisation of the unknown phase from an 8:1 phenol:MAP VODES. The data shown are from the heating ramp starting at -70 °C. (left) Stacked pXRD patterns with a colour scale showing the change in temperature. Peaks due to the ambient phase of phenol are highlighted with orange arrows and peaks due to the unknown phase with blue arrows. (Right) Surface plot of the pXRD data with temperature to highlight to appearance of the peaks from the new phase. White arrows are used to indicate the appearance of each peak. Figure and caption from [172].

Rietveld analysis highlighted that the phase appearing at T_c corresponded to the ambient structure of phenol.[179] Additionally, fitting using the structures of the known forms of metacetamol[180,181] was attempted on the peaks appearing at T_t, which did not fit given any reasonable constraint of the structures. Figure 4.16 shows the fitting of X-ray diffraction patterns below and above T_t. Due to calibration of the refinement, the 2θ range is shown based on the synchrotron wavelength. Direct comparison of the diffraction patterns of potential components is shown in Figure 4.17, where the peaks that could not be fit to any known structures are highlighted in red.

As the structures present during the thermal cycling of the phenol:metacetamol VODES could not be directly identified, it is not possible to directly compare the amount of each of the samples at any temperature. However, by integration of peaks for each of the independent structures, it is possible to see where the amount of each phase is increasing or decreasing. Figure 4.19 highlights the appearance of each of the phases via integration of their most prominent peak. This highlights that the appearance of the unknown phase occurs duing the melting (or transformation) of the phenol structure.

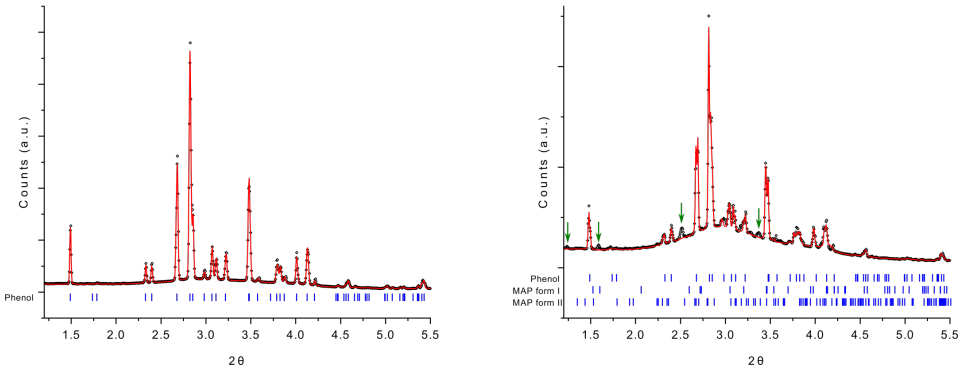

Figure 4.16: Rietveld analysis for diffraction patterns from the 8:1 phenol:metacetamol VODES. (Left) Diffraction pattern after the first crystallisation event, matched to the ambient crystal structure of phenol. (Right) Diffraction pattern after the second crystallisation event. Phenol peaks are matched, and tick marks for the crystal structures of MAP forms I and II are shown. Green arrows show the positions of unmatched reflections. Figure and caption from [172].

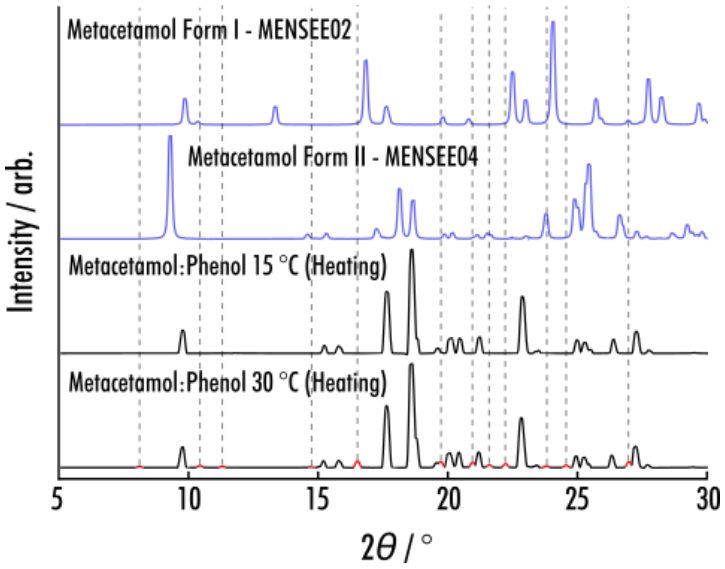

Figure 4.17: Diffraction patterns of the 8:1 phenol:metacetamol VODES. The 30 °C pattern shows both the phenol phase and the new unknown phase. The peaks from the new phase are highlighted in red and vertical dashed lines are shown to allow comparison to reference patterns. The diffraction pattern at 15 °C shows only the phenol phase. The patterns shown in blue are the only known forms of MAP. Figure and caption from [172].

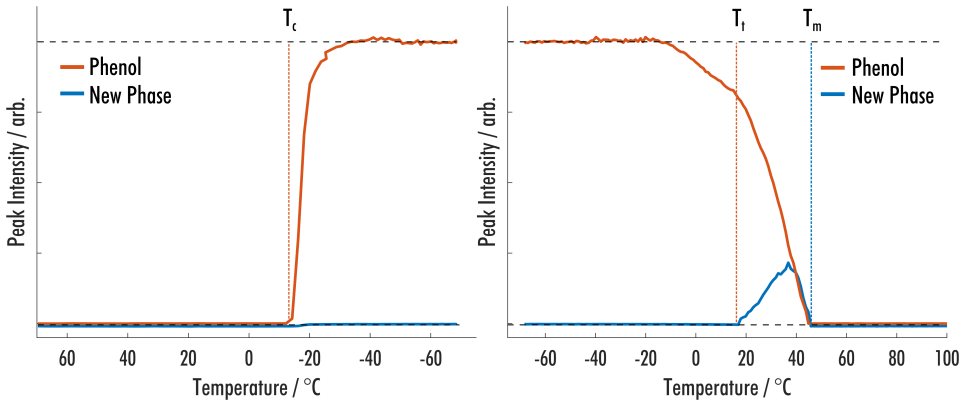

Figure 4.18: Integration of the most prominent diffraction peak for each of the phases present in the phenol:metacetamol 8:1 VODES. Figure adapted from [172].

4.4.3 CXRD-DSC of Phenol:2-Ethoxybenzamide VODES

Simultaneous X-ray diffraction and DSC data for the cooling and subsequent heating of the phenol:2-ethoxybenzamide 8:1 molar ratio sample is shown in Figure 4.14. The sample was run using the same thermal cycle as the phenol:metacetamol VODES. As the sample is cooled, an exothermic event is seen at T_{c1} = -10 °C. There are no transitions seen on further cooling down to -70 ° C, but another exotherm is seen on heating at T_{c2} = -21 °C. Following this transition, two endotherms of comparable enthalpies occur, which overlap. Analysis of the synchrotron data shows that the exothermic transitions both occur with the appearance of diffraction peaks. The endothermic transitions appear with the disappearance of the diffraction peaks, respectively, with the depletion of peak intensity occurring at T_{m1} = 18 °C and T_{m2} = 38 °C. The phase that crystallises first melts at the higher temperature, highlighting that it is the more stable phase.

Rietveld analysis highlighted that the phase appearing at T_{c1} corresponded to the ambient structure of phenol.[179] Additional analysis was attempted on the second set of peaks using the known structure of 2-ethoxybenzamide[182] and the phenol solvate of 2-ethoxybenzamide discussed in the previous chapter. Refinement of the second set of peaks did not fit either of the structures within reasonable constraints of unit cell parameters. The Rietveld fitting is highlighted in Figure 4.20. Comparison of the unknown phase to literature X-ray diffraction patterns is highlighted in Figure 4.21, where low-temperature powder X-ray diffraction was carried out on the 2-ethoxybenzamide structure to determine cell expansion/contraction with temperature. The peaks from the unknown phase are highlighted in red.

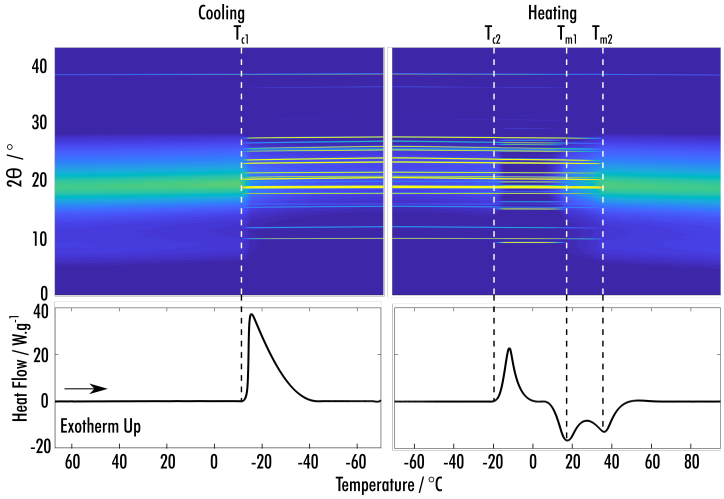

Figure 4.19: Simultaneous X-ray diffraction and DSC data for the cooling and subsequent heating of the phenol:2-ethoxybenzamide 8:1 molar ratio sample. The DSC and diffraction data are shown on the sample temperature x-axis, with the black arrow highlighting the direction of the temperature ramp. Figure adapted from [172].

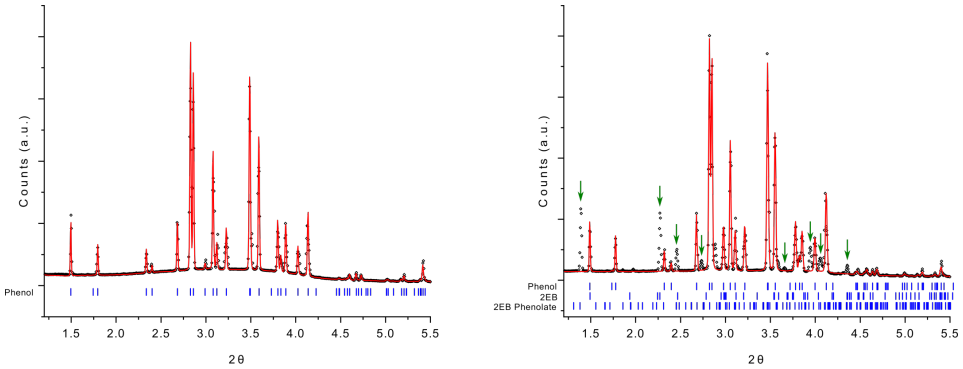

Figure 4.20: Rietveld analysis for diffraction patterns of the 8:1 phenol:2-ethoxybenzamide VODES. (Left) Diffraction pattern after the first crystallisation event, matched to the ambient crystal structure of phenol. (Right) Diffraction pattern after the second crystallisation event. Phenol peaks are matched and tick marks for the crystal structures of 2-ethoxybenzamide and 2-ethoxybenzamide phenolate are shown. Green arrows show the positions of unmatched reflections. Figure and caption from [172].

Examination of diffraction peaks during the crystallisation of the unknown phase within the phenol:2-ethoxybenmzaide system is shown in Figure 4.22. As the new phase appears, the amorphous background of the samples decreases, while the diffraction peaks of the phenol remain at the same intensity. This highlights that the new phase crystallises from the amorphous material left in the system and is therefore not a transformation of the crystalline phenol. Integration of diffraction peaks (Figure 4.23) shows that the amount of phenol increases when the new phase appears, indicating the crystallisation of residual phenol left after the formation of a co-crystal.

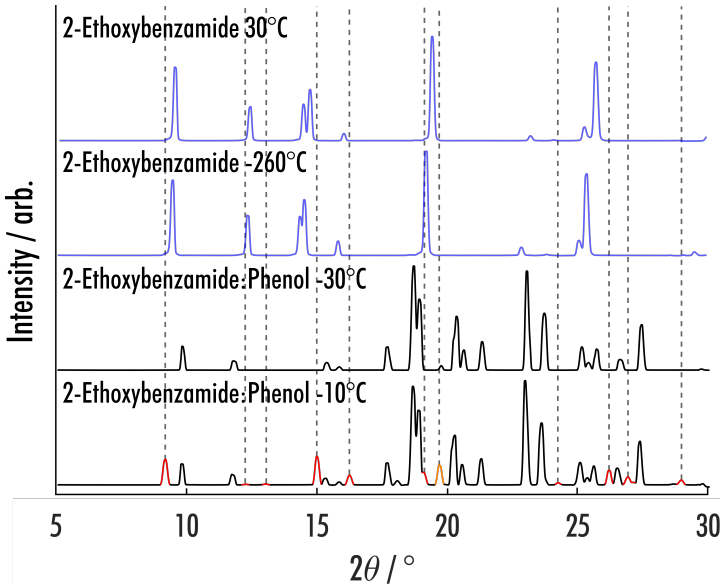

Figure 4.21: Diffraction patterns of an 8:1 phenol:2-ethoxybenzamide VODES. The -10 °C pattern shows both the ambient phenol phase and the new unknown phase. The peaks from the unknown phase are shown in red, and vertical dashed lines are shown for comparison with reference patterns. A peak that overlaps with one from the phenol structure is shown in orange. The -30 °C pattern shows the ambient phenol phase formed on cooling. Reference patterns for the known polymorph of 2-ethoxybenzamide are shown in blue. Patterns for this polymorph are shown at both 30 °C and -260 °C to illustrate how the peaks may shift with temperature. Figure and caption from [172].

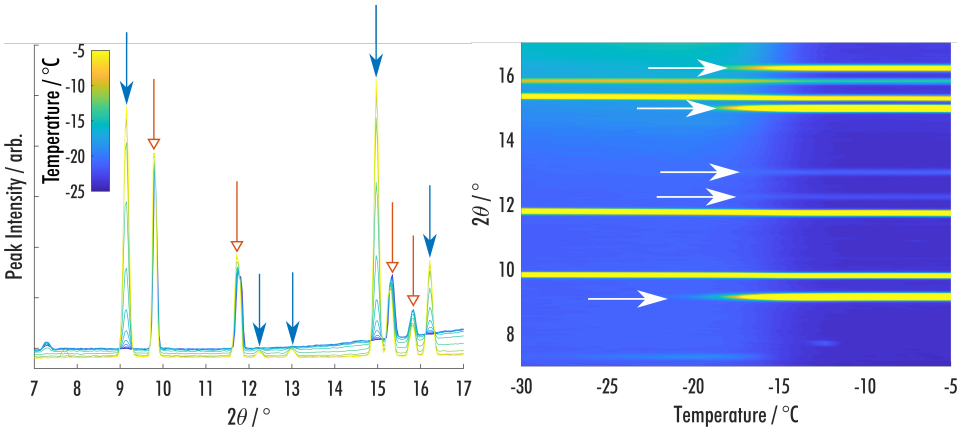

Figure 4.22: A detailed view of the diffraction data for the phenol:2-ethoxybenzamide VODES over the 2θ range 7 ° - 17 ° and temperature range - 30 °C to -5 °C to show the crystallisation of the unknown phase from an 8:1 phenol:2-ethoxybenzamide VODES. The data shown are from the heating ramp starting at -70 °C. (left) Stacked diffraction patterns with a colour scale showing the change in temperature. Peaks due to the ambient phase of phenol are highlighted with orange arrows and peaks due to the unknown phase, with blue arrows. (Right) Surface plot of the diffraction data with temperature to highlight to appearance of the peaks from the unknown phase. White arrows are used to indicate the appearance of each peak. Figure adapted from [172].

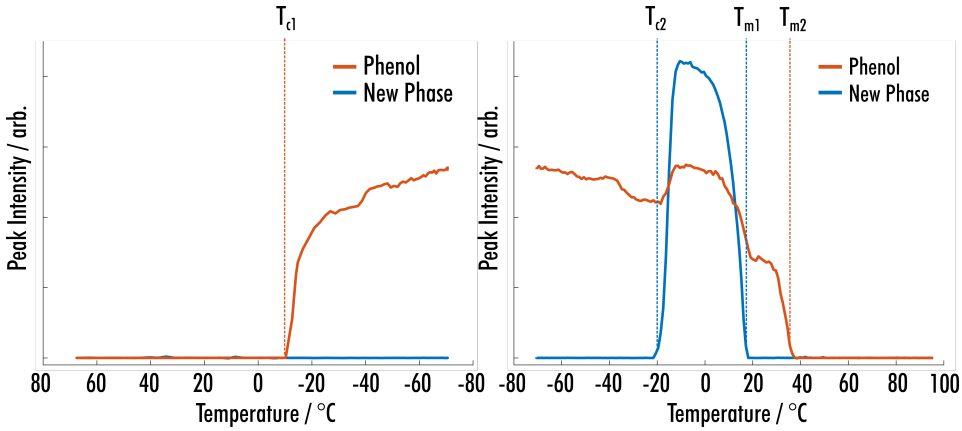

Figure 4.23: Integration of the most prominent diffraction peak for each of the phases present in the phenol:2-ethoxybenzamide 8:1 VODES. Figure adapted from [172].

4.4.4 CXRD-DSC of Phenol:Benzamide VODES

Simultaneous X-ray diffraction and DSC data for the cooling and subsequent heating of the phenol:benzamide 9:1 molar ratio sample is shown in Figure 4.24. On cooling from 70 °C two clear exothermic transitions can be seen at T_{c1} = -8 °C and T_{c2} = -24 °C, which persist down to -70 °C. On heating, there are no transitions until two overlapping endothermic events starting at 10 °C. Evaluation of the X-ray diffraction shows that the initial endothermic events both coincide with the appearance of independent sets of peaks. Furthermore, the endothermic events coincide with the disappearance of diffraction peaks (T_{m1} = 29 °C and T_{m2} = 44 °C), with the first phase to appear melting at the higher temperature.

Rietveld analysis highlighted that the phase appearing at T_{c1} corresponded to the ambient structure of phenol.[179] Similarly to the previous samples, analysis of the peaks forming at T_{c2} did not fit to any of the known forms of benzamide[145,183] to within any reasonable restraint of unit cell parameters. Rietveld analysis fitting is shown in Figure 4.25. A direct comparison of the phases seen from the VODES system and benzamide form I and III is shown in Figure 4.26.

As with the phenol:2-ethoxybenzamide system, the appearance of an unknown phase at T_{c2} coincides with a reduction of the amorphous background. The crystallisation of the new phase does not seem to affect the amount of phenol in the system, highlighting that the formation of this new structure is due to the crystallisation of the amorphous phase (Figure 4.27).

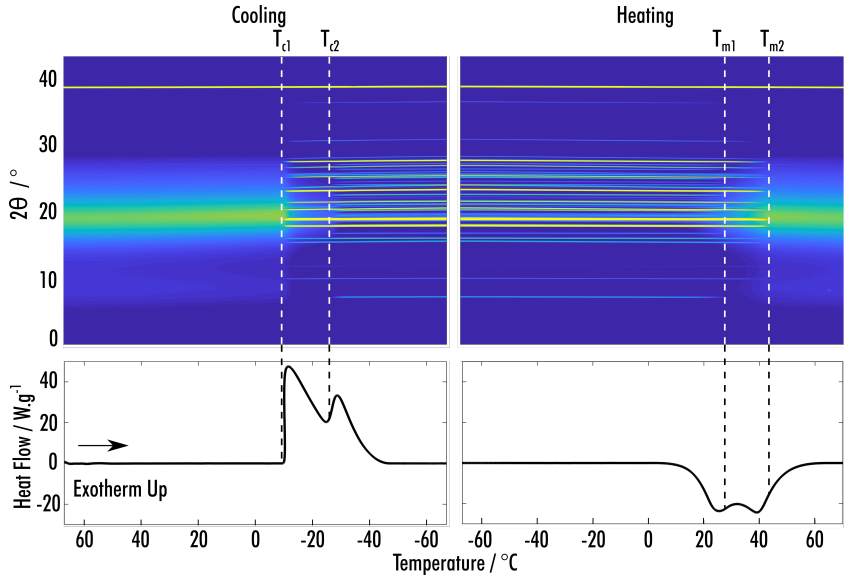

Figure 4.24: Simultaneous X-ray diffraction and DSC data for the cooling and subsequent heating of the phenol:benzamide 9:1 molar ratio sample. The DSC and diffraction data are shown on the sample temperature x-axis, with the black arrow highlighting the direction of the temperature ramp. Figure adapted from [172].

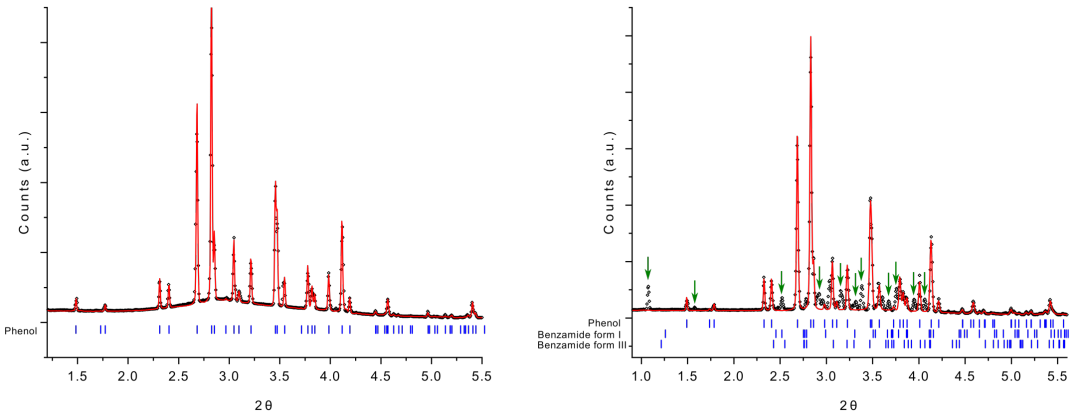

Figure 4.25: Rietveld analysis for diffraction patterns from a 9:1 phenol:benzamide VODES. (Left) Diffraction pattern after the first crystallisation event, matched to the ambient crystal structure of phenol. (Right) Diffraction pattern after the second crystallisation event. Phenol peaks are matched and tick marks for the crystal structures of benzamide forms I and III are shown. Green arrows show the positions of unmatched reflections. Figure and caption from [172]

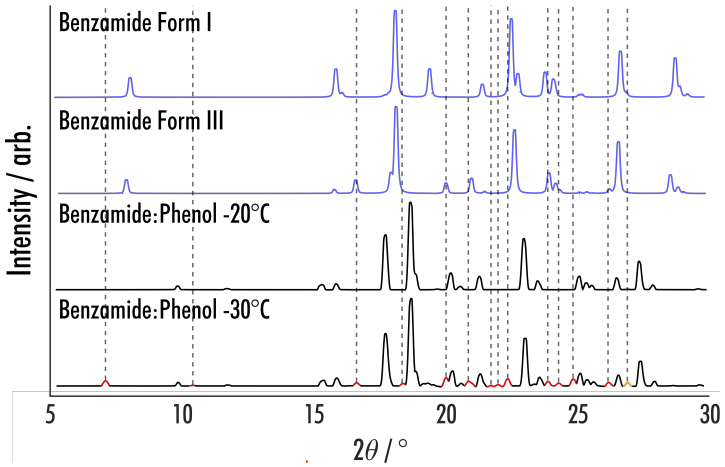

Figure 4.26: Diffraction patterns of a 9:1 phenol:benzamide VODES. The -30 °C pattern shows both the ambient phenol phase and the new unknown phase. The peaks from the unknown phase are shown in red and vertical dashed lines are shown to allow comparison with reference pattern. A peak that overlaps with one from the phenol structure is shown in orange. The -20 °C pattern shows the ambient phenol phase formed on cooling. Reference patterns of the common benzamide form I and III are shown in blue. Figure and caption from [172]

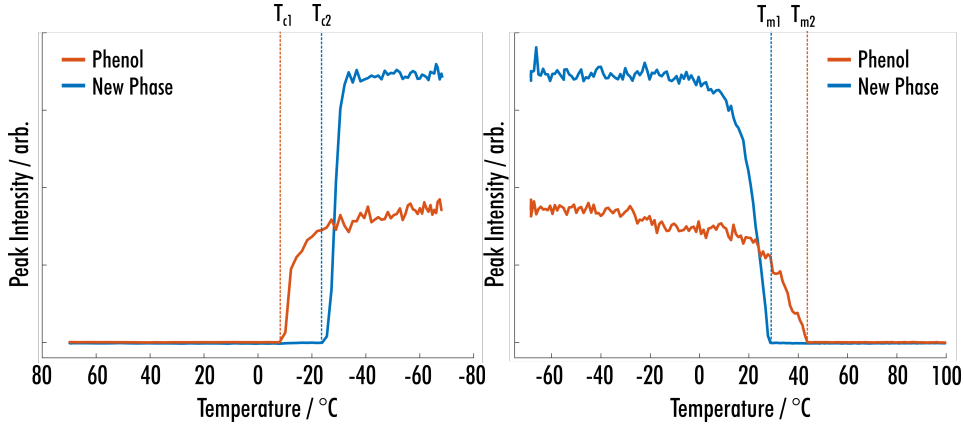

Figure 4.27: Integration of the most prominent diffraction peak for each of the phases present in the phenol:benzamide 9:1 VODES. Figure adapted from [172].

4.4.5 Evaluation of CXRD-DSC Results

CXRD-DSC of each of the VODES samples highlighted the formation of an unknown crystalline phase. In all three samples, the new phase appeared after the crystallisation of the ambient crystal structure of phenol and melted either before or at the same time as the crystalline phenol. This highlights that the new phases are metastable with respect to crystalline phenol, and are likely the formation of co-crystals from the remaining amorphous content in the system after the first crystallisation event.

The first point of discussion is that the DSC thermograms seen in the CXRD-DSC experiments are not exactly as expected from the initial DSC screening. Of particular note is that the appearance of three phases was expected for the metacetamol and benzamide systems, however, only two phases were seen in CXRD-DSC. Furthermore, the temperature of the transitions appears to be shifted to slightly higher values. As previously eluded to, the most likely cause for these differences is the presence of ethanol or water in the samples run during the preliminary DSC screening. Additional DSC thermograms were produced for samples to assess these differences further, prepared in the same manner as the samples run at the synchrotron. Thermograms taken out of the synchrotron were run using a TA Instruments DSC25, while the synchrotron experiments we run using a TA Instruments Q20 DSC.

A comparison of DSC thermograms for the phenol:metacetamol 8:1 VODES is shown in Figure 4.28. It is clear to see that the thermograms of samples produced via straight mixing of components are more alike than the sample produced from the evaporation of ethanol. An additional two endotherms in the sample produced by ethanol evaporation are highlighted, which are likely caused by the incorporation of ethanol molecules allowing more crystalline phases to form. The appearance of the first endotherm is also at a lower temperature for both the DSC25 thermograms, and the baselines are much flatter. Improvements in the baseline and resolution are expected with the DSC25, due to the improved specification of the model. There does appear to be a shift in temperature of 5 °C - 10 °C, but this is probably caused by modifications made to the Q20 DSC in preparing it for use with synchrotron radiation.

Comparison of DSC thermograms produced for the phenol:2-ethoxybenzamide 8:1 VODES is shown in Figure 4.29. Similarly to the metacetamol system, the thermograms of samples produced via mixing appear more comparable than those produced from the evaporation of ethanol. In this case, no additional endothermic events are seen; however, the exothermic events are more prominent in the mixed samples, and the endothermic events appear at more comparable temperatures.

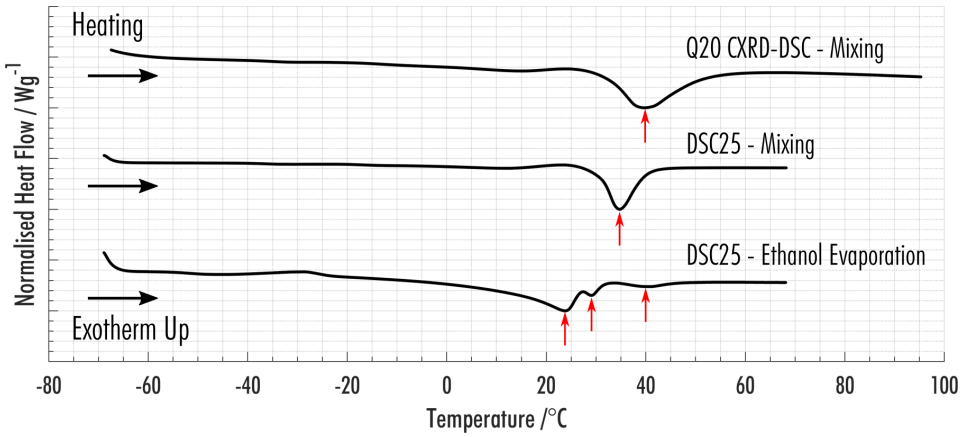

Figure 4.28: DSC thermograms for the phenol:metacetamol 8:1 VODES using different sample preparations and differential scanning calorimeters. Red arrows highlight the position of the peak of endothermic transitions. Black arrows highlight the direction of heating.

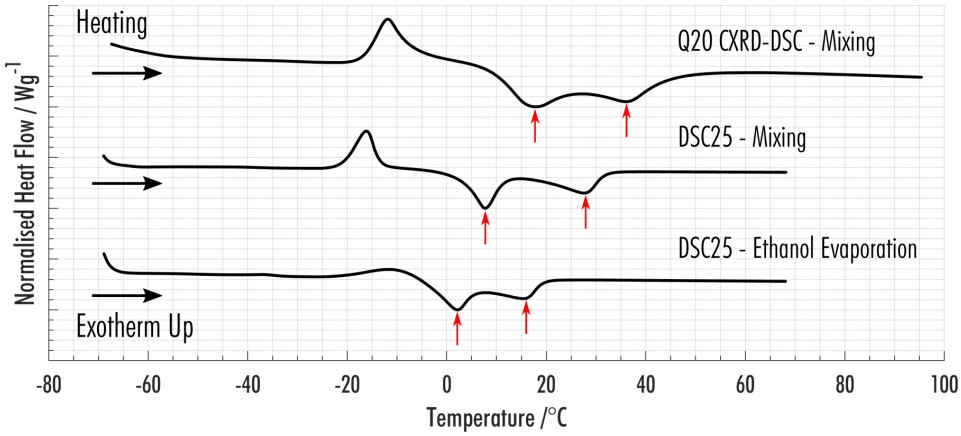

Figure 4.29: DSC thermograms for the phenol:2-ethoxybenzamide 8:1 VODES using different sample preparations and calorimeters. Red arrows highlight the position of the peak of endothermic transitions. Black arrows highlight the direction of heating.

Comparison of DSC thermograms produced for the phenol:benzamide 9:1 VODES is shown in Figure 4.30. The three endothermic events seen in the preliminary DSC screening were reduced to two endothermic events when the samples were prepared via solid-state mixing. It is again clear that the thermograms of samples produced from solid-state mixing are far more comparable, with only a slight shift in the temperature of thermodynamic transitions.

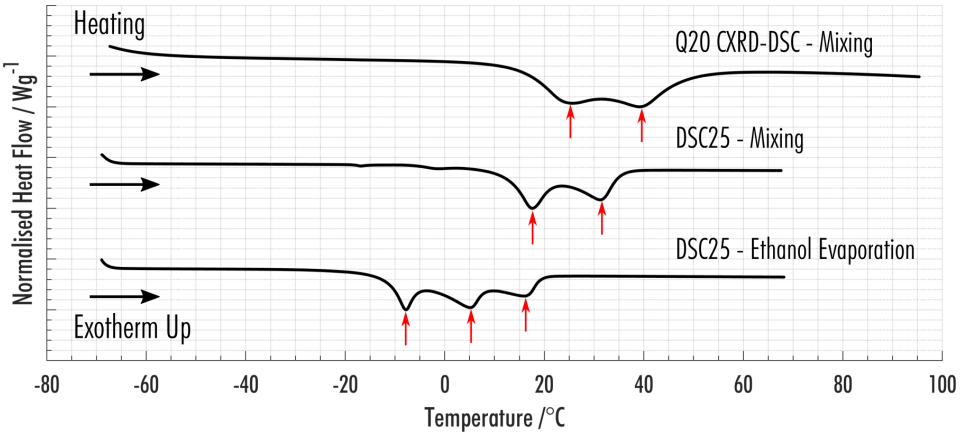

Figure 4.30: DSC thermograms for the phenol:benzamide 9:1 VODES using different sample preparations and calorimeters. Red arrows highlight the position of the peak of endothermic transitions. Black arrows highlight the direction of heating.

These comparisons highlight the importance of sample composition when evaluating the structural landscape of deep eutectic systems. Although the inclusion of an additional component was not intended during sample preparation, this exercise highlights the large array of potential complex multi-component systems that can exist. As hydrogen bonding is imperative to the formation of the phases of the eutectic mixtures, it is clear that many possible competing metastable phases can form on the cooling of samples. Indeed it seems likely that the energetic competition between these metastable phases is the driving force of the melting point suppression seen in eutectic mixtures.

It was highlighted during the analysis of the CXRD-DSC data that the crystallisation of new phases often occurred with the depletion of a proportion of an amorphous peak. This is expected, as the amorphous material is the eutectic liquid, crystallising sequentially as the sample is cooled. Analysis of this amorphous component, although difficult due to the number of peaks present in the diffraction patterns, highlights that even after the crystallisation of multiple phases some liquid component remains (Figure 4.31).

To evaluate any remaining amorphous material in the VODESs after partial crystallisation, additional DSC cycles were run using the DSC25, with samples prepared via the mixing of constituents. Figure 4.32 shows a DSC thermogram for the 8:1 phenol:metacetamol VODES, where the sample is held at the crystallisation temperature of the second phase and subsequently cooled back down to -70 °C. This altered temperature cycle allows for the deconvolution of phase transitions, as the initial crystallisation exotherm overlapped with the melting endotherm of the system. As multiple

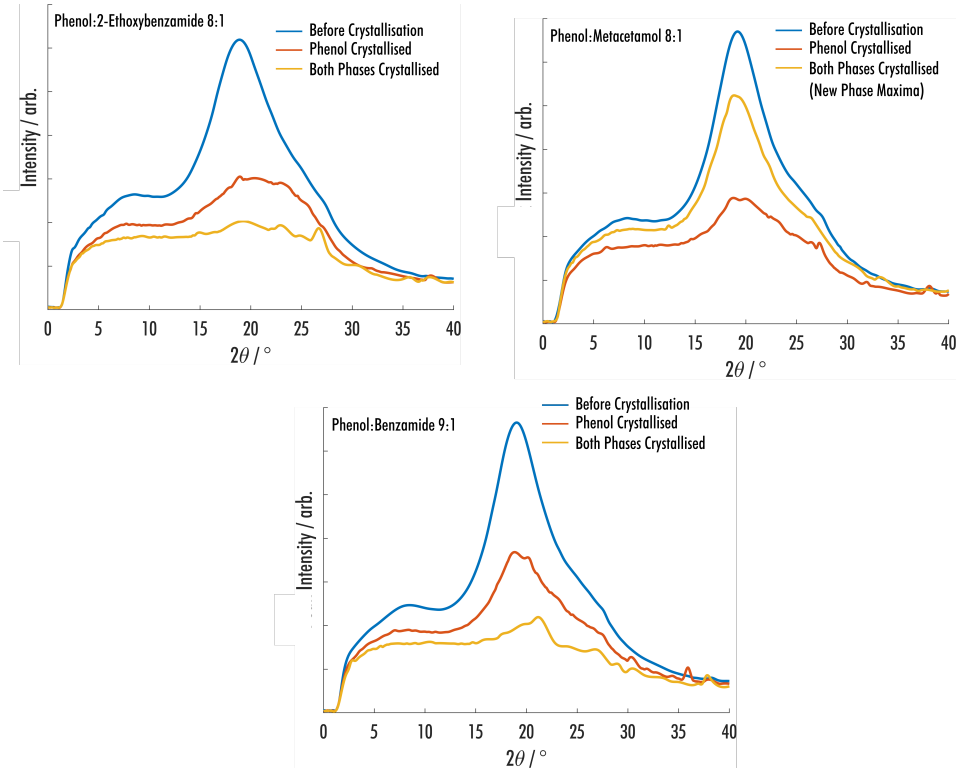

Figure 4.31: Amorphous backgrounds seen during different parts of the thermodynamic cycles for phenol:metacetamol 8:1, phenol 2-ethoxybenzamide 8:1 and phenol:benzamide 9:1 VODES. Figure from [172].

temperature cycles were run, the thermogram is shown with respect to time, with the temperature highlighted using a colour gradient. The crystallisation of the unknown phase took place with a small exothermic transition during the isothermal hold (blue arrow). On reheating after the isothermal hold, a small endothermic transition is seen (Figure 4.32 inset) at approximately the same temperature the crystallisation originally occurred. Integration of this transition highlights that the enthalpy is not large enough to be a melting transition (29.0 $J.g^{-1}$ exothermic transition vs. 0.5 $J.g^{-1}$ endothermic transition), so this is likely the thermal relaxation of a glassy phase. The enthalpy of the final endothermic event is larger than that of the first exothermic crystallisation event (55.3 $J.g^{-1}$ vs. 96.1 $J.g^{-1}$), meaning that both of the phases must be melting during the final event. This additional cycle did not reveal any more crystalline phases; however, it may suggest that the amorphous content left in the system remains glassy up to 0 °C.

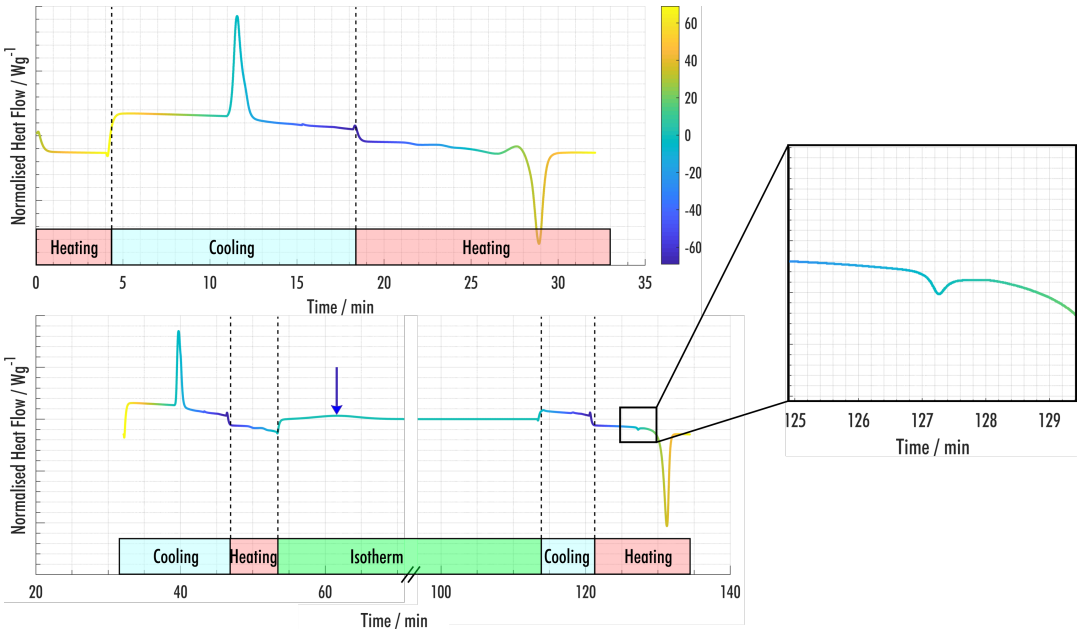

Figure 4.32: DSC thermogram of the phenol:metacetamol 8:1 VODES. The thermograms are shown with respect to time so that multiple heating ramps can be represented. (Top) Thermogram for a single cycle between -70 °C and 70 °C. (Bottom) Thermogram for a cycle including a isotherm at T_{c2}. A blue arrow highlights the position of a small exothermic event during the isotherm. The inset shows a detailed section of the thermogram to highlight a small endothermic event. The colour of the line represents the temperature at every point in time during the thermal cycle.

A similar experiment was run for the phenol:2-ethoxybenzamide 8:1 VODES, which is shown in Figure 4.33. When introducing a thermal cycle after the crystallisation of the unknown phase, another small exotherm is seen on cooling (blue arrow). Furthermore, on subsequent heating, an additional endothermic event is seen (red arrow). These events integrate to approximately the same enthalpy (1.5 $J.g^{-1}$ exothermic transition vs. 2 $J.g^{-1}$ endothermic transition), highlighting that the transitions likely represent the crystallisation and melting of a third phase. In this vein, the thermogram including the isothermal hold in Figure 4.33 could represent a very similar structural landscape to that proposed in Figure 4.11.

Finally, the phenol:benzamide 9:1 VODES was rerun using the DSC25 to highlight any transitions not seen due to the baseline in the thermograms produced by the CXRD-DSC. Figure 4.34 shows that multiple glass transitions can be seen during the heating of the sample (green arrows). This highlights the complex structural behaviour within the VODES mixtures, even if these particular glassy phases do not form a crystalline product at these temperatures. These multiple glassy phases show similar behaviour to those seen in the 9:1 and 10:1 phenol:verapamil mixtures highlighted in the previous chapter.

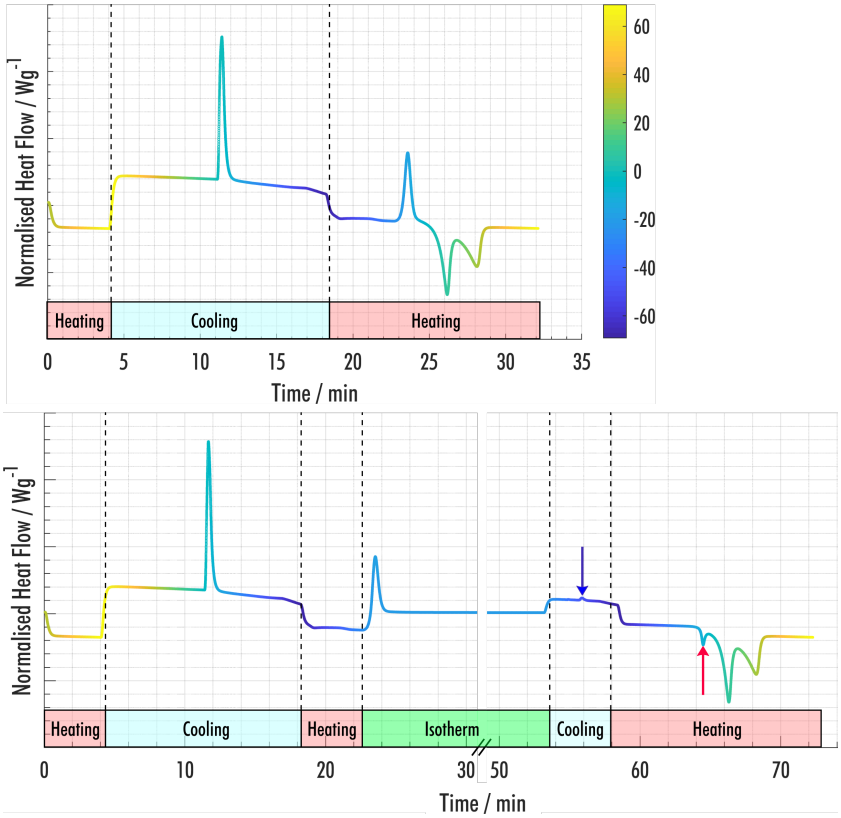

Figure 4.33: DSC thermogram of the phenol:2-ethoxybenzamide 8:1 VODES. The thermograms are shown with respect to time so that multiple heating ramps can be represented. (Top) Thermogram for a single cycle between -70 °C and 70 °C. (Bottom) Thermogram for a cycle including a isotherm at T_{c2}. The colour of the line represents the temperature at every point in time during the thermal cycle.

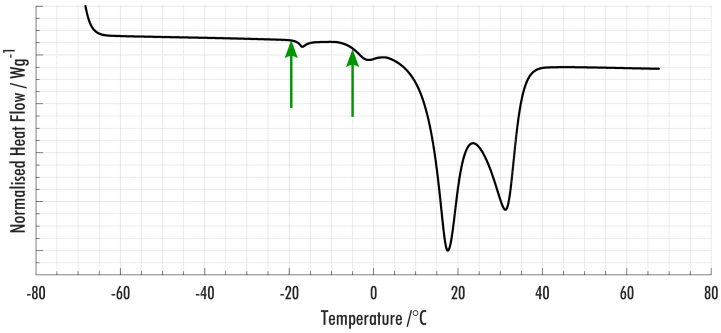

Figure 4.34: DSC thermogram for the heating of the phenol:benzamide 9:1 VODES. Green arrows highlight the position of glass transitions.

4.5 Summary

The use of DSC has allowed precise thermodynamic and structural analysis of three VODES systems. In this chapter, it has been highlighted that without concomitant structural analysis, it is almost impossible to fully understand the phase behaviour of these complex binary systems. The CXRD-DSC experiments ran undoubtedly showed that VODESs are inherently susceptible to metastable phase formation, giving support to the hypothesis presented in the previous chapter that intermediary phases are responsible for crystallographic control when using the VODES medium. This work highlights the need to understand a hierarchy of structures that can form during the cooling of a deep eutectic system and adds a level of complexity to the theoretical background of predicting the formation of DESs. With this structural understanding in place, future work can look into producing phase diagrams of VODES (appendix E), with the aim of understanding the melting point depression and the structural behaviour of these systems.

CHAPTER 5

COLOUR IN DIMETHYLAMINO, NITRO SUBSTITUTED CHALCONES

The results of this chapter were published in part in the paper: Color Differences Highlight Concomitant Polymorphism of Chalcones.[184] I would like to thank Dr Rui Guo, Prof Martijn Zwijnenburg and Prof Sally Price for carrying out the quantum chemistry calculations regarding the colour predictions included in this chapter. I would also like to thank Dr Iryna Andrusenko for carrying out 3D electron diffraction experiments, and Dr Louise Price for her work on the crystal structure prediction of the third polymorph of Gm8p-O. I would like to thank Dr Hazel Sparkes, Dr Natalie Pridmore and Dr Jason Potticary for their help and advice regarding single crystal X-ray diffraction. Finally, I would like to thank Prof Matthew Cremeens, Dr Stephen Warren and their team at Gonzaga University for synthesising the chalcones used in this work.

5.1 Colour and Polymorphism

The structural determination of a material is imperative in understanding the properties that it exhibits. However, direct ascertainment of the particular polymorph of a crystalline material often requires bespoke analysis, such as X-ray diffraction or calorimetric experiments. Even if an exact set of conditions is known to produce a particular polymorph, the phenomenon of 'disappearing polymorphs'[3] means it is best practice to check the structure of each batch of a material that is produced.

One of the main human observations that can be made to distinguish between polymorphs is that of colour. Although many common pharmaceutical crystals exist as white powders, there are a number of organic molecules that absorb light in the visible spectrum, and therefore exhibit a non-white appearance. The instantaneous observation of colour is likely why the molecule ROY (5-methyl-2-[(2-nitrophenyl)amino]-3-thiophenecarbonitrile) is often used as an archetypal exhibitor

of polymorphism, and the range of possible colours is probably why so many different polymorphs of it have been found.[19,185]

The different colours exhibited by organic crystals are due to the distribution of vibrational and electronic energy levels of their constituent molecules. Given that energy levels exist with the correct energy difference, incident electromagnetic radiation can excite a molecule into a state of elevated energy, which is dissipated either thermally (into vibrational states) or via luminescence. To humans, the absorbance of light of a material makes it appear as a complementary colour; for example, a material absorbing in the blue region of the visible spectrum will appear red-orange.

The energy levels of a molecule are often estimated using molecular orbital theory, which describes how the atomic orbitals of constituent atoms of a molecule interact. When considering organic molecules, the molecular orbitals of interest most commonly consist of contributions from σ-bonds (bonding s-orbitals), π-bonds (bonding p-orbitals) and lone pairs. Figure 5.1 highlights a number of the molecular orbitals of formaldehyde. The difference in energy between the highest occupied molecular orbital (HOMO) and lowest unoccupied molecular orbital (LUMO) is the smallest amount of energy (lowest wavelength radiation) that the molecule can absorb. The most tightly bound electrons sit in σ-orbitals, which are very stable and thus difficult to excite. The delocalisation of π-orbitals means the electrons are more 'free' and therefore take less energy to promote into unoccupied energy levels. Finally, lone pairs are the least stable orbitals, as they are not stabilised by any bonding interactions.

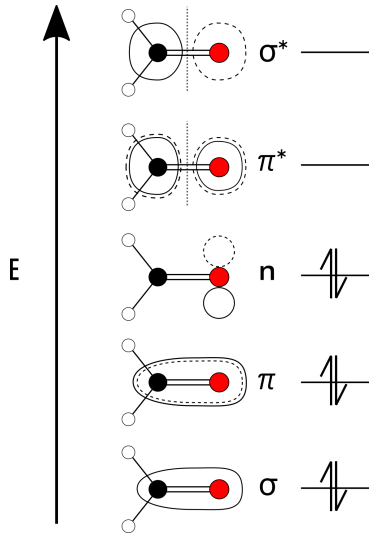

Figure 5.1: Molecular orbitals of formaldehyde increasing in energy from bottom to top. Dashed and solid lines highlight the positive and negative regions of the orbital, respectively. Dotted lines show the position of nodes.

The overlap of orbitals leading to σ- and π-bonds leads to the formation of a pair of bonding orbitals, known as bonding (σ and π) and anti-bonding (σ* and π*). The orthogonal nature of molecular orbitals means that orbitals of the same type spread out in energy. Anti-bonding orbitals

tend to have more regions where electrons cannot exist, known as nodes, and therefore are higher in energy than bonding orbitals. Due to their lower stability, HOMO-LUMO transitions are often either of type $\pi \rightarrow \pi^*$ or $n \rightarrow \pi^*$. Increasing the conjugation of molecules allows further delocalisation of the molecular orbitals, reducing the energy of $\pi \rightarrow \pi^*$ type transitions. An example of increasing the conjugation of molecules is shown in Figure 5.2a, highlighting the molecular orbitals of ethylene and 1,3-butadiene. In this system, the HOMO-LUMO transition is of $\pi \rightarrow \pi^*$ type, meaning the energy gap of 1,3-butadiene is smaller due to increased conjugation. This progression of HOMO-LUMO energy reduction with conjugation can be understood by looking at the quantum mechanical solutions to the 'particle in a box' potential, which is remarkably accurate at predicting the absorption spectra of cyanine dyes (Figure 5.2).[186] The accuracy of this modal is due to the functional groups at either end of the central conjugated chain acting like an infinite potential, where the π-electrons are forbidden to reside. The energy level of the n^{th} electronic state in this idealised system can be written as,

$$E_n = \frac{h^2 n^2}{8 m_e L^2}; n = 1, 2, 3 \ldots, \tag{5.1}$$

where h is the Planck constant, m_e is the mass of an electron, and L is the size of the box. Assuming that the length of the conjugated chain in the cyanine dyes is L, it is clear that the energy difference between states gets smaller as the length of the chain increases,

$$E_{n+1} - E_n = \frac{2n+1}{8 m_e L^2}. \tag{5.2}$$

Injection of electrons into conjugated systems is also known to increase the delocalisation of electrons, leading to a smaller HOMO-LUMO transition. Hence electron-donating groups, such as dimethylamino, are often seen to red-shift the absorption spectra of molecules.

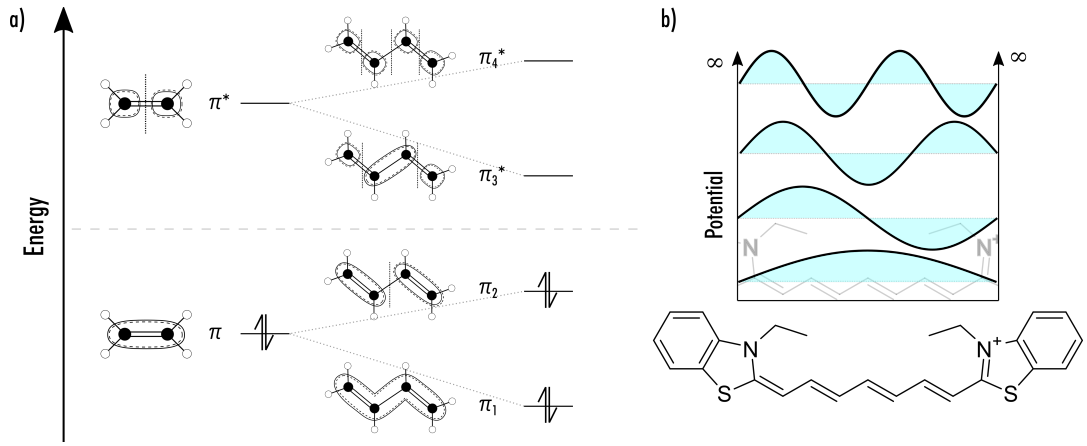

Figure 5.2: a) Comparison of the molecular orbitals of ethlyene and 1,3-butadiene. b) The 'particle in a box' wavefunctions highlighted on a cyanine dye.

The idea that radiation of the correct wavelength will promote an electron between an occupied molecular orbital and an unoccupied molecular orbital is a significant simplification. In reality, the probability of electron promotion between two energy levels needs to be calculated using a transition dipole moment integral. These integrals highlight how the probability of a transition is proportional to both the overlap of the molecular orbital wavefunctions in space and their combined dipole moment, $\hat{\mu}$. The transition dipole moment between two states n and m is given by the equation,

$$\mu_{m,n} = \langle \psi_n | \hat{\mu} | \psi_m \rangle, \tag{5.3}$$

where ψ represents the molecular orbital wavefunction. This equation highlights that orbitals differing in symmetry or with cancelling dipole moments will have a near negligible chance of electronic transition. The square of the transition dipole moment gives the probability of a particular transition. In general, due to their symmetries, low-lying $\pi \rightarrow \pi^*$ transitions tend to have the highest transition probabilities and $n \rightarrow \pi^*$ transition probabilities are often orders of magnitudes lower. However, divergence from this rule can be seen even in simple systems such as benzene, where two of the three low lying $\pi \rightarrow \pi^*$ transitions have near-vanishing transition probabilities.[187] The lifetime of an excited state with respect to re-emission is dependent on the transition dipole moment, which is particularly important for luminescence. This proportionality is given by the Einstein relationship,

$$A = \frac{1}{\tau_r} \propto | \mu_{21} |, \tag{5.4}$$

where A is the first Einstein coefficient, τ_r is the lifetime of an excited state to radiative decay and μ is the transition dipole moment. An observation of these trends was seen in work carried out by Rant et al., where the length of the conjugated system in phenylene-based materials was correlated to an increase in transition dipole moment between HOMO and LUMO states.[188]

The vibrational energy levels of molecules are also important when considering absorbance spectra, as they define the fine structure between electronic energy levels. The Franck-Condon approximation gives a method of calculating the transition probabilities between different vibrational states, utilising the Born-Oppenheimer approximation to assume that electronic and vibrational states can be decoupled. A result of this principle is that almost all transitions will result in the excitation to an elevated vibrational state. Kasha's rule tells us that the excited vibrational state rapidly converts to the ground state after excitation (internal conversion), meaning that any radiative emission occurs from the lowest vibrational energy level of an electronic state.[189] Radiative emission between the lowest vibrational state of an elevated electronic singlet state and the singlet ground state is known as fluorescence. An excited state may also undergo intersystem crossing, which involves the change of the system from a singlet to a triplet state (the flipping of an electron spin), leading to lower energy emission. Transitions between singlet and triplet states are theoretically forbidden; however, they occur due to a degree of spin-orbit coupling. The lifetimes of these transitions are therefore long, giving rise to the phenomenon known as phosphorescence. Possible molecular transitions are often highlighted on a Jablonski diagram, as shown in Figure 5.3.

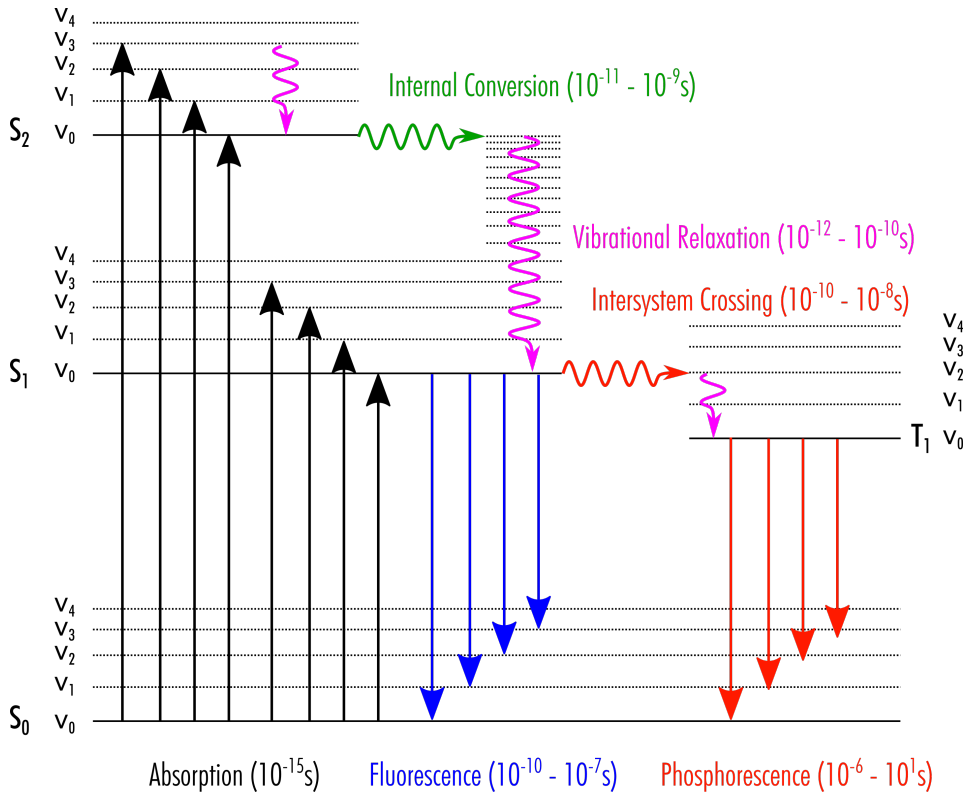

Figure 5.3: Jablonski diagram highlighting the different transitions that can occur between electronic and vibrational states.

Due to the time scales over which internal conversion occurs, fluorescence emission is highly dependent on the transition dipole moment between the HOMO and LUMO levels. As a general rule, highly conjugated molecules with low lying $\pi \rightarrow \pi^*$ HOMO-LUMO transitions exhibit strong fluorescence, and those with $n \rightarrow \pi^*$ HOMO-LUMO transitions exhibit little to no fluorescence. This is due to the level of wavefunction overlap of the excited and ground states. An exception to this rule is when lone pairs are donated into the conjugated system rather than sitting orthogonally to them. Kasha defined two different types of orbital to distinguish between lone pairs, which are donated 'ℓ', and non-bonding electrons 'n'.[190] This difference is clearly seen in the example shown in Figure 5.4, which highlights the difference in molecular orbitals between pyrrole and pyridine. When electrons are donated into a conjugated system, they exhibit similar properties to the π-orbitals and, therefore, can have a considerable overlap with the LUMO. On the other hand, non-bonding electron orbitals have little resemblance to π-orbitals and have little to no overlap with the LUMO.

The above theory highlights the complexities that can arise in the excitation of molecules via electromagnetic radiation. However, as systems grow, gaining more flexibility and molecular overlap, there is a huge amount of computation that needs to be carried out the predict the possible electronic and vibrational transitions of a material. The ideas of σ-, π-, ℓ- and n-orbitals, that approximate the absorption of simple molecules well, are less relevant as systems become more complex. Molecular

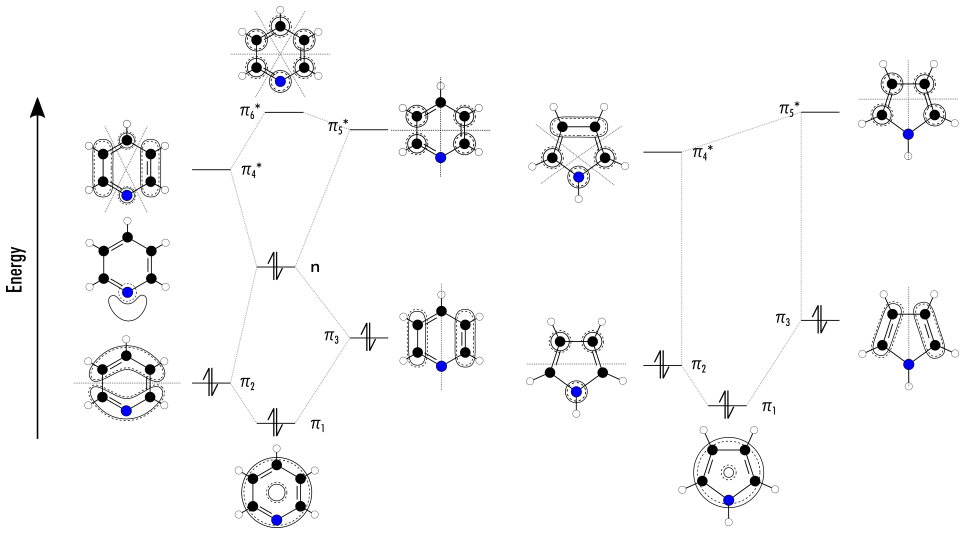

Figure 5.4: Molecular orbitals in Pyrrine and Pyridine. Dashed and solid lines highlight the positive and negative regions of the orbital, respectively.

orbitals of these systems tend to have the 'character' of the well-defined basic orbitals, but are not strictly any of them. In the gas phase, the molecules are sufficiently separated that molecular absorption spectra can be well approximated by calculations of an isolated molecule. However, in solution, the peaks of the spectrum often shift (solvatochromism), and interactions of the molecules with the solvent leads to spectral broadening, losing the sharp vibronic transitions seen for the isolated molecule in the gas phase. Moreover, the excitation of an electronic state often causes the re-distribution of molecular orbitals, meaning that the lowest energy transition may not be between the HOMO and LUMO orbitals, as expected given Koopmans' theorem.[191] These excited-state relaxations can be calculated using time-dependent density functional theory (TD-DFT); however, this requires the optimisation of many states to acquire the accurate ordering and distribution of molecular orbitals.[192]

When considering molecules in the solid-state, the absorption spectrum can shift due to changes in conformation induced by packing or because of intermolecular interactions between neighbouring molecules.[193] For example, the variation in colour of ROY is attributed to the differences in the conformation of the molecule leading to a change in π-delocalisation.[194–197] Similarly, differences in the position of the nitrogen lone pair relative to the aromatic rings were used to rationalise the colour variations in the polymorphs of picrytoluidine.[198] In contrast, in the case of rigid perylene derivatives,[199,200] which lack conformational degrees of freedom, the colour variation has been explained purely in terms of differences of crystal packing and π-stacks, which are generally well-defined in the crystals of such rigid molecules.

The difficulties predicting absorption spectra of molecules in the solid-state present a problem where theory and experiment need to coincide before dependable theory-driven molecular design can be carried out. Although many methods of calculations exist, such as TD-DFT utilising periodic

boundary conditions, they are very costly as thus-far not available with an adequate range-separated functional, such as ωB97x. As such, studies where molecular properties can be systematically modified are of great interest when looking for areas in which our current theoretical knowledge does not match experimental observation. One system for this type of study is the group of molecules known as chalcones ((2E)-1,3-diphenylprop-2-en-1-ones), a conjugated molecule that can readily and systematically be synthesised with a range of functional groups.

5.2 Crystallisation of Chalcones

Chalcones ((2E)-1,3-diphenylprop-2-en-1-ones) are naturally occurring compounds studied widely as a molecular scaffold in medicinal chemistry.[201] Functionalised chalcones can be synthesised using a number of synthetic routes,[202] the most common of which is the Claisen–Schmidt condensation reaction between appropriately functionalised acetophenone and benzaldehyde molecules. As a result, chalcone molecules can be readily synthesised with functional groups present on either ring in the *para*-, *meta*- and *ortho*-positions. The chalcone structure is highlighted in Figure 5.5, showing the naming convention of the aromatic rings and the possible positions of functional groups. The ring closest to the carbonyl oxygen is referred to as the 1-ring as, per the atom labelling convention, it is connected to **C1**. By a similar logic, the other aromatic ring is referred to as the 3-ring.

As part of a systematic study of crystallographic packing, a wide range of substituted chalcones have been synthesised. As such, a naming convention has been used to quickly determine which chalcone is being referred to. For chalcones with no more than one functional group on each ring, a four-character code is used. The first letter represents the functional group on the 1-ring. Following this, a letter represents the position of this functional group (p - *para*, m - *meta* or o - *ortho*). The following number then represents the functional group on the 3-ring, and finally the last letter represents the position of this functional group.

In medicinal chemistry chalcones have been analysed for their use as antioxidants,[203] anti-inflammatories,[204] and are known to show antibacterial properties.[205] Furthermore, the use of chalcones as anticancer treatments has been investigated for both necrosis of cells[206] and prevention of cell division.[207] It is thought that the main active functional group of these compounds is the α,β-unsaturated ketone,[208] which conjugates the two aromatic rings, allowing electronic interactions that directly affect molecular conformation and colour. Indeed, the name chalcone comes from the Greek word *'chalcos'* for bronze, highlighting how the compounds are often coloured.[209] Hence, the chalcone core is a relatively large conjugated system that is a model for the properties of pharmaceuticals that are linked to the π-system, in the way that pentacene is seen as the model system for organic optoelectronics.[210–213]

In general, the addition of functional groups to chalcones results in crystals differing only marginally in colour from the unsubstituted chalcone. However, the introduction of an electron-donating substituent, such as a dimethylamino group, onto either ring of the chalcone results in evident optical changes. The absorbance of such functionalised chalcones has been thoroughly com-

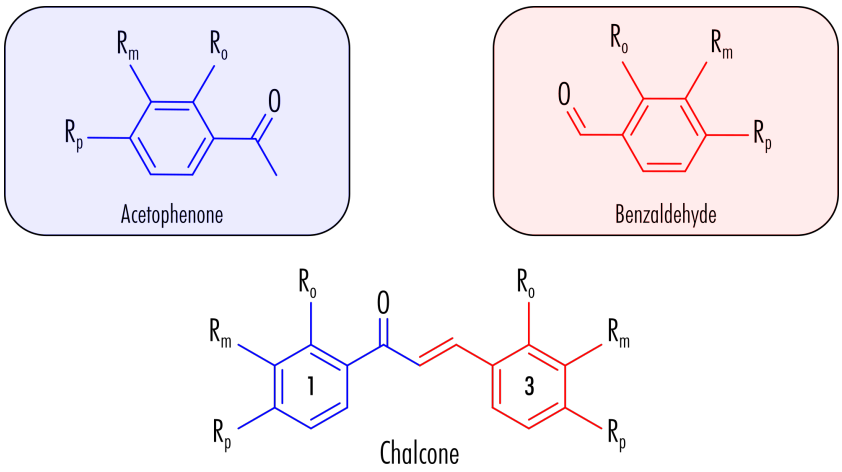

Figure 5.5: Representation of the chalcone backbone, highlighting the sections of the molecule that come from the acetophenone and benzaldehyde when synthesised using a Claisen-Schmidt condensation reaction. The *para*-, *meta*- and *ortho*-position on each ring are highlighted, along with the numbering convention for the aromatic rings.

putationally studied using TD-DFT, highlighting how simple substitutions should cause apparent differences between the HOMO and LUMO of chalcones.[214] Of the functional groups studied, the nitro-group in the *para*-position stabilised both the HOMO and LUMO by the most considerable amount and the dimethylamino-group in the *para*-position destabilised these orbitals the most. The relative shift of the HOMO and LUMO resulted in the largest bandgap for the nitro-group functionalised chalcones and the smallest for the dimethylamino-functionalised chalcones. Although, the lowest transition in unfunctionalised chalcone is considered to be $n \rightarrow \pi^*$,[215] it is clear that conjugation with the chalcone backbone causes a deviation from such a strict definition.[216] Moreover, the addition of functional groups has been shown to cause the reordering of the molecular orbitals in many cases, leading to stark differences in luminescent properties..[217]

Although the majority of chalcones do not exhibit strong fluorescence, the fluorescent properties of certain chalcones have been investigated for their uses as biological imaging probes. One of the main functional groups allowing for a low-lying $\pi \rightarrow \pi^*$ HOMO-LUMO transition is the dimethylamino-group, which is known to donate electrons into the aromatic chalcone system. 4-Dimethylaminochalcone has been widely studied for detecting micelle formation,[218,219] and 4'-dimethylamino-4-methylacryloylaminochalcone has been used to detect the water content of solutions.[220]

This chapter reports the structural solution of two polymorphic isomers, 3'-dimethylamino-3-nitrochalcone and 3'-dimethylamino-4-nitrochalcone, which, when recrystallised from acetone, both exhibit concomitant polymorphism of crystals differing in colour and morphology. The fluorescent and optical properties of each solid form are investigated spectroscopically, allowing direct comparison to computational predictions of electromagnetic absorption. In an attempt to realise a route to colour prediction without using computationally-expensive periodic boundary condition

calculations, analysis of clusters of each of the molecules cut from their respective crystal structures was carried out. These systematic calculations of the optical properties caused by different bonding motifs allowed for the isolation of the most optically-relevant intermolecular interactions in each system.

During the systematic synthesis of chalcones, the dimethylamino and nitro groups were denoted as 'G' and '8', respectively. Thus, 3'-dimethylamino-3-nitrochalcone will be referred to as Gm8m and 3'-dimethylamino-4-nitrochalcone as Gm8p. This system of four polymorphs exhibits colours ranging across the optical spectrum, raising questions as to the cause of such colour polymorphism. The molecules are highlighted in Figure 5.6, along with their electrostatic potential map. The electrostatic potential map highlights to clear differences between the effect of each functional group, with the nitro group taking charge away from the closest aromatic ring to it and the dimethylamino group donating charge. The mixture of these functional groups makes these systems a key benchmark for determining the accuracy of current predictions of optical absorption.

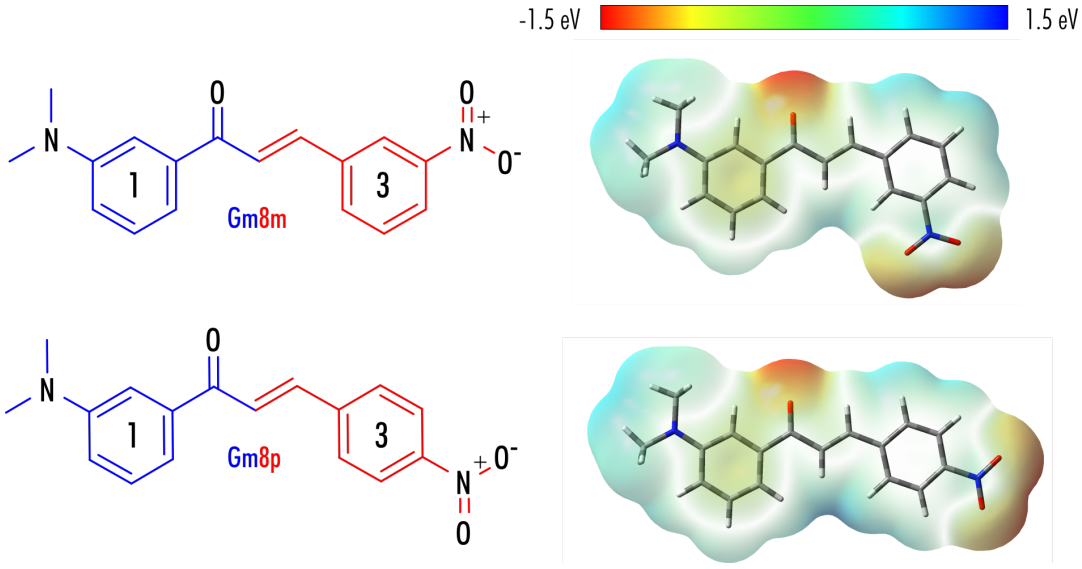

Figure 5.6: A representation of the two chalcone molecules discussed in this chapter, 3'-dimethylamino-3-nitrochalcone (Gm8m) and 3'-dimethylamino-4-nitrochalcone (Gm8p). The electrostatic potential map for each molecule is highlighted on the right, calculated using B3LYP/6311++G(2d,p) and plotted on the 0.0004 SCF density surface for the optimised isolated molecules.

5.3 Polymorphism in Gm8m and Gm8p

5.3.1 Synthesis

Chalcone synthesis was carried out following the procedure highlighted by Sweeting et al.[221] Gm8m and Gm8p were synthesised via a base-catalysed aldol condensation reaction between 3'-dimethylaminoacetophenone and an appropriately functionalised nitrobenzaldehyde. For Gm8m, 3 mmol solutions of 3'-dimethylaminoacetophenone and 3-nitrobenzaldehyde with 95% ethanol were used. 0.30 mL of 50% NaOH(aq) was added to the 3'-dimethylaminoacetophenone mixture, which was continuously stirred as the 3-nitrobenzaldehyde mixture was added. The solution was left for 30 minutes to react and then neutralised using HCl. After quenching with ice, the product was collected as a precipitate via vacuum filtration and washed with cold water. The resultant yellow-orange powder was recrystallised using ethanol. Scheme 1 shows the synthesis of Gm8m.

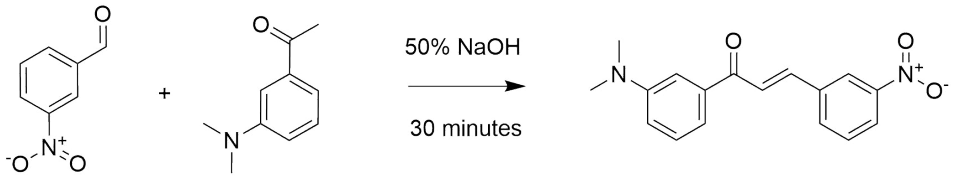

Scheme 1: Synthesis of Gm8m via a base-catalysed aldol condensation reaction between 3'-dimethylaminoacetophenone and 3-nitrobenzaldehyde

For Gm8p, a reaction analogous to that of Gm8m was carried out, replacing 3-nitrobenzaldehyde with 4-nitrobenzaldehyde. The precipitate from this reaction was a red powder, which was recrystallised from ethanol. Scheme 2 shows the synthesis of Gm8p.

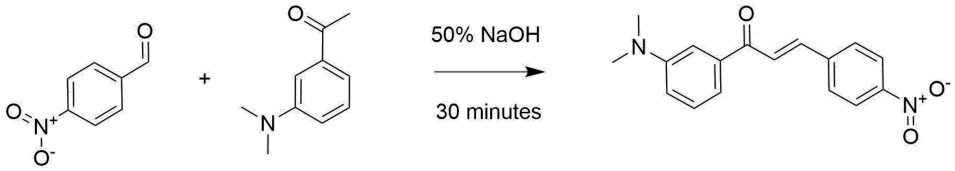

Scheme 2: Synthesis of Gm8p via a base-catalysed aldol condensation reaction between 3'-dimethylaminoacetophenone and 4-nitrobenzaldehyde

Figure 5.7 shows NMR for the final product of the Gm8m and Gm8p syntheses, which were used for crystallisation experiments. Each of the integrated peaks matched predicted values to within 3% in Gm8m and 9% in Gm8p. A small amount of impurity is seen in both samples, which are likely unreacted starting materials from the aldol condensation reaction.

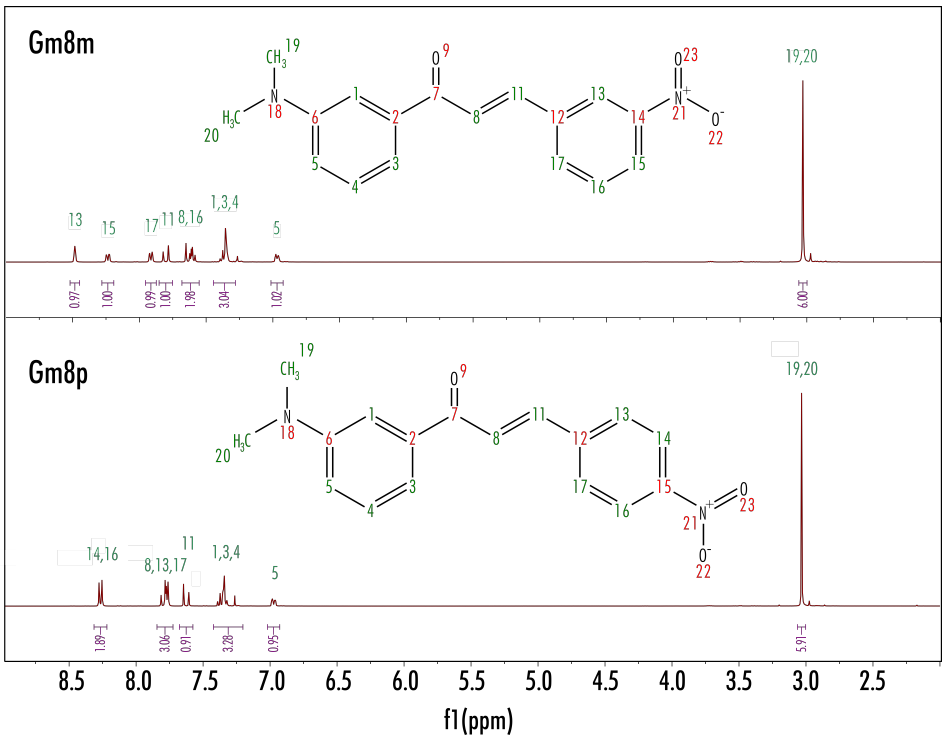

Figure 5.7: ^{1}H NMR spectrum of synthesised powders of Gm8m and Gm8p. Peaks are numbered to match the hydrogen atoms attached to different carbons on the chemical scheme. Peak integrals are shown below the trace, highlighting the experimental hydrogen relative intensity.

5.3.2 Polymorph Screening

To assess the polymorphic landscape of Gm8m and Gm8p, a screening process was carried out using a range of crystallisation conditions and techniques. As only a small amount of sample was initially available (< 1 g), conditions to produce high-quality crystals were first explored in a preliminary screen, followed by a further exploration of parameter space close to these conditions.

5.3.2.1 Preliminary Screening

A preliminary polymorph screen was carried out by conducting crystallisation via solvent evaporation of a range of solvents. Initially, crystallisation from acetone was carried out in a 100 mm diameter petri dish. Using 1 mL of 10 mg.mL^{-1} solutions of Gm8m and Gm8p, this initial experiment was carried out five times. In each case, apparent concomitant polymorphism was seen in both Gm8m and Gm8p. In Gm8m, yellow needle-like crystals and orange block-like crystals were observed, and in Gm8p, red garnet-like crystals and black block-like crystals formed. Each of the distinct crystals were separated and subsequently analysed via powder X-ray diffraction (pXRD), which revealed structural differences in the crystal structures. Due to the clear distinction in colour between the polymorphs

of Gm8m and Gm8p observed, each polymorph was labelled in reference to their colour: Gm8m-Y (Gm8m yellow), Gm8m-O (Gm8m orange), Gm8p-R (Gm8p Red) and Gm8p-B (Gm8p Black). Optical images for as-grown crystals and powder samples of each of the polymorphs are shown in Figure 5.8.

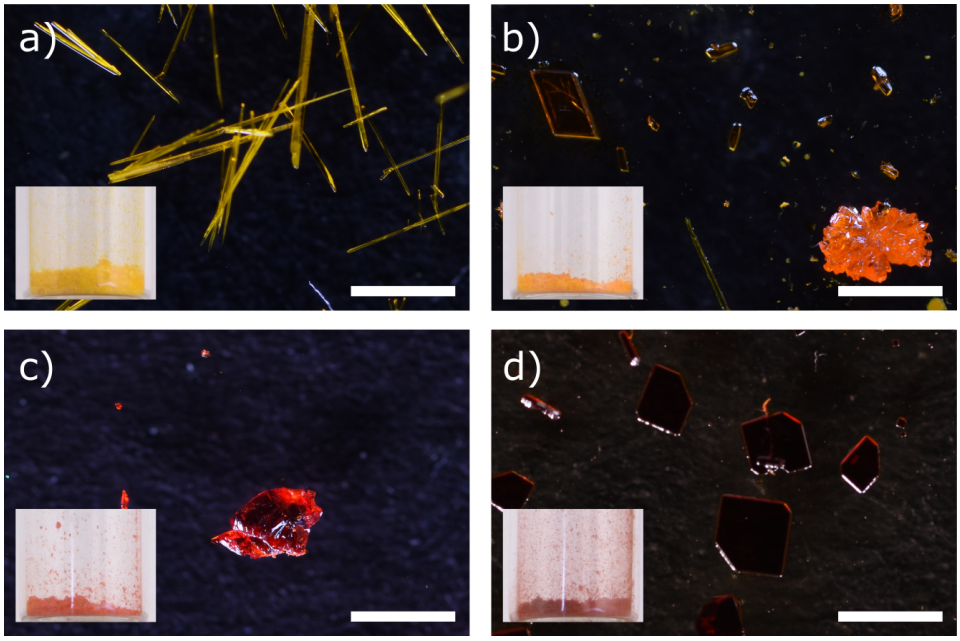

Figure 5.8: Crystals of the polymorphs of Gm8m and Gm8p. Insets show the crystals crushed into a powder in a small vial. a) Gm8m-Y b) Gm8m-O c) Gm8p-R d) Gm8p-B.

5.3.2.2 Structural Solution

The preliminary screen of Gm8m and Gm8p produced crystals of each observed polymorph (Gm8m-Y, Gm8m-O, Gm8p-R and Gm8p-B) of high enough quality to be solved by single-crystal X-ray diffraction (sc-XRD). The morphology of crystals of Gm8m-O, Gm8p-R and Gm8p-B meant that crystals of appropriate thickness in each dimension could be easily isolated. Crystals diffracted well and were stable down to a temperature of 100 K, where diffraction data were collected. The propensity of Gm8m-Y to grow as needles presented difficulties in finding a crystal that diffracted appropriately across each axis. Three separate collections of diffraction data provided the same unit cell; however, the high-resolution reflections were not of publishable standard in each case. By slowing the evaporation of ethanol during crystal growth, thicker crystals were grown which were of high enough quality to produce publishable data. This data highlighted a level of disorder in Gm8m-Y crystal structure (due to a rotation in the nitro group). Crystallographic data for the four polymorphs of Gm8m and Gm8p is shown in Table 5.1.

Table 5.1: Crystallographic data for the four polymorphs of Gm8m and Gm8p.

	Gm8m-Y	**Gm8m-O**	**Gm8p-B**	**Gm8p-R**
CCDC Identifier	1983905	1983906	1983902	1983910
Space group	$P2_1/c$	P-1	$P2_1/c$	$P2_1/n$
Temperature / K	100	100	100	100
a / Å	12.5686(6)	8.3376(3)	7.8173(5)	8.3419(2)
b / Å	6.2878(4)	9.4304(3)	13.4524(8)	8.0686(2)
c / Å	18.1107(10)	10.0957(3)	13.7886(7)	21.6440(5)
α / °	90	102.249(2)	90	90
β / °	92.988(4)	102.697(2)	97.479(4)	91.1060(15)
γ / °	90	104.847(2)	90	90
Z	4	2	4	4
Final R indexes [I≥2σ (I)]	R_1 = 0.0403, wR_2 = 0.0885	R_1 = 0.0349, wR_2 = 0.0923	R_1 = 0.0421, wR_2 = 0.0965	R_1 = 0.0418, wR_2 = 0.0952

5.3.2.3 Structural Motifs in Gm8m and Gm8p

The main objective of analysing the structural motifs of Gm8m and Gm8p polymorphs was to ascertain which intermolecular interactions lead to the greatest shift in the absorption wavelength of the molecules. The initial step was, therefore, to isolate the different possible interactions within each structure.

Gm8m-O crystallises in the triclinic space group $P\bar{1}$. Due to the complementary charges of the 1- and 3-ring of the molecule, both in-plane hydrogen bonding and stacking occur via inversion symmetry. Interactions in the plane of the molecule are mediated by CH…O=C and CH…O_2N close contacts (Figure 5.9a). A stacking interaction, which maximises the overlap of the 1- and 3-rings (which will be referred to as double 1,3-ring stacking), is present perpendicular to the plane of the molecules, with further stacking mediated via 1-ring…1-ring and 3-ring…3-ring overlap (Figure 5.9b).

Gm8m-Y crystallises in the monoclinic space group $P2_1/c$. Unlike the structure of Gm8m-O, there is no double 1,3-ring stacking, and instead, a half-stacking motif forms via a translation of the b-axis, extending into an infinite 1D stack (Figure 5.10a). Each 1D stack is related to a tilted stack via a c-glide plane, leading to 'zigzagging' 2D sheets at an angle of 64° to each other (Figure 5.10b). Finally, in-plane interactions are mediated by CH…O=C and CH…O_2N close contacts, which both form via inversion centres (Figure 5.10c).

The structures of Gm8m-O and Gm8m-Y clearly have large differences in the packing motifs that are present. Although the in-plane close contacts are very similar, the stacking interactions show clear differences, with the Gm8m-Y structure favouring a half-stacking motif over the double 1,3-ring stacking seen in Gm8m-O. Furthermore, the zigzag motif in Gm8m-Y leads to large deviations in the

appearance of the final 3D structures. Due to these differences, only 3 molecules of a 15-molecule cluster can be overlaid ($RMSD_3$ = 0.441 Å).

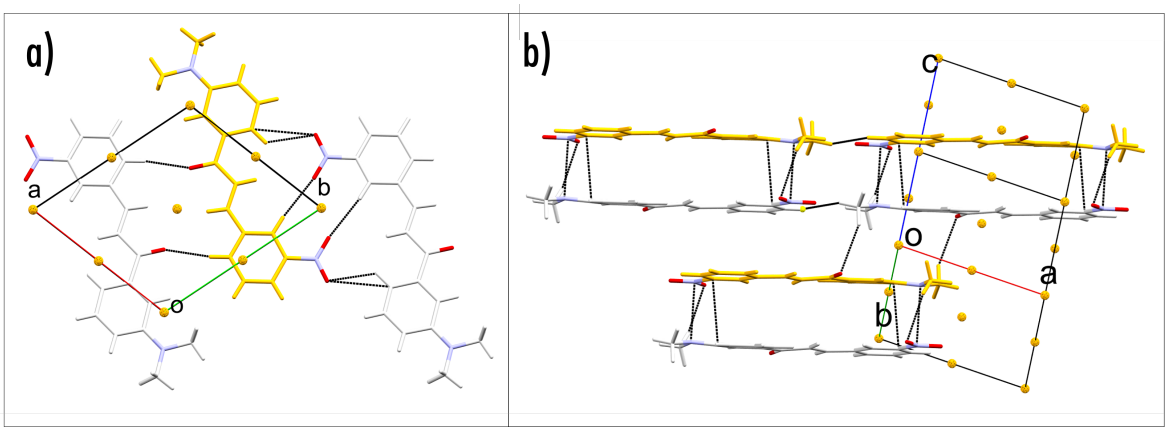

Figure 5.9: Bonding motifs in Gm8m-O. a) In-plane close-contact interactions. b) Interactions in the stacking direction. Molecules are coloured by symmetry operation: white - identity, orange - inversion. Inversion centres are shown by oranges spheres. Short contacts are highlighted with black dashed lines

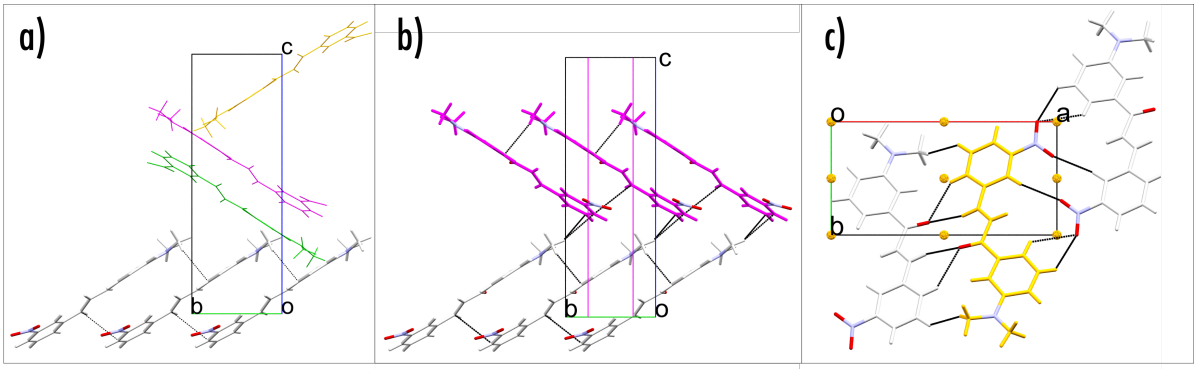

Figure 5.10: Bonding motifs in Gm8m-Y. a) 1D stack mediated by the half-stacking motif. b) 2D zigzagging sheets, highlighting molecules at a 64° angle. c) In-plane CH...O=C and CH...O_2N close contacts. Molecules are coloured by symmetry operation: white - identity, orange - inversion, purple - *c*-glide, green - 2_1 screw axis. Inversion centres are shown by oranges spheres, and glide planes are highlighted in purple. Short contacts are highlighted with black dashed lines.

Gm8p-R crystallises in the monoclinic space group $P2_1/n$. Similarly to Gm8m-O, dimerisation of molecules is present via the double 1,3-ring stacking motif; however, the para-substitution of the nitro group means that the molecules are shifted along the short axis relative to each other, compared to Gm8m-O. This shift allows for a greater overlap of the conjugated chain of each chalcone in the dimer, highlighted by a greater number of short-contacts. The dimers are extended into a 1D stacking motif via CH...O_2N interactions (Figure 5.11a). The 1D chains of stack dimers for a 2D zigzag structure

with adjacent tilted chains at an angle of 83° (Figure 5.11b). The 2D sheets translate along the *a*-axis to form the final 3D structure (Figure 5.11c).

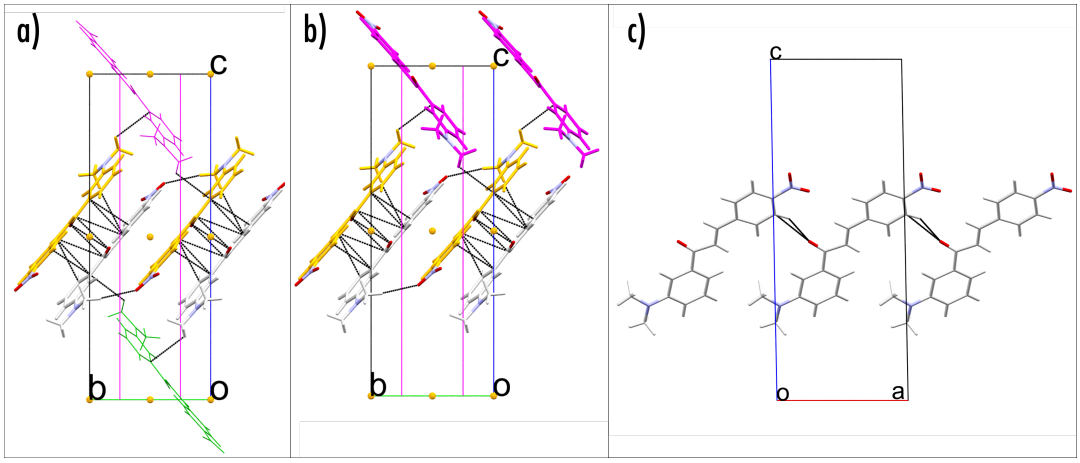

Figure 5.11: Bonding motifs in Gm8p-R. a) 1D stack mediated by double 1,3-ring stacking and CH...O_2N interactions. b) 2D zigzagging sheets, highlighting molecules at a 83° angle. c) Translation of molecules along the *a*-axis. Molecules are coloured by symmetry operation: white - identity, orange - inversion, purple - *c*-glide, green - 2_1 screw axis. Inversion centres are shown by oranges spheres, and glide planes are highlighted in purple. Short contacts are highlighted with black dashed lines.

Gm8p-B crystallises in the monoclinic space group $P2_1/c$. A double 1,3-ring stacking interaction is present, similar to the Gm8p-R structure, with further offset stacking between the dimers. Although this offset stacking involves no close contacts, the overlap of the rings is far greater than in Gm8p-R (Figure 5.12a). Translation along the long-axis of the molecule forms 2D sheets of stacked dimers (Figure 5.12b). Adjacent tilted dimers sit at 62° to each other, forming alternating stacks throughout the crystal structure (Figure 5.12c).

5.3.2.4 Solvent Evaporation Screen

A screen of crystallisation conditions via solvent evaporation was carried out to determine methods for producing quantitative yields of each polymorph of Gm8m and Gm8p. Three different crystallisation vessels were used to allow different rates of solvent evaporation and crystallisation surface. These vessels included 10 mm (diameter) x 50 mm (height) curved-bottomed test tubes, 10 mm (diameter) x 50 mm (height) flat-bottomed vials and 100 mm (diameter) x 10 mm (height) flat-bottomed Petri dishes. Solutions were made up to a known solute concentration and filtered into crystallisation vessels using 0.2 μm PTFE syringe filters. Polymorphs were identified by comparison of their pXRD patterns to a generated pattern of each solved crystal structure. Along with the polymorph produced, the morphology of each sample was noted, which was particularly important for Gm8p-R due to multiple morphological observations (needles, plates and garnets). These different morphologies appeared to depend on the evaporation rate of the solvent and the particular solvent used. It was

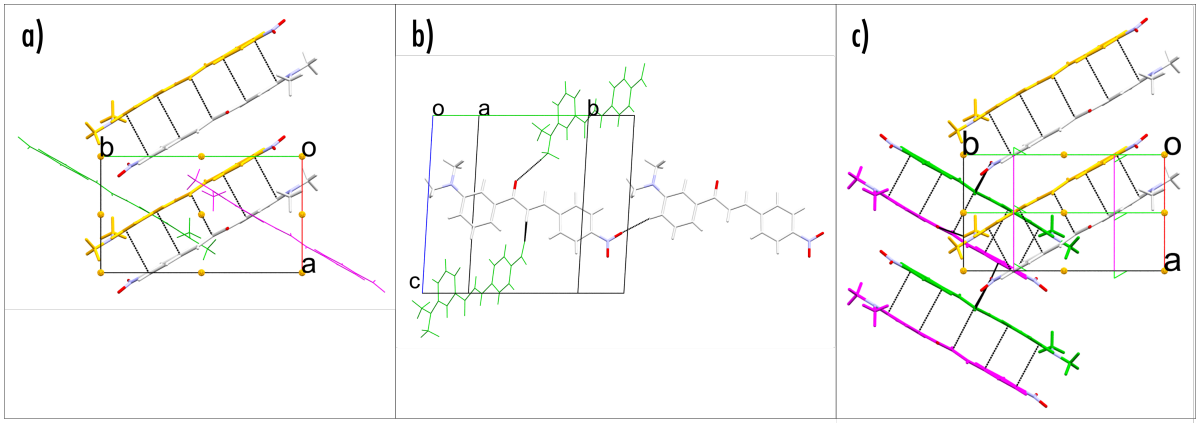

Figure 5.12: Bonding motifs in Gm8p-B. a) 1D stack mediated by double 1,3-ring stacking and $NO_2 \ldots H_3C$ interactions. b) Translation of molecules along the long axis of the molecule. c) Molecules tilted at 62° relative to the stacked dimers. Molecules are coloured by symmetry operation: white - identity, orange - inversion, purple - *c*-glide, green - 2_1 screw axis. Inversion centres are shown by oranges spheres, glide planes are highlighted in purple, and screw axes in green. Short contacts are highlighted with black dashed lines.

also noted that samples of Gm8m grown via solvent evaporation of toluene produced an amorphous sample within test tubes. Crystallisation results are highlighted in Table 5.2 - Table 5.4.

The solvent screen allowed for the identification of crystallisation parameters to produce polymorphs of Gm8m and Gm8p reproducibly. In Gm8m, most conditions appeared to favour the growth of Gm8m-O, which seemed to frequently nucleate on the surface of the crystallisation vessels, possibly due to crystals having a higher surface area than crystals of Gm8m-Y. Gm8m-Y was favoured when crystals were grown via solvent evaporation of alcohols in round-bottomed vessels, presumably to minimise adherence to the surfaces.

The crystallisation of Gm8p from narrow crystallisation vessels highly favoured the formation of Gm8p-R, which grew in several different morphologies depending on the evaporation rate and the solvent used. In general, crystals of Gm8p-B were much larger and of higher quality than Gm8p-R, suggesting that the surface of the Petri dish helped in the nucleation of this polymorph. A third polymorph of Gm8p was also observed (Gm8p-O), which formed very thin low-quality crystallites. When formed, the pXRD pattern of this third polymorph did not closely match generated patterns from the solved structures of Gm8p-R or Gm8p-B; however, the quality of these crystals did not allow for a structural solution via sc-XRD.

Table 5.2: Results from evaporative crystallisation experiments for Gm8m.

Gm8m	**Vial**				**Test Tube**			
Concentration	**5 mg.mL^{-1}**		**10 mg.mL^{-1}**		**5 mg.mL^{-1}**		**10 mg.mL^{-1}**	
Methanol	O/Y	O/Y			Y	Y		
Ethanol	O/Y	O/Y			Y	Y		
Chloroform	O/Y	O/Y	O/Y	O/Y	O/Y	O/Y	O/Y	O/Y
Toluene	O	O	O	O	Am	Am	Am	Am
Ethyl Acetate	O	O	O	O	O	O/Y	O	O
Tetrahydrofuran	O	O	O	O	O	O	O/Y	O/Y
Acetone	O	O	Y	Y	O	O	Y	Y

Table 5.3: Results from evaporative crystallisation experiments for Gm8p.

Gm8p	**Test Tube**				**Vial**			
Concentration	**5 mg.mL^{-1}**		**10 mg.mL^{-1}**		**5 mg.mL^{-1}**		**10 mg.mL^{-1}**	
Methanol	R (N)	R (N)			R (P)	R(N)		
Ethanol								
Chloroform	R (P)	R (P)	R (P)	R (P)	R (P)	R (P)	R (P)	R (P)
Toluene	R (N)	R (N)	R (N)	R (N)	R (N)	R (N)	R/B	R/B
Ethyl Acetate	3	R (P)	3	3	R (N)	R (N)	R (N)	R (N)
Tetrahydrofuran	R	R	R	R	3	3	R	R
Acetone	3	3	R(N)	R(N)	3	R (N)	R (N)	R (N)

Table 5.4: Results from evaporative crystallisation experiments for Gm8m and Gm8p within a Petri dish.

Gm8m	**Petri Dish**			**10 mg.mL^{-1}**					
Acetone	Y/O	Y/O	Y/O	Y	Y	Y/O	Y	O	Y/O
Gm8p	**Petri Dish**			**10 mg.mL^{-1}**					
Acetone	B	R(G)/B	R(G)/B	B	B	R(G)/B	B	B	B

5.3.2.5 Magnetic Field Growth

Magnetic anisotropy calculations for each polymorph of Gm8m and Gm8p were carried out using the methods described by Guo et al.[222] The diagonal elements of the diamagnetic susceptibility tensors are highlighted in Table 5.5, indicating the magnitude in the direction of the minimum, maximum and middle susceptibilities, along with the isotropic susceptibility and the magnetic anisotropy ($\chi_{max} - \chi_{min}$). All values in the table are negative as the diamagnetic susceptibility always opposes an applied magnetic field.

It has been suggested that the application of a magnetic field during crystal growth may allow selectivity between polymorphs, given that they lay close in energy and differ in magnetic anisotropy.[71,222] For the data given, this suggests that the magnetic field may favour the growth of

Table 5.5: Magnetic susceptibility tensors for Gm8m and Gm8p polymorphs.

Polymorphs	χ_{min}^{cryst}	χ_{mid}^{cryst}	χ_{max}^{cryst}	χ_{iso}^{cryst}	$\Delta\chi_{an}^{cryst}$
Gm8m					
Gm8m-Y	-109.5	-138.7	-222.1	-156.8	-112.6
Gm8m-O	-100.2	-108.1	-258.3	-155.5	-158.2
Gm8p					
Gm8p-R	-104.7	-168.9	-196.3	-156.6	-91.6
Gm8p-B	-110.7	-148.4	-232.8	-164.0	-122.2

Gm8m-O and possibly Gm8p-B. Gm8p-B is only possibly favoured, as χ_{min} is lower in Gm8p-R. As such, crystallisation experiments were carried out via the cooling of a saturated solution under the application of different external fields. Crystallisation conditions for the formation of Gm8m-O and Gm8p-R under no external field were initially formulated, which both grew from slow cooling of saturated ethanol solutions in flat-bottomed vials. The solutions were cooled from 65 °C to 0 °C over three days. A small hole in the lid of the vial allowed a slow rate of solvent evaporation to further increase the supersaturation over the three days. External magnetic fields between 0 T and 1.6 T were investigated; however, no clear evidence of polymorph selectivity was seen. Gm8m-Y was seen when a magnetic field of 1.6 T was applied, highlighting the proximity of the energy of the polymorphs, but there did not seem to be a clear switch at this field when further experiments were carried out. Crystallisation experiments carried out under external magnetic fields are highlighted in Table 5.6.

Table 5.6: Crystallisation of Gm8m and Gm8p via colling crystallisation of a saturated ethanol solution under external magnetic fields of 0 - 1.6 T.

Magnetic Field / T	**Run 1**	**Run 2**	**Run 3**	**Run 4**	**Run 5**	**Run 6**
0	Gm8m-O	Gm8m-O	Gm8m-O	Gm8m-O	Gm8m-O	Gm8m-O
0.5	Gm8m-O	Gm8m-O	Gm8m-O	Gm8m-O		
1	Gm8m-O	Gm8m-O	Gm8m-O	Gm8m-O		
1.5	Gm8m-O	Gm8m-O	Gm8m-O	Gm8m-O		
1.6	Gm8m-Y	Gm8m-Y	Gm8m-O	Gm8m-O	Gm8m-O	Gm8m-O
Magnetic Field / T	**Run 1**	**Run 2**	**Run 3**	**Run 4**	**Run 5**	**Run 6**
0	Gm8p-R	Gm8p-R	Gm8p-R	Gm8p-R	Gm8p-R	Gm8p-R
0.5	Gm8p-R	Gm8p-R				
1	Gm8p-R	Gm8p-R				
1.5	Gm8p-R	Gm8p-R				
1.6	Gm8p-R	Gm8p-R				

5.3.3 3D Electron Diffraction and Crystal Structure Prediction on the Third Polymorph of Gm8p

As previously mentioned, a third polymorph of Gm8p was seen crystallising from many of the evaporative crystallisation experiments. The crystals produced were low-quality, twinned, thin needles, which meant they were not adequate for structural-solution via sc-XRD. Powder diffraction of the crystals resulted in characteristic peaks; however, this was also of low-quality. Such data suggests that the crystallinity of the sample on a large-scale is likely poor, and changes in crystallisation conditions appeared to have little consequence on the quality of samples produced. Figure 5.13 shows crystals of Gm8p-O, highlighting the poor-quality nature of the sample.

To assess the crystal structure of this unknown polymorph, 3-dimensional electron diffraction (3DED) experiments were employed. Recent advances in the technique have allowed the structural solution of organic crystals by utilising a single-photon detector, which resulted in the first ab-initio structural solution via the technique.[5] The poor quality of Gm8p-O crystals meant that ab-initio structural solution was not possible; however, it was possible to determine the crystal system and unit cell parameters. Volume reconstructions from 3DED of two different crystals of Gm8p-O are shown in Figure 5.14, highlighting the construction of the unit cell. The crystal system was determined to be triclinic, highlighting that the space group could be either $P1$ or $P\bar{1}$. The size of the cell also highlighted that two molecules of Gm8p should be present ($P1$ Z'=2 or $P\bar{1}$ Z'=1).

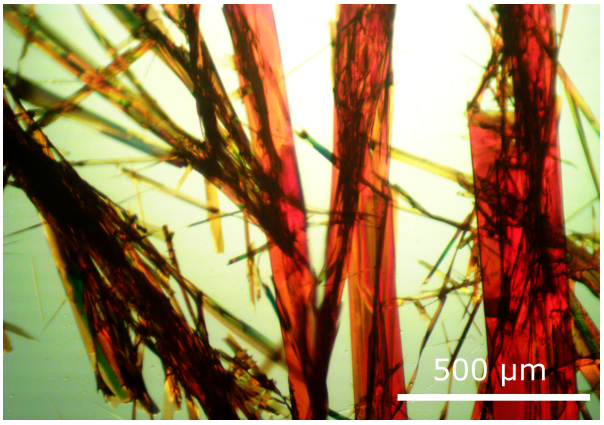

Figure 5.13: Optical images of crystals of Gm8p-O.

As the possible space groups of the crystal structure of Gm8p-O was dramatically reduced by using 3DED, it was possible to run crystal structure prediction calculations within a reduced crystallographic phase space. The calculations produced a large number of possible configurations; however, comparison to the experimental powder diffraction matched very closely to three of the predicted low-energy structures (Figure 5.15). Additional structural refinement of the closest structure resulted in a greater similarity with the experimental pattern. Although not a perfect match, the similarity highlights the likelihood that the structure predicted from crystal structure prediction contains much of the crystallographic order. Moreover, the predicted structure distinctly resembles

that of the known crystal structure of Gp8m (3'-Dimethylamino-4-Nitrochalcone).[223]

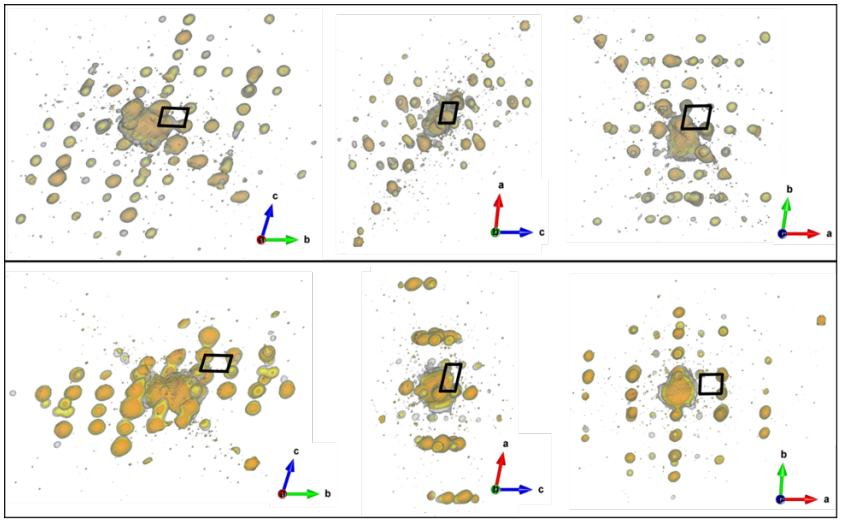

.

Figure 5.14: 3DED volume reconstructions of two different crystals inside the orange Gm8p sample. Cell edges are sketched in black. Top data from a crystal with 1st 3D ED cell, bottom data from a crystal with 2^{nd} 3DED cell. Figure produced by Dr. Iryna Andrusenko.[184]

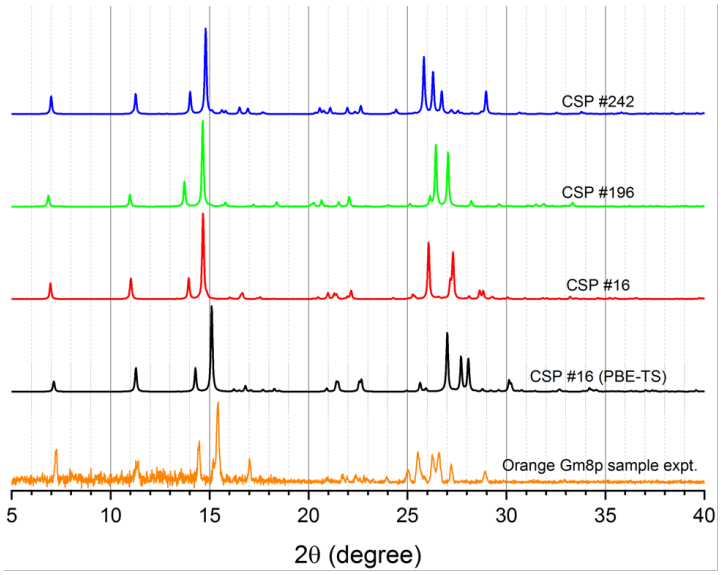

Figure 5.15: Powder X-ray diffraction patterns comparing Gm8p-O to structures from crystal structure prediction.

5.3.4 UV-Vis Spectroscopy

The optical properties of Gm8m and Gm8p in a number of solvents were assessed using UV-Vis spectroscopy. The solvents ethyl acetate, toluene, ethanol and chloroform were chosen due to their differing protic nature and polarity, along with having reasonably low solvent optical absorption cut-offs. To assess if any absorption was caused by the effects of molecular agglomeration, solutions were prepared at several known concentrations. Optical images show that the colour of the solutions varies by only a small amount, as shown in Figure 5.16. Gm8m samples range from light yellow to a darker yellow, and Gm8p samples from a dark yellow to orange. The colour appears to shift towards to red end of the spectrum as the solvents range from ethyl acetate, toluene, ethanol and is darkest for chloroform. These differences are challenging to make out by eye. However, this suggests that the solvent has little effect on the electronic configuration of Gm8m and Gm8p molecules. The aprotic nature of ethyl acetate likely means that it interacts least with the π-system of the chalcone molecules, which may be why it has the least effect on the colour. Toluene will also have little interaction with π-electrons due to it having a non-polar nature. Both chloroform and ethanol are more likely to interact with the π-system of the chalcones due to their intrinsic dipole moment.

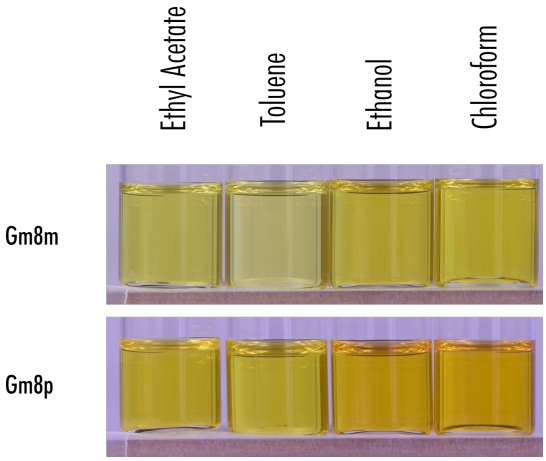

Figure 5.16: Optical images highlighting the difference in colour between Gm8m and Gm8p dissolved in ethyl acetate, toluene, ethanol and chloroform.

UV-Vis spectroscopy was initially carried out using 0.25 mg.ml^{-1} solutions of Gm8m and Gm8p. Experiments were carried out using 3 ml quartz cuvettes, which held sample and reference solutions. The reference cuvette held pure solvent and the sample cuvette held the solution of interest. Figure 5.17 shows the UV-Vis absorbance for 0.25 mg.ml^{-1} Gm8m and Gm8p solutions. Due to the solute concentration, the absorbance at low wavelengths was too high to give a reasonable signal. However, an absorption feature was observable at higher wavelengths for both samples. In Gm8m (Figure 5.17a), a secondary peak could be seen around 400 nm, which shifted to higher wavelengths in the order of solvents: ethyl acetate, toluene, ethanol and finally chloroform. The maximum of these peaks is highlighted with an arrow for each solvent. A similar pattern was seen in Gm8p (Figure 5.17b),

where a shoulder was seen around 450 nm. It was harder to determine the shift of this shoulder to higher wavelengths, but analysis of the inflexion points show the same shifting trend as the Gm8m sample. The inflexion point of each of the shoulders of the Gm8p absorption spectra is highlighted with an arrow. These absorption features at higher wavelengths are likely to be very important when considering the observed colour of the sample, as they sit within the wavelengths of the optical spectrum.

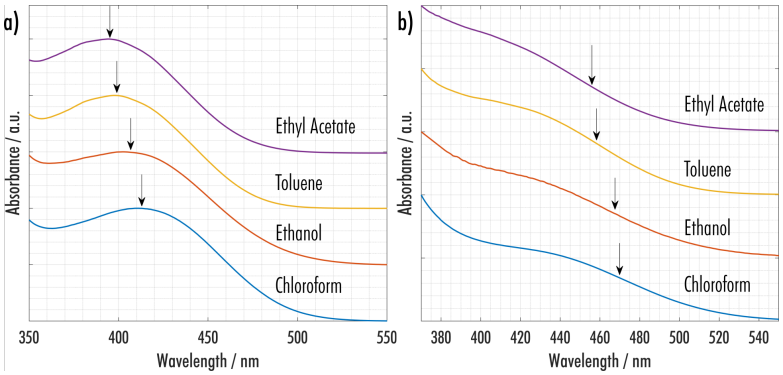

Figure 5.17: UV-Vis spectra of Gm8m and Gm8p dissolved in ethyl acetate, toluene, ethanol and chloroform at a concentration of 0.25 mg.ml^{-1}.

It is obvious from the initial UV-Vis experiments that a solute concentration of 0.25 mg.ml^{-1} did not give a clear UV-Vis absorption profile across the spectrum for any of the samples. Therefore, the samples were sequentially diluted until there was no longer any saturation of the absorption profile. UV-Vis spectra for solute concentrations of 0.008 mg.ml^{-1} are shown in Figure 5.18. The data below the solvent cut-off wavelength has been removed from each spectrum and marked with a vertical line for clarity. The solvents cut-off makes it difficult to directly compare the data for the different solvents for wavelengths below 300 nm; however, the profiles of each solvent look very similar for both Gm8m and Gm8p. Moreover, the region below 300 nm will have little effect on the colour of the sample, as these wavelengths sit within the UV region. In Gm8m, two overlapping features are seen in ethanol, with maxima at 265 nm and 295 nm. These features overlap slightly more in ethyl acetate and chloroform, with the second maximum disappearing in chloroform, leaving a shoulder. The features cannot be seen in toluene due to the solvent cut-off. In all Gm8p solutions, a peak centred around 330 nm can be seen, which is shifted to lower wavelengths in ethanol and chloroform. An additional peak can be seen in the ethyl acetate, ethanol and chloroform solutions, with maxima at 260 nm in ethyl acetate and ethanol, shifted to 270 nm in chloroform. In summary, only small changes in the absorption spectra are seen between solutions of Gm8m and Gm8p in different solvents, which is expected from the observations of their colour. The small changes seen in Figure 5.8 are due to shifts in small absorption peaks seen in both Gm8m and Gm8p at wavelengths above 400 nm.

When analysing UV-Vis data of solutions, it is important to determine whether absorption peaks are due to the electronic distribution of isolated molecules or molecular agglomeration. This is possible by analysing the relative intensity of absorption peaks as the concentration of the solutions

is reduced. Figure 5.19 and Figure 5.20 show the full set of absorption spectra for sequential dilutions of Gm8m and Gm8p solutions from 0.5 mg.ml^{-1} to 0.008 mg.ml^{-1}. An inset within each graph shows an enhanced view of the feature appearing at higher wavelengths for Gm8m and Gm8p. Analysis of the exact proportionality of peaks is difficult due to the initial saturation of the most intense peak; however, analysis of the lower concentration peaks shows that the ratio is constant. This highlights that the intensity of the feature is proportional to the concentration of the solution. Thus, the absorption arises from isolated molecules within the solution, meaning computational predictions based on an isolated molecule should predict absorption at this wavelength.

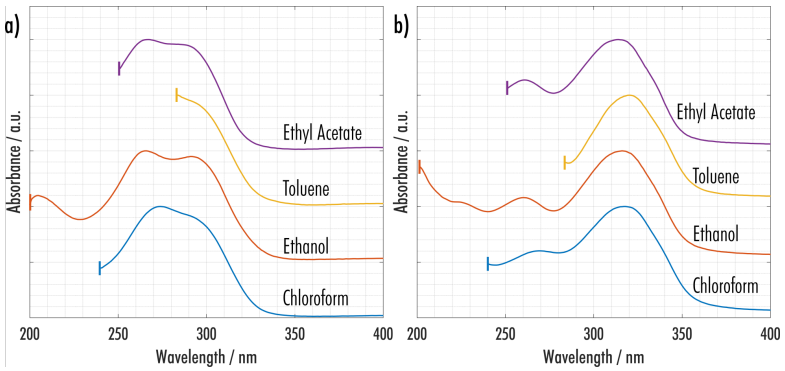

Figure 5.18: UV-Vis spectra of Gm8m and Gm8p dissolved in ethyl acetate, toluene, ethanol and chloroform at a concentration of 0.008 mg.ml^{-1}.

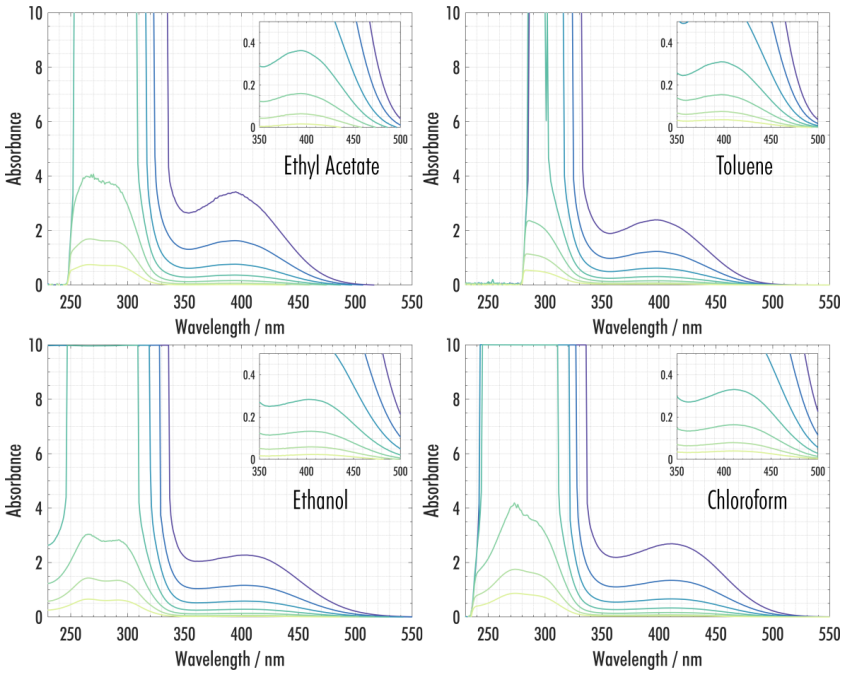

Figure 5.19: UV-Vis spectra of Gm8m dissolved in ethyl acetate, toluene, ethanol and chloroform at concentrations ranging from 0.5-0.008 mg.ml^{-1}.

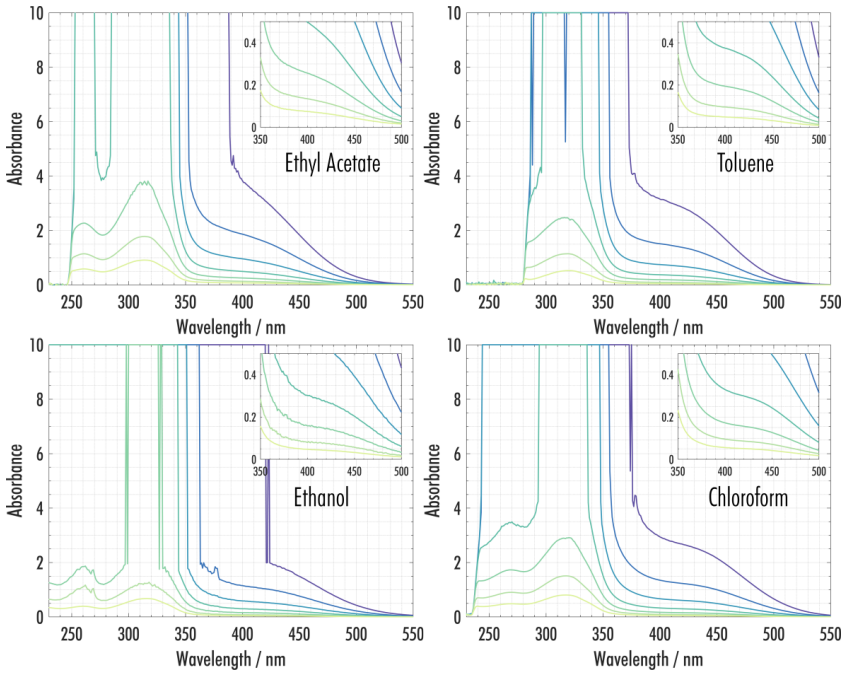

Figure 5.20: UV-Vis spectra of Gm8p dissolved in ethyl acetate, toluene, ethanol and chloroform at concentrations ranging from 0.5-0.008 mg.ml^{-1}.

Solid-state UV-Vis was carried out using pure samples of each polymorph of Gm8m and Gm8p, produced using the crystallisation parameters discussed in Section 5.3.2.4. To ensure each sample contained a single polymorph, pXRD analysis was carried out prior to UV-Vis measurements. Diffuse reflectance data was taken using a spectralon sample as a reference. The raw diffuse reflectance data for each sample is shown in Figure 5.21a. Although the reflectance data appears relatively featureless, a clear shift of wavelength at which the samples start reflecting the majority of incoming radiation can be seen. Moreover, this onset matches the colour of the samples, following the expected trend: yellow, orange, red and black.

Although the reflectance data trend is as expected, it is more common to view UV-Vis data in terms of absorbance. The reflectance data can be transformed to absorbance via the Kubela-Munk transformation,[224] approximating the sample to that of infinite thickness. As this transformation depends on the particle size and packing of the sample, care was taken to prepare samples in the same manner. All samples were ground with a pestle and mortar, and it was ensured that enough sample was used to cover the whole sample holder. The Kubelka-Munk transformation is given by the equation:

$$F(R) \equiv \frac{k}{s} = \frac{(1-R_\infty)^2}{2R_\infty}, \tag{5.5}$$

where $F(R)$ is the Kubelka-Munk function, k is the absorption coefficient of the sample, s is the scattering coefficient (which is assumed to be independent of wavelength), and R_∞ is the experimental diffuse reflectance. Figure 5.21b shows the absorbance data for samples of Gm8m and Gm8p

transformed via the Kubelka-Munk transformation of their diffuse reflectance. The samples are stacked based on their observed colour, and a horizontal dashed line is used to highlight the onset of the absorbance of each sample.

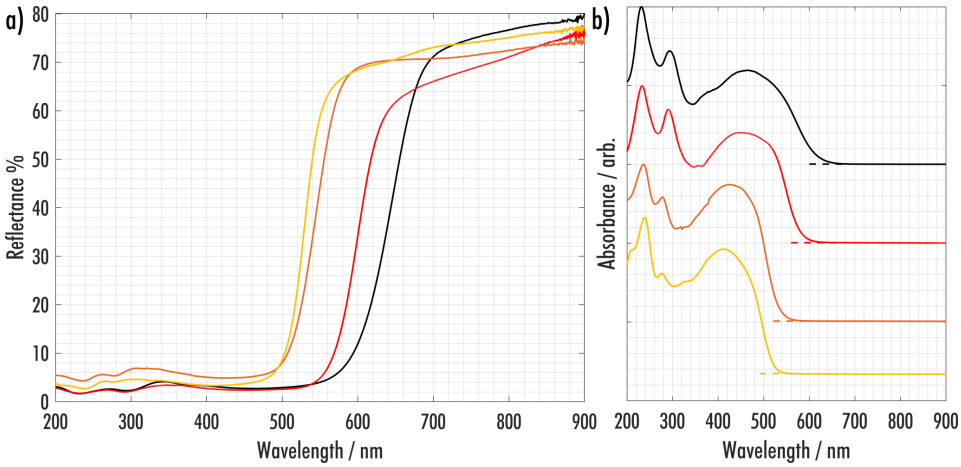

Figure 5.21: a) Solid-state UV-Vis reflectance of each of the polymorphs of Gm8m and Gm8p. b) Reflectance data transformed to absorbance via the Kubelka-Munk transformation.

Using the Tauc relationship and assuming a direct bandgap (E_g) allows one to equate the absorbance of a sample to the equation,[225]

$$(F(R)h\nu)^2 = B(h\nu - E_g), \tag{5.6}$$

where $h\nu$ is the energy of the transition and B is the band-tailing parameter. By plotting $(F(R)h\nu)^2$ against $h\nu$, an estimate for the bandgap can be made via extrapolation of the onset of the broad absorption peak. This process is used to discard the effect of the band-tailing parameter. Extrapolation for Gm8m and Gm8p samples is shown in Figure 5.22, where the x-axis is shown in eV. The approximated bandgaps are summarised in Table 5.7. As can be seen, the band gap of the samples progressively gets smaller as the colour changes from yellow to black. This is expected, as the appearance of the samples is based on the contrasting wavelengths of visible light that are absorbed.

Table 5.7: Band gaps calculated for each of the polymorphs of Gm8m and Gm8p.

Sample	**Absorption onset from K-M (eV)**
Gm8m-Y	2.45
Gm8m-O	2.41
Gm8p-R	2.21
Gm8p-B	2.11

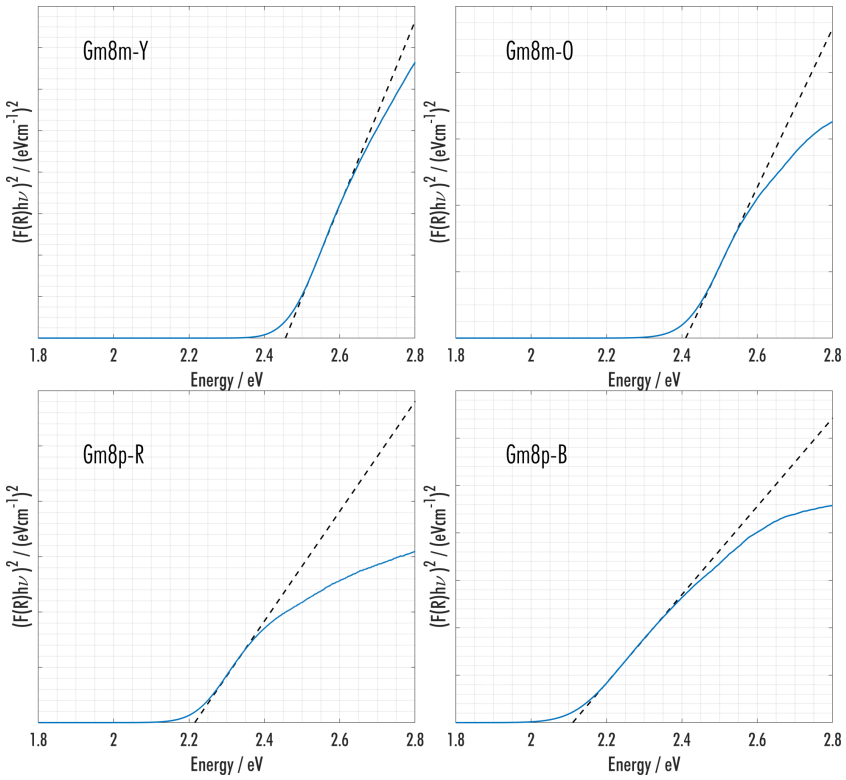

Figure 5.22: Construction of Tauc plots to estimate the band gaps of each of the polymorphs of Gm8m and Gm8p.

5.3.5 Fluorescence Spectroscopy

Fluorescence spectroscopy of Gm8m and Gm8p was carried out in the solution and solid states. Similarly to UV-Vis spectroscopy, modifying the molecular environment of the species can have a stark effect on the fluorescent wavelength and yield. The initial observation of fluorescence was carried out via optical imaging under a 365 nm UV lamp. An obvious difference in fluorescence was seen between the polymorphs of Gm8m, as shown in Figure 5.23. The yellow polymorph emitted a strong yellow fluorescence, and the orange polymorph emitted minimal radiation. This luminescence made the observation of concomitant polymorphism very easy in cases where crystallisation yielded only small amounts of polycrystalline material. A similar analysis of Gm8p polymorphs highlighted that neither sample showed strong fluorescence in the solid-state. An observation of the fluorescence of all four polymorphs was made by crushing each sample and placing them in vials with a white background. Figure 5.24 shows the four samples under ambient light and 365 nm UV radiation, where the stark difference in fluorescent intensity of the Gm8m-Y sample is clear.

Similarly to the UV-Vis absorption spectra, it is useful to record fluorescence spectra both in the solution and solid-state to assess the effect of intermolecular interactions. Figure 5.25a shows the excitation and emission fluorescence spectra for 0.5 mg.ml^{-1} ethanol solutions of Gm8m and Gm8p. Both samples fluoresce, with the excitation and emission red-shifted for the Gm8p sample, which

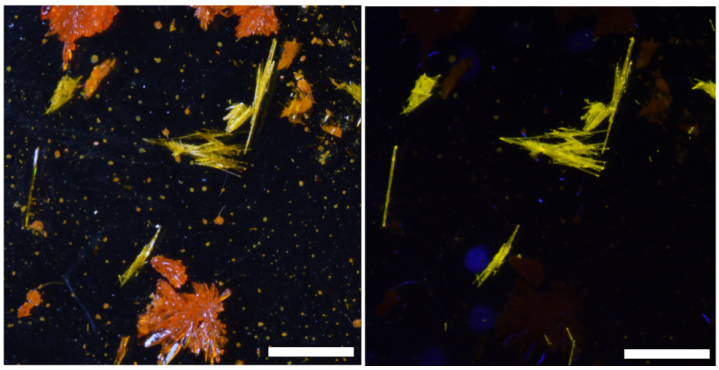

Figure 5.23: Optical images of Gm8m polymorphs under broadband light (left) and 365 nm UV radiation (right).

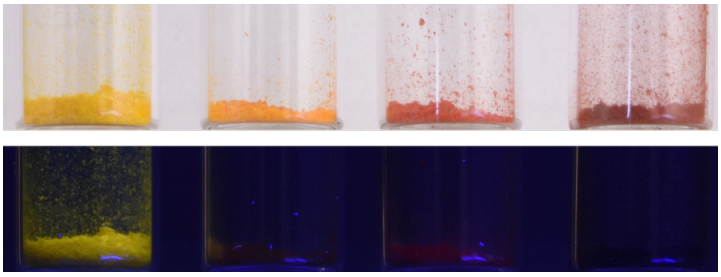

Figure 5.24: Powders of Gm8m and Gm8p polymorphs imaged under broadband and 365 nm UV light.

may be expected due to the colour of the solution observed in the previous section. The spectra for Gm8p are boarder than for Gm8m, with a smaller maximum intensity. For perspective, spectra were also taken for a similar fluorescent molecule, 4-dimethylaminochalcone. Figure 5.25b shows a comparison of the fluorescence spectra, highlighting that the Gm8m and Gm8p samples have a comparatively low fluorescent intensity.

To quantify the fluorescence of Gm8m and Gm8p in the solid-state, fluorescence spectra of powders of all four samples were recorded. The excitation spectra for all samples were broad and featureless; however, the emission for Gm8m-Y, Gm8m-O and Gm8p-R showed clear features. The Gm8p-B powder did not show any appreciable emission or excitation fluorescence intensity. The emission spectra for Gm8m-Y, Gm8m-O and Gm8p-R are shown in Figure 5.26. As the excitation spectra were broad, each sample was excited at 365 nm. It is clear to see that the emission intensity of Gm8m-Y is far larger than for Gm8m-O and Gm8p-R, and an expected shift in the wavelength of the maxima is seen. Interestingly, the most fluorescent sample in the solid-state is the only structure not containing the double 1,3-ring stacking motif. The reduction in fluorescence intensity in the other samples is likely because the double 1,3-ring stacking motif allows the nitro group to sit in the proximity of the π-conjugated system. Nitro groups are known to quench fluorescence in the solid-state due to their electron-withdrawing nature, which allows the decay of excited states via non-radiative pathways.[226–228]

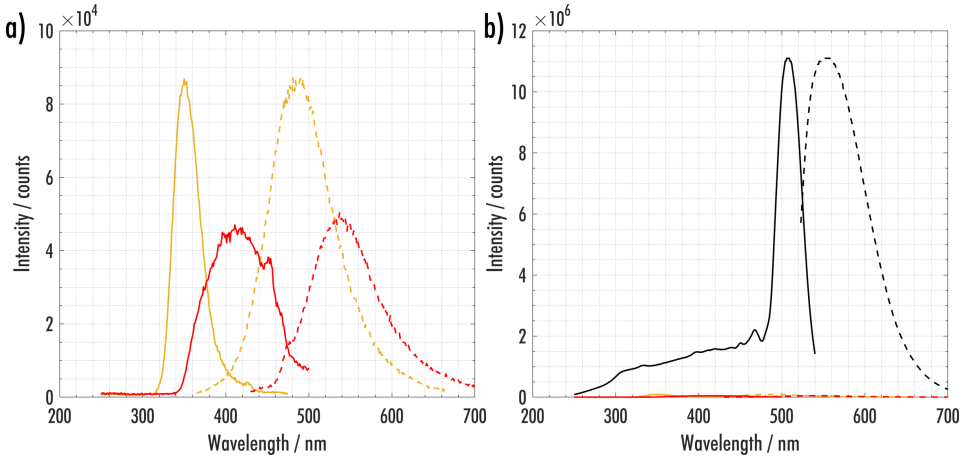

Figure 5.25: a) Fluorescence spectra of 0.5 mg.ml^{-1} ethanol solutions of Gm8m and Gm8p. b) Comparison of the same data with the fluorescence spectra of a 0.5 mg.ml^{-1} ethanol solution of 4-dimethylaminochalcone. Emission spectra are shown with solid lines and excitation with dashed lines.

It should be noted that the fluorescence experiments conducted here only scratch the surface of the possible information that can be extracted in both the solid and solution states. A full description of fluorescence requires the calculation of quantum yields by carefully assessing the difference in photons absorbed and emitted in each system, along with information about excited-state lifetimes. The field of fluorescent imaging uses this information to give information about molecular environments far more precisely and conclusively than discussed in this work. The differences in fluorescence between the solid-state samples show a clear case of an aggregation-induced phenomenon, of which aggregation-induced fluorescence and aggregation-caused quenching have both been heavily studied in the literature. Without a quantitative comparison of solvent and solid-state fluorescence quantum yields, it is difficult to say which type of aggregation phenomena is being seen in the Gm8m and Gm8p systems. Moreover, fluorescence in solution can be highly dependent on solvent polarity and solute concentration, so additional experiments would have to be carried out. As the nitro group often acts to quench fluorescence, an increase in solute concentration would likely increase the amount of quenching taking place in solution. However, from the experiments that have been carried out, it is still clear to see that Gm8m and Gm8p both fluoresce in solution, and it is likely that the proximity of the nitro and dimethylamino groups in the solid-state dictates the fluorescent yield.

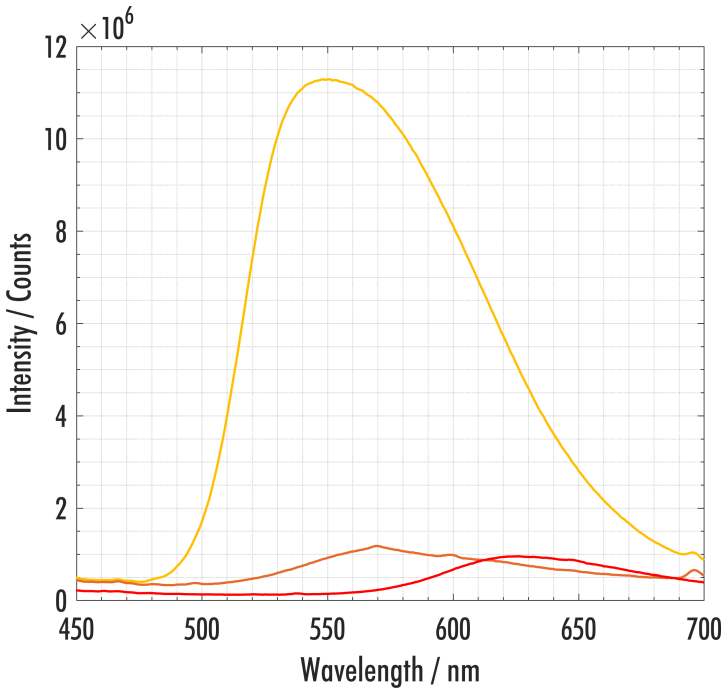

Figure 5.26: Solid-state fluorescence emission spectra from Gm8m and Gm8p polymorphs.

5.3.6 Thermal Analysis

5.3.6.1 Thermograms of Gm8m and Gm8p

The thermodynamic landscape of polymorphs of Gm8m and Gm8p were analysed by producing differential scanning calorimetry (DSC) thermograms between room temperature the melting points of the respective polymorphs. Initial scans were taken at 5 °C.min^{-1} and 10 °C.min^{-1} to assess the melting point of each structure and any obvious phase transitions. A summary of thermograms is shown in Figure 5.27, highlighting the heating of all four polymorphs above their melting points. All samples were crushed and structurally analysed via pXRD before experiments were run.

Interestingly, in both Gm8m-O and Gm8p-R there appear to be multiple thermodynamic events. At 100 °C an event involving an endotherm followed by an exotherm is seen in Gm8m-O. This type of event is indicative of a melt-mediated phase transition to a lower energy crystalline state. The depth of the initial endotherm gives information about the speed of the transition, as there will be a maximum overlap of the melting (endothermal) and crystallisation (exothermal) events for rapid transitions. When the Gm8m-O sample is heated beyond this initial phase transition, a melting endotherm is seen at 120 °C. Comparing the thermogram of Gm8m-O to the thermogram of Gm8m-Y, which has only a single endothermic transition at 122 °C, it appears that Gm8m-O is transforming to Gm8m-Y and subsequently melting upon further heating. As there is no structural data taken concomitantly with these experiments, further experimental data are needed to confirm this.

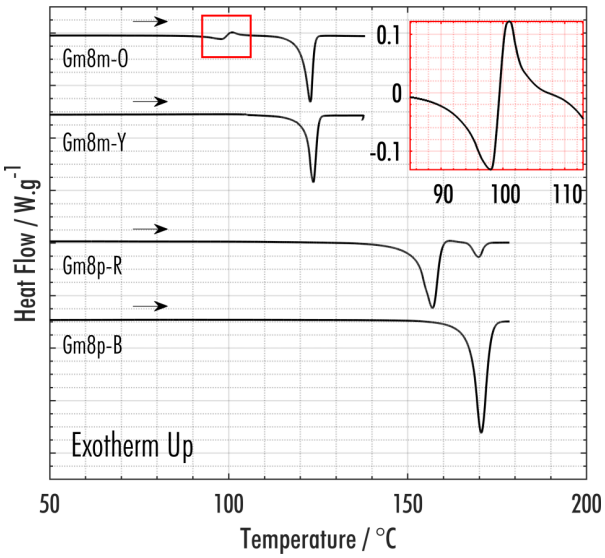

Figure 5.27: Thermograms of Gm8m and Gm8p polymorphs from DSC. The inset shows an enhanced view of the event seen at ~100 °C in Gm8m-O. The units for the *y*-axis in the inset is W.g^{-1}.

A similar transition occurs in Gm8p-R, where an initial endothermic and subsequent exothermic event is seen at 152 °C. This is again followed by a further endothermic event at 167 °C. The final endothermic event is also seen in the thermogram of Gm8p-B, suggesting that Gm8p-R transforms to Gm8p-B at 152 °C, which subsequently melts at 167 °C. Interestingly, the initial endothermic event seen in Gm8p-R is far larger than that of Gm8m-O, which suggests that the transition from Gm8m-O to Gm8m-Y is faster than the transition from Gm8p-R to Gm8p-B.

As the polymorphic transformations in Gm8m-O and Gm8p-B appear to be melt-mediated, it should be the case that their thermograms are dependent on the rate of heating. As the rate of heating of the sample is increased, the amount that melts before the polymorphic transformation takes place should increase. To evaluate this pattern, samples of Gm8p-R and Gm8m-O were heated at rates between 5 °C.min^{-1} and 100 °C.min^{-1}. Regardless of the heating rate, only a small amount of the Gm8m-O sample melted before the transformation took place. This is highlighted by only a small endothermic event appearing before the melting of Gm8m-Y, even when the sample was heated at 100 °C.min^{-1}. Thermograms showing the heating of Gm8m-O at 5 °C.min^{-1} and 100 °C.min^{-1} are shown in Figure 5.28.

As the heating rate of Gm8p-R samples is increased, more of the sample melts before the transformation takes place. Thermograms of Gm8p-R samples heated at rates between 5 °C.min^{-1} and 50 °C.min^{-1} are shown in Figure 5.29a, where it is clear to see an increase in the size of the first endotherm and a decrease in the size of the second endotherm as the heating rate is increased. The broadening of the endotherm as the heating rate is increased may be masking a small amount of the second endotherm still present; however, it is clear that by a heating rate of 50 °C.min^{-1} almost all of the sample is melting during the first transition, with no transformation. Mapping of the enthalpy of

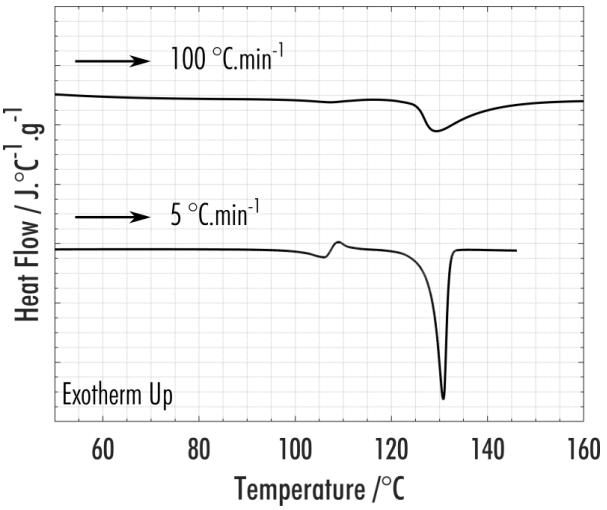

Figure 5.28: DSC thermograms of Gm8m-O heated at rates of 5 °C.min^{-1} and 100 °C.min^{-1}. The heat flow is divided by the ramp rate to normalise the intensity of each of the thermograms.

the endothermic transitions supports this hypothesis (Figure 5.29b), as heating rates of 20 °C.min^{-1} and above show a consistent value for the enthalpy of the first endotherm. This allows a prediction for the enthalpy of fusion for the Gm8p-R samples using heating rates above 20 °C.min^{-1}. However, for complete conformation, structural information should be obtained to ensure no polymorphic transformation occurs.

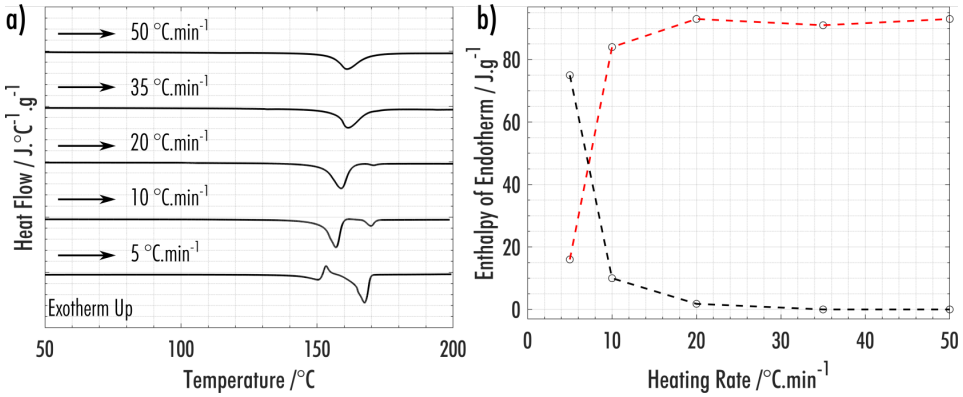

Figure 5.29: a) DSC thermograms of Gm8p-R heated at rates between 5 °C.min^{-1} and 50 °C.min^{-1}. b) Plot of the enthalpy of the first (black) and second (red) endotherms for each ramp rate of the data in a).

5.3.6.2 Low-Temperature Powder X-ray Diffraction

To assess the stability of Gm8m and Gm8p polymorphs at temperatures lower than the range accessible via DSC measurements, low-temperature pXRD was carried out down to 12K. During the cooling

of powders of each of the polymorphs, continuous shifts in the pXRD peaks represent the contraction or expansion of the unit cells. Unit cell changes with temperature are often anisotropic, as they are caused by slight relaxations in molecular configurations or changes in intermolecular bonding motifs. Phase transitions can be detected by looking for discontinuous changes in the pXRD patterns as the samples are cooled, representing a more rapid change of molecular configuration or intermolecular bonding over a small temperature range. The temperature dependence of lattice parameters is useful to identify when computationally assessing crystal properties, as the disregard for such information can cause large errors in predicted free energies.[229] In particular, phonon modes can be affected by large expansions/contractions, which play a role in determining temperature-dependent polymorph stability.

The temperature dependence of crystallographic parameters for polymorphs of Gm8m and Gm8p is highlighted in Table 5.8, with the differences shown in Table 5.9. The unit cells of polymorphs at 300K and 12K are shown in Figure 5.30, with molecules at 300K shown in red and 12K shown in blue. The unit cells were produced by carrying out Rietveld refinement on the powder diffraction patterns for samples at the two temperatures. These experiments show that the unit cell of Gm8m-Y contracts substantially in the direction of the *c*-axis as the crystal is cooled, with a small expansion in the direction of the *b*-axis. This change is due to a relaxation of the zigzag motif, leading to a more acute angle between molecules. In contract, the unit cells of Gm8m-O and Gm8p-R contract by a small amount in all axes due to a reduced distance between molecules in the 1,3-stacking motif on cooling. The only outlier is the *a*-axis direction in Gm8m-O, which is perpendicular to these stacks and, therefore, increases by a small amount.

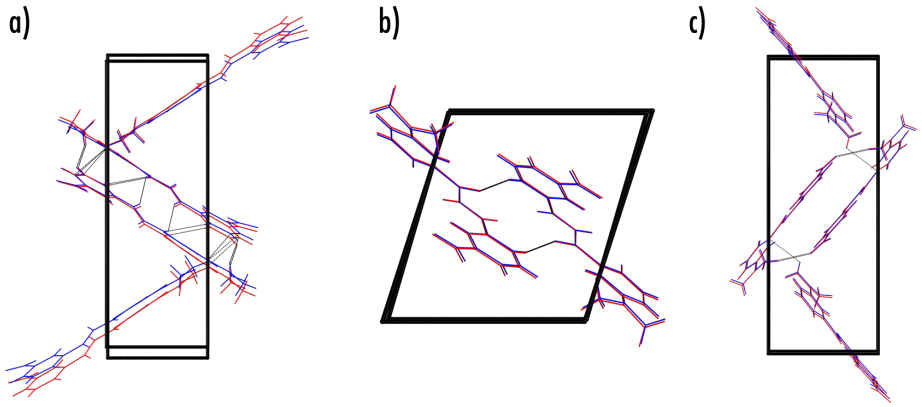

Figure 5.30: Unit cells of each polymorph of Gm8m and Gm8p at 12K (blue) and 300K (red). a) Gm8m-Y b) Gm8m-O c) Gm8p-R.

As the powder of Gm8p-B is cooled, a sharp discontinuity is seen in the pXRD data between 110-170 K. Although the changes in the position of the peaks are not large, the fact that they do not match the continuous trend seen at higher temperatures suggests a phase transition rather than a simple temperature dependence of lattice parameters. As the original structural solution from Gm8p-

Table 5.8: Crystallographic data from low-temperature pXRD of Gm8m-Y, Gm8m-O and Gm8p-R at 300K and 12K.

Identification code	**Gm8m-Y**	**Gm8m-O**	**Gm8p-R**
Temperature / K	**300**	**300**	**300**
a / Å	12.6332(12)	8.3370(9)	8.386(2)
b / Å	6.2561(8)	9.5613(9)	8.1743(5)
c / Å	18.942(2)	10.3919(8)	22.013(2)
α / °	90	103.544(5)	90
β / °	92.647(6)	103.003(8)	91.751(13)
γ / °	90	104.395(7)	90
Temperature / K	**12**	**12**	**12**
a / Å	12.5644(14)	8.341(11)	8.3232(14)
b / Å	6.3401(12)	9.415(12)	8.0437(6)
c / Å	17.882(2)	10.059(9)	21.583(3)
α / °	90	102.056(6)	90
β / °	92.910(7)	102.46(11)	91.010(9)
γ / °	90	105.018(8)	90

Table 5.9: Difference in crystallographic parameters of Gm8m-Y, Gm8m-O and Gm8p-R between 300K and 12K.

Identification Code	**Gm8m-Y**	**Gm8m-O**	**Gm8p-R**
a / Å	-0.0688	0.004	-0.0628
b / Å	0.084	-0.1463	-0.1306
c / Å	-1.06	-0.3329	-0.43
α / °	0	-1.488	0
β / °	0.263	-0.543	-0.741
γ / °	0	0.623	0

B was carried out at 100 K, this transition suggests a different structure exists at room temperature. Figure 5.31 shows a trace of the diffraction data for a powder of Gm8p-B cooled from 300 K to 12 K. The reverse transition occurs on heating, which highlights that the change is enantiotropic.

To assess the differences in the crystal structure of Gm8p-B before and after the phase transition, sc-XRD data was collected of a crystal of Gm8p-B at 300 K, before being cooled to 100 K and rerun. The unit cell for each structure is shown in Figure 5.32a, which highlights a change in the angle between the double 1,3-ring stacked dimers, causing a reduction in the a-axis for the low-temperature structure. Thermal ellipsoid plots for the asymmetric unit of Gm8p-B at 100 K and 300 K are shown in Figure 5.32b, highlighting that there is little change in the conformation of the molecular unit. The unit cell parameters for Gm8p-B at both temperatures are highlighted in Table 5.10, which shows that there are only small changes in the unit cell lengths between polymorphs; however, there is a large change in the β angle, increasing by over 5 ° in the low-temperature structure. It should be noted that this is only being classified as a polymorphic transition due to the rapid change of cell parameters

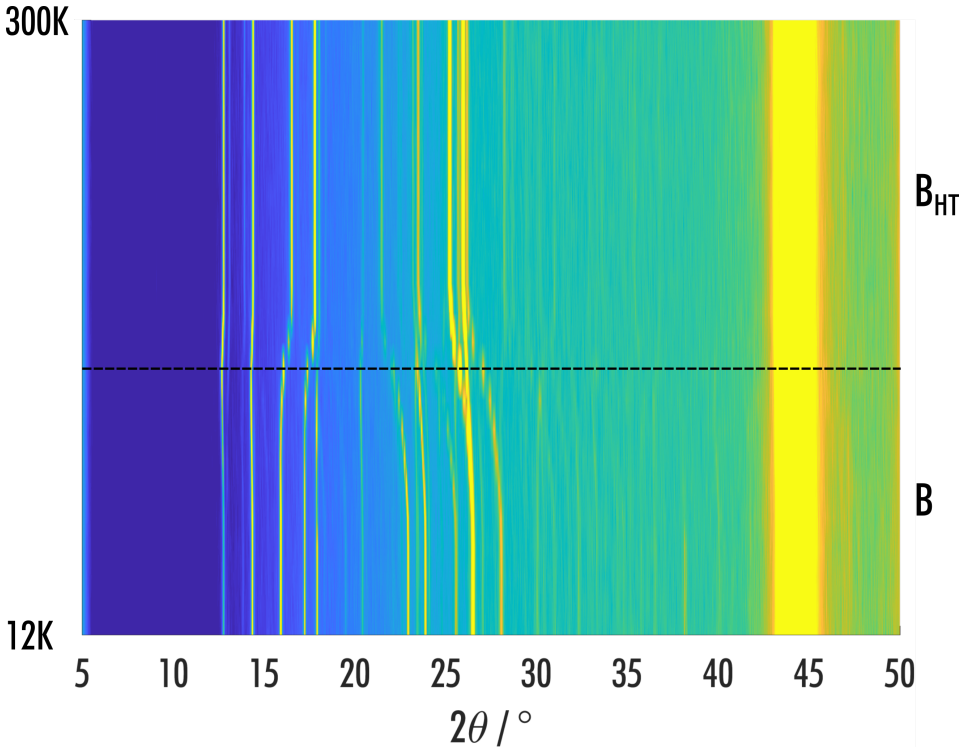

Figure 5.31: Low-temperature pXRD of Gm8p-B plotted from a cooling ramp between 300K and 12K.

over a small temperature range. A more definitive observation of polymorphism would be to observe an enthalpic change between the two structures. DSC down to the temperatures required to observe this transition was not possible, meaning the polymorphic transition is defined tentatively. Indeed, the structures converged to a single energy minimum during structural optimisations, meaning any calculations can be carried out on this single optimised structure.

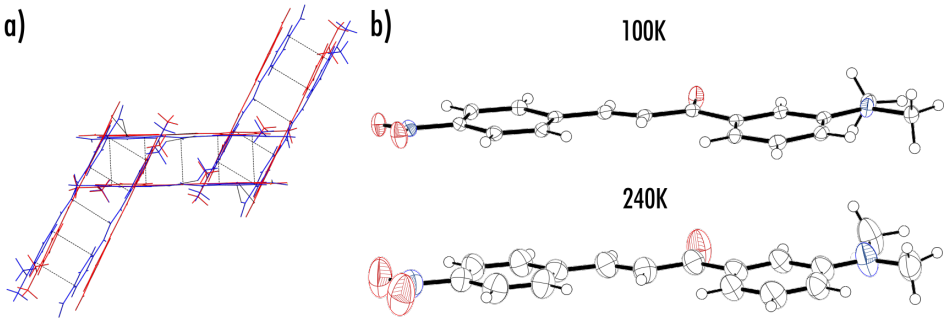

Figure 5.32: a) Difference in molecular packing in Gm8p-B low-temperature structure (blue) and high-temperature structure (red). b) ORTEP plots of the high and low-temperature polymorphs of Gm8p-B.

Table 5.10: Difference in unit cell parameters between the Gm8p-B high and low temperature polymorphs.

	Gm8p-B Low-Temperature	**Gm8p-B High-Temperature**	**Difference**
CCDC Identifier	1983904	1983908	
Space group	$P21/c$	$P21/c$	
a / Å	7.8167(2)	8.1180(5)	-0.3013
b / Å	13.4438(4)	13.3417(7)	0.1021
c / Å	13.7862(5)	13.6713(8)	0.1149
α / °	90	90	0
β / °	97.413(2)	92.261(4)	5.152
γ / °	90	90	0
Z	4	4	
Final R indexes [I>=2σ (I)]	R_1 = 0.0336, wR_2 = 0.0860	R_1 = 0.0465, wR_2 = 0.1124	

5.3.6.3 Analysis of Polymorphic Transitions of Gm8m and Gm8p

The polymorphic transitions between structures of Gm8m and Gm8p should be visible by eye due to their stark differences in optical properties. In Section 5.3.5, it was highlighted that the fluorescent intensity of Gm8m-Y was observably higher than Gm8m-O when illuminated with UV light. Therefore, the transition of Gm8m-O to Gm8m-Y should be able to be mapped via time-lapse imaging of a powder sample on a heated stage under UV lighting. This experiment was carried out using a heating rate of 1 °C.min^{-1} and a 365 nm UV lamp. A sample of Gm8m-O was grown from solvent evaporation of a toluene solution. Images from the time-lapse are shown in Figure 5.33a, highlighting the clarity of the polymorphic transition when viewed under UV light. To ensure that the transition was taking place between the expected crystal structures, pXRD was taken before and after the heating ramp, shown in Figure 5.33b. The diffraction patterns clearly show the transition between the expected polymorphs; however, the background increase suggests that the Gm8m-Y formed after the transition is of lower quality, either due to fracturing of the crystals or partial melting causing amorphisation of some of the material.

As the rate of transformation between Gm8p-R and Gm8p-B was slow enough to measure the heat of fusion of Gm8p-R, additional analysis of the Gibbs free energy of each crystal structure could be carried out. To ensure that no intermediate phases were forming during the transformation, which may lead to an inaccurate heat of fusion, a concomitant synchrotron X-ray diffraction and DSC heating ramp was carried out. This allowed analysis of the structure of the sample throughout the whole of the polymorphic transition. The synchronised DSC thermogram and diffraction data are shown in Figure 5.34. The experiment was carried out by heating a powdered sample of Gm8p-R at a ramp rate of 10 °C.min^{-1}. A clear transition between two crystalline phases can be seen in the diffraction data around 165 °C, which coincides with the appearance of two endothermic transitions

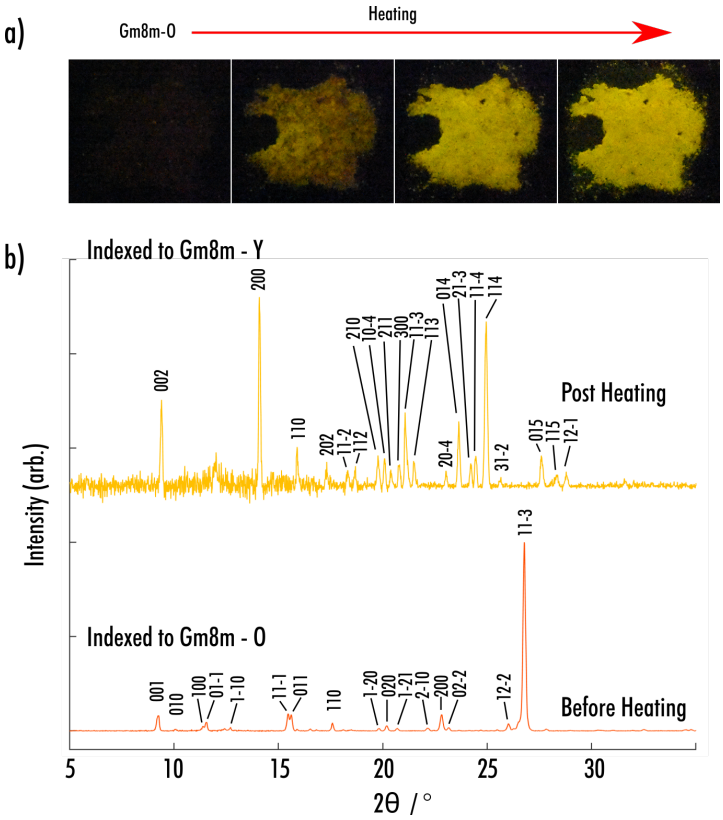

Figure 5.33: a) Time-lapse images of the transition between Gm8m-O and Gm8m-Y with increased temperature under 365 nm UV light. b) Powder X-ray diffraction patterns before and after the time-lapse.

in the DSC thermogram. It is clear that the transition is melt-mediated, as an amorphous background appears around the point of the transition in the diffraction data, and there is no point where the second crystalline structure appears without any amorphous material.

Rietveld analysis of diffraction patterns before and after the transition confirmed that the crystalline phases were Gm8p-R (before) and Gm8p-B (after). Given that there appear to be no intermediate phases (other than the melt) during the transformation, it can be assumed that the calculated enthalpy of fusion for Gm8p-R is accurate. As described in the previous section, the acquisition of this value is possible using a ramp rate of 50 °C.min^{-1}. Additionally, it is simple to determine the heat capacities of both polymorphs of Gm8p and the liquid state via modulated DSC. The heat capacities from modulated DSC experiments run on powders of Gm8p-R and Gm8p-B are shown in Figure 5.35.

The heat capacity of each phase is shown fitted to a second-order polynomial (black line), and heat capacities during phase transitions (dotted line) are disregarded due to the dramatic divergence of the data at these temperatures. After the melting of both phases, the heat capacity of the liquid (blue) is the same for both samples. By extrapolating the heat capacity of all phases across the range of interest, which is valid in the range of a few hundred of Kelvin, the Gibbs free energy of Gm8p-R and Gm8p-B can be plotted with respect to the Gibbs free energy of the liquid phase. The Gibbs free

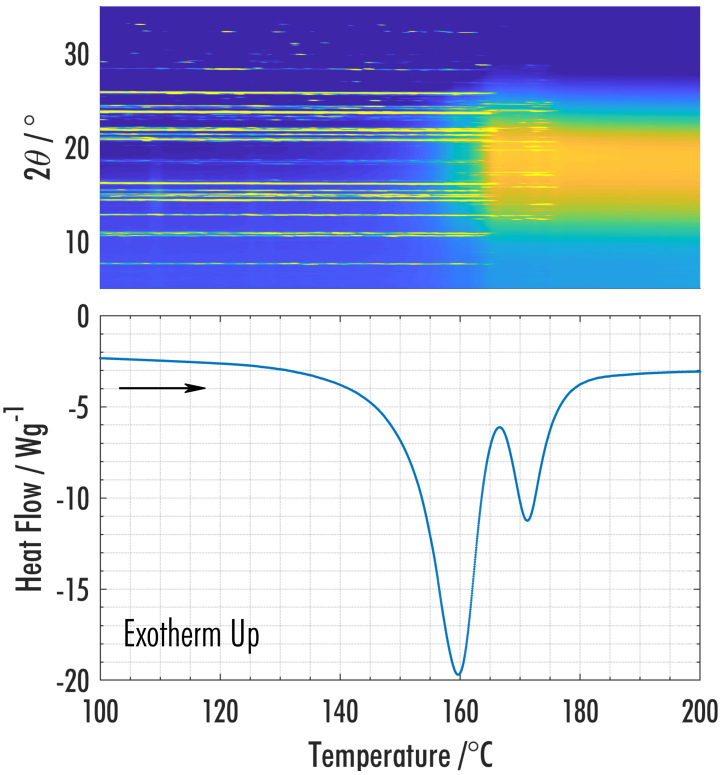

Figure 5.34: Concomitant synchrotron powder diffraction and differential scanning calorimetry of Gm8p-R. A black arrow shows the direction of the temperature ramp.

energy of each crystalline phase is given by combining equations 1.8 and 1.7 from Chapter 1,

$$\Delta G_C(T) = -\Delta H_{fus} - \int_T^{T_{fus}} \Delta C_p(T) dT + T\frac{\Delta H_{fus}}{T_{fus}} + T\int_T^{T_{fus}} \frac{\Delta C_p(T)}{T} dT \tag{5.7}$$

where $\Delta G_C(T)$ is the difference in Gibbs free energy between the crystalline and liquid states at temperature T, $\Delta C_p(T)$ is the difference in heat capacity between the crystalline and liquid states at temperature T, ΔH_{fus} is the enthalpy of fusion of the crystal, and T_{fus} is the melting temperature of the crystalline state. The integrals can be analytically solved by writing the heat capacity of each phase as a power series,

$$C_{p,i}(T) \approx \sum_{n=0}^{m} a_n T^n, \tag{5.8}$$

where $C_{p,i}(T)$ is the heat capacity of phase i at temperature T, m represents the order of the power series, and a_n are the coefficients of the n^{th} term. In general, heat capacities are fit to order 1 or 2 over small temperature ranges. This allows for a full energy diagram of the two polymorphs to be produced, which is shown in Figure 5.36. The energy diagram highlights that there is no cross-over between the free energies of Gm8p-R and Gm8p-B, confirming that the transition from Gm8p-R to Gm8p-B is monotropic. This type of analysis is critical when looking at new polymorphic systems as

it allows a clear view of the structural landscape of a molecule. This type of transition could have been determined using Burger's rules, as the enthalpy of fusion of Gm8p-R is less than that of Gm8p-B.[230]

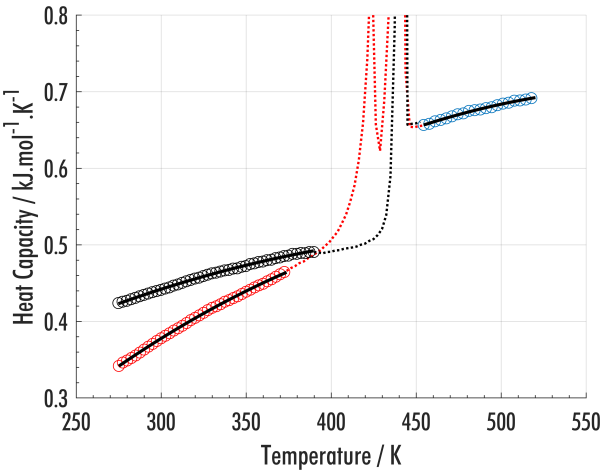

Figure 5.35: Heat capacity of Gm8p-R and Gm8p-B calculated using modulated differential scanning calorimetry.

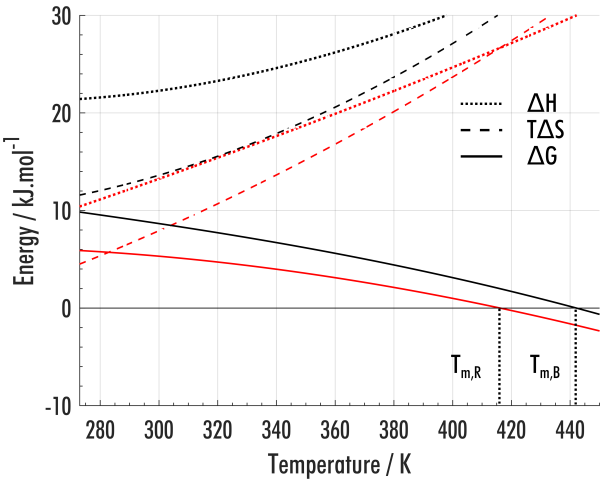

Figure 5.36: Phase diagram highlighting the relative free energies, entropies and enthalpies of Gm8p-R and Gm8p-B.

5.3.6.4 Disorder in Gm8m-Y

The structural solution of Gm8m-Y highlighted that there was an element of disorder present in the nitro group. Disorder within crystal structures can be either dynamic or static, highlighting whether the atoms of a single molecule can transform between the different configurations. Dynamic disorder becomes a problem when carrying out quantum chemistry calculations, as the harmonic approximation is often a fundamental element of the computation. If there is a large amount of dynamic disorder, then the harmonic approximation will not hold.

To test if the disorder is static or dynamic, the same single-crystal of Gm8m-Y was solved via sc-XRD at temperatures between 100 K and 250 K. If the disorder is static, then the percentage occupation of the different configurations will stay constant, whereas they will change if the disorder is dynamic. Structural solution of Gm8m-Y was carried out at 100 K, 150 K, 200 K and 250 K. The same experimental method was used for diffraction data collection at each temperature, which meant that the quality of the data did decrease slightly as the temperature was varied; however, all cells were of publishable quality (CCDC reference codes: DUZQOH05, DUZQOH04, DUZQOH01, DUZQOH). ORTEP plots of the asymmetric unit of Gm8m-Y at the different temperatures are shown in Figure 5.37, which highlights the difference in thermal motion of the atoms. Although the thermal ellipsoids changes in size, the disorder is shown to be in a similar position for each temperature.

Modelling of the disorder highlighted that as the temperature of the sample was increased, the occupation of the minor component increased. A summary of the occupancies is shown in Table 5.11. This shows that the order within the Gm8m-Y crystal structure is dynamic, and should be considered when commenting on the accuracy of calculations that utilise the harmonic approximation. Helmholtz free energy calculations of Gm8m-Y and Gm8m-O, without modelling disorder, predict Gm8m-O to be the stable polymorphs until temperatures above the melting points of both solids. This highlights the stabilisation that can arise due to disorder, and that care must be taken when modelling crystal structure energies at non-zero temperatures.

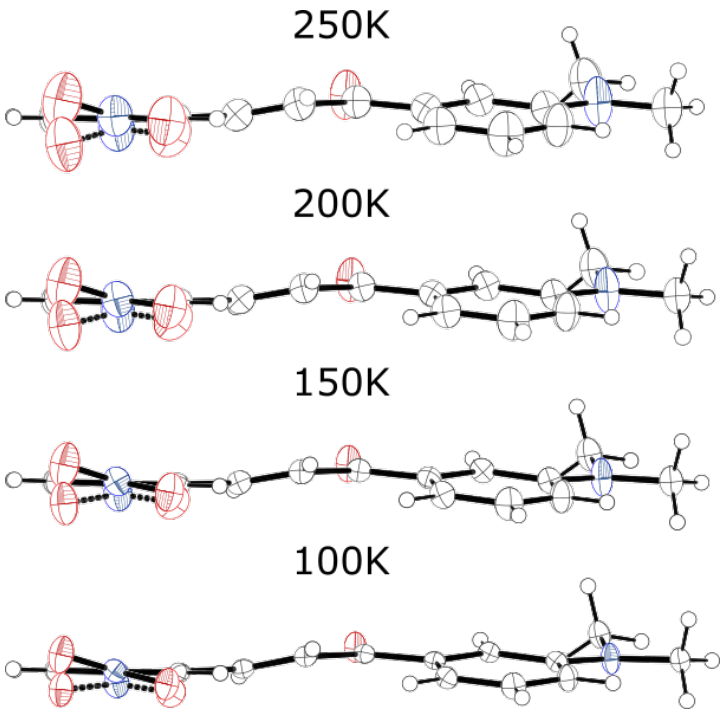

Figure 5.37: ORTEP plots showing the asymmetric unit of Gm8m-Y at temperatures between 100 K and 250 K. Covalent bonds in the disordered fragment are shown with dotted lines.

Table 5.11: Major and minor occupancies of the disordered component in Gm8m-Y.

Temperature / K	**Major**	**Minor**
250	0.668(11)	0.332(11)
200	0.721(11)	0.279(11)
150	0.786(11)	0.214(11)
100	0.862(11)	0.138(11)

5.3.7 Computational Prediction of Colour

A full description of the thorough calculations carried out are covered in the supplementary information of the publication: Color Differences Highlight Concomitant Polymorphism of Chalcones.[184] *In this section, I will summarise the computational predictions in reference to the experimental results shown in the previous sections.*

As discussed in the introduction to this chapter, the colour of a particular sample is based on the electronic and vibrational transitions that occur when a sample is excited by electromagnetic radiation. In a physical sense, these transitions are well understood; knowledge of the potential caused by the atoms of a molecule allows us to calculate the molecular orbitals dictating electronic energy levels, which allows us to calculate dipole transition integrals between different states. However, as a system becomes more complex, our ability to run ab initio calculations diminishes, and experimental analysis is often more time-efficient than the necessary computationally-expensive calculations.

As the Gm8m and Gm8p systems offer four polymorphs that exhibit distinctive structurally-dependent optical absorption properties, they were proposed as an example system for the prediction of colour in the solid-state. The computational method to be tested was to take small clusters of molecules from each crystal structure, and see how the absorption spectra were shifted depending on the differing intermolecular interactions. The utilisation of this method allows TD-DFT calculations to be carried out without the need for periodic-boundary conditions, greatly reducing the computational expenditure. This reduction allows for the use of a range-separated functional. The more molecules included in the calculations, the closer the calculations should get to the true absorption spectra of the materials. However, the systematic nature of these calculations allows one to determine the most important intermolecular interactions for absorption, and should indicate the number of molecules needed for convergence to crystallographic spectra.

Figure 5.38 highlights the predicted absorbance for each of the investigated polymorphs, from a variety of TD-DFT calculations. The shape of the curve for the monomer matched well with the experimental UV-Vis from solution, presented in the previous section. The predictions are blue-shifted with respect to the experimental data by ~100 nm, but clearly show the appearance of two peaks, with a greater overlap between the peaks in Gm8p. The blue-shift is likely due to the absence of solvent interactions and the tendency for range-separated functions blue-shift the entire spectrum.[231]

Numerous calculations were carried out on different dimers cut from crystal structures of each

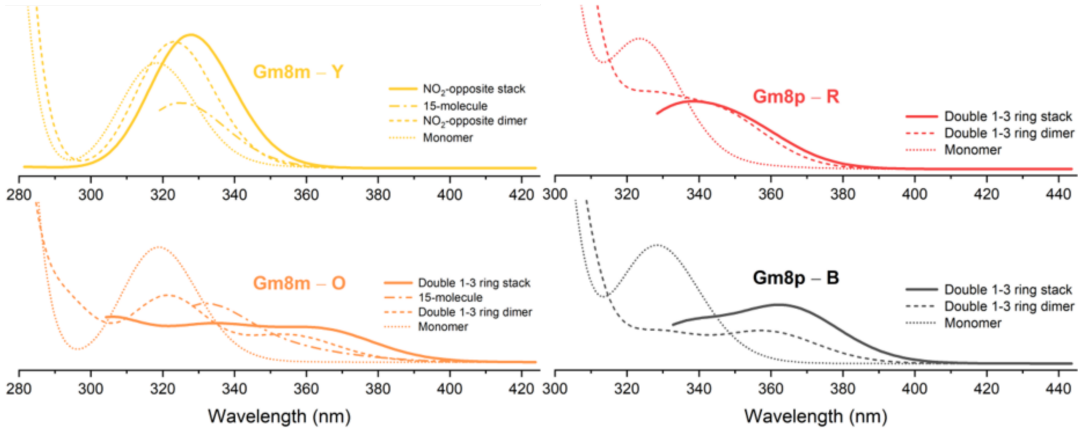

Figure 5.38: Computational predictions of the absorbance spectra of polymorphs of Gm8m and Gm8p.

polymorph. These dimers were found by isolating molecules within a molecular shell of 3.2 Å of the asymmetric unit. This resulted in 15-molecule clusters for Gm8m-Y, Gm8m-O and Gm8p-R, and a 19-molecule cluster for Gm8p-B. Calculations on these full clusters were carried out for Gm8m-Y and Gm8m-O; however, not enough computer time was available to run the full clusters of Gm8p molecules. Following this, each of the individual pairs of molecules were isolated, and separate TF-DFT calculations carried out. Analysis of the absorption spectra of these pairs of molecules highlighted that stacking interactions led to the largest red-shifts in absorption for Gm8m-O, Gm8p-R and Gm8p-B, with the double 1,3-ring stacking motif present in all of these structures leading to the largest red-shifts in absorption. Conversely, in Gm8m-Y, the only stacking motif led to a blue-shift in the absorption peak. For Gm8m-Y, the structural motif leading to the greatest red-shift in absorption was an offset dimer involving the carbonyl oxygen and a hydrogen from the 3-ring.

For the motifs that red-shifted the absorption spectra the most, extended stacks of molecules were input into the TD-DFT calculations, to see if this resulted in a further red-shift of the spectra. Four different calculations were carried out for comparison, systematically increasing the length of the stack from a dimer (two molecules) to an octamer (eight molecules). The molecular stacks are shown in Figure 5.39, with each of the clusters calculated shown within a dashed red box. Views both perpendicular to the short- and long-axis of the molecules are shown. This figure helps to highlight the different amount of overlap of the stacking interactions within each polymorph. The overlap in the short-axis of the molecule of Gm8m-O is greater than that of Gm8p-R, however the overlap in the long-axis is greater for Gm8p-R. The overlap for Gm8p-B is similar to that of Gm8m-O along the short-axis of the molecule and to that of Gm8p-R along the long-axis. Therefore, the extended stacking in Gm8p-B involves the largest amount of molecular overlap. There is very little overlap for the stack shown in Gm8m-Y.

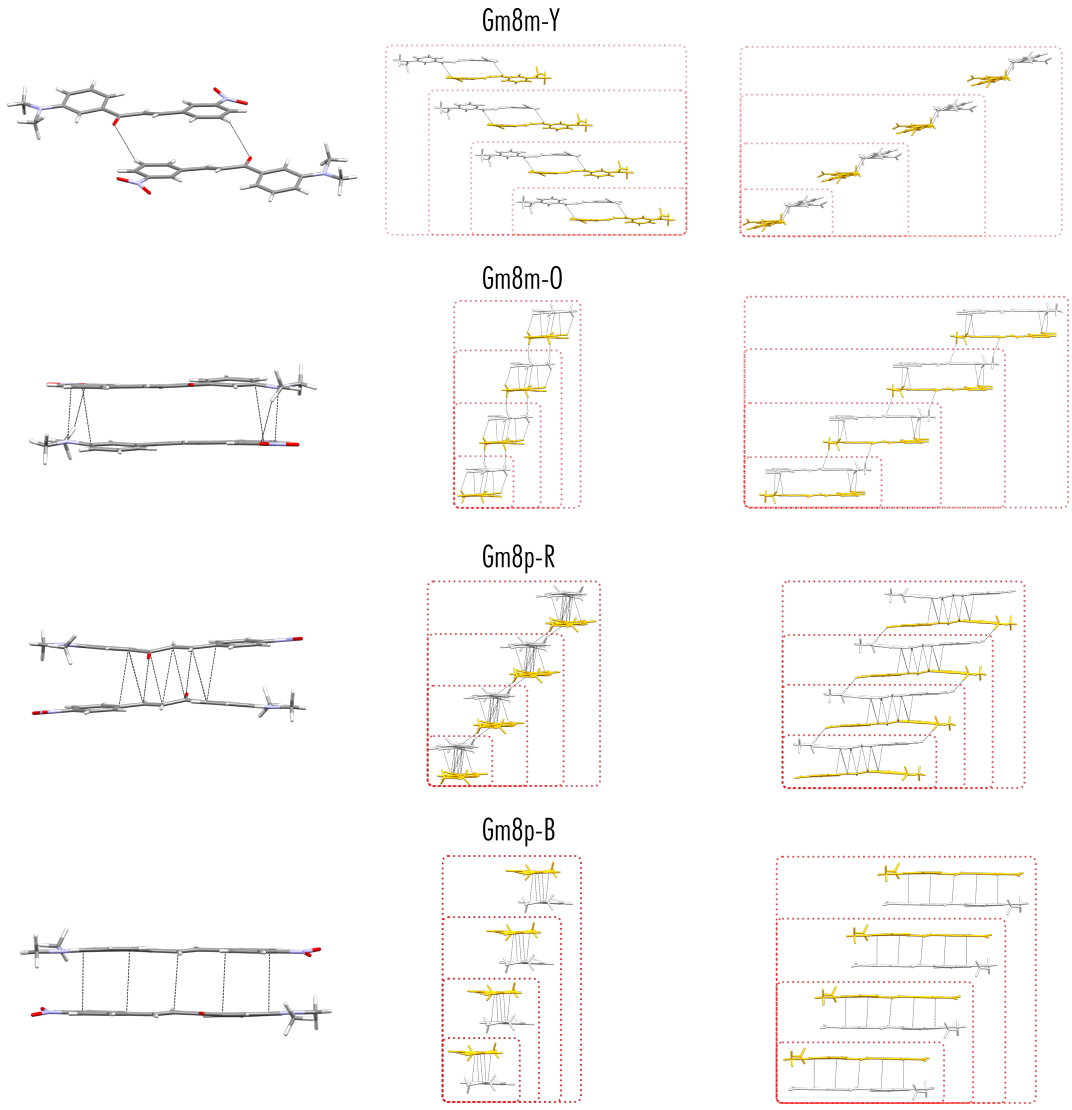

Figure 5.39: Stacks within the crystal structures of Gm8m-Y, Gm8m-O, Gm8p-R and Gm8p-B leading to spectra red-shifted by the greatest amount. The dimer motif from each stack is shown on the left. On the right, extended stacks are shown perpendicular to the short and long axes of the molecules. Molecules are coloured by symmetry operation, with white showing the asymmetric unit (or translated molecule) and yellow showing an inverted molecule.

The effect these stacking interactions have on the bandgap of each polymorph is highlighted in Table 5.12 and Table 5.13, where the transition energy of the lowest-lying transition is shown for each motif, along with the oscillator strength (OS), which is proportional to the transition dipole moment. It is clear that there is a trend towards a lower energy bandgap as the size of the stack is increased. Something not shown in these tables is that the number of transitions around these wavelengths increases as the size of the stack increases, which itself induces a red-shift in the absorption peak. Referring back to Figure 5.38, it is clear that the extended stacks cause a much larger red-shift than the 15-molecule cluster.

Table 5.12: Transition energies of the lowest energy transition and oscillator strengths of Gm8m-Y and Gm8m-O. Data is shown for the monomer and stacks of molecules up to an octamer (eight molecules).

Intermolecular Motif	Transition Energy / eV (/ nm)	Oscillator Strength
Gm8m-Y		
Monomer	3.89 (318.4)	0.0607
NO_2-Opposite dimer	3.83 (323.4)	0.0811
Tetramer	3.77 (329.1)	0.0467
Hexamer	3.77 (329.2)	0.0559
Octamer	3.76 (329.4)	0.0622
Gm8m-O		
Monomer	3.89 (318.9)	0.0769
Double 1-3 Ring Stacking Dimer	3.49 (355.4)	0.0174
Tetramer	3.39 (365.5)	0.0106
Hexamer	3.38 (367.3)	0.0090
Octamer	3.38 (367.3)	0.0121

Table 5.13: Transition energies of the lowest energy transition and oscillator strengths of Gm8p-R and Gm8p-B. Data is shown for the monomer and stacks of molecules up to an octamer (eight molecules).

Intermolecular Motif	Transition Energy / eV (/ nm)	Oscillator Strength
Gm8p-R		
Monomer	3.83 (323.8)	0.1066
Double 1-3 Ring Stacking Dimer	3.57 (349.6)	0.0400
Tetramer	3.55 (349.6)	0.0285
Hexamer	3.51 (353.6)	0.0097
Octamer	3.51 (353.7)	0.0155
Gm8p-B		
Monomer	3.78 (327.8)	0.0917
Double 1-3 Ring Stacking Dimer	3.45 (359.2)	0.0513
Tetramer	3.39 (365.6)	0.0138
Hexamer	3.38 (367.2)	0.0079
Octamer	3.38 (366.9)	0.0087

It is important to note the change in OS as the size of the stacks increases, as this will determine the contribution that each transition has to the final absorption spectra. In general, for polymorphs excluding Gm8m-Y, the OS for the lowest energy transition decreases as the size of the stack is increased. This is the case up until the octamer stack, where the OS increases for all of the polymorphs, although it is still far less than the OS seen for the transition in the monomer. In Gm8m-Y, the OS is actually larger for the octamer than for the monomer and increases as the stack is increased in size. The differences in the OS of the lowest-lying transitions may explain the differences in the fluorescent behaviour between the different polymorphs. The OS in Gm8m-Y is five times larger than that of Gm8m-O and over seven times larger than Gm8p-B when considering the octamer stacks. This difference means that the lifetime of the lowest energy state will be lower for Gm8m-Y, which will certainly increase the fluorescent yield.

Overall it is clear that the calculated absorption spectra are substantially blue-shifted when compared to the experimental absorption spectra. Although the functional used is known to blue-shift spectra, it is clear that the number of molecules used in the clusters did not result in convergence to accurate crystallographic data. Indeed, a change could be seen when increasing the extended stacks to more molecules, even up to the octamer. However, this study does allow the identification of certain structural motifs that cause particularly large red-shifts in absorption spectra. It has been shown with a high level of confidence that the change in colour of Gm8m and Gm8p polymorphs from yellow to black is a result of the increased overlap of molecules within the stacking motifs. Moreover, these trends will undoubtedly be useful when considering the design of molecules with particular optical properties, as they can be engineered with such structural motifs in mind.

5.4 Conclusion

This chapter has highlighted the experimental analysis of two sets of polymorphic chalcones, exhibiting colours ranging across the optical spectrum. Their colours aided in identifying the crystallisation of the different polymorphs, and later helped in following the thermodynamic transition between Gm8m-O and Gm8m-Y. This chapter highlights a range of techniques available to a crystallographer in determining both the structural and thermodynamic properties of organic crystals. Each crystal structure was solved using sc-XRD, allowing computational studies to be carried out. The structural properties of Gm8m and Gm8p are highlighted in Figure 5.40, where the conditions for the crystallisation parameters used for structural determination are shown.

The experiments carried out demonstrate the structural complexity that can arise even in simple organic systems. The results in the chapter highlight chalcone molecules as a useful backbone for the systematic study of properties stemming from the structure of materials. From a study based on systematically realising the differences between current theory and experimental data, it is clear that there is still a way to go before the accurate prediction of material properties such as colour can be achieved. However, the use of functionalised chalcones has allowed the observation of clear trends in

structural, thermodynamic and spectroscopic properties, which has set the foundation for a much broader systematic study in the future.

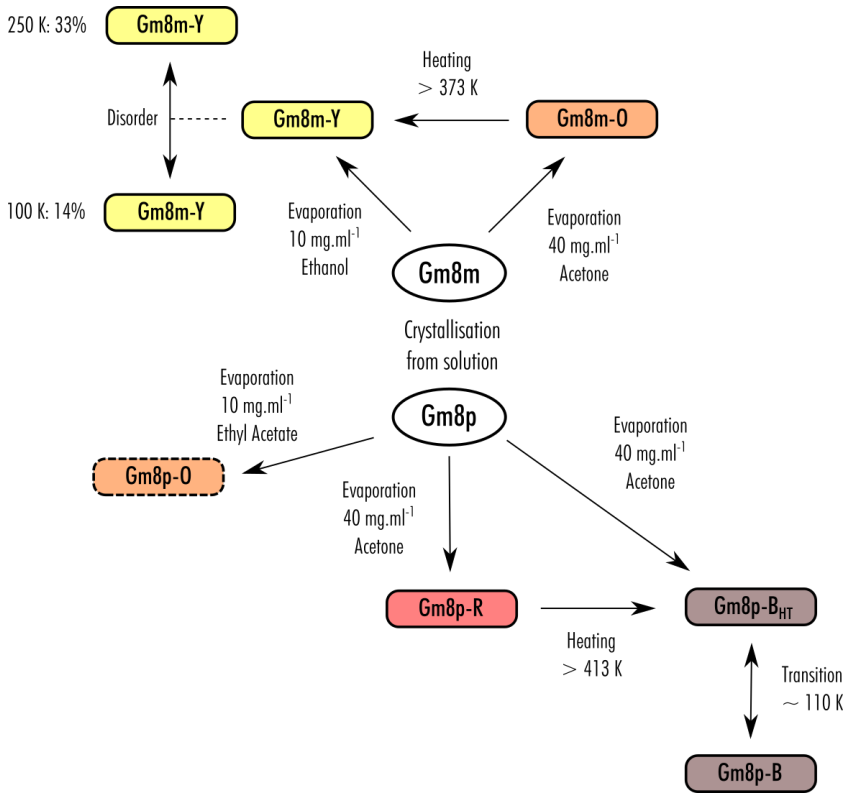

Figure 5.40: Experimental solid form landscape of Gm8m and Gm8p, summarising the forms discovered by solvent screen and inter-conversion revealed through DSC and low-temperature pXRD.

CHAPTER 6

CONCLUSIONS

6.1 Summary and Outlook

Throughout this work, the crystallisation of pharmaceutically relevant compounds has been carried out to elucidate novel routes of crystallisation, the rationale behind the tracking of such crystallisation pathways, and the factors affecting the properties of the final crystalline products. The project was generally split into two parts, although the intricacies present in crystallographic studies meant that there are many possible divergences from the main topics, with much promise for future work.

The first two chapters of this thesis highlight the development of volatile deep eutectic solvents (VODESs) as a novel crystallisation medium for the control of crystalline structure and properties. As a result of this crystallographic medium, polymorphic control of paracetamol was incontrovertibly obtained, with the metastable form II crystal structure forming from VODESs where the molar ratio was above 6:1 phenol:paracetamol. Time-lapse imaging of the formation of paracetamol crystals from VODES showed that the formation of form II paracetamol occurred at a far later time than that of form I, accentuating the idea that the internal structure of the VODES changes as the molar ratio of the internal constituents is changed. In turn, it was hypothesised that the internal structure of VODESs leads to the formation of metastable crystalline phases, which act as intermediaries to the formation of hard-to-reach and novel crystal structures. Direct and indirect observation of these metastable phases in several systems strengthened this hypothesis, including the crystal structure of a 2-ethoxybenzamide phenol co-crystal.

Studies of crystallisation from VODES solutions were performed with a variety of pharmaceutically active molecules, each with differing functional groups and flexibility. Evaluation of benzamide solutions afforded the first crystallisation of the metastable form III structure from a binary system. Supplementary work highlighted morphological control of crystallites in the metacetamol system, without affecting the structure of the resultant crystal. Furthermore, it was shown that the VODES

system containing metaxalone allowed enantiomeric control over the crystal structure. Studies on VODES systems of 2-methoxybenzamide, verapamil and estradiol did not result in any direct crystallographic control, but did highlight the widespread applicability of VODESs as a crystallographic medium.

The second experimental chapter delved more thoroughly into the crystallographic pathway leading to a final crystalline form from the VODES medium. This analysis was carried out by monitoring the thermodynamic landscapes of VODESs via differential scanning calorimetry. This initial work highlighted an important subtlety about the thermodynamics of eutectic systems: upon crystallisation of a eutectic system, multiple phases may form, including structural polymorphs, co-crystals and amorphous phases. Co-crystalline phases require exact ratios of constituent components so that translational symmetry can form throughout the structure. In contrast, the liquid state is far more malleable in the composition it can possess. Indeed, the difference in energy between the possible crystalline states and the eutectic liquid is the driving force causing the melting point suppression of molecular mixtures. During the thermal cycling of VODESs, the formation of a hierarchy of crystal structures of varying stability was seen. Moreover, glass transitions were seen in most systems, indicating that some of the eutectic liquid was not crystallising.

To further investigate the hierarchy of crystal structures formed from VODESs, concomitant synchrotron powder X-ray diffraction and differential scanning calorimetry (CXRD-DSC) were used, utilising the I12 beamline at the Diamond synchrotron. This combination of experimental techniques allowed for the correlation of thermodynamic and structural changes in VODESs during thermal cycling. From these experiments, unknown crystalline phases were found in VODESs containing 2-ethoxybenzamide, metacetamol and benzamide. Supplementary experiments following the detection of these phases also highlighted that additional phases could be produced by re-cooling the remaining glassy component after the crystallisation of the first unknown phase. Structurally, it is clear that there is still a lot to learn about the formation of these systems, the understanding of which can only aid in utilising them to their full extent. For the VODESs, CXRD-DSC studies added significant weight to the hypothesis that metastable crystalline phases impact the crystallisation phenomena observed. However, on a larger scale, these experiments elucidate the inherent complex structure of deep eutectic systems that is still not well understood. The formation of co-crystals bears a striking resemblance to the formation of alloys in the eutectic systems of metals, which may lead to a convergence of these systems that involve seemingly-divergent length scales. The structural understanding of the crystallisation of deep eutectic solvents is undeniably an understudied area; however, the evolution of CXRD-DSC can now be used as an invaluable tool to revolutionise our knowledge of this area.

The second section of the project was dedicated to the study of functionalised chalcones as materials to readily analyse the crystal engineering of small, flexible, pharmaceutically-relevant molecules. The third experimental chapter focused on two particular chalcones, functionalised with dimethylamino and nitro groups. These chalcones both exhibited crystal polymorphism, form-

ing structures that exhibited colours ranging across the optical spectrum. These structures were thoroughly analysed in terms of their structural, optical and thermodynamic properties to allow a detailed comparison of properties with those predicted from modern theoretical calculations. In particular, the optical properties of the chalcones were evaluated using quantum chemical calculations using a novel technique, which involved cutting clusters of molecules from each of the experimental crystal structures. The technique highlighted relative shifts in the bandgaps of each of the crystal structures, clearly outlining the bonding motifs leading to the largest red-shifts in the optical spectra. Knowledge of these optically-active bonding motifs affords a clear foundation that can be utilised during the process of crystal engineering. Moreover, the use of functionalised chalcones allows for thorough systematic studies of the effect of intermolecular interactions on both the crystal structure of molecules and their subsequent properties, bringing into line our current theoretical and experimental knowledge.

The field of organic crystal engineering is still at an exciting point in its expansion. Although far more is now known about the field since the invention of X-ray crystallography and subsequent structural solution techniques, it is still the case that absolute property-driven crystal design is far from reality. Experimentally, crystallographers rely on a toolbox of generally well-established techniques to examine as much of the crystal landscape of a molecule as possible, and subsequently measure the crystal properties of each polymorph produced. The use of such a variety of tools is now commonplace in industries, including pharmaceutical and agrochemical crystal design, with more advanced methods and precise equipment constantly appearing. It is hoped that the crystallographic tools and systematic studies laid out in this thesis will sit as part of the foundation and growth for the vast amount of crystallographic knowledge that is still left to be uncovered, and in turn, aid in the ultimate goal of the precision control of crystal growth and design.

APPENDIX A

AN EXPERIMENTAL AND COMPUTATIONAL STUDY INTO THE CRYSTALLISATION PROPENSITY OF SECOND-GENERATION SULFLOWER

The publication based on this work was first-authored by Dr T Jensen. The complementary computational work that I carried out for this study is highlighted below. The work is published in [4].

A.1 Context

Second-generation sulflower (SGS) is a planar heterocyclic circulene, consisting solely of carbon and sulfur atoms. It is the second in the series of perfulfurated circulenes, making it the analogue of the polyaromatic hydrocarbon coronene (Figure A.1). Curiously, it was found that there was no simple route to producing SGS in the crystalline state; powder X-ray diffraction and 3D electron diffraction always showed an amorphous phase after attempted crystallisation of SGS. This case is very different from that of both coronene and sulflower, which are both known to be polymorphic.[71,232]

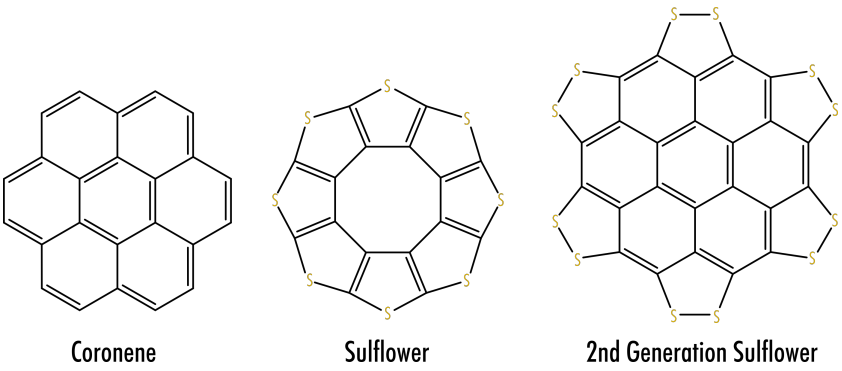

Figure A.1: Molecular scheme for coronene, sulflower and second-generation sulflower.

A.2 Molecular Optimisations

In an attempt to decipher the reasoning behind the non-crystallinity of SGS, molecular optimisations were carried out to pin-point differences in bonding motifs with respect to coronene. The functional/basis-set combination B3LYP/6-31G(d,p) was used to calculate the electron distribution of each molecule. Repeat molecular optimisations were carried out in ORIENT for clusters up to a size of 10 molecules, which were initialised using random positions and orientations of molecules on a sphere. After 100 repeat calculations, the final state of each cluster was categorised to allow trends in intermolecular interactions to be observed. For two and three-molecule clusters, the molecules optimised to a small number of final states. The optimised configurations for two molecules of coronene and SGS are summarised in Figure A.2. Highlighted in the figure are the energy of each configuration (shown with respect to the lowest energy configuration per cluster size and molecule), the offset perpendicular to the molecular stacking direction (o), the distance between molecules in the stacking direction (d), and the twist about the molecular centre of mass parallel to the stacking direction (ϕ). In each case, there are two different possible conformations that involve the face-face π-stacking of the molecules. In one of the optimised conformations, the molecule is offset a small amount perpendicular to the stacking direction with no rotation. In contrast, there is no offset in the other case, but the molecule is rotated by an angle ϕ. Analysis of the energy of each conformation shows stark differences. In coronene, both optimised conformations have very comparable energies ($<k_BT = 2.479$ kJ.mol^{-1} at room temperature), whereas the zero-offset stack has a much lower energy in SGS (7.7 kJ.mol^{-1}).

When the size of the cluster is increased to three molecules, there is an increased number of possible configurations for SGS; however, coronene is only seen in two configurations (Figure A.3). The introduction of the third molecule allows for both face-face and edge-face interactions. However, the face-face interaction is more favourable. Nevertheless, it can be seen that the difference in energy between the face-face and edge-face conformations is far greater for SGS than for coronene. In terms of the relative energies of the different face-face interactions, it appears that the zero-offset stack is not energetically viable in coronene as the number of molecules increases, whereas several SGS configurations are seen incorporating both the zero-offset and offset conformations. As the number of molecules in the cluster is increased, a similar trend is seen, with the zero-offset face-face stack becoming more energetically dominant with more molecules. In essence, this alone allows a hypothesis as to why a crystalline structure of SGS is not observed. If the extended face-face stacking motifs are too energetically dominant, it may be the case that the formation of a 3-dimensional structure of SGS is energetically inviable, meaning a reasonable crystalline state is difficult to nucleate. Additional crystal structure prediction and electrostatic potential analyses support this hypothesis,[4] highlighting that the 1-dimensional face-face stacks are far more energetically favourable than a 3-dimensional structure. Interestingly, there are also two small features in the X-ray diffraction of a powder of sulflower at 8.31 ° and 25.55 °, representing symmetry over 5.3 Å and 1.8 Å respectively, which may indicate the presence of stacks of molecules with internal symmetry.

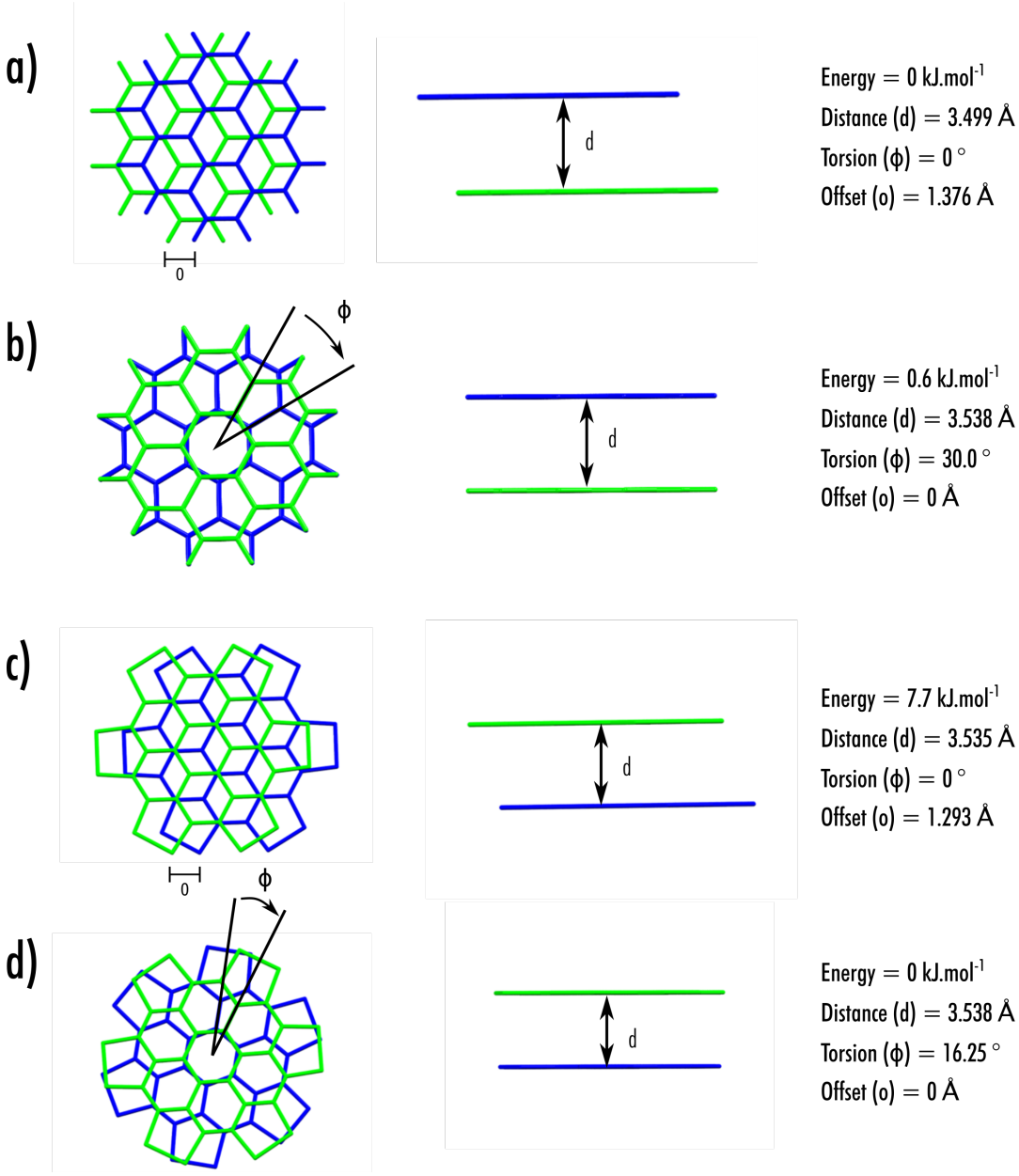

Figure A.2: Conformations of coronene and sulflower molecules after the optimisation of two molecules using the program ORIENT. Views parallel and perpendicular to the stacking direction are shown. Molecules are coloured to allow them to be easily distinguishable. a) and b) highlight the conformations of coronene, and c) and d) those of SGS. Energies are shown with respect with the lowest energy configuration per molecule.

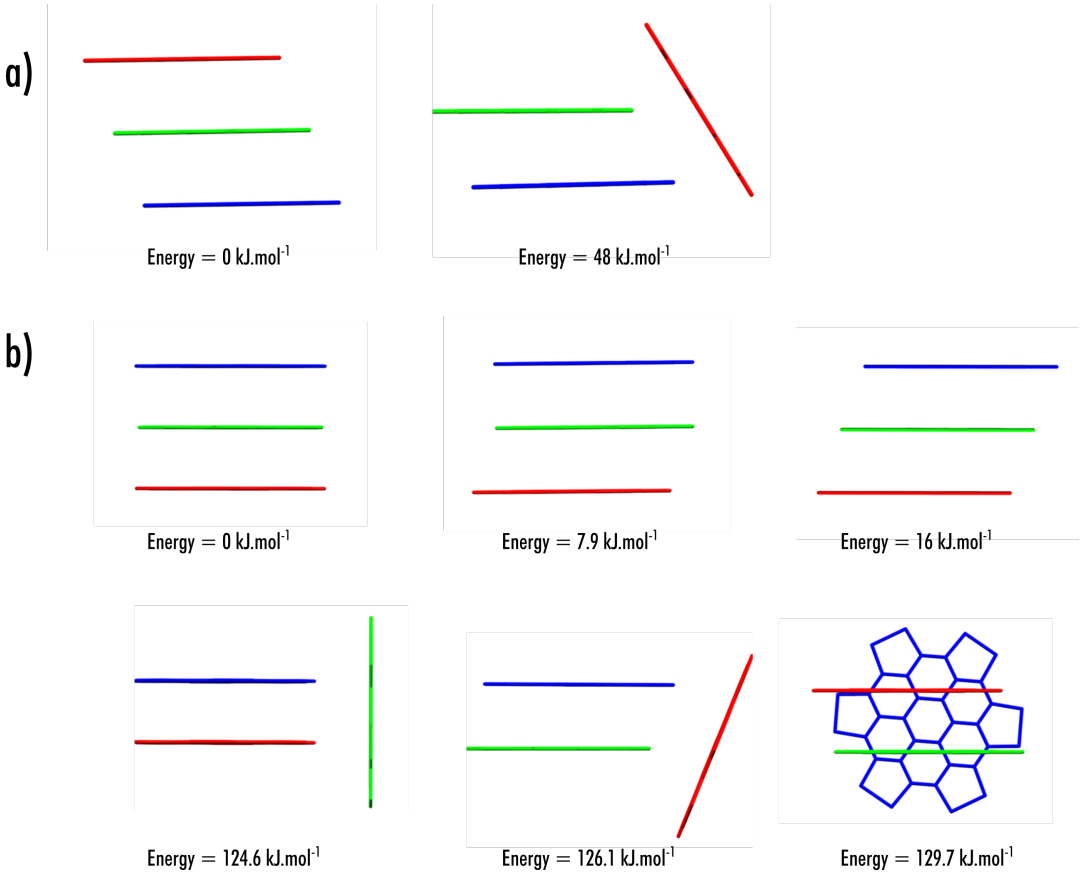

Figure A.3: Conformations of coronene and sulflower molecules after the optimisation of three molecules using the program ORIENT. Molecules are coloured to allow them to be easily distinguished. a) Shows optimisations of coronene molecules and b) of SGS. Energies are shown with respect to the lowest energy configuration per molecule.

APPENDIX B

DESIGN OF A COPPER CRYSTALLISATION COOLING RIG

B.1 Cooling Rig

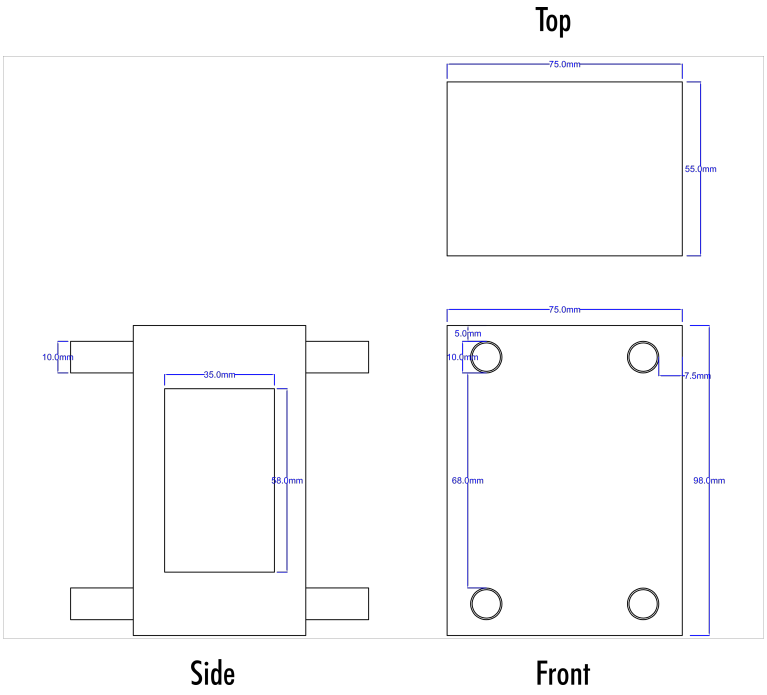

Figure B.1: Design for the cooper housing of the cooling rig. The circular elements are pipes that allow cooling fluid through.

B.2 Cooling Rig Inset

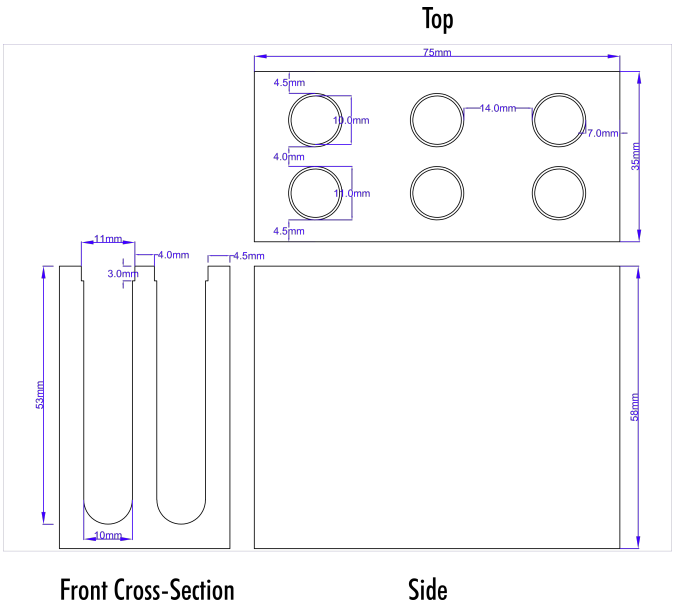

Figure B.2: Design for the copper inset of the cooling rig, which can hold up to six samples.

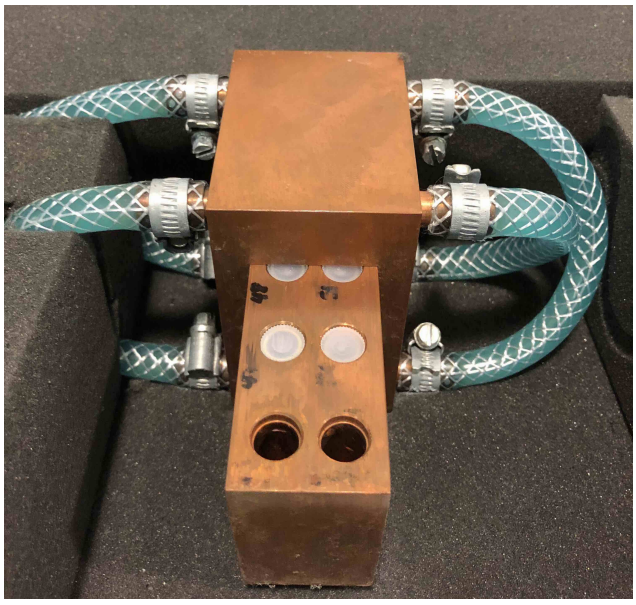

Figure B.3: An image of the cooper cooling rig, which sits in a polystyrene case to minimise heat conduction. The back four sample spaces are shown containing samples.

APPENDIX C

SCRIPTS FOR ORIENT OPTIMISATIONS

C.1 ORIENT Input File

```
ALLOCATE
  SITES 1000
  VARIABLES 4000
  MOLECULES 7
END

VARIABLES
x1    0.0000  Angstrom
y1    0.0000  Angstrom
z1    0.0000  Angstrom
x2    20.0000  Angstrom
y2    0.0000 Angstrom
z2    0.0000  Angstrom
END

TYPES
  H  Z  1
  Hn Z  1
  C  Z  6
  N  Z  7
  O  Z  8
END
```

```
UNITS Angstrom
MOLECULE Paracetamol AT x1 y1 z1

O -3.780346304 3.05446869 1.611640751 Rank 4 Type O
-0.386659624
-0.132523628 0.193608709 0.649400202
-0.277648253 -1.24635215 0.336105164 -0.077755768 -0.335317637
-0.484237294 0.210927329 0.296965209 -0.441004979 -0.101360654
1.045918758 0.263280949
0.922511194 -0.264664966 0.469173648 -0.520067241 -0.347763026
1.023695245 0.694101309 -0.174336464 -0.532753001

N 0.468699294 4.12703868 -1.839358273 Rank 4 Type N
-0.134144826
0.008698428 0.03318198 0.030302028
-0.70975778 -1.272094691 0.038145192 -0.45555778 -0.070415711
0.307035525 -0.274770944 -0.714474172 0.464258989 0.237818874
-0.723655344 -1.122651069
1.13739089 -1.369119022 0.72937012 -0.823286243 -0.348234002
-0.397358302 -0.139054484 0.700133529 -0.716716094

Further multipoles omitted due to space.

END

MOLECULE Phenol AT x2 y2 z2

Multipoles omitted due to space.

END

UNITS ANGSTROM eV
PAIRS
  Unit 1.0
  C  C  alpha  rho  C6
    00  00  0   3.6    2.29199    25.2867
  End
```

```
  Extra pairwise interactions omitted due to space.
END

UNITS kj/mol Angstrom

TIME

ENERGY

TIME

OPTIMIZE
  TITLE "Optimisation of Paracetamol-Phenol"
  FIX
   Paracetamol POSITION ORIENTATION
  END
  EVF VERBOSE
!  BFGS
  STEP 0.10 Angstrom
  SHOW steps
!  SHOW ENERGY VARIABLES
  ITERATIONS 500
!  CONVERGENCE 0.003
  PLOT XYZ FILE Paracetamol_FormII_HBRing.xyz
END

SHOW VARIABLES

FINISH
```

C.2 Perl Script

```
use strict;
use warnings;
use Math::Complex;
use Math::Trig;
use Cwd qw();
use File::Copy qw(copy);
```

```
sub main {

my $file = "input";

open(FILE, "<$file") or die "Can't open $file: $!\n";
my @lines = <FILE>;
close FILE;
my $currentRun = 1;

my $numberOfRuns = 10000;

while(1){
my $random_numberU = rand(2)-1;
my $random_numberV = rand(2)*pi;

my $distance = 40.0;

my $x = sqrt(1-$random_numberU**2)*cos($random_numberV)*$distance;
my $y = sqrt(1-$random_numberU**2)*sin($random_numberV)*$distance;
my $z = $random_numberU*$distance;


my $directory = "Phenol-Paracetamol"."$currentRun";

unless(-e $directory or mkdir $directory) {
die "Unable to create $directory\n";
}

my $path = Cwd::abs_path()."/".$directory."/input";

$lines[10] = "x2    ".$x."  Angstrom\n";
$lines[11] = "y2    ".$y."  Angstrom\n";
$lines[12] = "z2    ".$z."  Angstrom\n";

open(OUTFILE, '>>'.$path) or die "Couldn't open: $!";
print OUTFILE @lines;
close OUTFILE;
```

```
        copy Cwd::abs_path()."/run", Cwd::abs_path()."/".$directory."/run";
        chdir $directory;
        system("qsub run" );
        chdir "../";

$currentRun = $currentRun + 1;

if ($currentRun%50 == 0) {

sleep(300);

}

if ($currentRun == $numberOfRuns) {
last;
}
}
}

main();
```

APPENDIX D

THE CRYSTAL STRUCTURE OF ORTHOCETAMOL SOLVED BY 3D ELECTRON DIFFRACTION

The publication based on this work was first-authored by Dr I Andrusenko. The complementary computational work that I carried out for this study is highlighted below. The work is published in [5].

D.1 Context

Orthcetamol (2-acetamidophenol) is a structural isomer of paracetamol that has escaped crystallographic structural solution since it was first synthesised in 1876.[233] Its propensity to grow in a polycrystalline manner meant that structural solution was unobtainable through single-crystal X-ray diffraction. To rectify this gap in the structural knowledge of the cetamol family, 3D electron diffraction was utilised to solve the ubiquitous crystal structure of othocetamol. This successful experimental procedure stands as the first ab initio structural solution of an organic molecule without using single-crystal X-ray diffraction to confirm the final structure.

D.2 Computational Space Group Analysis

Although accurate molecular positions can be successfully obtained via 3D electron diffraction, it is often difficult to determine the exact space group due to secondary electron scattering. Due to the higher cross-section for electron scattering than X-ray scattering, it is possible to get finite intensities at points in reciprocal space were a systematic absence would be expected. During the final refinement of the orthocetamol structure, there was a choice of space group, either the centrosymmetric $C2/c$ or the non-centrosymmetric Cc. To analyse the differences in these structures, optimisations were carried out using fixed unit cells and restraints based on the individual space

groups in CRYSTAL14. Calculations were carried out using the function/basis-set combination PBE0/6-31G. The results of the optimisations are highlighted in Figure D.1, which shows that both optimisations resulted in the molecular coordinates of the centrosymmetric space group $C2/c$. Thus, this symmetry reduction was used to re-refine the original 3D electron diffraction data.

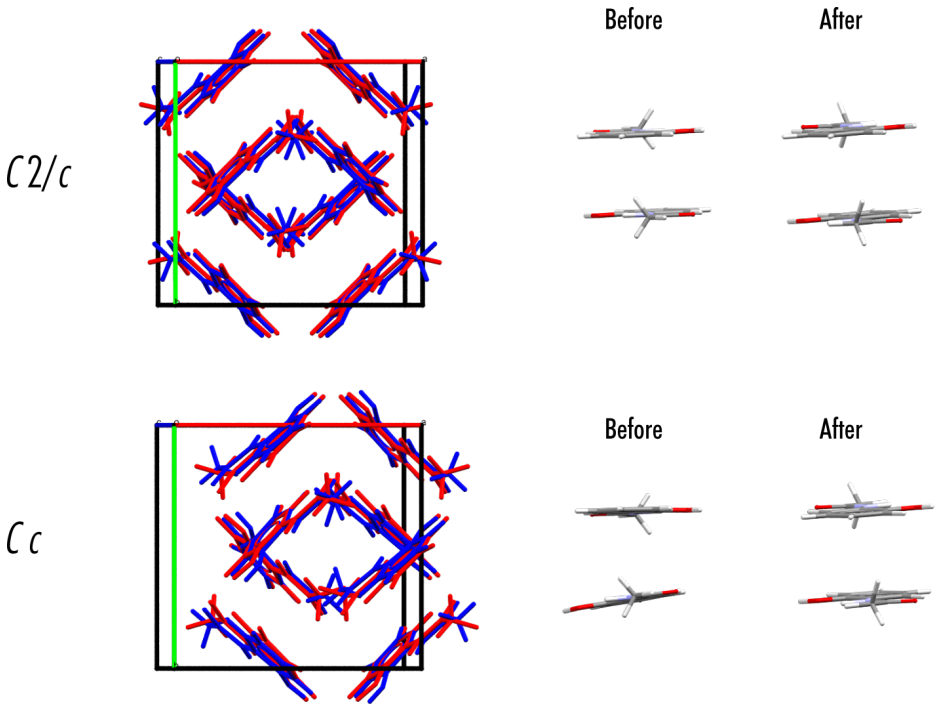

Figure D.1: The unit cell of orthocetamol before (blue) and after (red) structural optimisations in CRYSTAL14 restrained by the space groups $C2/c$ and Cc. The right-hand side shows the 2 molecules in the asymmetric unit of the Cc structure before and after optimisations. In the $C2/c$ structure, these molecules are related via an inversion symmetry.

APPENDIX E

PHASE DIAGRAMS OF VOLATILE DEEP EUTECTIC SOLVENTS

The data presented in this section are part of the second round of experiments run on the volatile deep eutectic solvents at Diamond Light Source, using concomitant powder X-ray diffraction and Differential Scanning Calorimetry. I would like to thank Dr Asma Buanz and Dr Oxana Magdysyuk for carrying out the synchrotron experiments.

E.1 Context

The data shown in chapter 4 highlights the complexities that can arise during the thermal cycling of binary systems. The use of concomitant synchrotron X-ray diffraction and differential scanning calorimetry (CXRD-DSC) allowed direct detection of the crystallographic ordering during these cycles, allowing an experimental interpretation of the eutectic phase diagram. Such an interpretation of the structure of deep eutectic mixtures is an important step in creating a model to predict and understand their formation, kinetics and thermodynamics.

As a large set of complementary information is needed to form a phase diagram, this section is written in the style of a tutorial, explaining how the data was interpreted at each step. The formation of the phase diagram used data collected by a TA Instruments Discovery DSC25, and structural information was gleaned using the CXRD-DSC data. Due to the ease of forming a eutectic with phenol, an amino-substituted analogue of paracetamol was used. 2'-aminoacetanilide (2AM - Figure E.1) produced a VODES with phenol over the range 1:1 - 10:1 VC:NVC, which formed almost spontaneously on contact. During the exploration of VODES containing paracetamol analogues, the crystal structures of the pure phases of 2AM and 3'-aminoacetanilide (3AM) were solved for the first time.[234,235] Interestingly, the structures contained sterically hindered hydrogen bonding between the amino and carbonyl functional groups (Figure E.2, similarly to the OH...O=C hydrogen bonds seen in metacetamol and paracetamol. Indeed, analysis of the melting points of the pure phases of 2AM

and 3AM via DSC showed melting points of 131.74 °C and 86.50 ° C, lower than the hydroxy cetamols. 3AM formed VODES down to a ratio of 1:1 VC:NVC; however, it was not used due to glass transitions occurring at a temperature too low to be seen on the discovery 25 DSC.

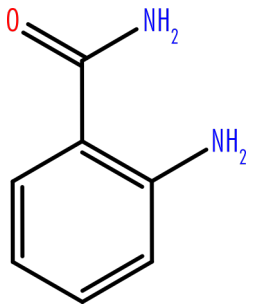

Figure E.1: Chemical scheme of 2'-aminoacetanilide.

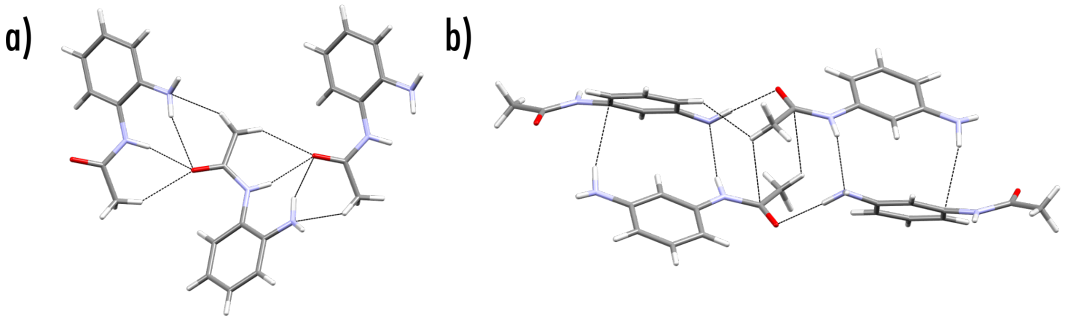

Figure E.2: Hydrogen-bonding interactions present in the crystal structures of 2'-aminoacetanilide and 3'-aminoacetanilide.

E.2 Phase Diagrams of phenol:2'-aminoacetanilide Volatile Deep Eutectic Solvent

The phase behaviour of VODESs consisting of various ratios of phenol and 2AM were assessed via differential scanning calorimetry (DSC). The variable considered was the relative molar concentration of 2AM with x = 0 denoting 100% phenol and x = 1 denoting 0% phenol. Samples were prepared by weighing and mixing both phenol and 2AM on a 4-point balance and allowing them to become a liquid at room temperature. Once a homogeneous liquid appeared, a drop of the sample was transferred to a hermetic DSC pan, weighed and sealed. Moderate heat (60 °C) was used to speed the process of eutectic formation in cases where mixing was slow. If no liquid occurred below room temperature, the sample was directly weighed into the DSC pan. In general, a standard heat-cool-heat run was used to assess phase transitions, between the temperatures of 70 °C and -70 °C. If no melt occurred by 70°C, then the sample was further heated up to the temperature of the melting

point of the 2AM. Throughout the experiments, at least three different types of transition were seen: crystallisation, melting and glass transition. For systems where x < x_e (the eutectic point), a crystallisation transition was most often seen upon cooling of the liquid. At low temperatures, a glass transition may then occur for any remaining liquid. On heating, a broad endotherm is seen, which is taken as the melt of the eutectic mixture and used to determine the point at which the system becomes liquid. An example of such a thermogram is shown in Figure E.3.

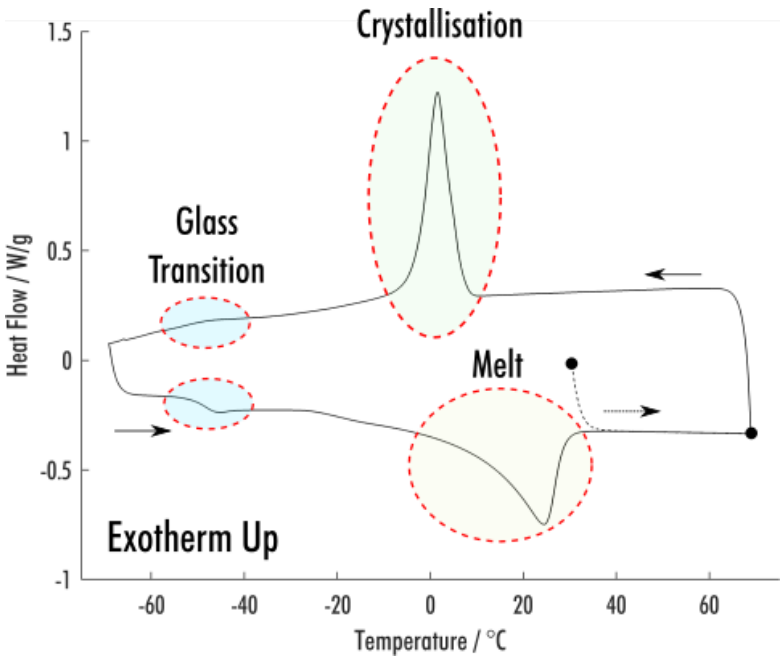

Figure E.3: Thermogram of a 7:1 phenol:2AM mixture highlighting a crystallisation, glass transition and melt. The start and end of the run are highlighted by black dots, while a dashed line indicates the initial heating ramp.

Initially, samples of the pure components were acquired for the melting points at x = 0 and x = 1. Polymorph screening was carried out for 2AM using a variety of solvents to check for any effect this may have on the melting point of the sample. From this preliminary screen, only one crystal structure was found, which also formed from the melt. Figure E.4 shows the thermograms of pure phenol (T_m = 40 °C) and 2AM (T_m = 135 °C).

In cases where x is close to x_e often a cold-crystallisation occurs, where an endotherm is seen on heating (Figure E.5). This is likely due to the increased viscosity of the system slowing down the nucleation rate of the crystallisation components. Three separate cases can occur: two endotherms are seen on heating; two endotherms are seen, one on cooling and one on heating; one endotherm is seen on heating. This may suggest that two separate components are crystallising out, one whose nucleation is hindered more by the viscosity of the system than the other. However, structural analysis would be needed to prove this.

In some cases, the cold-crystallisation of the sample overlaps with the subsequent melt, making

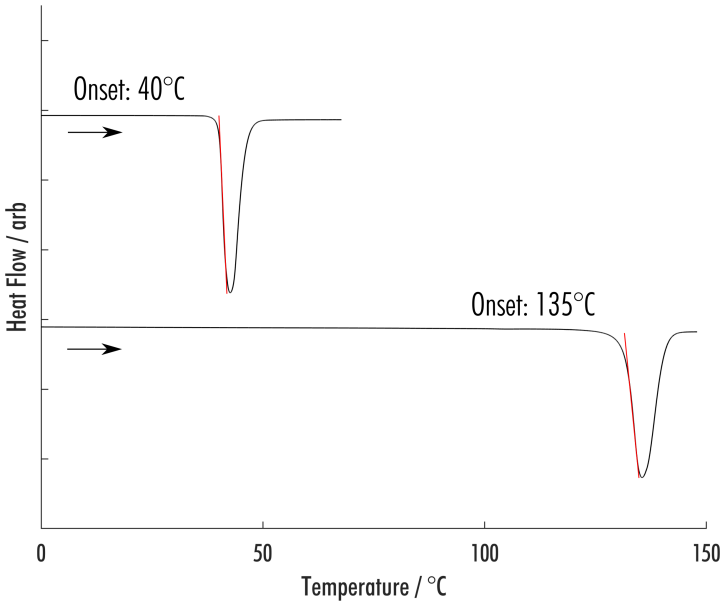

Figure E.4: Thermographs of pure phenol and 2AM highlighting the onset of the melting phase transition. Arrows indicate the direction of heating, with exothermic shown as a positive divergence from the baseline.

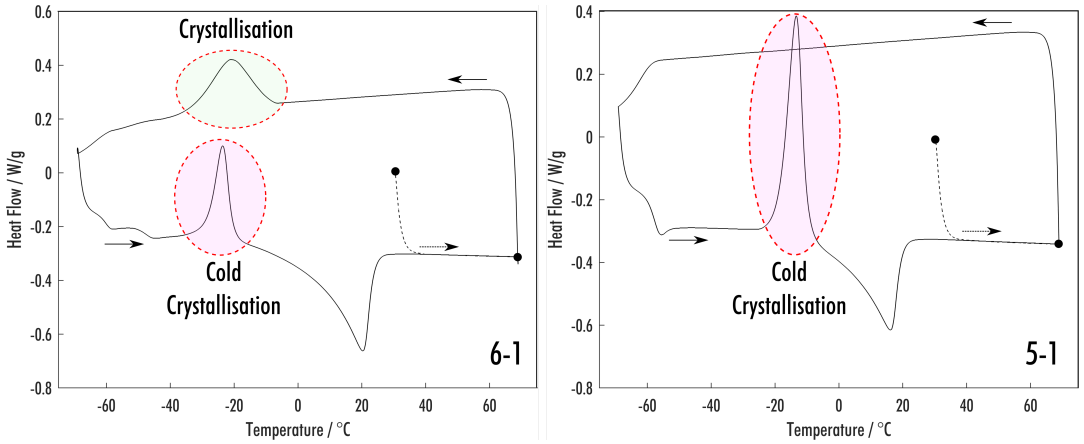

Figure E.5: Thermograms of 5:1 and 6:1 phenol:2AM mixtures, highlighting the two different cases of cold-crystallisation. The start and end of the run are highlighted by black dots, while a dashed line indicates the initial heating ramp. Arrows highlight the direction of the heat cycle. Exothermic events are shown as a positive divergence from the baseline.

it more difficult to isolate the exact melting point of the system. When this happens, the DSC method is changed to hold the temperature (isotherm) at the peak of the cold-crystallisation, cool back down to -70°C and then heat past the melting point (Figure E.6a). If the endotherm is removed on the second pass, it can be assumed that the system has fully crystallised. Interestingly, the glass transition often changes upon crystallisation and re-cooling, indicating a change in the composition of the amorphous component. Holding the isotherm for a variety of temperatures indicates how long is needed for the system to fully crystallise (Figure E.6b), for the phenol:2AM 5:1 system, there are only minimal changes for isotherms longer than 60 minutes.

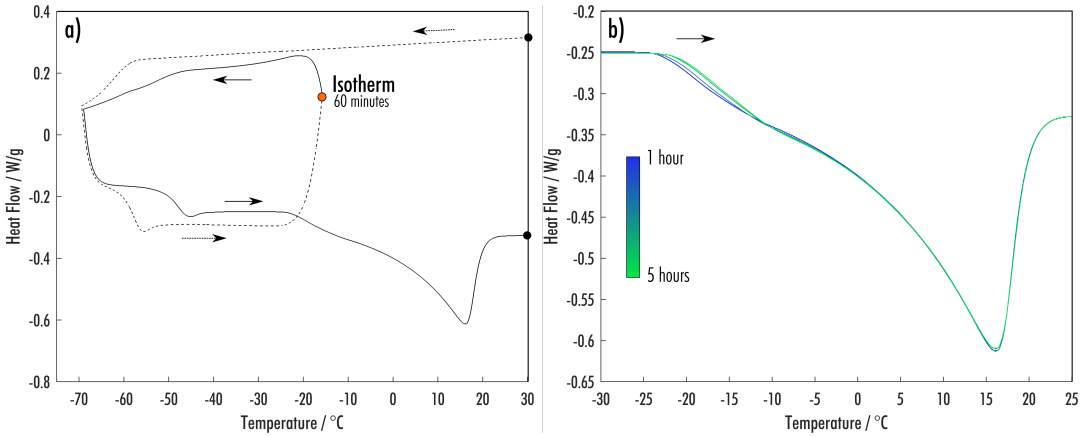

Figure E.6: a) Thermogram of a 5:1 phenol:2AM mixture highlighting the removal of the cold-crystallisation endotherm by re-cooling the system after crystallisation. The orange dot indicates that the system was held at a constant temperature (isotherm) for 60 minutes. Dashed lines indicate the initial ramps. b) Overlaid thermograms of 5:1 phenol:2AM VODES heated after an initial thermal cycle with an isothermal hold at -17 °C for times between 1 hour and 5 hours. Arrows highlight the direction of the heat cycle. Exothermic events are shown as a positive divergence from the baseline.

Above x_e is a range of concentrations where the only phase change seen is a glass transition (Figure E.7a). It is likely that either the viscosity of the system is high in this region, leading to kinetic frustration, or there is a ratio of VODES where it is not thermodynamically (or kinetically) favourable for a crystal for form. At larger volumes, it is commonly seen that one of the components crystalises out; however, this may be because or local fluctuations or nucleation sites on a larger scale. For these concentrations, we define the phase as a low-temperature transition mixture (LTTM) to differentiate it from the eutectic mixtures where a clear melting point (of a crystalline phase) is defined. To ensure that crystallisation cannot be reasonably obtained from these mixtures, thermograms were also obtained at a ramp rate of 1 °C.min^{-1}. In cases where the mixture was not liquid before placing in in the DSC pan, samples were initially run up to the melting point of the non-phenol component to ensure that the whole mixture was in the liquid state.

An interesting feature of the glass transitions exhibited by these phases and the cold-crystallisation phases is the appearance of a relaxation enthalpy on heating from below the glass transition. This

enthalpy represents a local ordering of a glass phase to a more stable configuration while the mixture is in an amorphous state. A larger relaxation can take place if the sample is held for a longer period under the glass transition temperature (Figure E.7b), meaning a larger relaxation enthalpy is seen on heating (Figure E.7d). The rate of enthalpy change gives information about the mobility of the sample in the glassy state and the accessibility of an ordered configuration. The glass transitions shown are defined by a midpoint (the temperature at half the glass transition height) and width (glass temperature end – glass temperature onset). The enthalpy relaxation is calculated using the baseline after the transition has taken place, as shown in Figure E.7c.

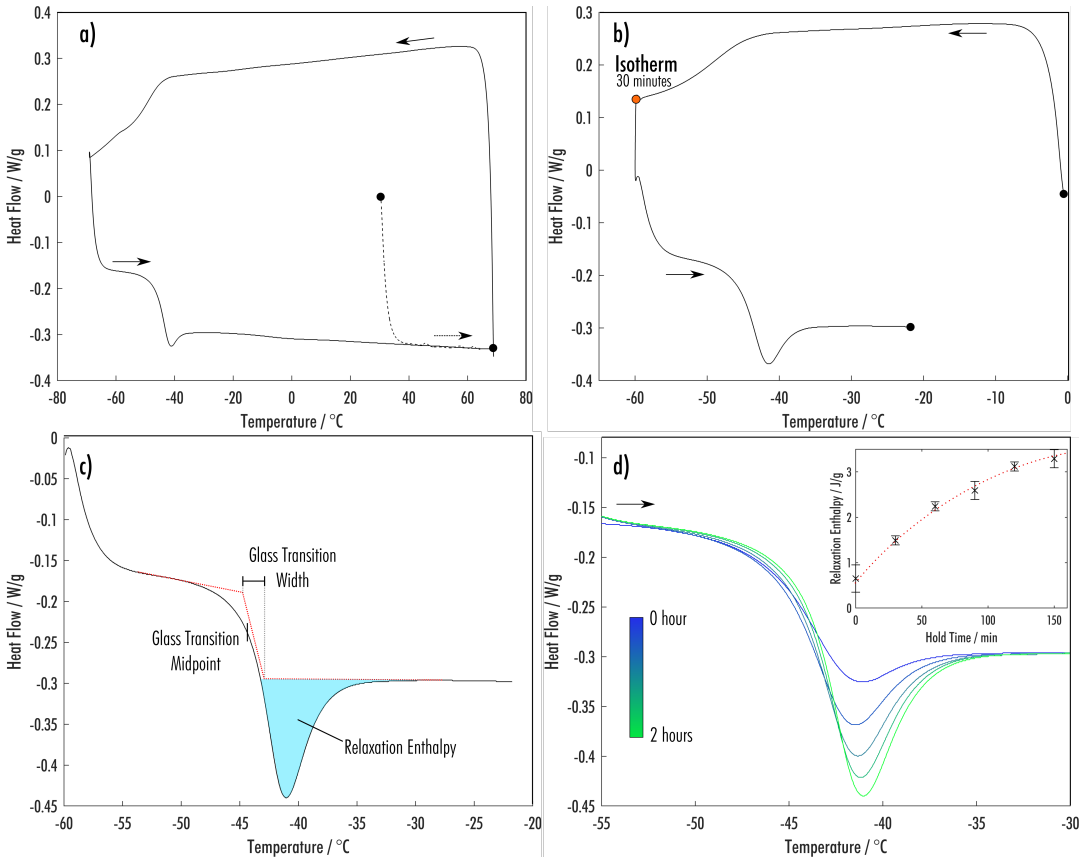

Figure E.7: Glass transitions of low-temperature transition mixtures. a) Thermogram of phenol:2AM 2:1 mixture. b) Thermogram of phenol:2AM 2:1 mixture with a 30-minute isotherm below the glass transition temperature. c) Glass transition on heating annotated with the parameters used to describe the transition. d) Glass transitions of phenol:2AM 2:1 upon heating for isotherms from 0 – 2 hours. Arrows indicate the direction of heating, with exothermic transitions shown as a positive divergence from the baseline.

At concentrations above the LTTM phase there is another region of cold-crystallisation mixtures. In this region the melting point of the VODES is often above room temperature and therefore the samples need to be weighed into the hermetic pan and heated above the temperature of 2AM. The acquisition of phase changes can be carried out in the same way as for cold-crystallisation systems

under the LTTM concentrations. On the first heating an endotherm will be seen for the initial melting of the system, however as the system will not be homogenous this melting point should not be used (Figure E.8).

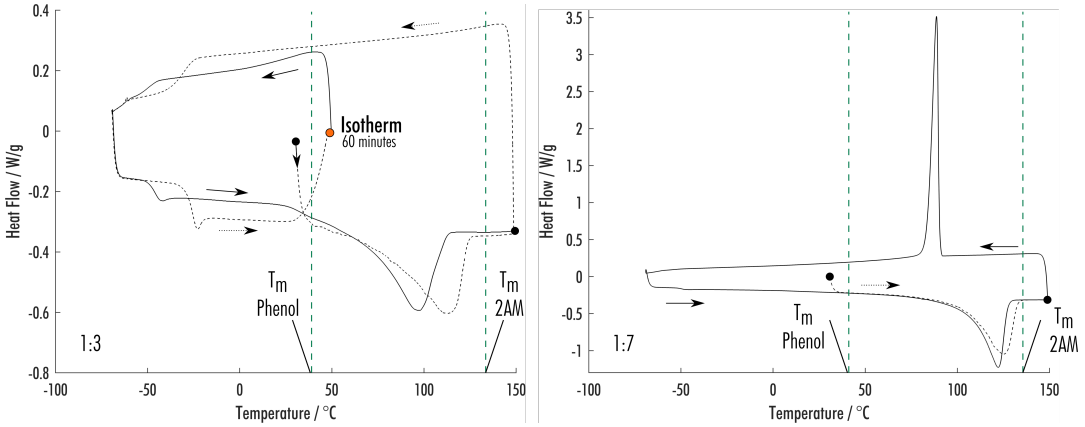

Figure E.8: a) Thermogram of Phenol:2AM 1:3 mixture showing an isotherm at the cold-crystallisation point, followed by a melt between the melting point of pure phenol and 2AM. b) Thermogram of Phenol:2AM 1:7 mixture showing a crystallisation on cooling from the melt and a single exotherm on heating. Arrows indicate the direction of heating, with exothermic shown as a positive divergence from the baseline.

Given the descriptions above, phase transitions of mixtures of 2AM and phenol at all mole fractions can be assessed. It is common to present such data as a phase diagram so that it is possible to assess what phase the mixture will be present in, given a particular temperature and concentration. Figure E.9 shows the phase diagram for mixtures of phenol and 2AM. Melting point onsets are calculated using a linear extrapolated onset of the melting endotherm, and the midpoint of the glass transitions are plotted.

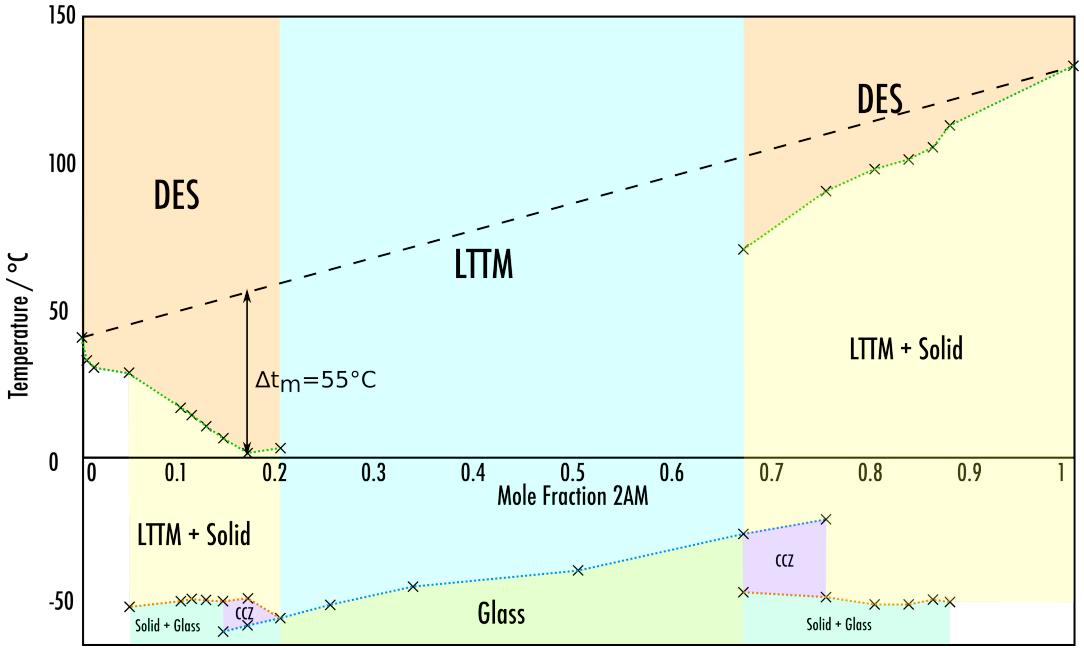

Figure E.9: Phase diagram for the eutectic system of phenol and 2AM, each point represents a phase transition as recorded from DSC.

Looking at trends with concentration, the three main sections described above are clear: the low x region where the mixture is a room temperature liquid; the LTTM region, where only glass transitions are seen; and the high x region where the crystallisation of the eutectic solvent occurs above room temperature. The phase diagram includes the metastable zone present because of the cold-crystallisation (CCZ) that occurs in many of the mixtures.

One of the most interesting features of the phase diagram is the trend in the position of the glass transitions that occur at low temperatures. There appears to be a glass transition temperature for all mixtures where there is a crystallisation (orange line – after cold-crystallisation), which suggests an optimum ratio for an amorphous phase that will always form.

To assess the stoichiometry of this amorphous phase, a 10 ml sample of 7:1 phenol:2AM was made and placed in the fridge (-6 °C) to crystallise. After crystallisation, the LTTM + solid mixture was gently stirred and then inverted. Over a time period of 24 hours, the liquid had drained to the bottom of the vial, with the solid remaining at the top. NMR of the extracted liquid was then carried out, and the stoichiometry determined by comparing the integrals of the phenol OH peak and 2AM NH peak (secondary amine). The resultant stoichiometry was close to a 4:1 mixture phenol:2AM. To follow on from this, the same procedure was carried out on a sample containing a 4:1 phenol:2AM mixture. Although some solid was still seen when the sample of this volume was cooled, the resulting stoichiometry from NMR was again close to a 4:1 phenol:2AM mixture.

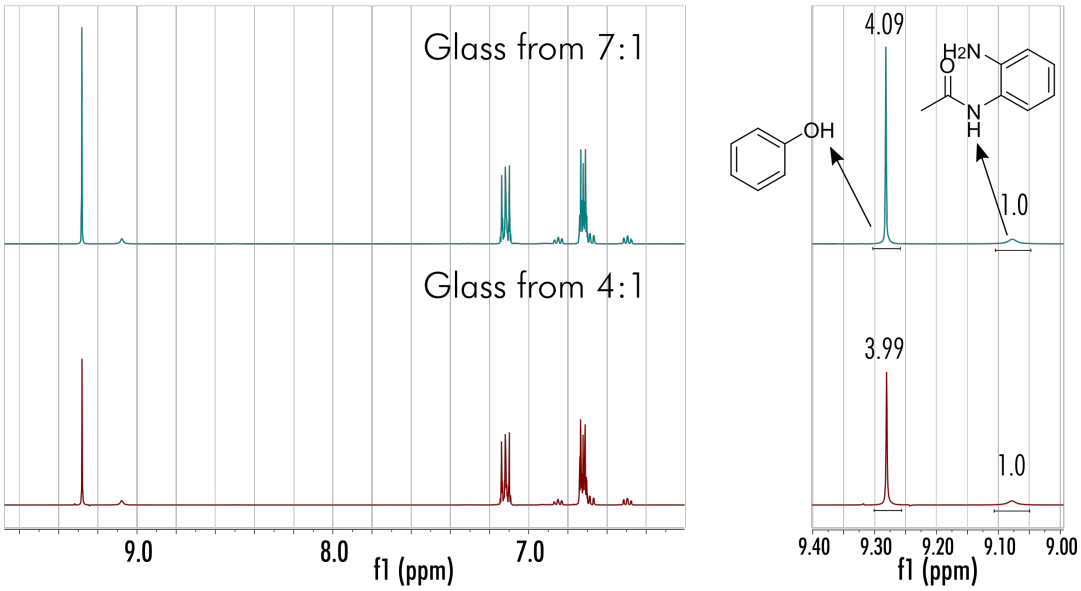

Figure E.10: ^{1}H NMR of the extracted liquid from cooled samples of 7:1 and 4:1 phenol:2AM. Representative peaks for both phenol and 2AM are highlighted with their chemical scheme, with an arrow pointing to the relevant hydrogen. Relative peak integrals are shown to give an approximate stoichiometry for each mixture.

To assess each of the points on the phase diagram more thoroughly, CXRD-DSC experiments were carried out of phenol:2AM VODES. For the first time, this study allowed a thorough analysis of both

the thermodynamics and structure across the phase diagram of a deep eutectic mixture. An example of the CXRD-DSC data is shown in Figure E.11. These data will allow for the phases presented in Figure E.9 to be analysed, which, along with the enthalpy data, allows for the stoichiometry of the glassy phases to be determined.

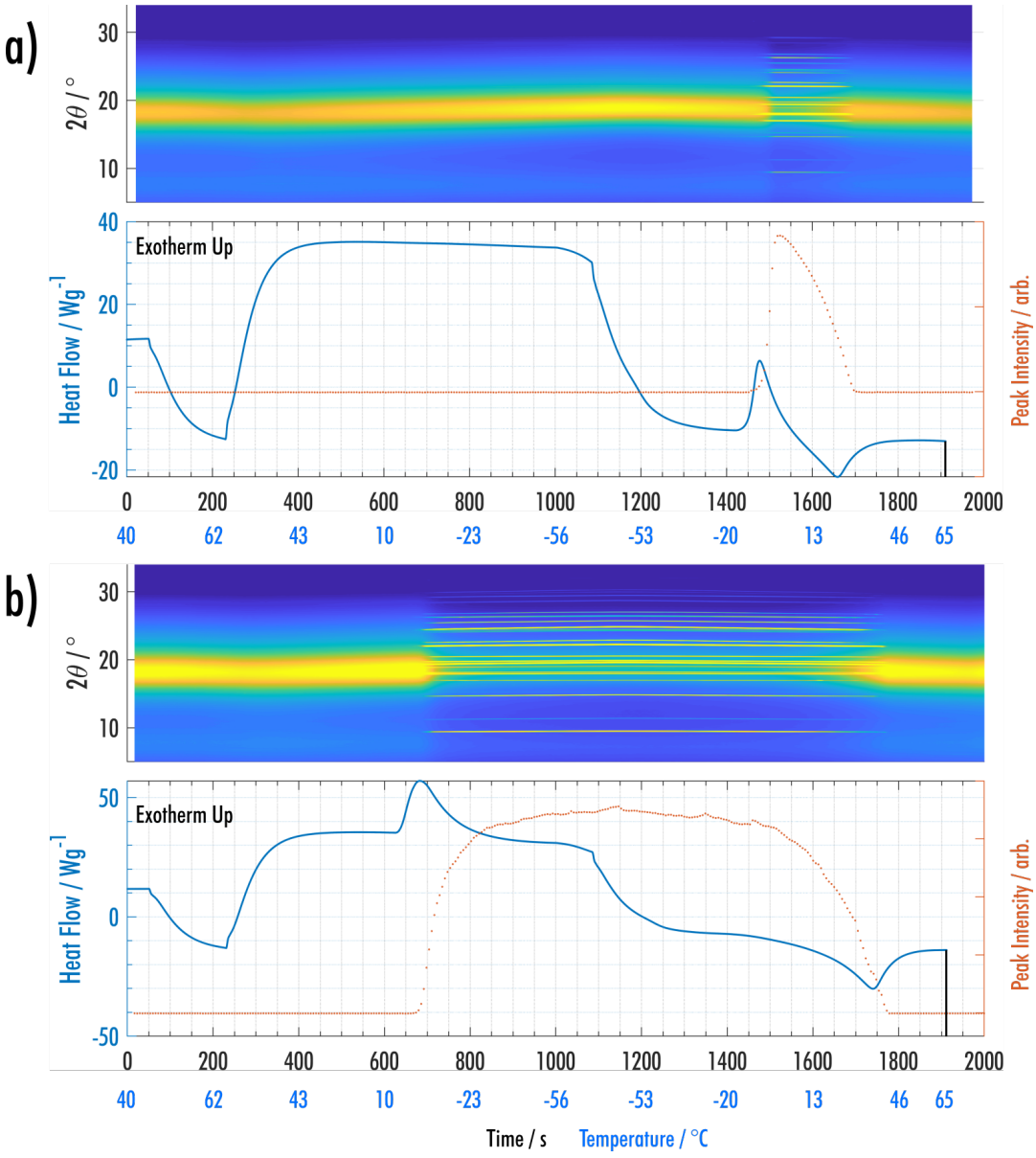

Figure E.11: CXRD-DSC measurements for VODES of 2AM:phenol of ratio a) 5:1 and b) 9:1. For each sample, both diffraction patterns (top) and DSC traces (bottom) are shown. The x-axis is shown with respect to time; however, the temperature is shown on the same axes to indicate the temperatures at which transitions occur. Integration of the diffraction peaks is shown to give an idea of how much crystalline material is present.

Evaluation of the diffraction patters from the CXRD-DSC highlighted that the crystalline structures formed below x_e was phenol and above x_e was 2AM. Using the known enthalpies of these phases, the glass compositions after crystallisation could be calculated, which are shown in Figure E.12. It is interesting to see that there are two different ratios of glassy solvents that form: a 4:1 phenol:2AM glass below x_e and a 1:2 phenol:2AM glass above x_e. Analysis of this data is ongoing, and it is hoped that this tutorial can set a strong foundation for the future structural analysis of deep eutectic systems.

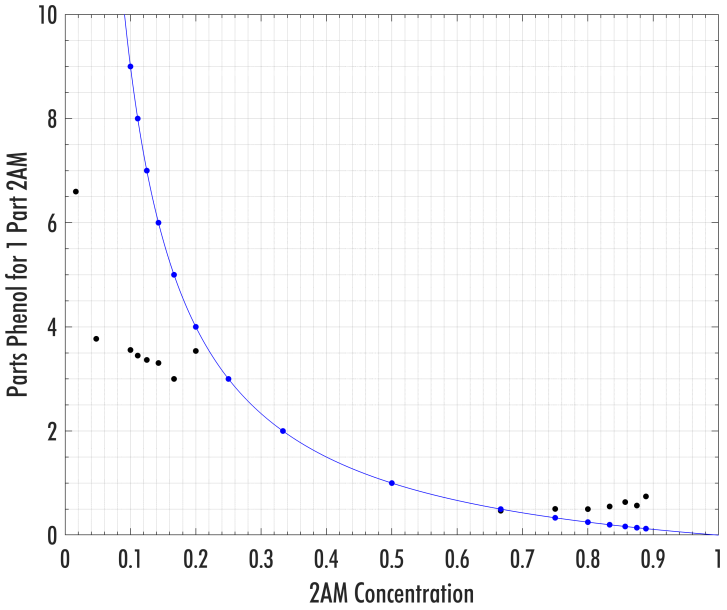

Figure E.12: Ratio of glassy phases formed after crystallisation events in VODESs containing phenol and 2'-aminoacetanilide. The blue line represents the concentration of the initial mixture, and the black dots represent the resultant ratio of the glassy phase.

APPENDIX F

LIST OF PUBLICATIONS

- **Color Differences Highlight Concomitant Polymorphism of Chalcones**, Hall, C. L., Guo, R., Potticary, J., Cremeens, M. E., Warren S. D., Andrusenko, I., Gemmu, M., Zwijntenburg M. A., Pridmore, N. E., Sparkes, H. A., Price., S. L. & Hall, S. R., *Crystal Growth & Design*, Aug 2020, 20, 10, 6346–6355.

- **Crystal structures of three functionalized chalcones: 4'-dimethylamino-3-nitrochalcone, 3-dimethylamino-3'-nitrochalcone and 3'-nitrochalcone**, Hall, C. L., Hamilton, V. A., Potticary, J., Cremeens, M. E., Pridmore, N. E., Sparkes, H. A., D'ambruoso, G. D., Warren S. D., Matsumoto, M. & Hall, S. R., *Acta Crystallographica E*, Aug 2020, 76, 1599-1604.

- **Metastable Crystalline Phase Formation in Deep Eutectic Systems Revealed by Simultaneous Synchrotron XRD and DSC**, Hall, C. L., Potticary, J., Hamilton, V. A., Gaisford, S., Buanz, A. & Hall, S. R., *Chemical Communications*, Aug 2020, 56, 10726-10729.

- **Racemic Conglomerate Formation via Crystallization of Metaxalone from Volatile Deep Eutectic Solvents**, Hamilton, V. A., Andrusenko, I., Potticary, J. L., Hall, C. L., Stenner, R. A., Mugnaioli, E., Lanza, A., Gemmi, M., & Hall, R. S., *Crystal Growth & Design*, Jun 2020, 20, 7, 4731–4739.

- **Crystallization of Volatile Deep Eutectic Solvents**, Potticary, J. L., Hall, C. L., Hamilton, V., McCabe, J. F. & Hall, S. R., *Crystal Growth & Design*, Apr 2020, 20, 2877-2844.

- **The Solubility and Stability of Heterocyclic Chalcones Compared to Trans-Chalcone**, Sweeting, S., Hall, C. L., Potticary, J. L., Pridmore, N. E., Warren, S., Cremeens, M., D'Ambrusco, G., Matsumoto, M. & Hall, S. R., *Acta Crystallographica B*, Feb 2020, 76, 1, p. 13-17.

- **Crystal structure and Hirshfeld surface analysis of (E)-3-(3-iodophenyl)-1- (4-iodophenyl)prop-2-en-1-one**, Spruce, K., Hall, C. L., Potticary, J. L., Pridmore, N. E., Cremeens, M., D'Ambrusco, G., Matsumoto, M., Warren, G., Warren, S. & Hall, S. R., *Acta Crystallographica E*, Jan 2020, 76, 1, p.72-76.

- **An Experimental and Computational Study into the Crystallisation Propensity of 2nd Generation Sulflower**, Jensen, T. T., Hall, C. L., Potticary, J. L., Andrusenko, I., Gemmi, M. & Hall, S. R., *Journal of the Chemical Society: Chemical Communications*, Nov 2019, 58, 32, p.14586-14589.

- **The Crystal Structure of Orthocetamol Solved by 3D Electron Diffraction**, Andrusenko, I., Hamilton, V., Mugnaioli, E., Lanza, A., Hall, C. L., Potticary, J., Hall, S. R. & Gemmi, M., *Angewandte Chemie*, Aug 2019, 58, 32, p.10919-10922.

- **Lamotrigine Ethanol Monosolvate**, Hall, C. L., Potticary, J., Sparkes, H. A., Pridmore, N. E. & Hall, S. R., *Acta Crystallographica E*, May 2018, 74, p.678-681.

REFERENCES

(1) Desiraju, G. R.; Vittal, J. J.; Ramanan, A. In *Crystal Engineering: A Textbook*, 2011; Chapter 1.

(2) Bernal, J. D. *Proceedings of the Royal Society of London. Series A, Containing Papers of a Mathematical and Physical Character* **1924**, *106*, 749–773.

(3) Dunitz, J. D.; Bernstein, J. *Accounts of Chemical Research* **1995**, *28*, 193–200.

(4) Jensen, T. T.; Hall, C. L.; Potticary, J.; Andrusenko, I.; Gemmi, M.; Hall, S. R. *Chemical Communications* **2019**, *55*, 14586–14589.

(5) Andrusenko, I.; Hamilton, V.; Mugnaioli, E.; Lanza, A.; Hall, C.; Potticary, J.; Hall, S. R.; Gemmi, M. *Angewandte Chemie - International Edition* **2019**, *58*, 10919–10922.

(6) Burckhardt, J. J. *Archive for History of Exact Sciences* **1967**, *4*, 235–246.

(7) Nespolo, M.; Aroyo, M. I. *Acta Crystallographica Section A: Foundations and Advances* **2016**, *72*, 523–538.

(8) Pauling, L. In *Journal of Chemical Education*, 1992; Chapter 1.

(9) Li, X.; Yang, X.; Zheng, X.; Bai, M.; Hu, D. *International Journal of Molecular Sciences* **2020**, *21*, 1–16.

(10) Lin, X.; Li, X.; Lin, X. *Molecules* **2020**, *25*, 1375.

(11) Li, T.; Mattei, A. In *Pharmaceutical Crystals: Science and Engineering*, 2018; Chapter 1, pp 1–512.

(12) Wan, X.; Woods, A. T.; Salgado-Montejo, A.; Velasco, C.; Spence, C. *Food Quality and Preference* **2015**, *45*, 171–182.

(13) Singh, H.; Tiwari, K.; Tiwari, R.; Pramanik, S. K.; Das, A. *Chemical Reviews* **2019**, *119*, 11718–11760.

(14) Moran, M. J. In *The Mechatronics Handbook*, 2002; Chapter 5.

(15) Ansermet, J.-P.; Brechet, S. D. In *Principles of Thermodynamics*, 2018; Chapter 4, pp 388–398.

(16) Marti, E. *Journal of Thermal Analysis* **1988**, *33*, 37–45.

(17) Hsieh, D. S.; Roberts, D.; Rosner, T.; Rosenbaum, T.; Lai, C.; Gao, Q. *Crystal Growth & Design* **2016**, *16*, 12–24.

(18) Braga, D.; Grepioni, F.; Maini, L.; Polito, M. *Structure and Bonding* **2009**, *132*, 25–50.

(19) Lévesque, A.; Maris, T.; Wuest, J. D. *Journal of the American Chemical Society* **2020**, *142*, 11873–11883.

(20) Censi, R.; Di Martino, P. *Molecules* **2015**, *20*, 18759–18776.

(21) Beyer, T.; Day, G. M.; Price, S. L. *Journal of the American Chemical Society* **2001**, *123*, 5086–5094.

(22) Braun, D. E.; Gelbrich, T.; Kahlenberg, V.; Laus, G.; Wieser, J.; Griesser, U. J. *New Journal of Chemistry* **2008**, *32*, 1677–1685.

(23) Nangia, A. *Accounts of Chemical Research* **2008**, *41*, 595–604.

(24) Debye, P. *Annalen der Physik* **1912**, *344*, 789–839.

(25) Lutsko, J. F. *New Journal of Physics* **2018**, *20*, 103015.

(26) Karthika, S.; Radhakrishnan, T. K.; Kalaichelvi, P. *Crystal Growth & Design* **2016**, *16*, 6663–6681.

(27) Vekilov, P. G. *Nanoscale* **2010**, *2*, 2346–2357.

(28) Vekilov, P. G. In *ACS Symposium Series*; American Chemical Society: 2020; Vol. 1358, pp 19–46.

(29) Gebauer, D.; Cölfen, H. *Nano Today* **2011**, *6*, 564–584.

(30) Sauter, A.; Roosen-Runge, F.; Zhang, F.; Lotze, G.; Feoktystov, A.; Jacobs, R. M.; Schreiber, F. *Faraday Discussions* **2015**, *179*, 41–58.

(31) Warzecha, M.; Safari, M. S.; Florence, A. J.; Vekilov, P. G. *Crystal Growth & Design* **2017**, *17*, 6668–6676.

(32) Cookman, J.; Hamilton, V.; Hall, S. R.; Bangert, U. *Scientific Reports* **2020**, *10*, 19156.

(33) Shahar, C.; Dutta, S.; Weissman, H.; Shimon, L. J. W.; Ott, H.; Rybtchinski, B. *Angewandte Chemie International Edition* **2016**, *55*, 179–182.

(34) Van Santen, R. A. *Journal of Physical Chemistry* **1984**, *88*, 5768–5769.

(35) Bauer, J.; Spanton, S.; Henry, R.; Quick, J.; Dziki, W.; Porter, W.; Morris, J. *Pharmaceutical Research* **2001**, *18*, 859–866.

(36) Lee, E. H. *Asian Journal of Pharmaceutical Sciences* **2014**, *9*, 163–175.

(37) Aguiar, A. J.; Krc, J.; Kinkel, A. W.; Samyn, J. C. *Journal of Pharmaceutical Sciences* **1967**, *56*, 847–853.

(38) Liebenberg, W.; De Villiers, M. M.; Wurster, D. E.; Swanepoel, E.; Dekker, T. G.; Lötter, A. P. *Drug Development and Industrial Pharmacy* **1999**, *25*, 1027–1033.

(39) Price, S. L. *Chemical Society Reviews* **2014**, *43*, 2098–2111.

(40) Price, S. L. *Acta Crystallographica Section B: Structural Science, Crystal Engineering and Materials* **2013**, *69*, 313–328.

(41) Haüy, R. J. *Gogué et Née de La Rochelle* **1784**.

(42) Docherty, R.; Clydesdale, G.; Roberts, K. J.; Bennema, P. *Journal of Physics D: Applied Physics* **1991**, *24*, 89–99.

(43) Donnay, J. D. H.; Harker, D. *Am. Mineral.* **1937**, *22*, 446.

(44) Stone, A. J.; Price, S. L. *The Journal of Physical Chemistry* **1988**, *92*, 3325–3335.

(45) Pudasaini, N.; Upadhyay, P. P.; Parker, C. R.; Hagen, S. U.; Bond, A. D.; Rantanen, J. *Organic Process Research and Development* **2017**, *21*, 571–577.

(46) Waknis, V.; Chu, E.; Schlam, R.; Sidorenko, A.; Badawy, S.; Yin, S.; Narang, A. S. *Pharmaceutical Research* **2014**, *31*, 160–172.

(47) Park, Y.; Koo, J. Y.; Choi, H. C. *Crystal Growth & Design* **2018**, *18*, 7239–7243.

(48) Zhu, D.; Zhang, S.; Cui, P.; Wang, C.; Dai, J.; Zhou, L.; Huang, Y.; Hou, B.; Hao, H.; Zhou, L.; Yin, Q. *Crystals* **2020**, *10*, 316.

(49) Rosbottom, I.; Ma, C. Y.; Turner, T. D.; O'Connell, R. A.; Loughrey, J.; Sadiq, G.; Davey, R. J.; Roberts, K. J. *Crystal Growth & Design* **2017**, *17*, 4151–4161.

(50) Lechuga-Ballesteros, D.; Rodríguez-Hornedo, N. *International Journal of Pharmaceutics* **1995**, *115*, 151–160.

(51) Munk, T.; Baldursdottir, S.; Hietala, S.; Rades, T.; Kapp, S.; Nuopponen, M.; Kalliomäki, K.; Tenhu, H.; Rantanen, J. *Molecular Pharmaceutics* **2012**, *9*, 1932–1941.

(52) Simone, E.; Steele, G.; Nagy, Z. K. *CrystEngComm* **2015**, *17*, 9370–9379.

(53) Constance, E. N.; Mohammed, M.; Mojibola, A.; Egiefameh, M.; Daodu, O.; Clement, T.; Ogundolie, T.; Nwawulu, C.; Aslan, K. *Journal of Physical Chemistry C* **2016**, *120*, 14749–14757.

(54) Song, L.; Zhao, F. Q.; Xu, S. Y.; Ju, X. H.; Ye, C. C. *Scientific Reports* **2020**, *10*, 2317.

(55) Aaltonen, J.; Allesø, M.; Mirza, S.; Koradia, V.; Gordon, K. C.; Rantanen, J. *European Journal of Pharmaceutics and Biopharmaceutics* **2009**, *71*, 23–37.

(56) Getsoian, A.; Lodaya, R. M.; Blackburn, A. C. *International Journal of Pharmaceutics* **2008**, *348*, 3–9.

(57) Parmar, M. M.; Khan, O.; Seton, L.; Ford, J. L. In *Crystal Growth & Design*, 2007; Vol. 7, pp 1635–1642.

(58) Ostergaard, I.; Szilagyi, B.; Nagy, Z. K.; De Diego, H. L.; Qu, H. *Crystal Growth & Design* **2020**, *20*, 1337–1346.

(59) Cavallo, D.; Gardella, L.; Alfonso, G. C.; Portale, G.; Balzano, L.; Androsch, R. *Colloid and Polymer Science* **2011**, *289*, 1073–1079.

(60) Hu, C.; Testa, C. J.; Shores, B. T.; Wu, W.; Shvedova, K.; Born, S. C.; Chattopadhyay, S.; Takizawa, B.; Mascia, S. *CrystEngComm* **2019**, *21*, 5076–5083.

(61) Bobrovs, R.; Seton, L.; Dempster, N. *CrystEngComm* **2015**, *17*, 5237–5251.

(62) Trask, A. V.; Shan, N.; Motherwell, W. D.; Jones, W.; Feng, S.; Tan, R. B.; Carpenter, K. J. *Chemical Communications* **2005**, 880–882.

(63) Boldyreva, E. V.; Shakhtshneider, T. P.; Ahsbahs, H.; Sowa, H.; Uchtmann, H. In *Journal of Thermal Analysis and Calorimetry*, 2002; Vol. 68, pp 437–452.

(64) Smith, S. J.; Montgomery, J. M.; Vohra, Y. K. *Journal of Physics Condensed Matter* **2016**, *28*, 035101.

(65) Bai, Y.; Yu, Z.; Liu, R.; Li, N.; Yan, S.; Yang, K.; Liu, B.; Wei, D.; Wang, L. *Scientific Reports* **2017**, *7*, 5321.

(66) Okumura, T.; Ishida, M.; Takayama, K.; Otsuka, M. *Journal of Pharmaceutical Sciences* **2006**, *95*, 689–700.

(67) Adrjanowicz, K.; Paluch, M.; Richert, R. *Physical Chemistry Chemical Physics* **2018**, *20*, 925–931.

(68) Alexander, L. F.; Radacsi, N. *CrystEngComm* **2019**, *21*, 5014–5031.

(69) Garetz, B. A.; Matic, J.; Myerson, A. S. *Physical Review Letters* **2002**, *89*, 175501.

(70) Alexander, A. J.; Camp, P. J. *Journal of Chemical Physics* **2019**, *150*, 040901.

(71) Potticary, J.; Terry, L. R.; Bell, C.; Papanikolopoulos, A. N.; Christianen, P. C. M.; Engelkamp, H.; Collins, A. M.; Fontanesi, C.; Kociok-Köhn, G.; Crampin, S.; Da Como, E.; Hall, S. R. *Nature Communications* **2016**, *7*, 11555.

(72) Yang, H.; Song, C. L.; Lim, Y. X.; Chen, W.; Heng, J. Y. *CrystEngComm* **2017**, *19*, 6573–6578.

(73) Parambil, J. V.; Poornachary, S. K.; Tan, R. B.; Heng, J. Y. *CrystEngComm* **2014**, *16*, 4927–4930.

(74) Parambil, J. V.; Poornachary, S. K.; Tan, R. B.; Heng, J. Y. *Journal of Crystal Growth* **2017**, *469*, 84–90.

(75) Parambil, J. V.; Poornachary, S. K.; Heng, J. Y.; Tan, R. B. *CrystEngComm* **2019**, *21*, 4122–4135.

(76) Hiremath, R.; Basile, J. A.; Varney, S. W.; Swift, J. A. *Journal of the American Chemical Society* **2005**, *127*, 18321–18327.

(77) Caridi, A.; Kulkarni, S. A.; Di Profio, G.; Curcio, E.; Ter Horst, J. H. *Crystal Growth & Design* **2014**, *14*, 1135–1141.

(78) Case, D. H.; Srirambhatla, V. K.; Guo, R.; Watson, R. E.; Price, L. S.; Polyzois, H.; Cockcroft, J. K.; Florence, A. J.; Tocher, D. A.; Price, S. L. *Crystal Growth & Design* **2018**, *18*, 5322–5331.

(79) Foster, J. A.; Steed, J. W. *Angewandte Chemie - International Edition* **2010**, *49*, 6718–6724.

(80) Foster, J. A.; Damodaran, K. K.; Maurin, A.; Day, G. M.; Thompson, H. P.; Cameron, G. J.; Bernal, J. C.; Steed, J. W. *Chemical Science* **2016**, *8*, 78–84.

(81) Srčič, S.; Kerč, J.; Urleb, U.; Zupančič, I.; Lahajnar, G.; Kofler, B.; Šmid-Korbar, J. *International Journal of Pharmaceutics* **1992**, *87*, 1–10.

(82) MacRae, C. F.; Sovago, I.; Cottrell, S. J.; Galek, P. T.; McCabe, P.; Pidcock, E.; Platings, M.; Shields, G. P.; Stevens, J. S.; Towler, M.; Wood, P. A. *Journal of Applied Crystallography* **2020**, *53*, 226–235.

(83) Bruker SAINT+, Madison, Wisconsin, USA, 2012.

(84) Sheldrick, G. M. Bruker AXS Area Detector Scaling and Absorption Correction, Madiston, Wisconsin, USA, 2001.

(85) Dolomanov, O. V.; Bourhis, L. J.; Gildea, R. J.; Howard, J. A.; Puschmann, H. *Journal of Applied Crystallography* **2009**, *42*, 339–341.

(86) Palatinus, L.; Chapuis, G. *Journal of Applied Crystallography* **2007**, *40*, 786–790.

(87) Palatinus, L.; Prathapa, S. J.; Van Smaalen, S. *Journal of Applied Crystallography* **2012**, *45*, 575–580.

(88) Sheldrick, G. M. *Acta Crystallographica Section C* **2015**, *71*, 3–8.

(89) Doebelin, N.; Kleeberg, R. *Journal of Applied Crystallography* **2015**, *48*, 1573–1580.

(90) Taylor, G. *Acta crystallographica. Section D, Biological crystallography* **2003**, *59*, 1881–90.

(91) Parsons, S. In *Acta Crystallographica - Section D Biological Crystallography*, International Union of Crystallography: 2003; Vol. 59, pp 1995–2003.

(92) Price, S. L. *Chemical Society Reviews* **2014**, *43*, 2098–2111.

(93) Kimura, F.; Kimura, T. *CrystEngComm* **2018**, *20*, 861–872.

(94) Kolb, U.; Gorelik, T.; Kübel, C.; Otten, M.; Hubert, D. *Ultramicroscopy* **2007**, *107*, 507–513.

(95) Lanza, A.; Margheritis, E.; Mugnaioli, E.; Cappello, V.; Garau, G.; Gemmi, M. *IUCrJ* **2019**, *6*, 178–188.

(96) Gonen, T. *Acta Crystallographica Section A Foundations and Advances* **2014**, *70*, 1063–1063.

(97) PerkinElmer *Control* **2004**, 1–72.

(98) TA Instruments *Thermal Analysis & Rheology* **2012**, 12.

(99) Basham, M. et al. *Journal of Synchrotron Radiation* **2015**, *22*, 853–858.

(100) Filik, J.; Ashton, A. W.; Chang, P. C.; Chater, P. A.; Day, S. J.; Drakopoulos, M.; Gerring, M. W.; Hart, M. L.; Magdysyuk, O. V.; Michalik, S.; Smith, A.; Tang, C. C.; Terrill, N. J.; Wharmby, M. T.; Wilhelm, H. *Journal of Applied Crystallography* **2017**, *50*, 959–966.

(101) Frisch, M. J. et al. *Gaussian 09 Revision C.01* **2010**, Gaussian Inc., Wallingford CT.

(102) Dennington, R.; Keith, T.; Millam, J. GaussView, Version 5. 2009.

(103) Stone, A. J. *Journal of Chemical Theory and Computation* **2005**, *1*, 1128–1132.

(104) Potticary, J.; Hall, C.; Hamilton, V.; McCabe, J. F.; Hall, S. R. *Crystal Growth & Design* **2020**, *20*, 2877–2884.

(105) Sudha, C.; Srinivasan, K. *Crystal Research and Technology* **2014**, *49*, 865–872.

(106) Wang, Y.; Liang, Z. *CrystEngComm* **2017**, *19*, 3198–3205.

(107) Takiyama, H.; Minamisono, T.; Osada, Y.; Matsuoka, M. *Chemical Engineering Research and Design* **2010**, *88*, 1242–1247.

(108) Kitamura, M.; Hara, T.; Takimoto-Kamimura, M. *Crystal Growth & Design* **2006**, *6*, 1945–1950.

(109) Wilkes, J. S. *Green Chemistry* **2002**, *4*, 73–80.

(110) Walden, P. *Bulletin de l'Académie Impériale des Sciences de St.-Pétersbourg.* **1914**, *8*, 405–422.

(111) Klein, N.; Leveritt, C. S. *Thermochimica Acta* **1990**, *166*, 231–239.

(112) Gontrani, L.; Caminiti, R.; Salma, U.; Campetella, M. *Chemical Physics Letters* **2017**, *684*, 304–309.

(113) Hurley, F. H.; WIer, T. P. *Journal of The Electrochemical Society* **1951**, *98*, 207.

(114) Yoke, J. T.; Weiss, J. F.; Tollin, G. *Inorganic Chemistry* **1963**, *2*, 1210–1216.

(115) Porterfield, W. W.; Yoke, J. T. In *Inorganic Compounds with Unusual Properties*, 1976, pp 104–111.

(116) Wilkes, J. S.; Zaworotko, M. J. *Journal of the Chemical Society, Chemical Communications* **1992**, 965–967.

(117) Freemantle, M. *Chemical and Engineering News* **1998**, *76*, 32–37.

(118) Chauvin, Y.; Gilbert, B.; Guibard, I. *Journal of the Chemical Society, Chemical Communications* **1990**, 1715–1716.

(119) Earle, M. J.; McCormac, P. B.; Seddon, K. R. *Chemical Communications* **1998**, 2245–2246.

(120) Fischer, T.; Sethi, A.; Welton, T.; Woolf, J. *Tetrahedron Letters* **1999**, *40*, 793–796.

(121) Xia, Z.; Li, J.; Zhang, J.; Zhang, X.; Zheng, X.; Zhang, J. *Journal of Bioresources and Bioproducts* **2020**, *5*, 79–95.

(122) Ye, C.; Liu, W.; Chen, Y.; Yu, L. *Chemical Communications* **2001**, *21*, 2244–2245.

(123) Salar-García, M. J.; Ortiz-Martínez, V. M.; Hernández-Fernández, F. J.; de los Ríos, A. P.; Quesada-Medina, J. *Journal of Hazardous Materials* **2017**, *321*, 484–499.

(124) Egorova, K. S.; Gordeev, E. G.; Ananikov, V. P. *Chemical Reviews* **2017**, *117*, 7132–7189.

(125) Abbott, A. P.; Capper, G.; Davies, D. L.; Rasheed, R. K.; Tambyrajah, V. *Chemical Communications* **2003**, 70–71.

(126) Smith, E. L.; Abbott, A. P.; Ryder, K. S. *Chemical Reviews* **2014**, *114*, 11060–11082.

(127) Ashworth, C. R.; Matthews, R. P.; Welton, T.; Hunt, P. A. *Phys. Chem. Chem. Phys* **2016**, *18*, 18145.

(128) Qin, H.; Hu, X.; Wang, J.; Cheng, H.; Chen, L.; Qi, Z. *Green Energy and Environment* **2019**, *5*, 8–21.

(129) Osowska, N.; Ruzik, L. *Food Analytical Methods* **2019**, *12*, 926–935.

(130) Liu, F.; Xue, Z.; Zhao, X.; Mou, H.; He, J.; Mu, T. *Chemical Communications* **2018**, *54*, 6140–6143.

(131) Emami, S.; Shayanfar, A. *Pharmaceutical Development and Technology* **2020**, 1–18.

(132) Choi, Y. H.; van Spronsen, J.; Dai, Y.; Verberne, M.; Hollmann, F.; Arends, I. W.; Witkamp, G. J.; Verpoorte, R. *Plant Physiology* **2011**, *156*, 1701–1705.

(133) Aroso, I. M.; Silva, J. C.; Mano, F.; Ferreira, A. S.; Dionísio, M.; Sá-Nogueira, I.; Barreiros, S.; Reis, R. L.; Paiva, A.; Duarte, A. R. C. *European Journal of Pharmaceutics and Biopharmaceutics* **2016**, *98*, 57–66.

(134) Hammond, O. S.; Bowron, D. T.; Edler, K. J. *Green Chem.* **2016**, *18*, 2736–2744.

(135) Krossing, I.; Slattery, J. M.; Daguenet, C.; Dyson, P. J.; Oleinikova, A.; Weingärtner, H. *Journal of the American Chemical Society* **2006**, *128*, 13427–13434.

(136) Smith, S. J.; Bishop, M. M.; Montgomery, J. M.; Hamilton, T. P.; Vohra, Y. K. *Journal of Physical Chemistry A* **2014**, *118*, 6068–6077.

(137) Telford, R.; Seaton, C. C.; Clout, A.; Buanz, A.; Gaisford, S.; Williams, G. R.; Prior, T. J.; Okoye, C. H.; Munshi, T.; Scowen, I. J. *Chemical Communications* **2016**, *52*, 12028–12031.

(138) Shtukenberg, A. G.; Tan, M.; Vogt-Maranto, L.; Chan, E. J.; Xu, W.; Yang, J.; Tuckerman, M. E.; Hu, C. T.; Kahr, B. *Crystal Growth & Design* **2019**, *19*, 4070–4080.

(139) Thomas, L. H.; Wales, C.; Zhao, L.; Wilson, C. C. *Crystal Growth & Design* **2011**, *11*, 1450–1452.

(140) Mijangos, F.; Varona, F.; Villota, N. *Environmental Science and Technology* **2006**, *40*, 5538–5543.

(141) FDA Inactive Ingredients Search for Approved Drug Products, 2020.

(142) Tirado-Rives, J.; Jorgensen, W. L. *Journal of Chemical Theory and Computation* **2008**, *4*, 297–306.

(143) Wöhler; Liebig *Annalen der Pharmacie* **1832**, *3*, 249–282.

(144) Blagden, N.; Davey, R.; Dent, G.; Song, M.; David, W. I.; Pulham, C. R.; Shankland, K. *Crystal Growth & Design* **2005**, *5*, 2218–2224.

(145) Thun, J.; Seyfarth, L.; Senker, J.; Dinnebier, R. E.; Breu, J. *Angewandte Chemie - International Edition* **2007**, *46*, 6729–6731.

(146) Butterhof, C.; Martin, T.; Ectors, P.; Zahn, D.; Niemietz, P.; Senker, J.; Näther, C.; Breu, J. *Crystal Growth & Design* **2012**, *12*, 5365–5372.

(147) Fischer, F.; Greiser, S.; Pfeifer, D.; Jäger, C.; Rademann, L.; Emmerling, F. *Angewandte Chemie*, *128*, 14493–14497.

(148) Back, K. R.; Davey, R. J.; Grecu, T.; Hunter, C. A.; Taylor, L. S. *Crystal Growth & Design* **2012**, *12*, 6110–6117.

(149) Aitipamula, S.; Chow, P. S.; Tan, R. B. *Crystal Growth & Design* **2010**, *10*, 2229–2238.

(150) Sarmah, K. K.; Boro, K.; Arhangelskis, M.; Thakuria, R. *CrystEngComm* **2017**, *19*, 826–833.

(151) World Health Organization (WHO) *Model list of essential medicines - 21st List*; tech. rep.; 2019.

(152) Carpy, A.; Léger, J. M.; Melchiorre, C. *Acta Crystallographica Section C Crystal Structure Communications* **1985**, *41*, 624–627.

(153) Seaton, C. C.; Parkin, A. *Crystal Growth & Design* **2011**, *11*, 1502–1511.

(154) Moribe, K.; Tsuchiya, M.; Tozuka, Y.; Yamaguchi, K.; Oguchi, T.; Yamamoto, K. *Journal of Inclusion Phenomena* **2006**, *54*, 9–16.

(155) Stevenson, E. L.; Lancaster, R. W.; Buanz, A. B.; Price, L. S.; Tocher, D. A.; Price, S. L. *CrystEngComm* **2019**, *21*, 2154–2163.

(156) Hamilton, V.; Andrusenko, I.; Potticary, J.; Hall, C.; Stenner, R.; Mugnaioli, E.; Lanza, A. E.; Gemmi, M.; Hall, S. R. *Crystal Growth & Design* **2020**, *20*, 4731–4739.

(157) Earle, M. J.; Esperança, J. M.; Gilea, M. A.; Lopes, J. N.; Rebelo, L. P.; Magee, J. W.; Seddon, K. R.; Widegren, J. A. *Nature* **2006**, *439*, 831–834.

(158) Hall, C. L.; Potticary, J.; Hamilton, V.; Gaisford, S.; Buanz, A.; Hall, S. R. *Chemical Communications* **2020**, *56*, 10726–10729.

(159) Chiu, M.; Prenner, E. *Journal of Pharmacy and Bioallied Sciences* **2011**, *3*, 39–59.

(160) Clas, S. D.; Dalton, C. R.; Hancock, B. C. *Pharmaceutical Science and Technology Today* **1999**, *2*, 311–320.

(161) Kollau, L. J.; Vis, M.; Van Den Bruinhorst, A.; De With, G.; Tuinier, R. In *Pure and Applied Chemistry*, 2019; Vol. 91, pp 1341–1349.

(162) Morrison, H. G.; Sun, C. C.; Neervannan, S. *International Journal of Pharmaceutics* **2009**, *378*, 136–139.

(163) Gaisford, S.; Buanz, A. B.; Jethwa, N. *Journal of Pharmaceutical and Biomedical Analysis* **2010**, *53*, 366–370.

(164) Gaisford, S.; Buanz, A. B. *Journal of Thermal Analysis and Calorimetry* **2011**, *106*, 221–226.

(165) Yoshioka, M.; Hancock, B. C.; Zografi, G. *Journal of Pharmaceutical Sciences* **1994**, *83*, 1700–1705.

(166) Ford, J. L.; Mann, T. E. *Advanced Drug Delivery Reviews* **2012**, *64*, 422–430.

(167) Buanz, A. B.; Parkinson, G. N.; Gaisford, S. *Crystal Growth & Design* **2011**, *11*, 1177–1181.

(168) Saunders, M.; Podluii, K.; Shergill, S.; Buckton, G.; Royall, P. *International Journal of Pharmaceutics* **2004**, *274*, 35–40.

(169) Faroongsarng, D.; Kadejinda, W.; Sunthornpit, A. *AAPS PharmSciTech* **2000**, *1*, 62–68.

(170) Faroongsarng, D. *AAPS PharmSciTech* **2016**, *17*, 572–577.

(171) Meng, X.; Ballerat-Busserolles, K.; Husson, P.; Andanson, J. M. *New Journal of Chemistry* **2016**, *40*, 4492–4499.

(172) Hall, C. L.; Potticary, J.; Hamilton, V.; Gaisford, S.; Buanz, A.; Hall, S. R. *Chemical Communications* **2020**, *56*, 10726–10729.

(173) Shawe, J.; Riesen, R.; Widmann, J.; Schubnell, M. Interpreting DSC curves Part 1: Dynamic measurements, 2000.

(174) Clout, A.; Buanz, A. B.; Prior, T. J.; Reinhard, C.; Wu, Y.; O'Hare, D.; Williams, G. R.; Gaisford, S. *Analytical Chemistry* **2016**, *88*, 10111–10117.

(175) Clout, A. E.; Buanz, A. B.; Gaisford, S.; Williams, G. R. *Chemistry - A European Journal* **2018**, *24*, 13573–13581.

(176) Askin, S.; Cockcroft, J. K.; Price, L. S.; Gonçalves, A. D.; Zhao, M.; Tocher, D. A.; Williams, G. R.; Gaisford, S.; Craig, D. Q. *Crystal Growth & Design* **2019**, *19*, 2751–2757.

(177) Pang, Y.; Buanz, A.; Telford, R.; Magdysyuk, O. V.; Gaisford, S.; Williams, G. R. *Journal of Applied Crystallography* **2019**, *52*, 1264–1270.

(178) Clout, A. E.; Buanz, A. B.; Pang, Y.; Tsui, W. M.; Yan, D.; Parkinson, G.; Prior, T. J.; Bučar, D. K.; Gaisford, S.; Williams, G. R. *Chemistry - A European Journal* **2020**, *26*, 14645–14653.

(179) Gillier-Pandraud, H. *Bulletin de la Societe Chimique de France* **1967**, 1988–1995.

(180) Hansen, L. K.; Perlovich, G. L.; Bauer-Brandl, A. *Acta Crystallographica Section E: Structure Reports Online* **2006**, *62*, 3627–3628.

(181) McGregor, L.; Rychkov, D. A.; Coster, P. L.; Day, S.; Drebushchak, V. A.; Achkasov, A. F.; Nichol, G. S.; Pulham, C. R.; Boldyreva, E. V. *CrystEngComm* **2015**, *17*, 6183–6192.

(182) Pagola, S.; Stephens, P. W. *Acta Crystallographica Section C: Crystal Structure Communications* **2009**, *65*, 583–586.

(183) David, W. I.; Shankland, K.; Pulham, C. R.; Blagden, N.; Davey, R. J.; Song, M. *Angewandte Chemie - International Edition* **2005**, *44*, 7032–7035.

(184) Hall, S. R.; Hall, C. L.; Guo, R.; Potticary, J.; Cremeens, M. E.; Warren, S. D.; Andrusenko, I.; Gemmi, M.; Zwijnenburg, M. A.; Sparkes, H. A.; Pridmore, N. E.; Price, S. L. *Crystal Growth & Design* **2020**, *20*, 6346–6355.

(185) Yu, L. *Journal of Physical Chemistry A* **2002**, *106*, 544–550.

(186) Autschbach, J. *Journal of Chemical Education* **2007**, *84*, 1840–1845.

(187) Karwowski, J. *Journal of Molecular Structure* **1973**, *19*, 143–166.

(188) Rant, U.; Scherf, U.; Rehahn, M.; Galda, P.; Brédas, J. L.; Zojer, E. *Synthetic Metals* **2002**, *127*, 241–245.

(189) Kasha, M. *Discussions of the Faraday Society* **1950**, *9*, 14–19.

(190) KASHA, M. *Radiation research* **1960**, *Suppl 2*, 243–275.

(191) Koopmans, T. *Physica* **1934**, *1*, 104–113.

(192) Escudero, D.; Laurent, A. D.; Jacquemin, D. In *Handbook of Computational Chemistry*, 2017, pp 927–961.

(193) Nogueira, B. A.; Castiglioni, C.; Fausto, R. *Communications Chemistry* **2020**, *3*, 34.

(194) Stephenson, G. A.; Borchardt, T. B.; Byrn, S. R.; Bowyer, J.; Bunnell, C. A.; Snorek, S. V.; Yu, L. *Journal of Pharmaceutical Sciences* **1995**, *84*, 1385–1386.

(195) Fletton, R. A.; Lancaster, R. W.; Harris, R. K.; Kenwright, A. M.; Packer, K. J.; Waters, D. N.; Yeadon, A. *Journal of the Chemical Society, Perkin Transactions 2* **1986**, 1705–1709.

(196) Li, H.; Stowell, J. G.; Borchardt, T. B.; Byrn, S. R. *Crystal Growth & Design* **2006**, *6*, 2469–2474.

(197) Harty, E. L.; Ha, A. R.; Warren, M. R.; Thompson, A. L.; Allan, D. R.; Goodwin, A. L.; Funnell, N. P. *Chemical Communications* **2015**, *51*, 10608–10611.

(198) Braun, D. E.; Gelbrich, T.; Jetti, R. K.; Kahlenberg, V.; Price, S. L.; Griesser, U. J. *Crystal Growth & Design* **2008**, *8*, 1977–1989.

(199) Kazmaier, P. M.; Hoffmann, R. *Journal of the American Chemical Society* **1994**, *116*, 9684–9691.

(200) Klebe, G.; Graser, F.; Hädicke, E.; Berndt, J. *Acta Crystallographica Section B* **1989**, *45*, 69–77.

(201) Zhuang, C.; Zhang, W.; Sheng, C.; Zhang, W.; Xing, C.; Miao, Z. *Chemical Reviews* **2017**, *117*, 7762–7810.

(202) Rammohan, A.; Reddy, J. S.; Sravya, G.; Rao, C. N.; Zyryanov, G. V. *Environmental Chemistry Letters* **2020**, *18*, 433–458.

(203) Aoki, N.; Muko, M.; Ohta, E.; Ohta, S. *Journal of Natural Products* **2008**, *71*, 1308–1310.

(204) Nowakowska, Z. *European Journal of Medicinal Chemistry* **2007**, *42*, 125–137.

(205) Nielsen, S. F.; Boesen, T.; Larsen, M.; Schønning, K.; Kromann, H. *Bioorganic and Medicinal Chemistry* **2004**, *12*, 3047–3054.

(206) Szliszka, E.; Czuba, Z. P.; Mazur, B.; Sedek, L.; Paradysz, A.; Krol, W. *International Journal of Molecular Sciences* **2010**, *11*, 1–13.

(207) Ducki, S. *Anti-Cancer Agents in Medicinal Chemistry* **2012**, *9*, 336–347.

(208) Batovska, D.; Todorova, I. *Current Clinical Pharmacology* **2010**, *5*, 1–29.

(209) V. Kostanecki, S.; Tambor, J. *Berichte der deutschen chemischen Gesellschaft* **1899**, *32*, 1921–1926.

(210) Rao, A.; Wilson, M. W.; Albert-Seifried, S.; Di Pietro, R.; Friend, R. H. *Physical Review B - Condensed Matter and Materials Physics* **2011**, *84*, 195411.

(211) Sharifzadeh, S.; Biller, A.; Kronik, L.; Neaton, J. B. *Physical Review B - Condensed Matter and Materials Physics* **2012**, *85*, 125307.

(212) Sharifzadeh, S.; Darancet, P.; Kronik, L.; Neaton, J. B. *Journal of Physical Chemistry Letters* **2013**, *4*, 2197–2201.

(213) Li, J.; D'Avino, G.; Duchemin, I.; Beljonne, D.; Blase, X. *Journal of Physical Chemistry Letters* **2016**, *7*, 2814–2820.

(214) Xue, Y.; Mou, J.; Liu, Y.; Gong, X.; Yang, Y.; An, L. *Central European Journal of Chemistry* **2010**, *8*, 928–936.

(215) Sukhorukov, A. A.; Zadorozhnyi, B. A.; Lavrushin, V. F. *Theoretical and Experimental Chemistry* **1973**, *6*, 490–494.

(216) Xue, Y.; Gong, X. *Journal of Molecular Structure* **2009**, *901*, 226–231.

(217) Komarova, K. G.; Sakipov, S. N.; Plotnikov, V. G.; Alfimov, M. V. *Journal of Luminescence* **2015**, *164*, 57–63.

(218) Jiang, Y. B.; Wang, X. J.; Lin, L. *Journal of Physical Chemistry* **1994**, *98*, 12367–12372.

(219) Jiang, Y. B.; Wang, X. J. *Journal of Photochemistry and Photobiology, A: Chemistry* **1994**, *81*, 205–209.

(220) Niu, C. G.; Guan, A. L.; Zeng, G. M.; Liu, Y. G.; Li, Z. W. *Analytica Chimica Acta* **2006**, *577*, 264–270.

(221) Sweeting, S. G.; Hall, C. L.; Potticary, J.; Pridmore, N. E.; Warren, S. D.; Cremeens, M. E.; D'Ambruoso, G. D.; Matsumoto, M.; Hall, S. R. *Acta Crystallographica Section B: Structural Science, Crystal Engineering and Materials* **2020**, *76*, 13–17.

(222) Guo, R.; Uddin, M. N.; Price, L. S.; Price, S. L. *Journal of Physical Chemistry A* **2020**, *124*, 1409–1420.

(223) Hall, C. L.; Hamilton, V.; Potticary, J.; Cremeens, M. E.; Pridmore, N. E.; Sparkes, H. A.; D'ambruoso, G. D.; Warren, S. D.; Matsumoto, M.; Hall, S. R. *Acta Crystallographica Section E: Crystallographic Communications* **2020**, *76*, 1599–1604.

(224) Christy, A. A.; Kvalheim, O. M.; Velapoldi, R. A. *Vibrational Spectroscopy* **1995**, *9*, 19–27.

(225) Mir, F. A. *Results in Physics* **2014**, *4*, 103–104.

(226) Zhang, S.; Lü, F.; Gao, L.; Ding, L.; Fang, Y. *Langmuir* **2007**, *23*, 1584–1590.

(227) Ding, L.; Fang, Y. *Chemical Society Reviews* **2010**, *39*, 4258–4273.

(228) Shanmugaraju, S.; Joshi, S. A.; Mukherjee, P. S. *Journal of Materials Chemistry* **2011**, *21*, 9130–9138.

(229) Brandenburg, J. G.; Potticary, J.; Sparkes, H. A.; Price, S. L.; Hall, S. R. *Journal of Physical Chemistry Letters* **2017**, *8*, 4319–4324.

(230) Burger, A.; Ramberger, R. *Mikrochimica Acta* **1979**, *72*, 259–271.

(231) Jacquemin, D.; Moore, B.; Planchat, A.; Adamo, C.; Autschbach, J. *Journal of Chemical Theory and Computation* **2014**, *10*, 1677–1685.

(232) Bukalov, S. S.; Leites, L. A.; Lyssenko, K. A.; Aysin, R. R.; Korlyukov, A. A.; Zubavichus, J. V.; Chernichenko, K. Y.; Balenkova, E. S.; Nenajdenko, V. G.; Antipin, M. Y. *Journal of Physical Chemistry A* **2008**, *112*, 10949–10961.

(233) Ladenburg, A. *Berichte der deutschen chemischen Gesellschaft* **1876**, *9*, 1524–1530.

(234) Hall, C.; Potticary, J.; Hamilton, V.; Sparkes, H. A.; Pridmore, N. E.; Hall, S. R. *CSD Communication* **2021**, DOI: 10.5517/ccdc.csd.cc279p19.

(235) Hall, C.; Potticary, J.; Hamilton, V.; Sparkes, H. A.; Pridmore, N. E.; Hall, S. R. *CSD Communication* **2021**, DOI: 10.5517/ccdc.csd.cc279p2b.